

Multisource Evaporation of Perovskite Solar Cells



Yu-Hsien Chiang

Department of Physics
University of Cambridge

This thesis is submitted for the degree of
Doctor of Philosophy

Girton College

September 2022

Declaration

I hereby declare that my thesis: is the result of my own work and includes nothing which is the outcome of work done in collaboration except as declared in the Preface and specified in the text. It is not substantially the same as any that I have submitted, or, is being concurrently submitted for a degree, diploma or other qualification at the University of Cambridge or any other University or similar institution except as declared in the Preface and specified in the text. I further state that no substantial part of my dissertation has already been submitted, or, is being concurrently submitted for any such degree, diploma or other qualification at the University of Cambridge or any other University of similar institution except as declared in the Preface and specified in the text. This thesis does not exceed the prescribed word limit from the Degree Committee.

Multisource evaporation of perovskite solar cells

Abstract

Yu-Hsien Chiang

This thesis focuses on the emerging semiconductor family of metal-halide perovskites for their application in solar cells. Halide perovskite materials have shown several promising properties, such as high absorption coefficient, low exciton binding energy, high charge mobility, long diffusion length and low annealing temperature. Moreover, their tunable bandgaps, with emission from the blue to near-infrared spectrum region possible, demonstrates their potential for different optoelectronic applications, such as solar cells, light-emitting diodes and transistors.

The device performance of perovskite solar cells has increased rapidly to 25.7% in 12 years. This incredible improvement is based on a myriad of research works, mostly on solution-processed perovskites, as solution processing allows rapid screening of experiment protocols in the lab. However, scaling up perovskite solar cells for real-world impact is critical to solving energy demand crisis and climate change by using renewable energy with low-carbon emissions. Vacuum deposition, an industrially compatible deposition method, can provide smooth, uniform and solvent-free thin films for solar cell fabrication.

In this thesis, the deposition and characterisation of multisource evaporated perovskite films with MA-free composition for solar cells has been studied. Chapter 4 shows that the underlying substrate can affect the perovskite quality, form different grain sizes and preferred structure orientations. Excess PbI_2 during the evaporation can improve the film moisture stability and photoluminescence quantum efficiency. The importance of deposition rate is also highlighted here, showing the issue with halide uniformity. Furthermore, non-radiative losses in p-i-n architecture has been identified. After optimising the amount of excess PbI_2 , solar cell device performance of 18.1% can be achieved, which was the highest MA-free perovskite solar cell from multisource evaporation system at the time of the work.

In chapter 5, the loss between perovskite and hole-transporting layer is minimised, leading to an even further improved device performance of 20.7% from a bandgap of 1.62 eV perovskite.

A tandem solar cell is a promising route to exceed the single-junction Shockley–Queisser limit. A wide bandgap perovskite with bandgap from 1.62 eV to 1.8 eV, fabricated by multisource evaporation, is explored by controlling the PbBr_2 evaporation rate. The photoluminescence, time-resolved photoluminescence and phase segregation have been studied and these results indicate the most optimised material under these conditions for tandem solar cells has a 1.77 eV bandgap. Perovskite solar cells with these bandgap absorbers have been fabricated and tested. Their device open-circuit voltage (V_{OC}) increases monotonically to 1.24 V for a bandgap of 1.77 eV perovskite, compared to a V_{OC} of 1.1 V from a bandgap of 1.62 eV. To understand the non-radiative loss, PLQE measurements have been performed, and the surface passivation treatment by Ethane-1,2-diammonium iodide (EDAI) leads to an improvement in V_{OC} and fill factor. The narrow bandgap perovskite with Pb/Sn composition is prepared and the film morphology, crystal structure, and photoluminescence has been characterised and optimised to make all-perovskite tandem solar cell. The same EDAI passivation is also useful for the Pb/Sn perovskite as surface passivation by further improving the device V_{OC} and FF. The interconnect layer by atomic layer deposition for SnO_x layer is developed to connect the wide and narrow bandgap perovskite. A 2-terminal all-perovskite tandem solar cell with a PCE of 24.1% is shown, where at least one subcell is prepared by multisource evaporation.

Chapter 6 presents the versatility of evaporated perovskite in different applications. We have demonstrated a proof of concept of evaporated perovskite for perovskite/Si tandem solar cells, solar fuel device and large-scale deposition. Finally, chapter 7 provides a conclusion and outlook. To sum up, this thesis provides a deep understanding of the multisource evaporation process, non-radiative loss in the device, solar cells optimisation and all-perovskite tandem solar cells.

Acknowledgement

There are so many people to acknowledge during my PhD journey. First, I would like to thank my supervisors, Prof. Sam Stranks and Dr Miguel Anaya, for their constant support, guidance and patience over the last four years. They provided more than sufficient freedom for me to explore various projects. Their insights, knowledge, and experience are helping me to stick to the right path to the end of my PhD. Furthermore, their excitement about science deeply affects, inspires, and motivates me. All my works presented in this thesis or ongoing projects cannot be done or continued without them at every step.

I would like to thank Dr Miguel Anaya, Kyle Fronha and Cullen Chosy for the support of hyper spectral measurement and valuable scientific discussion. I would like to thank Hayden Salway for the help with TCSPC measurement and the support from Anna Abfalterer to setup and calibrate a new TCSPC system. I would like to thank Dr George Kakavelakis for sharing his valuable experience in making perovskite solar cells and providing useful discussion. I would like to thank Dr Elena Avila, who helps me, provides the delicious caramelised peanuts, and organises the lab.

Many thanks go to people in the optoelectronic group for providing a friendly and joyful environment for discussion and work. A special acknowledgement to Richard Gymer, Steve Haws, Cheng Liu and Giovanni Orlando for technical support, which are really helpful. Also, I appreciate the liquid N₂ team for providing a lot of dewars for the perovskite evaporator.

I am grateful to my funding sources: the Taiwan-Cambridge Trust scholarship and the RankPrize fund, for supporting my research. I am thankful to my college, Girton, for providing modern accommodation during my first-year PhD. Also, I would like to thank my tutor Sophia Shellard-Von Weikersthal, for helping me source any potential funding. I would like to thank Prof. Michael McCarthy and Jeanne McCarten for providing very meaningful and joyful lessons.

Besides the research, I would like to thank Miguel Anaya, Kyle Fronha, Elena Avila, Tiarnan Doherty, Stuart MacPherson, Darcy Unson, Daniel Sowood, Anna Abfalterer Alessandro James Mirabelli, Melissa Fitzsimmons, and Affan Iqbal for the fun. Also, I appreciate the help and support from Fei-Yang Huang, Wilson Chen, Emma Lin, Yu-Kai Chao, Hao-Che Niu, Shih-Cun You, David Lu, Jen Kang, Chu-Cheng Lin, Wei-Haw Huang and Yi-Teng Huang.

Finally, I am hugely grateful to my parents, who keep encouraging, motivating, and supporting me my whole life. Nothing can be achieved without them. Also, I acknowledge my sister's support and my nephew/niece, who make me happy during the phone call. Last but not least, thanks to my girlfriend, Mei Chun Chen, for her support and encouragement during my study and keep me smiling and calm. Without her, for sure, I have quit my PhD.

List of publications

1. Ligang Wang, Zher Ying Ooi, Feng-Yan Jia, Yuqi Sun, Yun Liu, Linjie Dai, Junzhi Ye, Jincan Zhang, **Yu-Hsien Chiang**, Sanyang Han, Alessandro James Mirabelli, Zhilong Zhang, Xiaodong Yang, Yu Tan, Hao Dong, Huanping Zhou, Samuel D. Stranks, Ling-Dong Sun, Chun-Hua Yan, Richard H. Friend. *Flash-Evaporating Polar Solvents Impart Efficient Nano-Perovskite LEDs with Energy Cascad*. In preparation.
2. **Yu-Hsien Chiang**, Kyle Frohna, Hayden Salway, Anna Abfalterer, Bart Roose, Miguel Anaya, Samuel D Stranks. *Efficient all-perovskite tandem solar cells by dual-interface optimisation of vacuum-deposited wide-bandgap perovskite*. **under review**. 2022
3. Edoardo Ruggeri, Miguel Anaya, Krzysztof Gałkowski, Anna Abfalterer, **Yu-Hsien Chiang**, Kangyu Ji, Zahra Andaji - Garmaroudi, Samuel D Stranks. *Halide Remixing under Device Operation Imparts Stability on Mixed-Cation Mixed-Halide Perovskite Solar Cells*. **Advanced Materials**. 2022
4. Stuart Macpherson, Tiarnan AS Doherty, Andrew J Winchester, Sofiia Kosar, Duncan N Johnstone, **Yu-Hsien Chiang**, Krzysztof Galkowski, Miguel Anaya, Kyle Frohna, Affan N Iqbal, Satyawan Nagane, Bart Roose, Zahra Andaji-Garmaroudi, Kieran WP Orr, Julia E Parker, Paul A Midgley, Keshav M Dani, Samuel D Stranks. *Local nanoscale phase impurities are degradation sites in halide perovskites*. **Nature**. 2022.
5. Kyle Frohna, Miguel Anaya, Stuart Macpherson, Jooyoung Sung, Tiarnan AS Doherty, **Yu-Hsien Chiang**, Andrew J Winchester, Kieran WP Orr, Julia E Parker, Paul D Quinn, Keshav M Dani, Akshay Rao, Samuel D Stranks. *Nanoscale chemical heterogeneity dominates the optoelectronic response of alloyed perovskite solar cells*. **Nature Nanotechnology**. 2022.

6. T Jesper Jacobsson, Adam Hultqvist, Alberto García-Fernández, Aman Anand, Amran Al-Ashouri, Anders Hagfeldt, Andrea Crovetto, Antonio Abate, Antonio Gaetano Ricciardulli, Anuja Vijayan, Ashish Kulkarni, Assaf Y Anderson, Barbara Primera Darwich, Bowen Yang, Brendan L Coles, Carlo AR Perini, Carolin Rehermann, Daniel Ramirez, David Fairen-Jimenez, Diego Di Girolamo, Donglin Jia, Elena Avila, Emilio J Juarez-Perez, Fanny Baumann, Florian Mathies, GS González, Gerrit Boschloo, Giuseppe Nasti, Gopinath Paramasivam, Guillermo Martínez-Denegri, Hampus Näsström, Hannes Michaels, Hans Köbler, Hua Wu, Iacopo Benesperi, M Ibrahim Dar, Ilknur Bayrak Pehlivan, Isaac E Gould, Jacob N Vagott, Janardan Dagar, Jeff Kettle, Jie Yang, Jinzhao Li, Joel A Smith, Jorge Pascual, Jose J Jerónimo-Rendón, Juan Felipe Montoya, Juan-Pablo Correa-Baena, Junming Qiu, Junxin Wang, Kári Sveinbjörnsson, Katrin Hirselandt, Krishanu Dey, Kyle Frohna, Lena Mathies, Luigi A Castriotta, Mahmoud Aldamasy, Manuel Vasquez-Montoya, Marco A Ruiz-Preciado, Marion A Flatken, Mark V Khenkin, Max Grischek, Mayank Kedia, Michael Saliba, Miguel Anaya, Misha Veldhoen, Neha Arora, Oleksandra Shargaieva, Oliver Maus, Onkar S Game, Ori Yudilevich, Paul Fassel, Qisen Zhou, Rafael Betancur, Rahim Munir, Rahul Patidar, Samuel D Stranks, Shahidul Alam, Shaoni Kar, Thomas Unold, Tobias Abzieher, Tomas Edvinsson, Tudur Wyn David, Ulrich W Paetzold, Waqas Zia, Weifei Fu, Weiwei Zuo, Vincent RF Schröder, Wolfgang Tress, Xiaoliang Zhang, **Yu-Hsien Chiang**, Zafar Iqbal, Zhiqiang Xie, Eva Unger. *An open-access database and analysis tool for perovskite solar cells based on the FAIR data principles*. **Nature Energy**. 2022
7. Tiarnan AS Doherty, Satyawan Nagane, Dominik J Kubicki, Young-Kwang Jung, Duncan N Johnstone, Affan N Iqbal, Dengyang Guo, Kyle Frohna, Mohsen Danaie, Elizabeth M Tennyson, Stuart Macpherson, Anna Abfalterer, Miguel Anaya, **Yu-Hsien Chiang**, Phillip Crout, Francesco Simone Ruggeri, Sean Collins, Clare P Grey, Aron

- Walsh, Paul A Midgley, Samuel D Stranks. *Stabilized tilted-octahedra halide perovskites inhibit local formation of performance-limiting phases*. **Science**. 2021.
8. Alan R Bowman, Felix Lang, **Yu-Hsien Chiang**, Alberto Jiménez-Solano, Kyle Frohna, Giles E Eperon, Edoardo Ruggeri, Mojtaba Abdi-Jalebi, Miguel Anaya, Bettina V Lotsch, Samuel D Stranks. *Relaxed current matching requirements in highly luminescent perovskite tandem solar cells and their fundamental efficiency limits*. **ACS Energy Letter**. 2021.
9. Xiaoyu Yang, Deying Luo, Yuren Xiang, Lichen Zhao, Miguel Anaya, Yonglong Shen, Jiang Wu, Wenqiang Yang, **Yu-Hsien Chiang**, Yongguang Tu, Rui Su, Qin Hu, Hongyu Yu, Guosheng Shao, Wei Huang, Thomas P Russell, Qihuang Gong, Samuel D Stranks, Wei Zhang, Rui Zhu. *Buried Interfaces in Halide Perovskite Photovoltaics*. **Advanced Materials**. 2021
10. Bart Roose, Krishanu Dey, **Yu-Hsien Chiang**, Richard H Friend, Samuel D Stranks. *Critical assessment of the use of excess lead iodide in lead halide perovskite solar cells*. **The Journal of Physical Chemistry Letters**. 2020
11. **Yu-Hsien Chiang**, Miguel Anaya, Samuel D Stranks. *Multisource Vacuum Deposition of Methylammonium-Free Perovskite Solar Cells*. **ACS Energy Letter**. 2020.
12. Tiarnan AS Doherty, Andrew J Winchester, Stuart Macpherson, Duncan N Johnstone, Vivek Pareek, Elizabeth M Tennyson, Sofiia Kosar, Felix U Kosasih, Miguel Anaya, Mojtaba Abdi-Jalebi, Zahra Andaji-Garmaroudi, E Laine Wong, Julien Madéo, **Yu-Hsien Chiang**, Ji-Sang Park, Young-Kwang Jung, Christopher E Petoukhoff, Giorgio Divitini, Michael KL Man, Caterina Ducati, Aron Walsh, Paul A Midgley, Keshav M Dani, Samuel D Stranks. *Performance-limiting nanoscale trap clusters at grain junctions in halide perovskites*. **Nature**. 2020

Conference proceedings

Material research society Fall meeting, 2022	Oral
International Conference on Hybrid and Organic Photovoltaics (HOPV), 2022	Oral
Material research society Fall meeting, 2021	Poster
International Conference on Hybrid and Organic Photovoltaics (HOPV), 2021 (ePoster Prize)	Poster
International Conference on Hybrid and Organic Photovoltaics (HOPV), 2020	

Table of Contents

Chapter 1. Introduction	1
Chapter 2. Theoretical background.....	6
2.1 Metal-halide perovskite overview	6
2.2 Carriers generation, recombination and defect in perovskite film	8
2.2.1 Photogenerated carriers and recombination pathway	8
2.2.2 Interfacial recombination.....	9
2.2.3 Quantify V_{OC} loss in a solar cell.....	11
2.2.4 V_{OC} deficit calculation	13
2.3 Wide bandgap (WBG) perovskite	15
2.3.1 Phase segregation in WBG	15
2.3.2 A-site composition engineering to mitigate phase segregation	17
2.3.3 Bulk perovskite passivation and contact layers optimisation	18
2.3.4 Defects in WBG perovskite	20
2.4 Vacuum deposited perovskite by multisource evaporation.....	21
2.4.1 The motivation for Vacuum deposited perovskite	21
2.4.2 History of vacuum deposited perovskite	21
2.4.3 The deposition parameter effect on evaporated perovskite quality	23
2.4.4 MA-free perovskite and the PCE roadmap.....	28
2.5 Two terminal (2T) All-perovskite tandem solar cells	30
2.5.1 Structure of tandem perovskite solar cells.....	30
2.5.2 The recombination junction in 2T all-perovskite tandem solar cell	32
2.5.3 Optical loss in RJ layer.	34
2.5.4 Summary and the outlook for all-perovskite tandem solar cell.....	36
Chapter 3. Experimental Methods	37

3.1 Perovskite evaporator system.....	38
3.2 Material, film, and device preparation	42
3.2.1 Film or solar cell fabrication	42
3.3 Film and device characterisation	47
3.3.1 X-ray diffraction pattern measurement.....	47
3.3.2 Scanning electron microscopy (SEM).....	48
3.3.3 Photoluminescence quantum efficiency (PLQE)	48
3.3.4 Hyperspectral optical microscopy measurements	49
3.3.5 Time-resolved photoluminescence (TRPL) measurements.....	49
3.3.6 UV–Vis measurements	49
3.3.7 Solar cell performance.....	49
3.3.8 Suns- V_{OC} measurement	52
3.3.9 Radiative V_{OC} and Urbach energy calculation ^{45,103}	52
3.3.10 External quantum efficiency (EQE)	53
Chapter 4. High-efficiency perovskite solar cells based on multisource evaporation.....	55
4.1 Introduction	56
4.2 Multisource evaporation of perovskite films	58
4.2.1 Determination of chemical formula.....	59
4.2.2 Optimisation of film annealing temperature.....	61
4.2.3 Substrate dependence	63
4.3 Evaporated film stability.....	64
4.4 Characterise optoelectronic properties of evaporated perovskite films.....	69
4.4.1 Absorption and PL characteristics	69
4.5 Evaporated perovskite solar cells with inverted structure.....	72
4.5.1 composition engineering for high-efficient perovskite solar cells	72
4.5.2 Optimised perovskite solar cells.....	74
4.5.3 The effect of deposition rate on perovskite film and device quality.	77

4.6 Conclusion	78
Chapter 5. Efficient all-perovskite tandem solar cells by dual-interface optimisation of vacuum-deposited wide-bandgap perovskite	79
5.1 Introduction	80
5.2 Hole transporting/perovskite interface optimisation	83
5.2.1 Evaporated perovskite film quality.....	83
5.2.2 The effect of HTMs on solar cell performance	85
5.3 Composition engineering of evaporated WBG perovskite films.....	87
5.3.1 Structure, morphology and bandgap.....	87
5.3.2 Photoluminescence study on perovskites with different bandgaps	90
5.3.3 Single junction solar cell performance	92
5.4 Perovskite/electron transport layer interface optimisation.....	95
5.4.1 Surface passivation of EDAI treatment on WBG perovskite film	95
5.4.2 Solar cell performance of EDAI treatment on WBG perovskite film	98
5.4.3 Performance loss analysis in WBG solar cells	100
5.5 Narrow bandgap perovskite for all-perovskite tandem solar cells.....	102
5.5.1 Film characterisation of solution-processed Pb/Sn perovskite solar cells.....	102
5.5.2 EDAI passivation effect on NBG perovskite solar cells	104
5.6 All-perovskite tandem solar cells	108
5.6.1 ALD SnO _x deposition.....	108
5.6.2 Development of all-perovskite tandem solar cells	110
5.7 Toward 30% of all-perovskite tandem solar cells (ongoing work).....	115
5.8 Conclusion	119
Chapter 6. Evaporated perovskite for a broad range of applications.....	120
6.1. Evaporated perovskite for perovskite-Silicon tandem solar cells	120
6.2 Fully-evaporated perovskite solar cells for solar fuel production.....	125
Chapter 7. Conclusion and outlook.....	129

7.1 Perovskite evaporation summary.....	129
7.2 Summary of this thesis.....	129
7.3 Key findings from cumulative experience	130
7.4 Outlook and future work.....	132
Reference	134

List of Figures

Figure 1.1. The global energy consumption by different sources, including biomass, coal, oil, natural gas, nuclear, hydropower, wind, solar, biofuels, and other renewable sources. Adapted with permission from our world in data. ¹	1
Figure 1.2. The historic photovoltaics performance of Silicon solar cells (single crystal) and perovskite solar cells is based on the data from NREL. ⁶	3
Figure 2.1. (a) A typical 3D ABX ₃ structure perovskite, ¹⁶ (b) the tunable perovskite PL emission from 400 nm to 1100 nm spectrum region, with different composition. ²³ Reproduced with permission from (a) Nature Publishing Group, (b) Elsevier.....	7
Figure 2.2. (a) the photon absorption/charge generation and thermalisation process in a semiconductor (E_v and E_c are valence band and conduction band) (b) charge recombination dynamic, including radiative recombination and non-radiative recombination (defect-assisted and auger recombination), (c) interface-induced recombination process, Type I: deep defects in perovskite, Type II: defects in perovskite and mismatch energy alignment at the interface, Type III: back transfer recombination and Type IV: electron transporting layer induced defects, (same in the hole transporting layer). The figure is adapted from ³² . Reproduced with permission from Nature Publishing Group.	9
Figure 2.3. (a) Commonly used hole transporting layer, PEDOT:PSS, P3HT, PolyTPD, PTAA, Spiro-OMeTAD, and electron transporting layer, SnO ₂ , TiO ₂ , PCBM and C60. (b) The quasi-fermi level splitting and dark current of perovskite with different contact layers. ⁴² Reproduced with permission from RSC Publishing.	11
Figure 2.4. An absorbed photon flux for different bandgap semiconductors, assuming where the photons energy higher than the bandgap are absorbed to achieve one sun AM1.5G equivalent steady-state power density. The right axis shows the power density for different excitation wavelengths. The figure is adapted from. ⁴³	12
Figure 2.5. (a) Bandgap determination of MAPbI ₃ solar cells based on different methods in the literature. (b) the estimated bandgaps and the radiative V_{oc} (red line) of MAPbI ₃ solar cell. The figure is adapted from ⁵⁰	14
Figure 2.6. (a) the PL spectra shift from high energy to low energy under light-soaking conditions. (b) the energy diagram of phase segregation. This figure is adapted from ⁵²	16

Figure 2.7. The phase segregation analysis with different perovskite compositions under 10 mins of light soaking at various light intensities. The figure is adapted from.....	18
Figure 2.8. The V_{OC} (a) and J_{SC} (b) of different WBG perovskite in 2T all-perovskite tandem solar cells. This figure is adapted from ⁶⁰ . Reproduced with permission from Nature Publishing Group.	21
Figure 2.9. The co-evaporation system shows dual-source deposition, two QCM monitors and a rotated substrate stage. (b) the SEM image of evaporated perovskite solar cells demonstrates the uniform perovskite coating. ⁷³ (C) A fully evaporated perovskite solar cell with p-i-n device architecture and corresponding cross-sectional SEM image. (d) the device performance of a fully-evaporated perovskite solar cell with MAPbI ₃ composition and a power conversion efficiency of 20.3%. ⁷⁶ Reproduced with permission from Nature Publishing Group and RSC publication.....	23
Figure 2.10. MAPbI ₃ perovskite composition analysis, deposited on different substrates (PEIE, ITO, PEDOT:PSS or MoO _x), (a) with 3 nm and 200 thickness by XPS spectra of C1s and N1s measurement. (b) SEM surface morphology characterisation. Scale bars are 500 nm. The figure is adapted from ⁷⁷	26
Figure 2.11. The effect of substrate temperature variation as a function of time during co-evaporated MAPbI ₃ . (a) temperature change diagram (b) the cross-sectional SEM images, and (c) the top-view morphology, showing noticeable grain size variation. (d) the J-V curve scan of the MAPbI ₃ device, prepared by different substrate temperatures and (e) the stabilised PCE output. This figure is adapted from ⁷⁸	27
Figure 2.12. The PCE roadmap of perovskite solar cells performance based on solution process or multisource evaporated perovskite with or without MA during deposition. This device performance is this figure is updated until 2018. ^{73,76,83-87}	29
Figure 2.13. The device architecture of 2-terminal and 4-terminal tandem solar cells. This figure is adapted from ⁹⁰	31
Figure 2.14. Theoretical limitation of 2-terminal tandem perovskite solar cells (a) without and (b) with luminescence coupling (both calculations assume all the light above bandgap is fully absorbed, (c) the coupling effect plot, ratio of (b) and (a), (d) summarised device performance without and with coupling with a function of the bandgap. This figure is adapted from ⁹²	32
Figure 2.15. The commonly tandem device architecture for 2-T all-perovskite solar cells using (a) ALD-ZTO, SnO _x and sputter ITO, (b) ALD-SnO _x and 1 nm Au, (c) ALD-SnO _x with O ₂ -deficient structure as bipolar transportation layer as recombination layer. This figure is adapted from ^{89,93,94}	34

Figure 2.16. The optical loss study to improve the device performance of 2-T all-perovskite tandem solar cell with Arch 1. using $\text{MgF}_2/\text{glass}/\text{IOH}/2\text{-PACz}/\text{WBG}$ perovskite/ $\text{LiF}/\text{C60}/\text{SnO}_x/\text{ITO}/\text{thin-PEDOT:PSS}/\text{NBG}$ perovskite/ $\text{PCBM}/\text{C60}/\text{BCP}/\text{Cu}$, Arch 2, using $\text{glass}/\text{ITO}/2\text{-PACz}/\text{WBG}$ perovskite/ $\text{C60}/\text{SnO}_x/\text{Au}/\text{PEDOT:PSS}/\text{NBG}$ perovskite/ $\text{C60}/\text{BCP}/\text{Cu}$. (a) the device architecture with the choices of layers, the J-V curves (b) and EQE measurement of each subcell and the corresponding J_{CS} . (c)-(d) of device arch 2 and arch 1. This figure is adapted from ⁹⁶35

Figure 2.17. The state-of-the-art all-perovskite tandem solar cell with (a) cross-sectional SEM image of the device, (b) the J-V scans of reverse and forward measurement with 26.7 and 26.4%, (c) the EQE measurement of each subcell and the corresponding J_{SC} . Reproduced with permission from Nature Publishing Group.⁷²36

Figure 3.1. Diagram of the perovskite evaporator system.38

Figure 3.2. Example of tooling factor calibration of PbI_2 film with 9 substrates across the $10 \times 10 \text{ cm}^2$ size substrate holder. The film thickness is tested with substrates at a different location and the corresponding thickness is shown on the right.....41

Figure 3.3. A screenshot of the profilometer scan for PbI_2 film measurement. A sharp tweezer scratches the samples to provide the thickness variation. During the scan, the equipment tip scans from the direction of PbI_2 , glass to PbI_241

Figure 3.4. A JV curve showing different optoelectronic device applications.51

Figure 3.5. A calculated photon flux with the unit of $\text{mA}/\text{cm}^2\text{nm}$ based on AM 1.5 G spectra as a function of wavelength.54

Figure 4.1. Parameters of a multi-sourced evaporation process for a typical batch of a control film $\text{FA}_{0.7}\text{Cs}_{0.3}\text{Pb}(\text{I}_{0.9}\text{Br}_{0.1})_3$, showing the deposition rate (left panel) and sublimed temperature (right panel) of FAI , PbI_2 and CsBr58

Table 4.1. Parameters for the substrate rotation speed and the evaporation conditions for the different precursors employed for the optimised (5% excess PbI_2) perovskite films.....58

Figure 4.2. XRD patterns of a series of solution-processed films with $\text{FA}_{1-x}\text{Cs}_x\text{Pb}(\text{I}_{1-y}\text{Br}_y)_3$ composition, where x and y take a range of values between 0.1 – 0.46. The right panel shows a zoom around the key perovskite peaks used in the analysis in Figure 4.3.....60

Figure 4.3. Plot used to estimate the final composition of the evaporated film.....61

Figure 4.4. SEM top view images showing the morphology of evaporated $\text{FA}_{0.7}\text{Cs}_{0.3}\text{Pb}(\text{I}_{0.9}\text{Br}_{0.1})_3$ perovskite films as-deposited (a) and after 30 minutes of annealing at 150°C (b). (c) Room-temperature XRD patterns corresponding to evaporated perovskite films on glass following annealing at different temperatures for 30 minutes. Peaks corresponding to

additional PbI_2 and CsPbI_3 phases are labelled; the other peaks correspond to the alloyed perovskite. The perovskite XRD peaks are assigned based on Pawley refinements. (d) the experimental data of the XRD pattern of the stoichiometric control sample on ITO/PTAA (annealed at 135°C), and the Pawley refinement to determine the structure and phase. The blue lines corresponding to the reflection pattern for P-43n.62

Figure 4.5. SEM top view images displaying the morphology differences when the perovskite films are evaporated on glass (a) and PTAA (b) and annealed at an optimum temperature of 135°C , and their corresponding XRD patterns (c). The perovskite XRD peaks are assigned based on Pawley refinements.63

Figure 4.6. Structural characterisation of evaporated $\text{FA}_{0.7}\text{Cs}_{0.3}\text{Pb}(\text{I}_{0.9}\text{Br}_{0.1})_3$ perovskite thin films on ITO/PTAA substrates. (a) XRD diffraction patterns as prepared (and annealed), and after storage in air at 50% relative humidity for 5 days. We assign the peak at $\sim 10^\circ$ to CsPbI_3 , though we note that this phase could also contain fractions of bromide. (b) The structure stability test by XRD with evaporated perovskite films coated with different contact layers on top. CYTOP is an amorphous fluoropolymer with low moisture and air permeability ($<10^{-12} \text{ cm}^3 \text{ cm}/(\text{cm}^2 \text{ s Pa})$). The “air” and “dry box” labels in the figure indicate when the samples were stored in an atmosphere with a relative humidity of $50\pm 5\%$ and $<10\%$, respectively. To avoid moisture degradation, the fresh and “dry box” samples were kept in an air-tight sample holder during the XRD measurement.64

Figure 4.7. Structural characterisation of evaporated $\text{FA}_{0.7}\text{Cs}_{0.3}\text{Pb}(\text{I}_{0.9}\text{Br}_{0.1})_3$ perovskite thin films on ITO/PTAA substrates (a) Zoom-in XRD of the (011) perovskite peak with different excess PbI_2 during the evaporation, (b) with +10%, (c) with +20% perovskite before and after storage in air at 50% relative humidity for 5 days, (d) The air stability test comparison between control and +10% PbI_2 perovskite film deposited on PTAA/ITO substrate, storage in the air for 32 days.65

Figure 4.8. (a-b) XRD patterns and UV-vis spectra of evaporated perovskite films without or with annealing at 135°C for 90 or 480 mins.66

Figure 4.9. (a–c) SEM micrographs of the films with control, +10% and +20% excess PbI_2 in perovskite film. The grain size distribution of perovskite films with (d) control and (e) +10 PbI_2 perovskite film on PTAA/ITO substrate. The grain size was obtained by calculating the square-root of the grain area estimated using the software ImageJ.67

Figure 4.10. XRD pattern of a +10% PbI_2 evaporated perovskite film by using Lumtec PbI_2 as a precursor, indicating the sensitivity to the PbI_2 source and the deposition process in the final

characteristics of the perovskite. The XRD data was measured in air, and we saw degradation of the film after 15 mins, with the appearance of a CsPbI₃ peak.....68

Figure 4.11. UV-Vis absorption (a) and normalised photoluminescence (PL) (b) spectra (excitation at 520 nm) of evaporated FA_{0.7}Cs_{0.3}Pb(I_{0.9}Br_{0.1})₃ perovskite films with different quantities of excess PbI₂ with respect to the stoichiometric control.....69

Figure 4.12. (a) PL spectra (excitation at 520 nm) of evaporated perovskite with different excess of PbI₂. (b) The quasi-fermi level splitting analysis for the perovskite (10% sample) with n-type and p-type transporting layer, calculated from the PLQE results. The black and star symbols are based on film PLQE and device V_{oc} measurements (10% PbI₂ device), respectively. 70

Figure 4.13. (c) TRPL measurements for the different perovskite films with excitation at 407 nm (repetition rate of 0.5 MHz, fluence of 5 nJ/cm²/pulse). 71

Figure 4.14. J-V curves of evaporated perovskite for solar cells with different quantities of excess PbI₂ measured under AM 1.5G (100 mW/cm² irradiance), along with corresponding dark curves. The curves are from the reverse scan (sweeping from 1.2 V to -0.1 V). A cross-section SEM image (scale bar is 500 nm) and a schematic of the employed solar cell architecture are shown in the inset..... 73

Figure 4.15. The structural and morphological characterisation of the evaporated perovskite film with 5% excess PbI₂ deposited on a PTAA/ITO substrate. (a) XRD pattern and (b) top-view SEM image of the film..... 75

Figure 4.16. (a) Histogram of device performance from 35 independent devices with the FA_{0.7}Cs_{0.3}Pb(I_{0.9}Br_{0.1})₃ perovskite including 5% excess PbI₂. The results from reverse (1.2 V to -0.1 V, black curve) and forward (-0.1 V to 1.2 V, red curve) scans are distinguished. (b) EQE measurement for the champion device. (c) Forward (red) and reverse (black) J-V curves of a champion device. The inset figure is the stabilised power output (SPO) measurement, maintaining the bias at maximum power point of the reverse scan at 0.88 V and measuring the photocurrent. 75

Figure 4.17. Device performance for 5% PbI₂ excess evaporated perovskite solar cells from reverse scan measurement of J-V scan under 1 sun AM 1.5G illumination across five different batches..... 76

Figure 4.18. (a) The shelf-stability test of an encapsulated device measured over a period of 18 days, with the devices stored and measured in air. The J-V measurements are under 1 sun AM 1.5G illumination. The PCE here is the value from the reverse scan of the J-V curve. (b) Operational stability test of encapsulated solar cells in air under AM 1.5 G 1-sun intensity light

at maximum power point based on the initial reverse scan (0.8 V). We note there is no UV filter.....76

Figure 4.19. JV-curves for evaporated perovskite solar cells (+10% PbI₂) deposited with a stable (left panel) and unstable (right panel) rate. A more pronounced hysteresis effect can be seen in the device with an unstable rate during the film deposition. (b) Variation in PbI₂ rate during an unstable perovskite evaporation batch. (c) Hyperspectral photoluminescence (PL) maps of evaporated perovskite films (+10% excess PbI₂) on glass. The left and middle maps correspond to a sample obtained with an unstable deposition rate. The PL peak distributions are spatially and spectrally inhomogeneous, showing maxima at 770 and 814 nm, which is indicative of phase segregation. The right map is the PL signal from a film obtained with a stable deposition rate, showing a single peak emission spectrum with its maximum at 765 nm. (d) XRD patterns to understand the crystalline structure of the perovskite film (10% excess PbI₂) deposited with stable and unstable rates. When the evaporation rate is unstable, we observe an asymmetric perovskite peak with a shoulder at lower 2θ, corresponding to FAPbI₃-rich domains.⁸ For the perovskite film deposited with a stable rate, there is negligible asymmetry in the XRD peak (blue curve). Note: the hyperspectral measurement was conducted with the help of Dr. Miguel Anaya.77

Figure 5.1. (a) Diagram of the thermal evaporation system where four sources (i.e. FAI, PbBr₂, PbI₂ and CsBr) are employed to deposit high quality FA_{0.7}Cs_{0.3}Pb(I_xBr_{1-x})₃ thin films. FAI, PbI₂ and CsBr evaporation rates are kept at 1, 0.6 and 0.1 Å/s, respectively, and the PbBr₂:PbI₂ deposition rate ratio varies to tune the bandgap. (b) Effect of different HTMs (i.e. PTAA, and MeO-2PACz) on the V_{OC} statistics of evaporated FA_{0.7}Cs_{0.3}Pb(I_{0.9}Br_{0.1})₃ perovskite solar cells (PbBr₂ rate is 0). Inset device architecture employed. The box/whisker plot contains the 1.5 interquartile range, the median value and data distribution from 8 devices. (c) J-V curve of the champion FA_{0.7}Cs_{0.3}Pb(I_{0.9}Br_{0.1})₃ perovskite solar cells with the inset showing a stabilised power output measurement. (d) Operational stability test of an encapsulated device at 0.94 V fixed bias under continuous 1 sun illumination.84

Figure 5.2. SEM comparison between evaporated perovskite (1.62 eV) film deposited on PTAA, 2-PACz or MeO-2PACz layers.85

Figure 5.3. PL(QE) and XRD comparison of evaporated perovskite (1.62 eV) film on top of 2-PACz, MeO-2PACz or PTAA layers.85

Figure 5.4. (a) The V_{OC} statistics of evaporated FA_{0.7}Cs_{0.3}Pb(I_{0.9}Br_{0.1})₃ perovskite solar cells (PbBr₂ rate is 0) on PTAA or MeO-2PACz from 2 batches fabrication. The box/whisker plot

contains the 1.5 interquartile range, the median value. (b) JV curves of evaporated perovskite (1.62 eV, FA_{0.7}Cs_{0.3}Pb(I_{0.9}Br_{0.1})₃ perovskite) on PTAA, MeO-2PACz and 2-PACz HTMs...86

Figure 5.5. (a) Zoom in and (b) full region of XRD pattern of evaporated FA_{0.7}Cs_{0.3}Pb(I_xBr_{1-x})₃ thin films deposited on MeO-2PACz/ITO showing different bandgaps: 1.62 eV (dark red curve), 1.68 eV (red), 1.71 eV (orange), 1.77 eV (green) and 1.80 eV (blue). (c) The evolution of lattice constant versus perovskite composition of FA_{1-x}Cs_xPbI₃ (black), FAPb(I_{1-x}Br_x)₃ (red) and FA_{0.7}Cs_{0.3}Pb(I_{1-x}Br_x)₃ (green). (d) The first derivative of EQE to extract the bandgap of the perovskites in solar cells.88

Figure 5.6. The SEM morphology of different bandgap evaporated perovskite on MeO-2PACz/ITO.89

Figure 5.7. Synchrotron-based nXRF mapping for solution-processed triple-cation perovskite and evaporated perovskites with bandgaps of 1.62 eV, 1.77 eV and 1.80 eV. The Br:Pb mapping is shown in here. Scale bars are of 2 μm. Collaborators, Miguel Anaya and Kyle Frohna, conducted this measurement.....90

Figure 5.8. (a) normalised PL spectra of a series of evaporated FA_{0.7}Cs_{0.3}Pb(I_xBr_{1-x})₃ thin films deposited on MeO-2PACz/ITO showing different bandgaps: 1.62 eV (dark red curve), 1.71 eV (orange), 1.77 eV (green) and 1.80 eV (blue). PL peak evolution over time of (b) 1.62 eV, (c) 1.77 eV and (d) 1.8 eV evaporated perovskite films under continuous illumination at 5 Suns (300 mW/cm²) with a 520 nm laser. (e) Time-resolved photoluminescence decays for 1.62 eV and 1.77 eV evaporated perovskite films on MeO-2PACz excited with a 450 nm laser at a fluence of 8.5 nJ/cm²/pulse. Samples were excited and light collected from the top side. We attribute the fast decay during the first 40 ns results from the ITO/ MeO-2PACz quenching. (f) summarised PL peak position evolution of evaporated perovskite films with different bandgaps during light soaking with 5 sun intensity.....91

Figure 5.9. (a) J-V curves at AM1.5G illumination of evaporated solar cells based on perovskites with different bandgaps: 1.62 eV (dark red curve), 1.68 eV (red), 1.71 eV (orange), 1.77 eV (green) and 1.80 eV (blue). See Table 1 for compositions. EQE spectra and the corresponding integrated J_{SC} (b) and the V_{OC} statistics (c) for the series of devices are shown in panel (a). The box/whisker plots contain the 1.5 interquartile range, the median value, and the data distribution of the V_{OC}.....92

To gain further understanding on our device losses, we calculate the estimated V_{OC,rad} based on the Urbach fit of EQE spectra to obtain the extended EQE tail for dark current calculation (**Figure 5.10** see Experimental Methods section 3.3.9) and represent the V_{OC} loss associated with the different evaporated composition in **Figure 5.9**.^{44,102} We observe that the V_{OC} loss

increases from 196 mV to 251 mV when we tune the perovskite bandgap from 1.62 eV to 1.80 eV. The Urbach energy also rises with the bandgap energy from 13.5 meV to 19.0 meV. These observations indicate higher electronic disorder upon Br addition and are consistent with the increased trap densities revealed from the PL measurements.¹³⁰ These results suggest that the evaporated FA_{0.7}CS_{0.3}Pb(I_{0.64}Br_{0.36})₃ perovskite with a 1.77 eV bandgap is our best candidate for use as front absorber in a tandem architecture with sufficient photo-stability and remarkable, though still suboptimal, V_{OC}.93

Figure 5.10. (a) Measured V_{OC}, calculated V_{OC} loss and Urbach energy extracted from EQE for champion devices based on different bandgap, evaporated perovskite samples. (b)-(f) the Urbach tail fit for EQE spectra of different perovskite solar cells.94

Figure 5.11. PLQE values for FA_{0.7}CS_{0.3}Pb(I_{0.64}Br_{0.36})₃ (1.77 eV) evaporated perovskite film, with EDAI treatment and with EDAI treatment plus C60 contact layer.96

Figure 5.12. (a-b) SEM image of 1.77 eV bandgap evaporated perovskite with FA_{0.7}CS_{0.3}Pb(I_{0.64}Br_{0.36})₃ composition before and after EDAI passivation. (c) PL spectra of full stack evaporated perovskite FA_{0.7}CS_{0.3}Pb(I_{0.64}Br_{0.36})₃ with and without EDAI passivation, showing the outstanding passivation effect. (d-e)XRD of 1.77 eV evaporated perovskite film before and after EDAI passivation. The ITO substrate peak is shown as a reference peak. (f) TRPL of evaporated perovskite films (FA_{0.7}CS_{0.3}Pb(I_{0.64}Br_{0.36})₃) with and without EDAI passivation on MeO-2PACz/ITO glass. The measurement was conducted with a 448.4 nm pulsed laser and an excited density of 8.5 nJ/cm²/pulse.97

Figure 5.13. (a) J-V curves for control and EDAI-passivated FA_{0.7}CS_{0.3}Pb(I_{0.64}Br_{0.36})₃based solar cell in the dark (no symbols) and under 1 sun AM 1.5 G illumination (line and symbols). See device parameters in **Table 5.2**. (b) Literature survey of V_{OC} of solution-process or vacuum deposited wide bandgap (>1.7 eV) film perovskite solar cells with MA-free composition.98

Figure 5.14. (a) EQE of 1.77/1.76 eV perovskite solar cells with and without EDAI passivation. (b) the first derivative of EQE spectra 1.77/1.76 eV perovskite solar cells with and without EDAI passivation to show the bandgap shift after passivation. (c) The measured V_{OC}, estimated V_{OC,rad} and Urbach energy of wide gap perovskite solar cells (FA_{0.7}CS_{0.3}Pb(I_{0.64}Br_{0.36})₃) with and without EDAI passivation. The left axis is showing the V_{OC} and V_{OC,rad} and the right axis is showing the Urbach energy.....99

Figure 5.15. The batch-to-batch variation of V_{OC}, J_{sc}, FF and PCE with and without EDAI passivation of evaporated perovskite solar cell with 1.77 eV (FA_{0.7}CS_{0.3}Pb(I_{0.64}Br_{0.36})₃). 100

Figure 5.16. (a) Radiative limit, pseudo (non-radiative loss) from PLQE measurement and experimental values of the Voc (QFLS) (b) V_{OC} as a function of incident light intensity,

showing an ideal factor of 1.46 and 1.27, (c) FF calculation for control and EDAI-treated devices (d) and (e) The pseudo-JV curve measurement of control and EDAI-treated (FA_{0.7}Cs_{0.3}Pb(I_{0.64}Br_{0.36})₃) perovskite solar cells. In here, we set the current density value to 95% of the radiative limit at 1 sun illumination. (f) V_{OC} tracking under a function of time under AM 1.5 G illumination for control and EDAI-treated devices. 101

Figure 5.17. Solution-processed Pb/Sn perovskite with a composition of FA_{0.75}Cs_{0.25}Pb_{0.5}Sn_{0.5}I₃ on 2-PACz film. (a) XRD (Note: the rise curve between 2θ of 15° to 25° is from an air-tight sample holder), (b) SEM, (c) UV- Vis, PL spectra and (e) derivative EQE of NBG perovskite solar cells. 103

Figure 5.18. (a) J-V curves for control and EDAI-passivated, FA_{0.75}Cs_{0.25}Pb_{0.5}Sn_{0.5}I₃ solar cell in the dark (no symbols) and under AM 1.5 G illumination (line and symbols). See device parameters in **Table 5.3**. (b) EQE of solution-processed Pb/Sn perovskite solar cells without (black) and with (red) EDAI passivation. (c) PCE distribution of solution-processed Pb/Sn perovskite before and after EDAI passivation. (d) V_{OC} statistics for devices based on FA_{0.7}Cs_{0.3}Pb(I_{0.64}Br_{0.36})₃ and FA_{0.75}Cs_{0.25}Pb_{0.5}Sn_{0.5}I₃ with and without EDAI passivation. .. 105

Figure 5.19. SEM morphology of solution-processed Pb/Sn perovskite film without (left) and with (right) EDAI passivation..... 106

Figure 5.20. The measured V_{OC}, estimated V_{OC} and Urbach energy of solution-processed low gap perovskite solar cells (FA_{0.75}Cs_{0.25}Pb_{0.5}Sn_{0.5}I₃) with and without EDAI passivation. The left axis shows the V_{OC} and V_{OC,rad} and the right axis shows the Urbach energy..... 106

Figure 5.21. (a) Diagram of the position of the sources of TDMASn and H₂O injection position, and the N₂ purge direction in the ALD system. (b)-(e) photos of SnO_x film, growth on 8-inch Silicon wafer, based on the deposition recipe in **Table 5.4**..... 110

Figure 5.22. The J-V curve of passivated WBG perovskite solar cell with 1.76 eV with ALD-SnO_x on top of C₆₀ instead of BCP. In her PV is power-voltage scan..... 110

Figure 5.23. All perovskite tandem solar cells with different interlayers (a)2-PACz, 2-PACz/Au or 2-PACz/Cu and (B) SnO_x/PEDOT:PSS, PEIE/SnO_x/Au/PEDOT:PSS PEIE/SnO_x/PEDOT:PSS between wide bandgap and narrow bandgap perovskite films..... 112

Figure 5.24 (a) Schematics and (b) cross-sectional SEM image displaying the architecture of the all-perovskite tandem solar cell. (c) J-V curve of the champion tandem device, reaching a 24.1% PCE for forward scan. (d) EQE spectra of the evaporated-based WBG (blue curve) and solution-based NBG (orange) perovskite subcells comprising the all-perovskite tandem device. The distribution of device performance across four batches (28 devices) is shown in figure (e) and (f) with an average PCE of 22.1%. 112

Figure 5.25. The stabilised power output measurement of our device with a fixed bias at 1.74 V, reaching PCE of 23.2%.	113
Figure 5.26. The storage solar cells stability test in air of encapsulated (in N ₂ -filled glovebox) tandem device.	114
Figure 5.27. The evaporated WBG perovskite solar cell with different surface passivation treatments, (a) V _{OC} and (b) FF distribution of control, EDAI-treated and EDAI+2T treated solar cell, (c) the EQE measurement of these solar cells, showing nearly identical spectrum.....	116
Figure 5.29. (a) Molecule structure of Gallic acid (GA). (b-c) V _{OC} and (d-f) FF evolution of 2.2 and 2.4 M Pb/Sn perovskite solar cells with different amounts of GA incorporation. (f) the EQE spectrum of 2.4 M device without and with GA.....	118
Figure 6.1. (a) top-view and (a) cross-sectional SEM images of evaporated perovskite on textured Si solar cells.	121
Figure 6.2. (a) half-device architecture of evaporated perovskite on Si solar cells. Si cell is fabricated by Dr. Erkan Aydin and Dr. Michele De Bastiani. Hyperspectral images (measured with Dr. Miguel Anaya) of evaporated perovskite film on textured Si (b) reflection map, (c) PL intensity map, (d) and max PL peak map. Comparison between evaporated perovskite on MeO/ITO glass and MeO/ITO Si textured cell with (e) normalised PL and (f) XRD pattern.	122
Figure 6.3. (a) The deposition recipe and film thickness of evaporated perovskite on textured Si cell or ITO substrate. (b) the XRD pattern of recipe A to D, (c-e) the cross-sectional SEM images (measured by Dr. Erkan Aydin) of complete perovskite-Si tandem solar cell with the deposition recipes of A-C.	124
Figure 6.4. Perovskite-Si tandem solar cell based on different deposition protocols of A-C. (a) the JV-scans. (b) EQE measurement.	124
Figure 6.5. (a) A large-scale device pattern with a 5x3 cm ² size and an active area of 9.46 cm ² . (b) J-V curve of a large-scale device with a 9.46 cm ² active area. (c) the design of metal fingers to reduce resistance from FTO substrate. (d) A flexible substrate of 100 cm ² size with perovskite deposition by multisource evaporation.	126
Figure 6.5. (a) Photographs of the ~10 cm ² BiVO ₄ photoanode for O ₂ evolution (b) CuIn alloy for CO ₂ reduction. (c) Perovskite-BiVO ₄ tandem device shown from the CuIn catalyst. (d) an artificial leaf tandem photoelectrochemical device architecture. (e) a 10 x10 array (total device area: 1,000 cm ²) of perovskite-BiVO ₄ artificial leaves in a reactor. Figure (d) is adapted from	174
.....	127

Chapter 1. Introduction

Energy demand since industrialisation in the 18th century has rapidly increased. In 2021, global energy consumption reached 176,000 TWh (**Figure 1.1**) which is likely to increase significantly in the next few years.¹ The International Energy Agency (IEA) predicts that the energy and electricity demand will increase by 1 and 2% by 2040, respectively.² Fossil fuels (natural gas, oil and coal) are still dominating the energy supply, providing roughly 78% of total energy in 2021 worldwide. Though fossil fuels can provide enough power for today's global demand, they will eventually be exhausted. Furthermore, key byproducts such as carbon dioxide (CO₂) are emitted into the atmosphere, causing the enhanced greenhouse effect and triggering climate change. This massive quantity of CO₂ from fossil fuels has started to activate the public, governments and organisations, which motivates environmental protection policies. For example, the Paris Climate Agreement supports the development of low-carbon energy and renewable supplies to replace fossil fuels to reduce or mitigate human-made greenhouse gases and their effect on humanity, the environment and the entire planet.

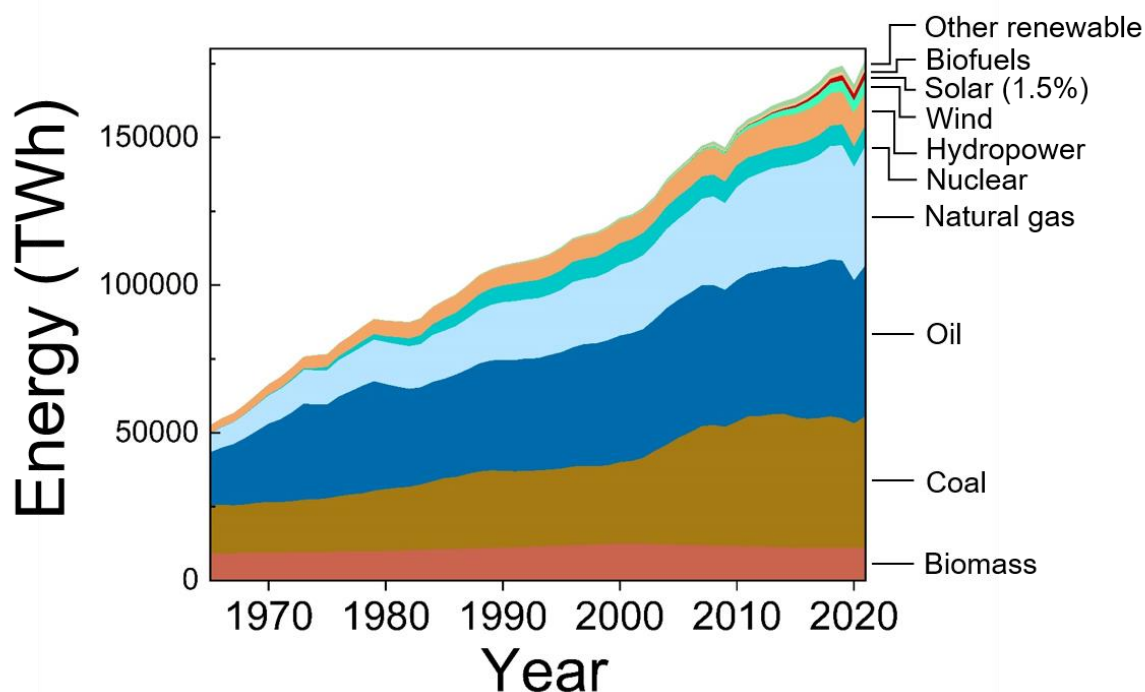


Figure 1.1. The global energy consumption by different sources, including biomass, coal, oil, natural gas, nuclear, hydropower, wind, solar, biofuels, and other renewable sources. Adapted with permission from our world in data.¹

The low-carbon energy transition is a primary development focus for a modern and sustainable society. Renewable energy sources are the most promising solutions to substitute fossil fuels and reduce CO₂ emissions; therefore, accelerating research, innovation and development is essential. Among renewable energy sources, solar energy, harvesting light from the sun to produce energy, is extremely promising as terrestrial sunlight can provide up to 10¹² TWh of energy.³ This number is 10⁷ times more than global demand. However, the current capacity of photovoltaic (PV) technology is generating only ~1,000 TWh in 2021,⁴ indicating the great potential to expand PV technologies. The IEA predicts that annual PV generation can reach 7,400 TWh, which requires a growth in power generation of 25% per year. The first concept of solar PV was presented in 1839 by Becquerel,⁵ but it wasn't until the 1950s when solar PV research attracted considerable attention for space activity.⁵ Currently, silicon (Si) PV is dominating the PV market for terrestrial applications. However, there has been no significant breakthrough in terms of Si PV performance in the past 20 years, showing a performance increase from 25% to 26% (**Figure 1.2**).⁶ Device optimisation for Si PV has put the technology close to its theoretical limit, though the fabrication cost has significantly dropped since 2000.⁷ Nowadays, the main cost of Si panels is the balance of system costs (wiring, installation, inverter etc.), leading to a limit for solar panel development.⁸ As the global population is still increasing and high technology industries are developing, the total energy consumption is expected to increase significantly. In this situation, new PV materials/panels with better device performance that are more affordable and scalable are stimulating continued research and development.

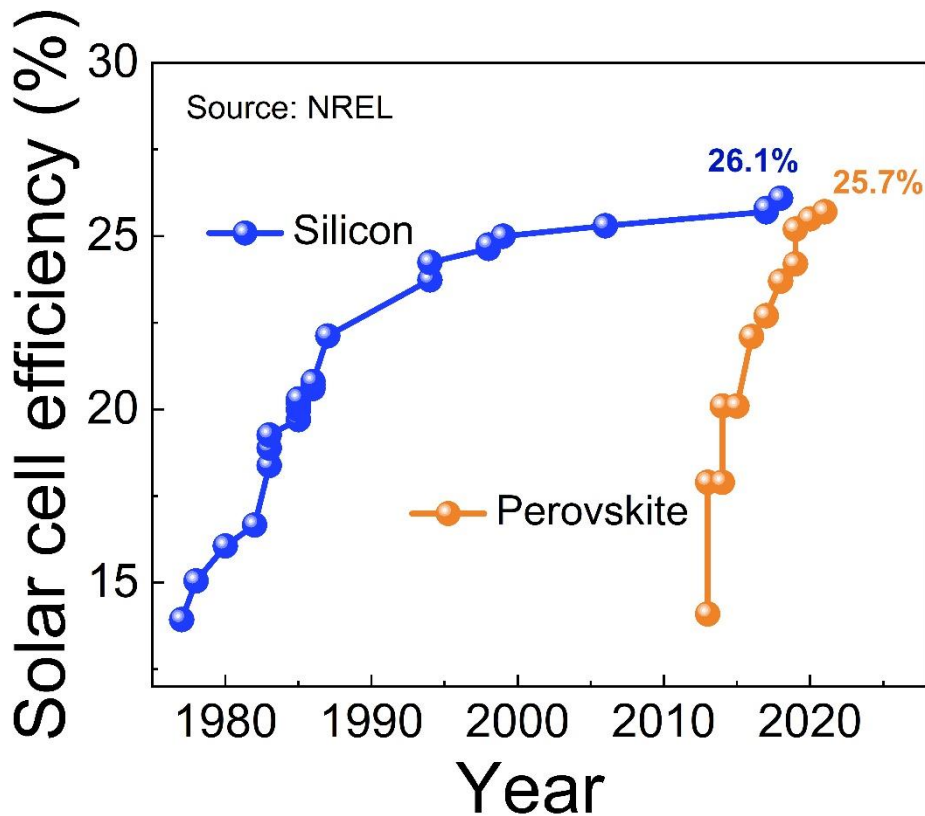


Figure 1.2. The historic photovoltaics performance of Silicon solar cells (single crystal) and perovskite solar cells is based on the data from NREL.⁶

One of the emerging PV technologies, metal-halide perovskite, reached an excellent device performance of 25.7% power conversion efficiency (PCE) in 2021 (**Figure 1.3**), demonstrating its promising future application. Perovskite solar cells can produce lightweight, tuneable colour, flexible and cheap devices. Furthermore, due to its tunable bandgap, tandem solar cell designs are feasible in perovskite-perovskite or perovskite-silicon configurations, among others, more efficiently harvesting the solar spectrum and thus having the capability of surpassing single junction thermodynamic limits to increase performance further beyond silicon.⁹⁻¹³

Though perovskite solar cells have reached high efficiency, most perovskite solar cells are made by lab-based spin-coating methods, and it is not clear that this method can be used for large-scale manufacture. Furthermore, this method requires using a toxic solvent, dimethylformamide (DMF),¹⁴ which can damage the human body, but it is almost necessary to produce high-efficiency perovskite films. Therefore, a solvent-free (dry) deposition approach

can provide an opportunity as an alternative method. Vacuum deposition is a well-established method for thin film semiconductor fabrication to produce uniform and large-scale samples. However, the study of vacuum deposition of perovskite solar cells is still in its infancy. Methylammonium (MA) is widely used in vacuum deposited perovskite to improve device performance. However, the limited thermal stability of MA in perovskite devices under operational conditions can induce device degradation. Furthermore, the MA vapour in the evaporator chamber is difficult to control, decreasing the reproducibility of perovskite films.¹⁵ Vapour processed perovskite solar cell performance is still lagging behind their solution-processed counterparts though the fundamental reason is unclear.

All these questions motivate this thesis, which focuses on multisource evaporation with MA-free perovskite compositions for solar cell applications whilst providing an understanding of the device performance loss. In chapter 2, I discuss the background of perovskite and give an overview of halide perovskites, focusing on photocarrier recombination, defect/surface passivation, wide bandgap (WBG) materials, vacuum deposition methods and all-perovskite tandem solar cells. Chapter 3 gives details of the experimental methods for perovskite film/solar cell fabrication and characterisation. Chapter 4 employs multisource evaporation to produce perovskite films and solar cells, and the effects of substrate dependence, excess PbI_2 , and deposition rate on perovskite stability and device performance will be discussed. Photoluminescence (PL) analysis is employed to understand non-radiative losses in the perovskite with different contact layers.

Chapter 5 will present the optimisation of the hole transport layer by minimising the non-radiative loss and improving the PCE of the solar cell. Furthermore, the perovskite bandgap can be varied by adding PbBr_2 to the evaporation system for the purpose of tandem solar cells. The device open-circuit voltage (V_{oc}) is significantly increased following the bandgap variation up to a bandgap of 1.8 eV, showing minimised phase segregation in evaporated perovskite films. The optimum perovskite bandgap is found to be 1.77 eV, based on PL, nano-X-ray fluorescence (n-XRF) and device performance measurements. Surface passivation is employed to reduce non-radiative recombination on 1.77 eV perovskites, attaining high V_{oc} and fill factor. All-perovskite tandem solar cells are developed to improve the device performance with a combination of WBG, recombination junction layer and the narrow bandgap (NBG) perovskite. The device performance reached 24.1% for the all-perovskite tandem solar cells. Chapter 6 will show the evaporated perovskite for different applications.

We first demonstrate how evaporated perovskite is deposited on textured Si solar cell. The substrate morphology can significantly affect the perovskite crystallographic structure and PL position. Second, the large-scale and fully-evaporated perovskite solar cell is prepared and integrated into an artificial leaf design for a solar fuel application. This technology shows a great potential to transfer electricity to chemical fuel with a better energy storage. Finally, we demonstrate a large reactor of 1000 cm² size to convert the solar energy to syngas (a mixture of CO and H₂). Chapter 7 will summarise the experience of perovskite evaporation, results and conclusion. The outlook of evaporated perovskite and all-perovskite tandem solar cells will be discussed, unveiling a path towards a sustainable future.

Chapter 2. Theoretical background

2.1 Metal-halide perovskite overview

The archetypal 3D perovskite composition with ABX_3 structure can be varied with different atoms or molecules such as Cs, methylammonium (MA) and/or formamidinium (FA) as A site, Pb and/or Sn as B site and, Cl, Br and/or I as X site (**Figure 2.1a**).¹⁶ The bandgap of perovskite can therefore be varied from 1.2 eV to 3.0 eV for different optoelectronic applications (**Figure 2.1b**).^{12,17–20} Halide perovskites are generating enormous excitement as thin film absorbers for high-performance solar cells, showing a unique combination of features that include low-temperature processing, high absorption coefficient, long charge carrier diffusion length, a resilience to electronic defects. All these features make these materials promising for both single and multi-junction thin film solar cells. The first metal halide perovskite was synthesized in 1958 by Moller with a composition of $CsPbX_3$ where $X=Cl, Br$ or I , who has characterised perovskite with cubic structure and observed the colour change of perovskite with different halides.²¹ In 1978, Dieter Weber replaced Cs with MA to form $MAPbX_3$ cubic structure which was the first organic-inorganic 3D perovskite material.²²

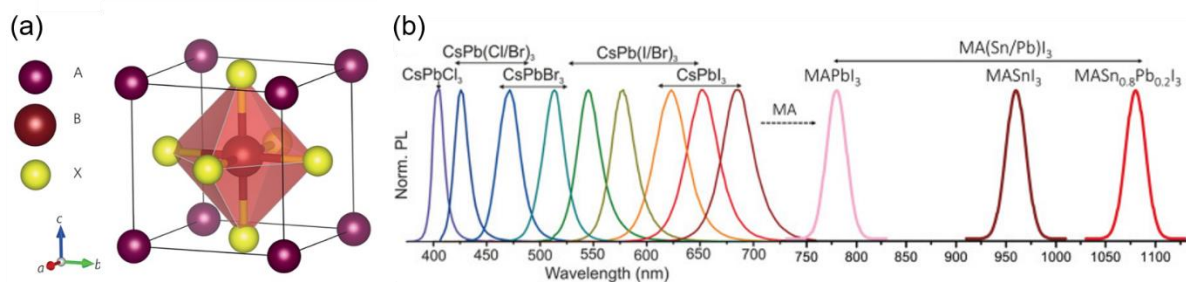


Figure 2.1. (a) A typical 3D ABX_3 structure perovskite,¹⁶ (b) the tunable perovskite PL emission from 400 nm to 1100 nm spectrum region, with different composition.²³ Reproduced with permission from (a) Nature Publishing Group, (b) Elsevier.

Until 2009, the group of Miyasaka used $MAPbI_3$ as a photo absorber, incorporated in mesoporous TiO_2 as a dye-sensitised solar cells architecture, showing a promising PCE of 3.8%.²⁴ However, the liquid electrolyte degraded perovskite rapidly in their work. In 2012, Kim et al. firstly reported a solid-state device architecture, using Spiro-OMeTAD as a hole-transporting layer (HTL), achieving a PCE of 9% with improved stability compared to the liquid-state device.²⁵ Almost at the same time, Lee et al. reported a PCE of 10.9% with solid-state perovskite solar cells as well.²⁶ In this work, they replaced TiO_2 with insulated Al_2O_3 mesoporous acting as a scaffold for the perovskite absorber. This result implies that the mesoporous TiO_2 structure is not necessary for charge transportation, confirming the excellent electron transporting ability of perovskite films. Stranks et al. revealed that the electron-hole diffusion length in perovskite film with a composition of the mixed halides can exceed $1 \mu m$ which is an order of magnitude higher than $MAPbI_3$ composition.²⁷ This composition tuning can improve optoelectronic properties significantly, and this long diffusion length demonstrates that a planar device architecture is feasible.

2.2 Carriers generation, recombination and defect in perovskite film

2.2.1 Photogenerated carriers and recombination pathway

When an incident photon has energy higher than the bandgap of a semiconductor, the photon is absorbed and electron-hole pair is generated. The absorption coefficient of halide perovskite can achieve up to 10^5 cm^{-1} due to its direct band-to-band transition, therefore, the absorber thickness of less than $1 \mu\text{m}$ can capture enough incident light for solar cells application.²⁸ To maximise the perovskite absorption, the reflection loss/absorption of the transparent conducting oxide layer and parasitic absorption in the charge transportation layer need to be considered. A thorough optical design/experiment is required to gain most of the incident photons. Once light is absorbed, hot charge carriers are generated and excited to the energy position higher than the bandgap, and the hot carriers undergo a thermalisation process, relaxing their energy to the conduction band (**Figure 2.2a**).^{29–32} The lifetime of this cool-down process is expected to be on a fs timescale but depends on the carrier concentration,³³ electrostatic screening and polaron effects.^{34,35} After the thermalisation process, the carrier recombination starts with the following different processes, trap-assisted (monomolecular), radiative (bimolecular) and Auger recombination (three-carriers) (see **Figure 2.2b**) and can be described as the following:³⁶

$$\frac{dn}{dt} = -k_1n - k_2n^2 - k_3n^3$$

where n is carrier density and k_1 , k_2 and k_3 are the first, second and third order recombination constant. These recombination constants can be measured based on power-dependent photoluminescence decay or pump-probe spectroscopy. In general, the defect-assisted (K_1) and Auger (K_3) non-radiative recombination dominate at low and high carrier densities, respectively.³⁷

One of the major non-radiative recombination processes in perovskite is the trap-assisted process which reduces PLQE and device V_{OC} . Those defects include interstitials, vacancies and antisite traps with shallow-level (with thermal activation energy lower than K_bT) and deep-level traps such as (Pb_i , I_{MA} and I_{Pb}), the latter showing significant impact on device V_{OC} .³⁸

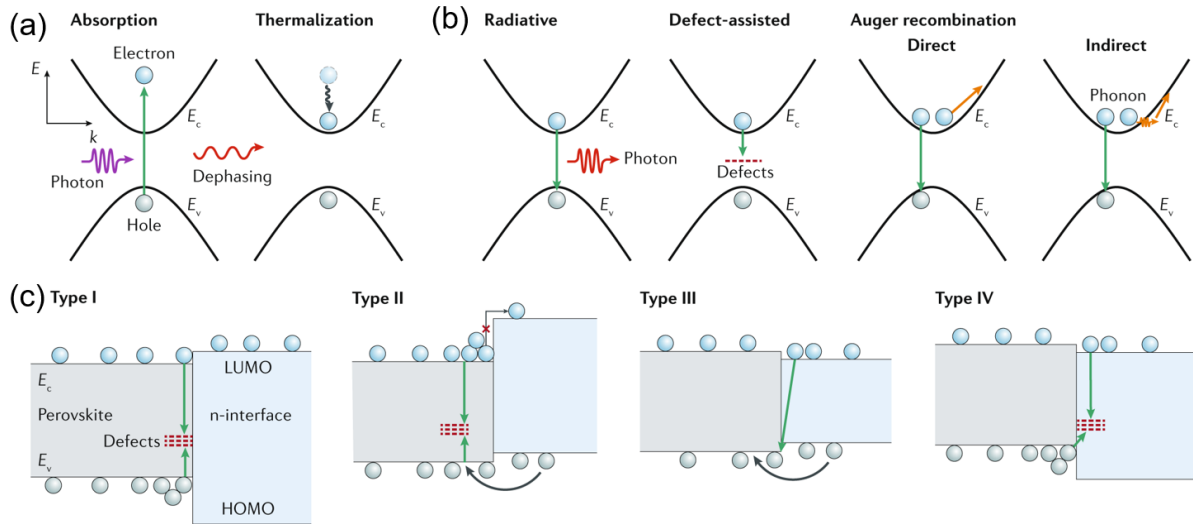


Figure 2.2. (a) the photon absorption/charge generation and thermalisation process in a semiconductor (E_v and E_c are valence band and conduction band) (b) charge recombination dynamic, including radiative recombination and non-radiative recombination (defect-assisted and auger recombination), (c) interface-induced recombination process, Type I: deep defects in perovskite, Type II: defects in perovskite and mismatch energy alignment at the interface, Type III: back transfer recombination and Type IV: electron transporting layer induced defects, (same in the hole transporting layer). The figure is adapted from³². Reproduced with permission from Nature Publishing Group.

2.2.2 Interfacial recombination

An ideal charge transportation layer (CTL) contact with perovskite is necessary to transfer the carriers without energy loss. This additional interface between the perovskite and charge transportation layer is another path for non-radiative recombination loss. Different interface-induced recombination pathways are shown in **Figure 2.3**, including surface defects, mismatch energy level and carrier back transfer. An ideal CTL requires (1) a selective extraction ability for the majority carriers (and block minority carriers), (2) minimum surface defect and (3) decent carrier mobility for efficient charge transport.

To investigate the interfacial loss, the PLQE and quasi-fermi level splitting (QFLS) can provide useful information to understand the defects between CTL and perovskite. PLQE equals the

ratio of current density from radiative recombination (J_{rad}) and current density from total carrier generation (J_G) as the equation below

$$PLQE = \frac{J_{rad}}{J_G} = \frac{J_{rad}}{J_{rad} + J_{non-rad}}$$

Here $J_{non-rad}$ includes all the non-radiative paths in bulk perovskite, interfaces loss between perovskite and CTL or CTL and metal contact. Also, based on Shockley-ideal diode equation,³⁹ QFLS (μ) can be described as a function of radiative efficiency.^{40,41}

$$J_{rad} = J_{0,rad} e^{\mu/k_B T}$$

$$\mu = k_B T \ln \left(\frac{J_{rad}}{J_{0,rad}} \right) = k_B T \ln \left(PLQE \frac{J_G}{J_{0,rad}} \right)$$

Where k_B , T and $J_{0,rad}$ are Boltzmann constant, temperature and thermal equilibrium recombination current density in the dark. With these equations, we can conduct the PLQE measurement of perovskite in contact with different CTLs. Stolterfoht *et al.* have studied the impact of interfacial recombination of $(CsPbI_3)_{0.05}[(FAPbI_3)_{0.83}(MAPbBr_3)_{0.17}]_{0.95}$ perovskite on a different hole or electron transporting layers.⁴² They have found that the internal QFLS is consistent with device V_{OC} output, showing that this approach can give us a first-hand analysis to study new CTL. Furthermore, the energy barrier between perovskite and CTL can affect charge transportation and recombination rate, leading to low V_{OC} . The studies have shown that the electron extraction ability is blocked when the mismatch energy between perovskite and electron transporting layer (ETL) is over 200 mV. On the other hand, any mismatched energy level between hole transporting layer (HTL) and perovskite can increase the recombination rate.

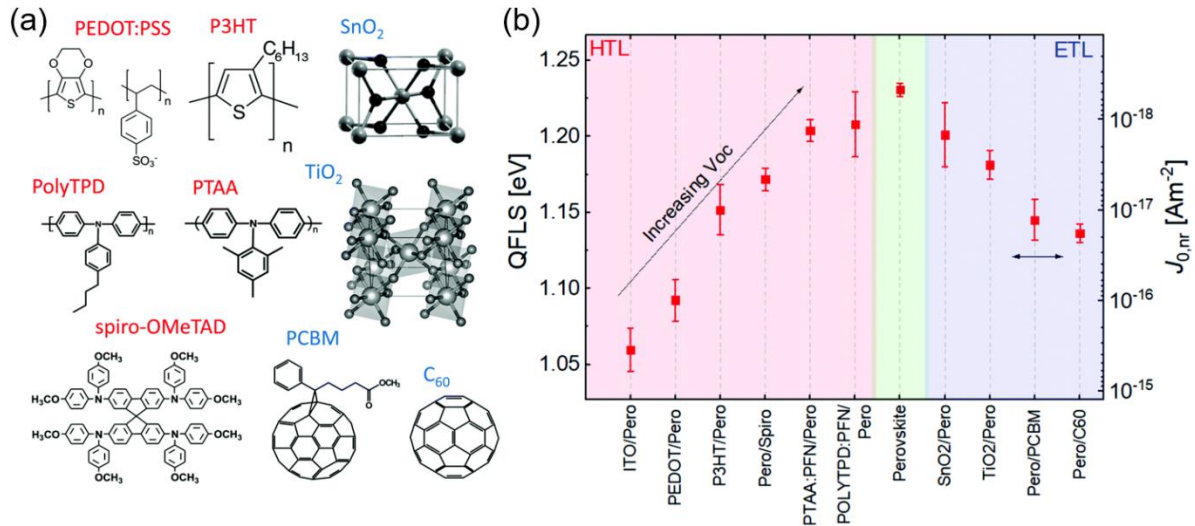


Figure 2.3. (a) Commonly used hole transporting layer, PEDOT:PSS, P3HT, PolyTPD, PTAA, Spiro-OMeTAD, and electron transporting layer, SnO₂, TiO₂, PCBM and C₆₀. (b) The quasi-fermi level splitting and dark current of perovskite with different contact layers.⁴² Reproduced with permission from RSC Publishing.

2.2.3 Quantify V_{OC} loss in a solar cell

As described above, the photogenerated carriers will conduct the recombination process, and radiative recombination can be measured based on PL spectra. An absolute PLQE measurement is a popular experiment to quantify the non-radiative loss and predict the V_{OC} in a complete device.

As the carrier densities in the semiconductor can affect the recombination process, the excitation condition during the experiment needs to be quantified to compare different measurements or labs. Numerous papers have employed one sun equivalent photon flux to measure their perovskite samples (as this illumination condition is close to the device measurement); therefore, the power density calculation using a power metre and a profilometer is required. The calculation for a specific material includes its absorption coefficient, material thickness and exciting laser wavelength. **Figure 2.4** shows a MAPbI₃ absorber with the corresponding generated photon flux from different excited lasers (continues-wave).⁴³

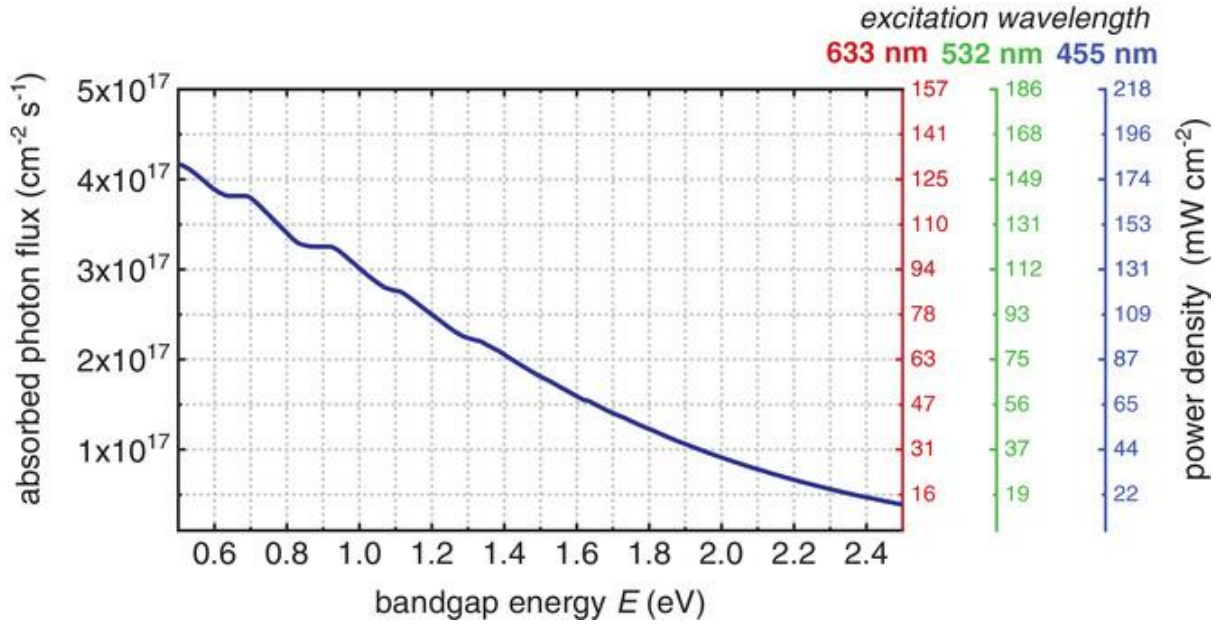


Figure 2.4. An absorbed photon flux for different bandgap semiconductors, assuming where the photons energy higher than the bandgap are absorbed to achieve one sun AM1.5G equivalent steady-state power density. The right axis shows the power density for different excitation wavelengths. The figure is adapted from.⁴³

When a solar cell keeps in the dark without voltage bias, the surrounding black body spectrum is absorbed partly based on the absorption coefficient of the absorber as a function of energy. At equilibrium condition, the absorber absorbs the same as it emits based on^{44,45}

$$\phi_{em,0} = \phi_{abs}(E) = \alpha(E)\phi_{BB}(E)$$

where $\alpha(E)$ is the absorption coefficient.

This equation provides a general reciprocity relation between absorption and emission spectrum. If an external bias is supplied to the solar cell, the photon emission is based on the recombination of electrons and holes from injected bias. This diode-emission relation can be described based on Wurfel's generalized Planck law where chemical potential $\mu = qV$ is introduced.⁴⁰ Therefore, the PL emission with injected bias follows the equation

$$\phi_{em}(E) = \frac{\alpha(E)2\pi E^2}{h^3 c^2} \frac{1}{\exp\left(\frac{E - \mu}{k_B T}\right) - 1}$$

where c is light speed, k_B is Boltzmann constant and T is temperature.

Under light illumination and V_{OC} conditions, the net current in a solar cell is zero, therefore, the radiative V_{OC} can be achieved with no non-radiative recombination process for ideal solar cells.

$$V_{OC,rad} = \frac{k_B T}{q} \ln\left(\frac{J_{SC}}{q\phi_{em,0}} + 1\right)$$

In a real solar cell, the non-radiative loss is almost inevitable, therefore, the PLQE or electroluminescence quantum efficiency (ELQE) is introduced to calculate the loss in a perovskite film or a complete device and the above equation can be adapted to

$$V_{OC} = \frac{k_B T}{q} \ln\left(PLQE \frac{J_{SC}}{q\phi_{em,0}} + 1\right) \approx V_{OC,rad} + \frac{k_B T}{q} \ln(PLQE)$$

Based on this equation, the relation between PLQE and V_{OC} can be observed. To simplify this equation to be a more intuitive, we can vary this equation to

$$V_{OC} = V_{OC,rad} + 60 \text{ mV} \log(PLQE)_{T=300 \text{ K}}$$

The $V_{OC,rad}$ can be achieved when the PLQE or ELQE (for a complete device) is unity. The V_{OC} reduces by around 60 mV with an order of magnitude less PLQE.

2.2.4 V_{OC} deficit calculation

V_{OC} loss (ΔV_{OC}) is commonly used to study the effect of passivation in the solar cells community. The most straightforward equation to calculate the voltage deficit is using $\Delta V_{OC} = \text{bandgap} - \text{measured } V_{OC}$. In this equation, bandgap estimation is required. However, for non-ideal semiconductors, defects, film thickness, and broad absorption tail due to electronic disorder can cause difficulty in accurately calculating the bandgap. In literature, different labs are using various approaches to determine their perovskite bandgaps, including Elliot fitting, absorption tail onset, Taut plot, differential of EQE spectra or 50% at EQE spectra tail (**Figure 2.5a**).^{46–50} However, these methods provide inconsistent bandgaps for the same perovskite material, leading to the overestimating or underestimating V_{OC} deficit and showing a challenge

to compare the results from one publication to another. **Figure 2.5b** demonstrates a bandgap estimation of the same MAPbI₃ perovskite film with different methods, revealing a bandgap variation from 1.57 eV to 1.65 eV (**Figure 2.5b**). This 80 mV variation is enormous, which is more than one order of PLQE variation if we compare it to the absolute PL measurement.

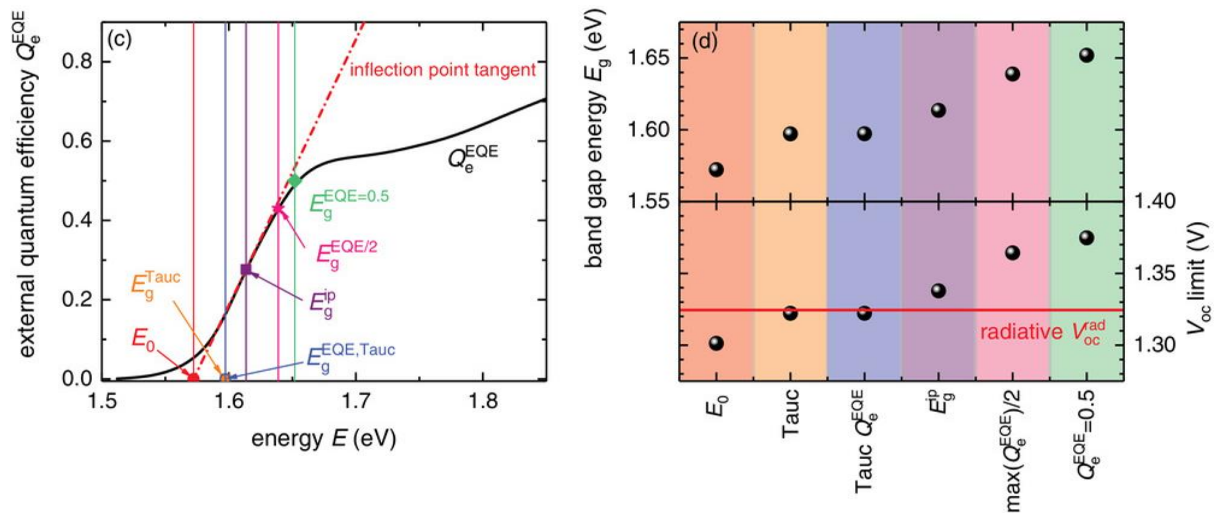


Figure 2.5. (a) Bandgap determination of MAPbI₃ solar cells based on different methods in the literature. (b) the estimated bandgaps and the radiative V_{oc} (red line) of MAPbI₃ solar cell. The figure is adapted from ⁵⁰.

Among these methods, differential of EQE spectra could provide more accurate calculation as the sub-band absorption at the band edge is minimised.⁵¹

$$E_g = \frac{\int_a^b E_g P(E_g) dE_g}{\int_a^b P(E_g) dE_g}$$

$$P(E_g) = \frac{d}{dE} EQE(E)$$

where $P(E_g)$ is the probability distribution of the bandgap energies, and a/b is the integration region. By this approach, a constant inflection point can be achieved.

Furthermore, to understand the V_{OC} deficit, the bandgap of a semiconductor is not necessary. From Shockley ideal diode equation, the

$$V_{OC,rad} = \frac{k_B T}{q} \ln\left(\frac{J_{SC}}{q\phi_{em,0}} + 1\right)$$

which can be adapted to

$$V_{OC,rad} = \frac{k_B T}{q} \ln\left(\frac{\int EQE_{PV}(E)\phi_{AM1.5}(E)dE}{\int EQE_{PV}(E)\phi_{BB}(E)dE}\right)$$

In this equation, $V_{OC,rad}$ can be calculated by measuring the EQE of solar cells and the measured V_{OC} can be achieved from a J-V scan, therefore the V_{OC} deficit is known. The details of this calculation can see in chapter 3.3.9.

2.3 Wide bandgap (WBG) perovskite

2.3.1 Phase segregation in WBG

It is well-known that the WBG perovskite with a high ratio of Br/I suffers from serious phase segregation under light intensity or electroluminescence conditions.^{52,53} Halides start to separate and migrate to form I-rich and Br-rich domains under external bias. This might induce a halide deficiency in the grain boundary and cause a carrier tunnel effect in which carriers transfer from the high energy level to the low energy level and reduce the device V_{OC} .⁵⁴ The observation of phase segregation was first reported by Hoke et al. in a mixed halide perovskite system, showing a red-shifted PL peak under one sun intensity within only 1 min illumination (**Figure 2.6**).⁵² X-ray diffraction pattern (XRD) also confirmed the changes in phase structure with splitting peak after light illumination. Though this photo-induced segregation effect can be reversed when the perovskite film is stored in a dark environment.⁵⁵ During the device operation, the mixed-halides perovskite undergoes phase segregation with sub-bandgap defect sites or trap states which can be seen as recombination centres to trap the free carriers. The segregation results in poor V_{OC} output in high bandgap perovskite systems and is a major impediment to the application of tandem solar cells.

However, the mechanism of photoinduced phase segregation is still under debate. Likely, the produced charge carrier (or excess energy from hot carriers) from light excitation in the perovskite absorber may trigger the halide migration via defect sites.^{54,56} The activation energy of halide defect formation is low (0.1-0.6 eV for iodine vacancy V_I^+ and interstitial I_I^- , and around 0.3 eV for bromine counterparts) and, therefore, become the mobile species under external bias.⁵⁷⁻⁵⁹ Besides, the formation energy of halide defects is lower than anion and metal vacancies, explaining the existence of halide segregation in WBG perovskite system.⁶⁰ One of the possible migration mechanisms could be that the formation of X_x^- is energy favourable, and this defect traps the photogenerated hole/electron to form neutralised halide interstitial (X_x^0).^{61,62} The calculation suggests the formation energy of neutral iodine and bromine are 0.29 eV and 0.12 eV, respectively. Furthermore, this neutralises halide interstitial (X_x^0) form X_2 by a bimolecular process, which depends on the concentration of halide interstitial. This process triggers the Frankel disorder: $X_x \rightarrow X_x^- + V_x^+$, increase more mobile defects. The whole process implies that the traps of photogenerated holes or electrons can boost the formation of ionic species. Several reports have shown that the fast hole transfer process can minimise phase segregation.^{11,63} Also the defect formation energy, ions movement speed and the hole/electron hopping under light-soaking are different, they generate the halides gradient and cause phase segregation.⁵⁴ Interestingly, the phase segregation process is reversible. After placing the excited sample in the dark, entropy drives all halides to a homogeneous system.

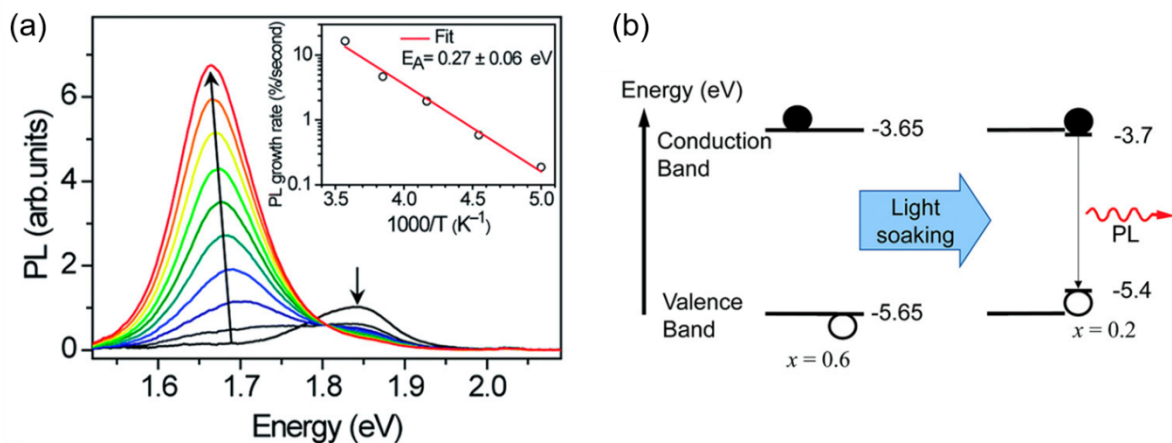


Figure 2.6. (a) the PL spectra shift from high energy to low energy under light-soaking conditions. (b) the energy diagram of phase segregation. This figure is adapted from⁵².

2.3.2 A-site composition engineering to mitigate phase segregation

McMeekin et al. found that introducing Cs in the $\text{FAPb}(\text{I}_{1-x}\text{Br}_x)_3$ structure can lower the cubic lattice constant from 6.306 to 5.955 Å,⁶⁴ which alleviates the phase transition and improves the stability.⁴⁴ Moreover, Bush et al. systematically varied the perovskite composition by changing the amount of Cs or Br in the $\text{FA}_{1-x}\text{Cs}_x\text{Pb}(\text{I}_{1-y}\text{Br}_y)_3$ structure and studied the effect on phase segregation.⁶⁵ They have found that with a higher fraction of Br, the amount of Cs in perovskite composition needs to be increased to minimise phase segregation. It is beneficial to improve the photostability and V_{oc} by using FA and Cs in the A site to control the bandgap instead of Br in the X site to tune the perovskite composition. Otherwise, a penalty in V_{oc} can be seen. They listed two promising composition, $\text{FA}_{0.75}\text{Cs}_{0.25}\text{Pb}(\text{I}_{0.80}\text{Br}_{0.20})_3$ and $\text{FA}_{0.60}\text{Cs}_{0.40}\text{Pb}(\text{I}_{0.70}\text{Br}_{0.30})_3$ for WBG perovskite solar cell. The reason is that A-site cations in perovskite structure provide different polarity and affect the halide defect movement. Mosconi et al. have used ab initio molecular dynamics simulation to understand the effect of MA on vacancy defect migration.⁶⁶ They have revealed that the polarity of MA can facilitate iodine migration. Therefore, using FA or Cs with less polar A-site cation might show less phase segregation.

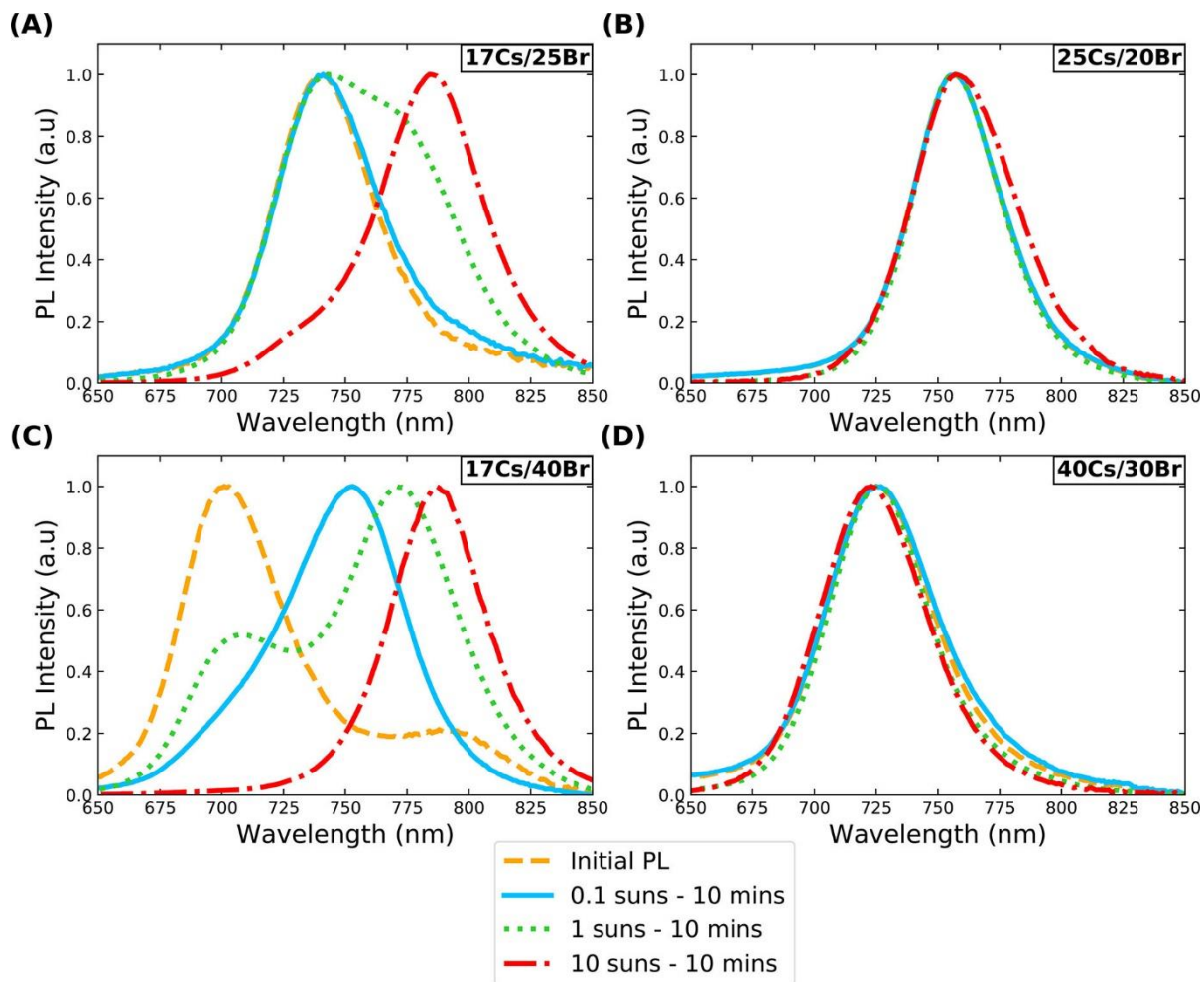


Figure 2.7. The phase segregation analysis with different perovskite compositions of $\text{FA}_{0.83}\text{Cs}_{0.17}\text{Pb}(\text{I}_{0.75}\text{Br}_{0.25})_3$, $\text{FA}_{0.75}\text{Cs}_{0.25}\text{Pb}(\text{I}_{0.8}\text{Br}_{0.2})_3$, $\text{FA}_{0.83}\text{Cs}_{0.17}\text{Pb}(\text{I}_{0.6}\text{Br}_{0.4})_3$ and $\text{FA}_{0.6}\text{Cs}_{0.4}\text{Pb}(\text{I}_{0.7}\text{Br}_{0.3})_3$ under 10 mins of light soaking at various light intensities. The figure is adapted from⁶⁵.

2.3.3 Bulk perovskite passivation and contact layers optimisation

Inhomogeneous distribution of elements in perovskite film could be the reason for defects and phase segregation, either these defects are intrinsic or photoinduced in the structure.⁶⁷ It should be noted that the activation energy for ion migration and formation energy for trap-states are considerably smaller than to the energy that is applied during device operation.⁶⁸ In this regard, the inhomogeneous problem in perovskite film should be thoroughly investigated to deposit intrinsic defect-free or fewer halide vacancies in the grain boundary. Some strategies have been investigated to minimize phase segregation by controlling the crystallinity, morphology and

reducing halide defects to suppress the V_{OC} deficit. Some literature suggests that defects are mainly located around the grain boundary. Therefore, a popular strategy is to enlarge the grain size and improve crystallinity to reduce defects. For example, combining a solvent annealing process and using lead thiocyanate ($Pb(SCN)_2$) as an additive in WBG perovskite significantly improves the grain size from 66 to 1036 nm, as well as increases the V_{OC} by 80 mV.⁶⁹ Zhou et al. studied the control of nuclear growth dynamic by inducing $Pb(SCN)_2$ and FAX in perovskite precursor solution to enlarge the grain size with a better crystallinity. The light-stress experiment shows that the perovskite film improves its photostability under continuous light illumination (1 sun) for 4 h. They achieved a V_{OC} of 1.24 and 1.28 V from a bandgap of 1.72 and 1.79 eV, respectively, from a normal device configuration which was the highest reported V_{OC} from WBG perovskite solar cell.

Lin et al. studied the energy levels matching between Indene-C60 Bisadduct (ICBA) and the perovskite layer for inverted perovskite solar cells to increase the V_{OC} and PCE.⁵² They isolated ICBA-tran3 from the ICBA mixture to lower energy disorder and increase carrier mobility. The device architecture, ITO/PTAA/Perovskite/ICBA/ C_{60} /BCP/Cu, can achieve a V_{OC} of 1.21 V and a PCE of 18.5% for a perovskite bandgap of 1.71 eV. Another interface optimisation report by Hu et al. is introducing thin wide bandgap layers MoO_x and ZrO_2 between perovskite and contact layers to reduce back transfer recombination.⁵³ This interfacial engineering demonstrates the importance of charge recombination at the interfaces and shows the improvement in device V_{OC} . They have employed this approach on different bandgaps of perovskite solar cells, $MAPbI_3$, $MAPbBrI_2$ and $MAPbBr_3$, with a bandgap of 1.58, 1.75 and 2.25 eV, respectively. They propose that the blocking effect of back transfer recombination by MoO_x and ZrO_2 is more prevalent in WBG perovskite solar cells due to reduced energy level mismatch. Besides, using metal oxide layers provides robust stability as a protective layer for the whole device. Although these strategies demonstrate a promising improvement, the V_{OC} deficit is still severe in WBG perovskite (V_{OC} deficit > 0.45 V) in comparison to NBG counterpart (V_{OC} deficit < 0.40 V).

2.3.4 Defects in WBG perovskite

To achieve a 30% all-perovskite tandem solar cell, a V_{OC} of at least 1.3 V from WBG subcell is necessary. However, developments of WBG in tandem solar cells have reached the plateau that the V_{OC} does not increase according to the bandgap (**Figure 2.8**).⁶⁰ Beyond phase segregation, other fundamental factors need to be considered here. The commonly used charge transporting layers in PSCs are not optimised for WBG materials, and energy level mismatch could induce charge recombination between the contact layer and perovskite absorber. Furthermore, the high trap density in WBG perovskite with low PLQE is vital to the V_{OC} penalty. Mahesh et al. have comprehensively studied V_{OC} loss in WBG perovskite with mixed halide composition.⁷⁰ They have found that the low ELQE in their device is the dominated loss from non-radiative recombination, leading to the low V_{oc} , not phase segregation. They deconvoluted the V_{OC} loss and found that ~ 400 mV loss is from trap-assisted recombination and ~ 100 mV from phase segregation. Besides, during the phase segregation, the high carrier density funnels to the low bandgap region to increase the radiative recombination, resulting in less V_{OC} loss. From their work, a V_{oc} of 1.33 V can be achieved for a 1.77 eV perovskite, even the phase segregation exists, showing the path to minimise non-radiative loss as the priority.

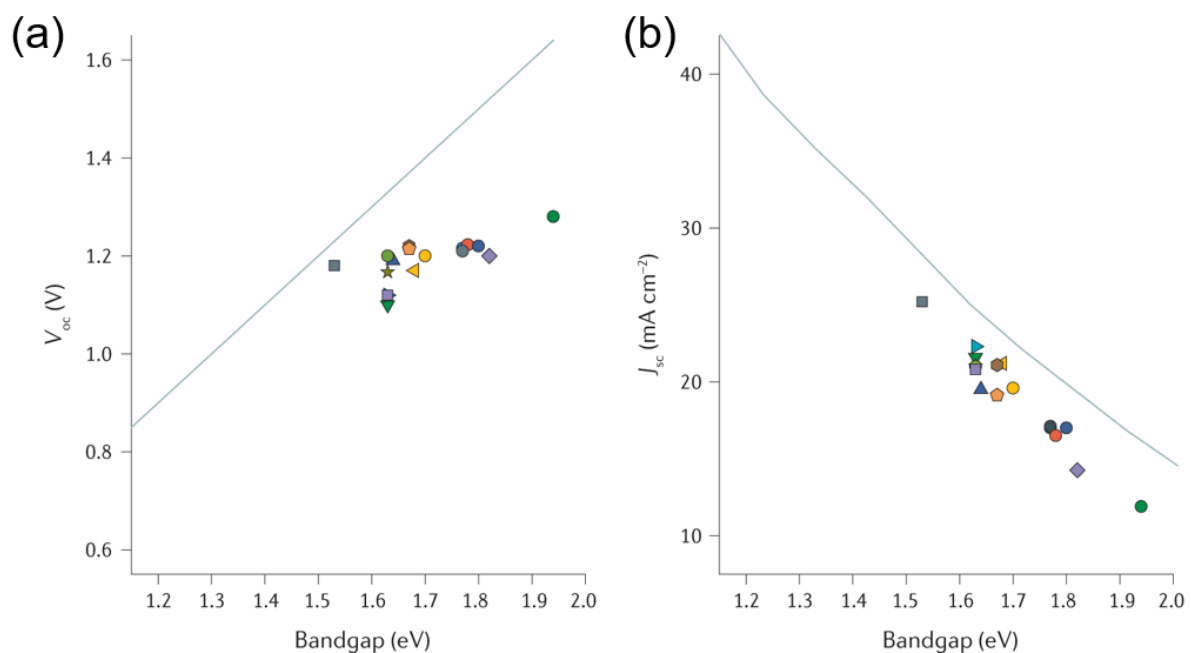


Figure 2.8. The V_{OC} (a) and J_{SC} (b) of different WBG perovskite in 2T all-perovskite tandem solar cells. This figure is adapted from ⁶⁰. Reproduced with permission from Nature Publishing Group.

2.4 Vacuum deposited perovskite by multisource evaporation

2.4.1 The motivation for Vacuum deposited perovskite

To date, the record PCE single-junction perovskite and all-perovskite tandem solar cells have reached PCEs of 25.7% and 26.4%,^{71,72}, respectively, representing the most efficient emerging PV systems to date. These outstanding outcomes result from years of work from myriads of research groups mostly working with solution-processed approaches that allow rapid screening and optimisation. However, solution approaches ultimately present limitations for manufacturing due to the use of toxic solvent, DMF,¹⁴ and potential issues with dissolving underlying layers, the latter limiting the underlying materials and substrates.

Vacuum deposition processes show great promise to overcome barriers related to large-area coating, integration into flexible, lightweight substrates and novel device patterns while ensuring high thickness control and conformal film uniformity, all with a solvent-free technique. Notably, the dry nature of the technique represents an ideal approach to stack different perovskite films for single junction device to tandem device architectures on a range of underlying contacts and substrates, an approach that opens avenues for a highly efficient yet low-cost thin film, light-weight perovskite technology. Also, the perovskite precursors can be thermal evaporated individually, providing a path to precisely control composition or stoichiometry. Nevertheless, only a handful of works have reported fully-evaporated perovskites for their application.

2.4.2 History of vacuum deposited perovskite

The first evaporated perovskite solar cell has demonstrated by Liu et al. in 2013, who first co-evaporated MAI and $PbCl_2$ perovskite on the compact- TiO_2 layer for n-i-p solar cells and

achieved a PCE of 15% (**Figure 2.9a**).⁷³ During the evaporation process, the film quality and composition can be fine-tuned to control the perovskite stoichiometry and film thickness, monitoring by individual quartz crystal microbalance (QCM). Furthermore, the cooling water and rotation system for the substrate stage are used to achieve high-quality perovskite film. The advantage of the vacuum deposition method here has demonstrated a smooth and uniform perovskite film (**Figure 2.9b**), compared to the solution-processed counterpart and prevented the current leakage. This work presents the possibility of using the industrial-scale technique for perovskite deposition with a solvent-free approach, indicating the promise for modular and multi-stack devices. Malinkiewicz et al. co-evaporated MAI and PbI₂ on the organic charge transportation layer, Poly-TPD, to finish the solar cell with p-i-n device architecture and achieved a PCE of 12% (**Figure 2.9c**).⁷⁴ Interestingly, as-deposited film has shown the formation of perovskite without thermal annealing, which could be used for thermal-sensitive applications. Ono et al. have developed an evaporator system to monitor the MAI vapour during the co-evaporation and demonstrated perovskite on a large-scale with 5 x 5 cm² size with excellent uniformity and high reproducibility.⁷⁵ Momblona et al. have been working on doped organic charge transportation layers by partial oxidising hole transportation layer and reducing the electron transportation layer to improve device charge transfer and achieve the PCEs of 20% and 16% for n-i-p and p-i-n architecture, respectively.⁷⁶ This was the first paper demonstrating a PCE >20% with evaporated perovskite solar cells (**Figure 2.9d**). Also, this work employed a fully evaporated process for the entire device architecture, a solvent-free fabrication to prevent the use of toxic solvents.

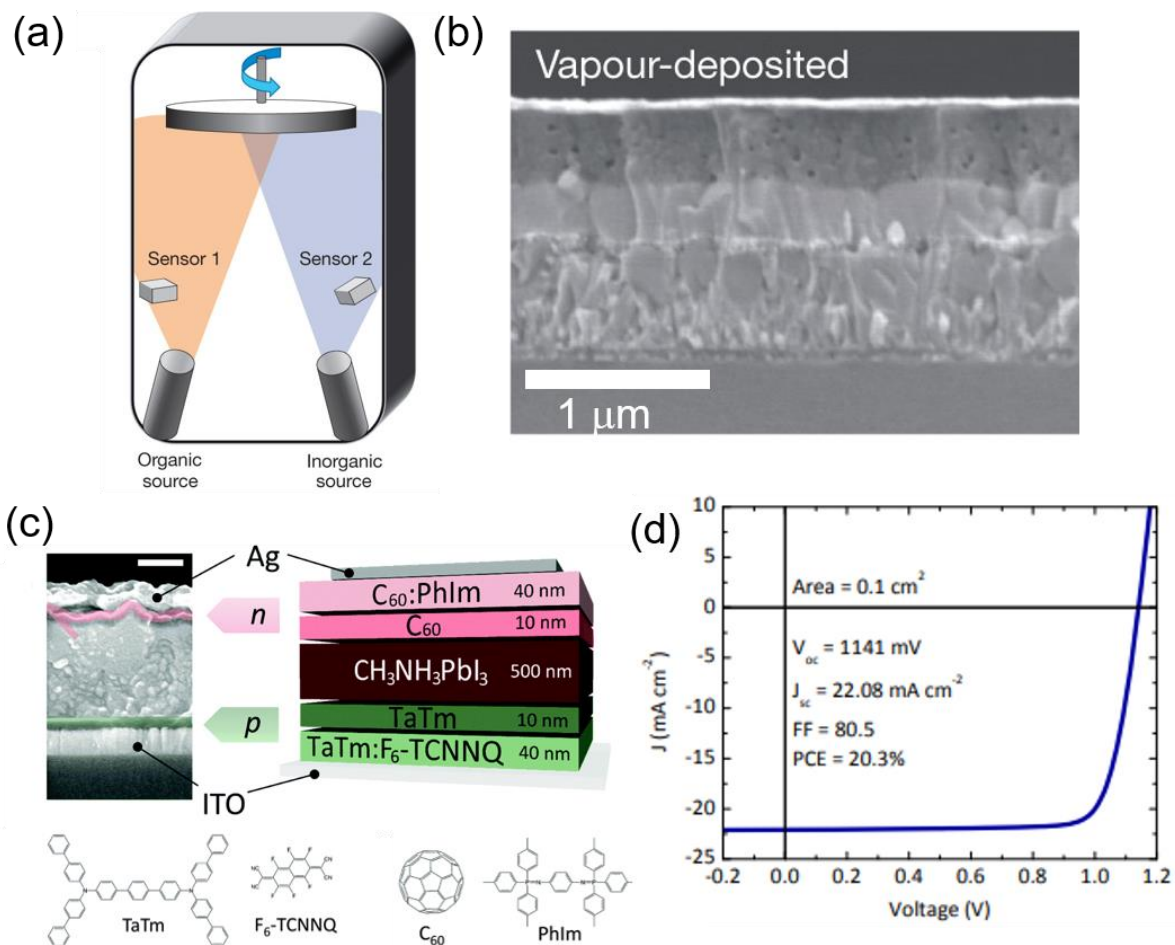


Figure 2.9. The co-evaporation system shows dual-source deposition, two QCM monitors and a rotated substrate stage. (b) the SEM image of evaporated perovskite solar cells demonstrates the uniform perovskite coating.⁷³ (c) A fully evaporated perovskite solar cell with p-i-n device architecture and corresponding cross-sectional SEM image. (d) the device performance of a fully-evaporated perovskite solar cell with MAPbI₃ composition and a power conversion efficiency of 20.3%.⁷⁶ Reproduced with permission from Nature Publishing Group and RSC publication.

2.4.3 The deposition parameter effect on evaporated perovskite quality

Evaporated perovskite film quality is dominated by the followings: chamber pressure, deposition rate, substrate temperature, precursor purity, potential cross-contamination and the underlying substrate. The latter is related to the sticking coefficient of the exposed surface of

the substrate to evaporated material. Olthof and Meerholz have reported that the nature of substrate material can affect nuclei growth of perovskite film when vaporised precursors reach the substrate (**Figure 2.10**).⁷⁷ They investigated MAPbI₃ perovskite formation on different substrates, PEIE, ITO, MoO_x and PEDOT:PSS by ultraviolet photoelectron spectroscopy (UPS) and X-ray photoelectron spectroscopy (XPS) to understand the surface chemical states. From the UPS and XPS, the perovskite signal is detectable with only 3 nm thickness on PEIE and PEDOT:PSS, suggesting faster formation on the organic surface.

On the contrary, the perovskite formation on the metal oxide layers, ITO and MoO_x, was detected after a 30 nm and 10 nm deposition, respectively. The explanation here is that the hydroxyl group can dissociate MAI to its byproduct and hinder the sticking of MAI on the surface. Therefore, perovskite formation only starts once the hydroxyl group is occupied. The perovskite grain size is also different on these layers, suggesting that the perovskite deposition condition should be fine-tuned on different layers.

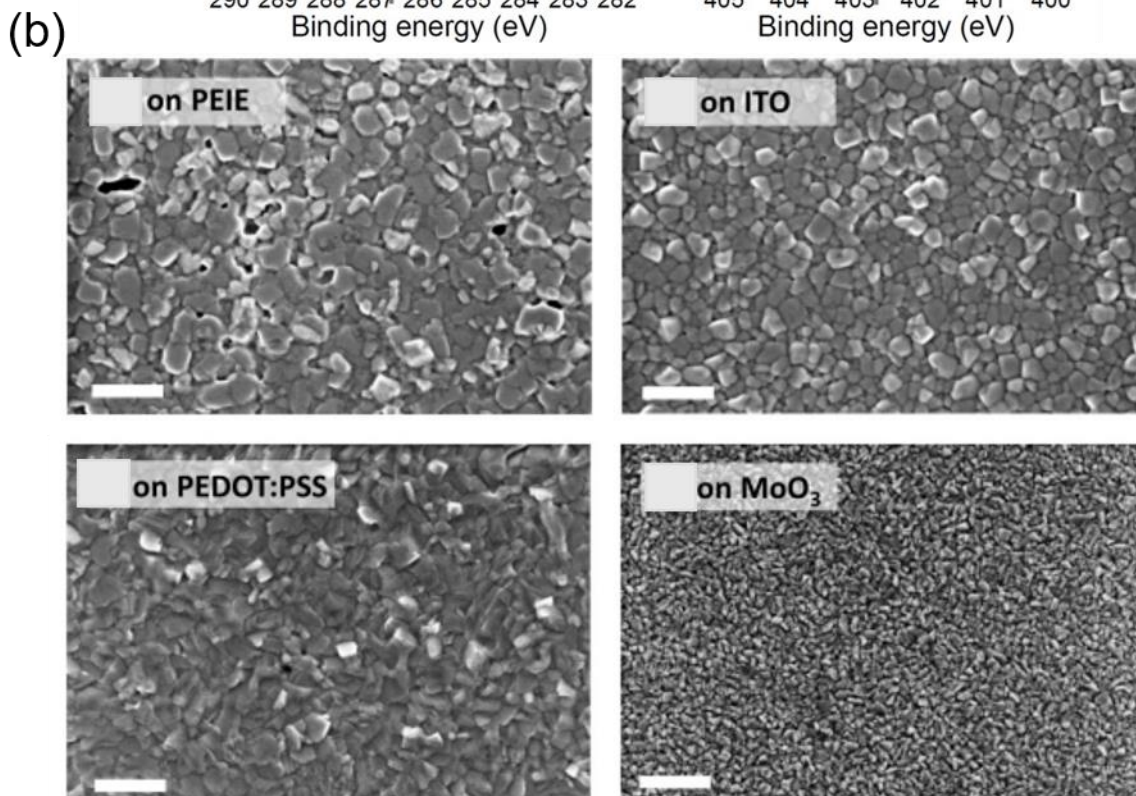
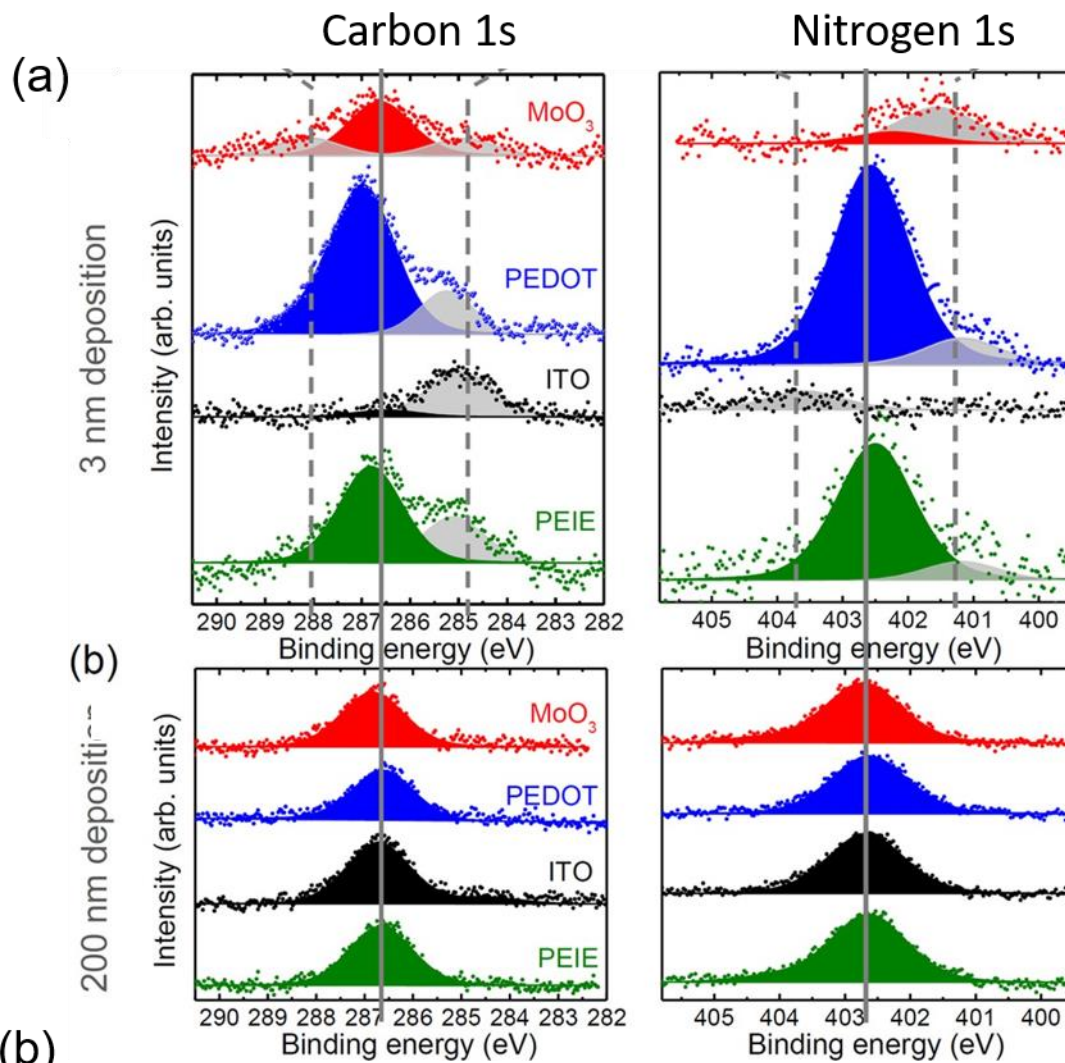


Figure 2.10. MAPbI₃ perovskite composition analysis, deposited on different substrates (PEIE, ITO, PEDOT:PSS or MoO_x), (a) with 3 nm and 200 nm thickness by XPS spectra of C1s and N1s measurement. (b) SEM surface morphology characterisation. Scale bars are 500 nm. The figure is adapted from ⁷⁷.

Beyond the underlying material, Lohmann et al. have found that the substrate temperature during the evaporation can affect the perovskite crystal size (based on SEM image), crystal structure and solar cells performance (**Figure 2.11**).⁷⁸ They have found that the formation of MAPbI₃ is through the presence of PbI₂ (as the sticking coefficient of MAI on the substrate is relatively low) and followed by MAI deposition to convert to perovskite. Therefore, the substrate temperature can affect the sticking coefficient of MAI and the perovskite conversion from PbI₂ to MAPbI₃. Therefore, the excess PbI₂ during the co-evaporation not only helps passivation but also provides the nucleation template for perovskite formation. They have used optical-pump THz-probe spectroscopy to investigate the carrier mobility of perovskite and growth under different substrate temperatures. Interestingly, the carrier mobility in smaller grain size (13.0 cm²/(Vs)) is larger grain perovskite film (6.87 cm²/(Vs)), indicating that the traps are not associated with grain boundaries. The explanation here is that the traps might be located on the perovskite surface or the trap formation is less during the deposition process of small grains.

Roß et al. have also found that the substrate temperature can affect MAPbI₃ co-evaporation and change the sticking factor of organic MAI and inorganic PbI₂.⁷⁹ The MAI sticking coefficient is greatly affected by substrate temperature and decreases by four times from a substrate temperature of -30°C to 60°C meanwhile the PbI₂ sticking coefficient shows almost no change. The high substrate temperature might also be involved in the adhesive MAI's desorption process on the substrate. The fine control of substrate temperature is critical as at high temperature (60°C), there is not enough MAI for perovskite, and at low temperature (-30°C), the perovskite conversion is inhibited. Their work shows that the surface morphology and crystal structure of perovskite films on PTAA or MeO-2PACz are different, suggesting the variation of the perovskite growth mechanism. In their summary, the optimum window of perovskite deposition on MeO-2PACs for solar cells is wider than the PTAA counterpart. The former show higher V_{OC} and FF, leading to better device performance. Instead of controlling the deposition rate of MAI, Heinze et al. have shown that the partial pressure of MAI during

MAPbI₃ co-evaporation can significantly affect the film morphology and crystallographic structure on different charge transportation layers, resulting in composition variation.⁸⁰

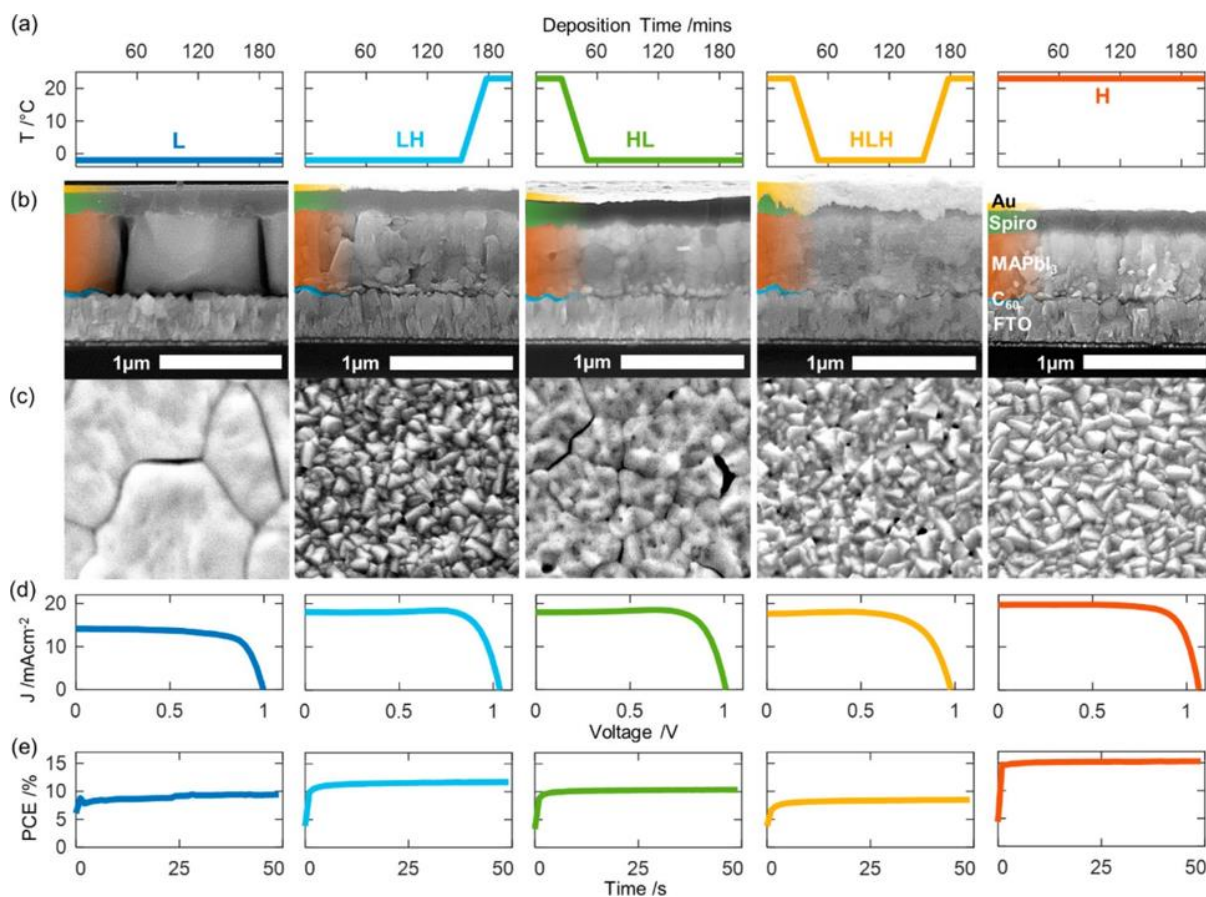


Figure 2.11. The effect of substrate temperature variation as a function of time during co-evaporated MAPbI₃. (a) temperature change diagram (b) the cross-sectional SEM images, and (c) the top-view morphology, showing noticeable grain size variation. (d) the J-V curve scan of the MAPbI₃ device, prepared by different substrate temperatures and (e) the stabilised PCE output. This figure is adapted from ⁷⁸.

Though the MAPbI₃ evaporation for solar cells has shown high device performance with over 20%, there are some concerns regarding MA cation, (1) due to the high MAI vapour pressure, the deposition rate is challenging to control, and this compound tends to condense outside the evaporation cone area, triggering the cross-contamination issue, (2) the sticking coefficient of MAI is low and it tends to decompose during the evaporation which rises the reproducibility issue of MA-based perovskite film.⁸¹ Also, MA cation shows the thermal stability issue, which

can evaporate from perovskite structure at high temperature, leading to the potential risk for commercialisation.⁸² In summary, MAI for perovskite evaporation is not beneficial to chamber condition, batch-to-batch reproducibility and device thermal stability; therefore, MA-free based evaporated perovskite has been studied.

2.4.4 MA-free perovskite and the PCE roadmap

Gil-Escrig et al. have been working on evaporating MA-free perovskite with a composition of $\text{FA}_{0.5}\text{Cs}_{0.5}\text{Pb}(\text{I}_{0.83}\text{Br}_{0.17})_3$ for n-i-p solar cells.⁸³ In their work, they obtained a PCE of 9% for this MA-free composition. Interestingly, they have also demonstrated that the solar cell performance improved to 16% with MA incorporation into perovskite structure. This suggests that the MA is a boost for highly efficient solar cells. In 2017, Borchert et al. prepared FAPbI_3 perovskite and showed a uniform film over $8 \times 8 \text{ cm}^2$ size with a low surface roughness of 6.2 nm. Terahertz (THz) photoconductivity measurements revealed the high charge-carrier mobility of $26 \text{ cm}^2 \text{ V}^{-1} \text{ s}^{-1}$. They fabricated an n-i-p solar cell with evaporated FAPbI_3 , demonstrating a PCE of 15.8%.⁸⁴

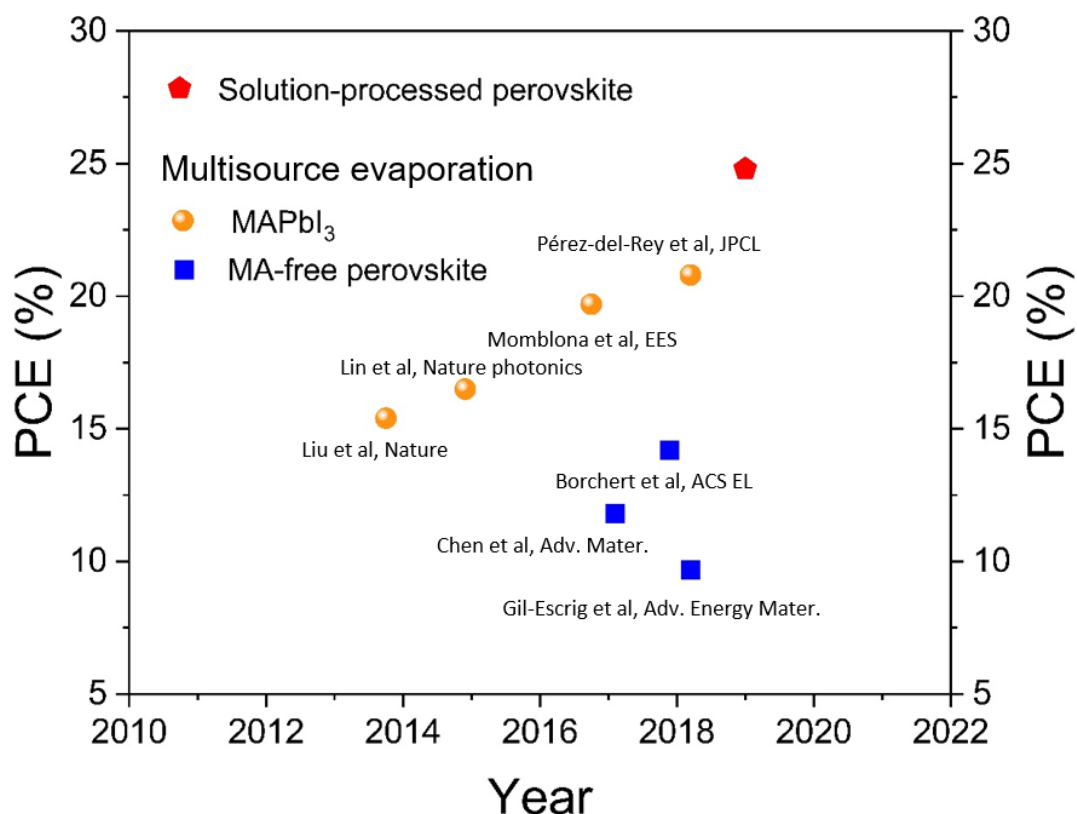


Figure 2.12. The PCE roadmap of perovskite solar cells performance based on solution process or multisource evaporated perovskite with or without MA during deposition. This device performance is this figure is updated until 2018.^{73,76,83–87}

In October 2018, when I joined the StranksLab to start my PhD, the multisource evaporated perovskite with MA-free composition showed relative low device performance (blue), compared to MA-based counterparts (orange) (see **Figure 2.12**). Pure FAPbI₃ perovskite is suitable for single junction solar cells as its bandgap is close to the ideal value based on the SQ limit. However, the FAPbI₃ film suffers from operational stability as the black-phase can convert to a yellow δ -phase at room temperature due to the tolerance mismatch. In this thesis, Cs and Br are incorporated into our perovskite composition to have a more stable film.

2.5 Two terminal (2T) All-perovskite tandem solar cells

For light harvesting, a semiconductor can only absorb the photon energy higher than its bandgap and create an hole and electron in the valence and conduction bands. However, when the energy of the photon is higher than the bandgap, the hot carries with excess energy undergo the thermalisation process in which the excited hole and electron relax their energy to the conduction band and valence band for recombination or charge extraction. During this relaxation process, the photon energy higher than the semiconductor bandgap is lost. The tradeoff between minimising thermalisation (use WBG semiconductor) and increasing light harvesting (use NBG semiconductor) is the fundamental limitation of solar cells performance.⁸⁸ Based on the thermodynamic principle, the SQ limit indicates that the maximum PCE of a single junction solar cell is around 34%, with a semiconductor bandgap of 1.37 eV.³⁹ To exceed the SQ limit, the multijunction solar cells with different bandgap absorbers are used in the stack in which a WBG semiconductor captures the high energy photons to minimise the thermalisation loss, and the low energy photons are passed to a NBG semiconductor for absorption. Ideally, the two junction solar cells and triple junction solar cells can reach 46% and 52%, respectively.

2.5.1 Structure of tandem perovskite solar cells

Here, we focus on a 2T tandem solar cell where the multilayer absorbers are stacked on the same substrates, and these layers are connected by a recombination junction (RJ) in series. This monolithic device architecture requires only two external circuits for output connection and a less transparent conductive oxide (TCO) substrate, compared to 4 terminal tandem solar cell.⁸⁹ Therefore, most commercial tandem solar cell products use 2T tandem design (**Figure 2.13**). However, the 2T design requires stricter current matching. Metal-halide perovskite has demonstrated its excellent optoelectronic properties for photovoltaics and the single junction perovskite solar cells have achieved a certified PCE of 25.6%, comparable to silicon counterparts. This striking performance has approached the SQ limit, therefore, an add-on layer(s), tandem solar cells, is necessary to improve the light-harvesting and to reduce the thermalisation loss. Due to the bandgap tunability of perovskite, the bandgap of perovskite film

is between 1.2 to 2.3 eV, showing the promising opportunity for all-perovskite tandem solar cells.

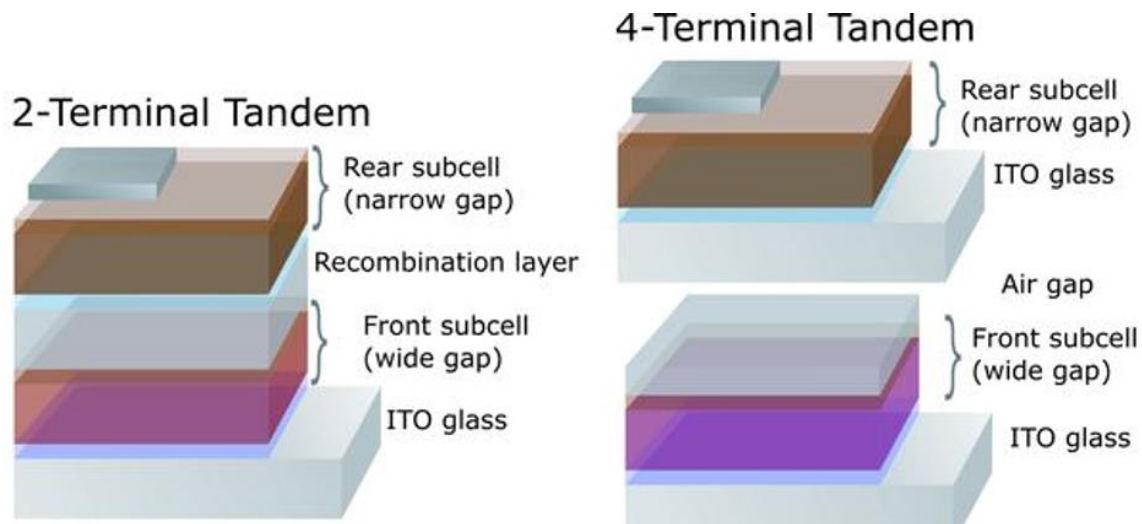


Figure 2.13. The device architecture of 2-terminal and 4-terminal tandem solar cells. This figure is adapted from ⁹⁰.

As the two absorbers are connected in series, the tandem device V_{oc} is the sum of two subcells and the lowest photocurrent of the subcell limits the current. Therefore, current matching is extremely important in a tandem system, in which the bandgap choice of two absorbers should be optimised to maximise the PCE. For 2T all-perovskite tandem solar cells, the ideal bandgap for top and bottom absorbers is between 1.7 to 1.8 eV, and 1.2 to 1.3 eV narrow bandgap, respectively. Theoretical calculations suggest the PCE of a two-terminal tandem solar cell can achieve up to 35%.^{88,91} However, those calculations did not include intrinsic recombination and luminescence outcoupling. Bowman et al. have included the recombination rate and absorption coefficient of WBG ($FA_{0.7}Cs_{0.3}Pb(I_{0.7}Br_{0.3})_3$) and NBG perovskite ($FAPb_{0.5}Sn_{0.5}I_3$) and suggest that the high radiative recombination in both subcells can improve the PCE limit to 40% (**Figure 2.14**).⁹² To date, the highest PCE of all-perovskite tandem solar cells have achieved 26.2%, though the challenges from both subcells and the RJ are not fully addressed yet.

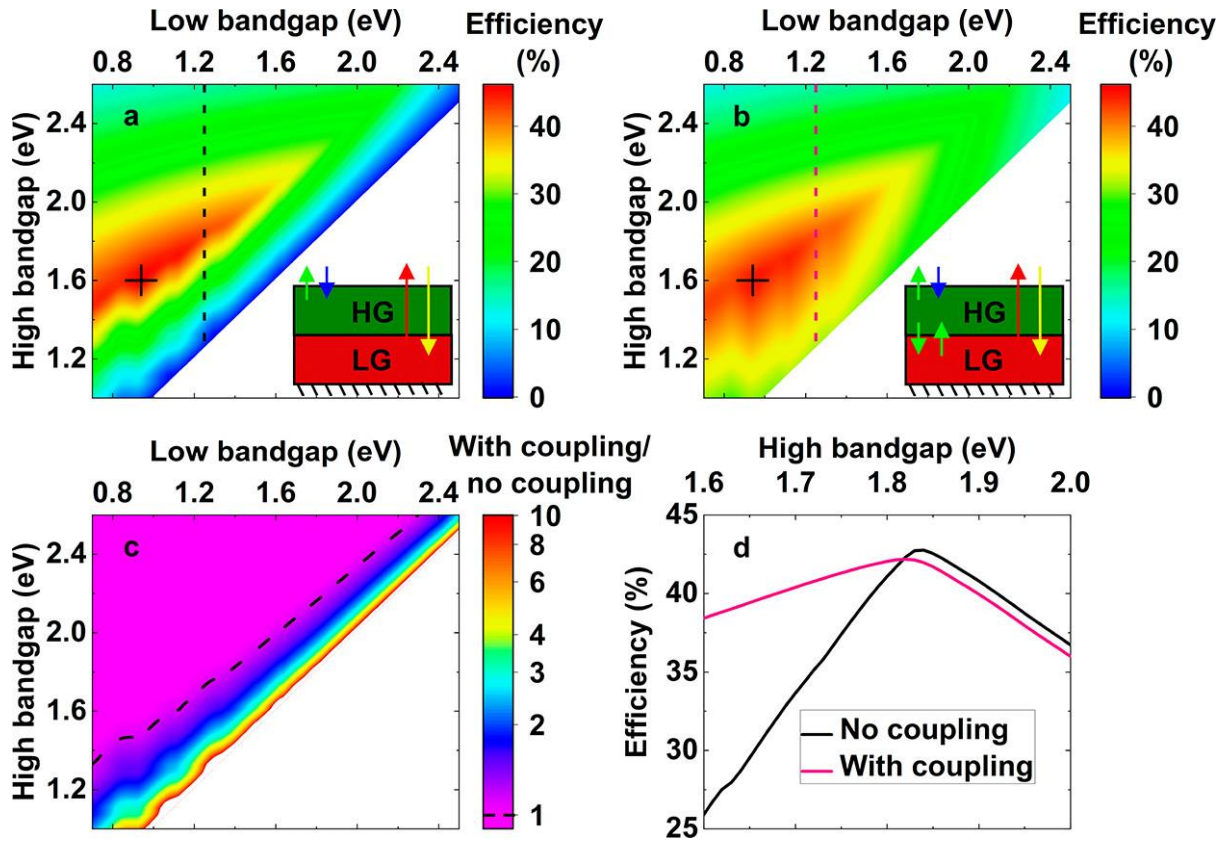


Figure 2.14. Theoretical limitation of 2-terminal tandem perovskite solar cells (a) without and (b) with luminescence coupling (both calculations assume all the light above bandgap is fully absorbed), (c) the coupling effect plot, ratio of (b) and (a), (d) summarised device performance without and with coupling with a function of the bandgap. This figure is adapted from⁹².

2.5.2 The recombination junction in 2T all-perovskite tandem solar cell

The first 2T all-perovskite tandem solar cell was demonstrated by Eperon et al., who performed the composition engineering of Pb/Sn perovskite to obtain $\text{FA}_{0.75}\text{Cs}_{0.25}\text{Sn}_{0.5}\text{Pb}_{0.5}\text{I}_3$ with a PCE of 14.8% and a V_{OC} of 0.83 V (**Figure 2.15a**).⁸⁹ They have found that incorporating Cs into Pb/Sn perovskite can greatly improve the solar cells performance without changing the bandgap. Furthermore, the Pb/Sn combination shows promising thermal and air stability compared to pure Sn-based perovskite. Combining the wide bandgap perovskite with 1.8 eV of $\text{FA}_{0.83}\text{Cs}_{0.17}\text{Pb}(\text{I}_{0.5}\text{Br}_{0.5})_3$, they fabricated tandem solar cells with the following architecture: ITO/NiO/WG-perovskite/PCBM/SnOx/ZTO/ITO/PEDOT:PSS/NG-PSK/C₆₀/BCP/Ag, and

showed the device performance of 17%. Their work demonstrated the possibility of fabricating all-perovskite tandem solar cells to boost the performance of the solar cell.

One of the major issues in 2T all-perovskite tandem solar cell is that the RJ layer requires ~100 nm TCO (indium tin oxide or indium zinc oxide, for example) by sputtering deposition which can cause the device shunting problems. To solve this issue, Lin et al. have demonstrated that using a 1 nm Au cluster layer between the p-n junction of PEDOT:PSS and ALD-SnO_x layers is sufficient for charge transportation (**Figure 2.15b**).⁹³ Furthermore, the notorious problem of Pb/Sn narrow bandgap perovskite is that it suffers from high Sn vacancy defects that tend to oxidise Sn²⁺ to Sn⁴⁺ and degrade the perovskite. In their work, they added metallic Sn powder in their Pb/Sn solution as the redox potential is favourable to reducing Sn⁴⁺ to Sn²⁺. This strategy increased the thickness of Pb/Sn perovskite from 650 nm to 920 nm without sacrificing optoelectronics properties and improved the single junction solar cells performance from 17.8% to 20.1%. As for tandem solar cells, they employed the device architecture, glass/ITO/PTAA/WBG perovskite/C60/ALD-SnO₂/Au(~1 nm)/PEDOT:PSS/NBG perovskite/C60/BCP/Cu and showed the PCE of 24.8%. In 2020, Yu et al. simplified the interconnection structure by modifying the ALD-SnO_x process with an incomplete oxidation process to form SnO_{1.76}. This oxygen-deficient layer has an ambipolar charge transportation property which can be used for electron or hole recombination, therefore, they can simplify the interconnection layer from C60/SnO_x/ITO/PEDOT:PSS layer to C₆₀/SnO_{1.76} structure and achieve a PCE of tandem solar cell with 24.6% (**Figure 2.15c**).⁹⁴

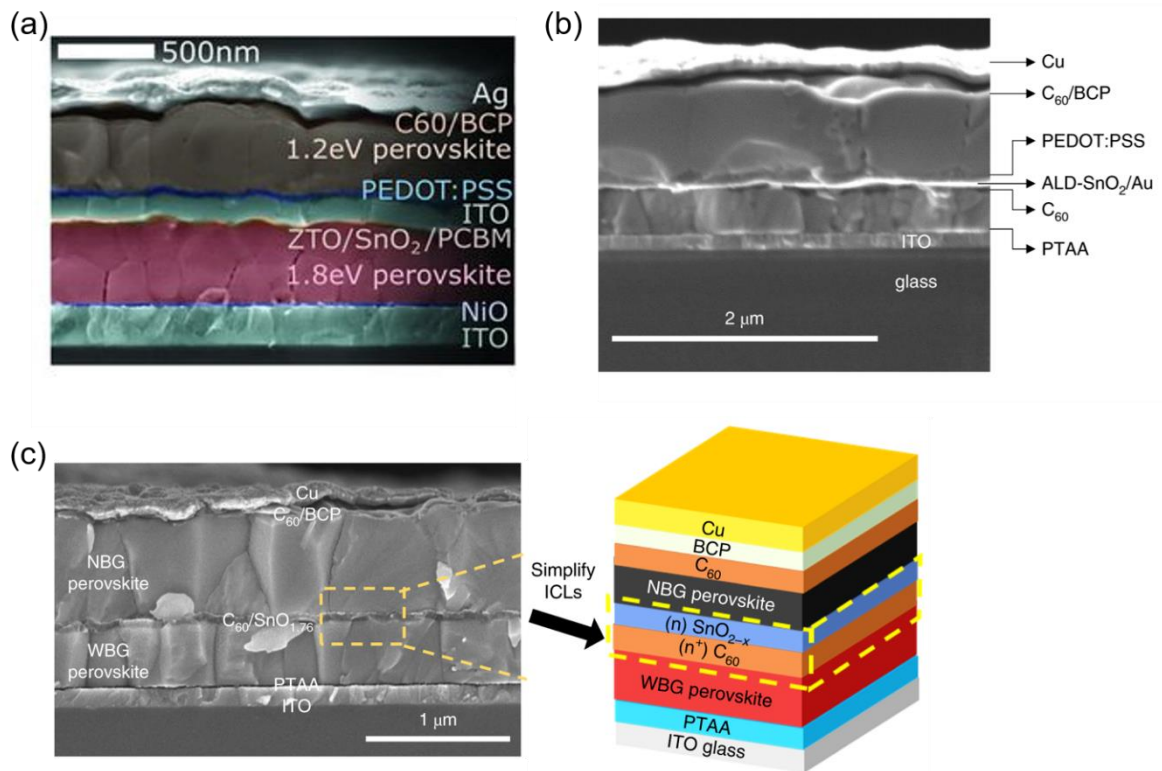


Figure 2.15. The common tandem device architecture for 2-T all-perovskite solar cells using (a) ALD-ZTO, SnO_x and sputter ITO, (b) ALD- SnO_x and 1 nm Au, (c) ALD- SnO_x with O_2 -deficient structure as bipolar transportation layer as recombination layer. This figure is adapted from ^{89,93,94}.

2.5.3 Optical loss in RJ layer.

Few reports have tried to minimise the optical loss from TCO or RJ layer in the near-infrared (NIR) region for Pb/Sn perovskite absorption. Datta et al. have shown that hydrogenated indium oxide (IOH) is more suitable than commercial ITO glass substrates as the former has a higher reflective index for a better transmission, especially in the NIR region. On the contrary, NIR transmission of ITO is dominated by free-carrier absorption and reduces the light-harvesting for perovskite. Moreover, the PEDOT:PSS thickness is reduced to 5 nm in their work to minimise parasitic absorption by a factor of 5%.⁹⁵ Another report by Nejad et al. have analysed the optical loss in the tandem architecture and found that the loss from commercial ITO, Au interconnection layer and PEDOT:PSS layers are significant (**Figure 2.16**).⁹⁶ After optimisation with anti-reflective coating, MgF_2 , on the glass side, their tandem solar cell gained

the current from 12.6 mA/cm^2 to 15.8 mA/cm^2 and improved the PCE from 18.1% to 23.5%. Furthermore, they have demonstrated a tandem solar module with 12.25 cm^2 size by blade-coating and achieved a device performance of 19.1% with a geometry fill factor (GFF) of 94.7%.

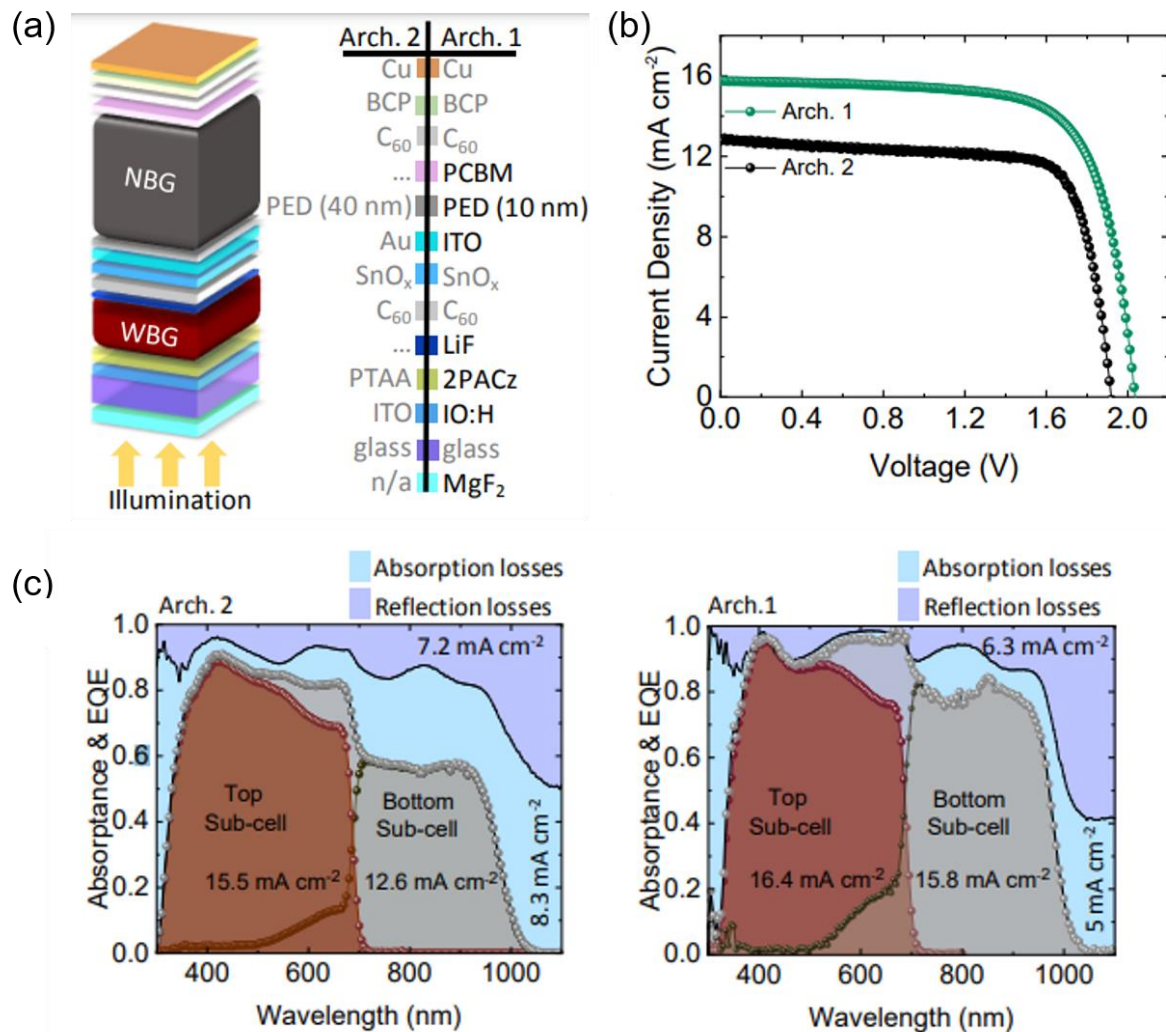


Figure 2.16. The optical loss study to improve the device performance of 2-T all-perovskite tandem solar cell with Arch 1. using $\text{MgF}_2/\text{glass}/\text{IOH}/2\text{-PACz}/\text{WBG}$ perovskite/ $\text{LiF}/\text{C}_60/\text{SnO}_x/\text{ITO}/\text{thin-PEDOT:PSS}/\text{NBG}$ perovskite/ $\text{PCBM}/\text{C}_60/\text{BCP}/\text{Cu}$, Arch 2, using $\text{glass}/\text{ITO}/2\text{-PACz}/\text{WBG}$ perovskite/ $\text{C}_60/\text{SnO}_x/\text{Au}/\text{PEDOT:PSS}/\text{NBG}$ perovskite/ $\text{C}_60/\text{BCP}/\text{Cu}$. (a) the device architecture with the choices of layers, the J-V curves (b) and EQE measurement of each subcell and the corresponding J_{CS} . (c)-(d) of device arch 2 and arch 1. This figure is adapted from ⁹⁶.

2.5.4 Summary and the outlook for all-perovskite tandem solar cell

To date, the highest PCE of all-perovskite tandem solar cell in literature is 26.4% by improved surface grain passivation with 4-trifluoromethyl-phenylammonium chloride (CF₃-PA Cl) dopant in perovskite solution. By adding CF₃-PA Cl into Pb/Sn perovskite solution, the carrier diffusion length increases to more than 5 μm , enabling to produce thick perovskite layer (1.2 μm) without losing the device performance (**Figure 2.17**).⁷²

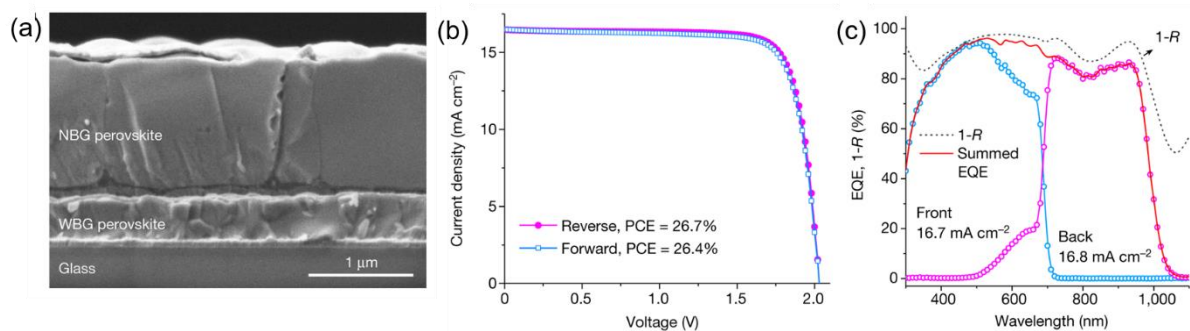


Figure 2.17. The state-of-the-art all-perovskite tandem solar cell with (a) cross-sectional SEM image of the device, (b) the J-V scans of reverse and forward measurement with 26.7 and 26.4%, (c) the EQE measurement of each subcell and the corresponding J_{sc}. Reproduced with permission from Nature Publishing Group.⁷²

In summary, to achieve a PCE of 30% all-perovskite tandem solar cell, several scientific questions need to be addressed. (1) low PLQE and photostability of WBG perovskite, (2) the optical loss from either commercial ITO substrate or the parasitic absorption from RJ layer, (3) increase J_{sc} of narrow bandgap perovskite while maintaining high V_{oc} output.

Chapter 3. Experimental Methods

This chapter presents details of the perovskite evaporator, the experimental methods for perovskite film and solar cell fabrication, and the characterisation of samples for further study in this thesis.

3.1 Perovskite evaporator system

The perovskite evaporator chamber is designed by CreaPhys, a commercial vacuum system/material company. The evaporator is integrated into a N₂-filled glovebox to prevent the degradation of materials sensitive to air, moisture, and other environmental agents. The system is suited for the deposition of organics (FAI or FABr), inorganics (PbI₂, PbBr₂, CsI or CsBr) and metals (Cu or Ag) under a high-vacuum environment.

The evaporator system is shown in the following figure.

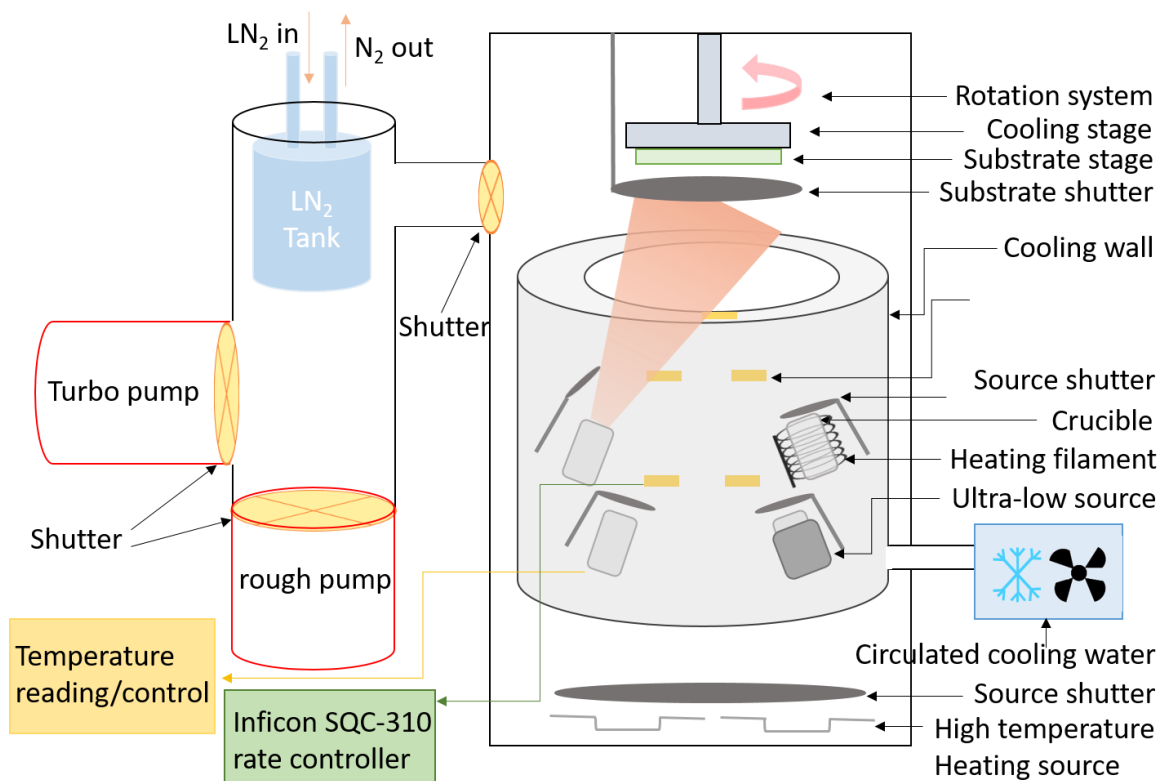


Figure 3.1. Diagram of the perovskite evaporator system.

In this evaporator, there are four independent heating sources, including three low-temperature sources (LTS) (below 800°C) and one ultra-low temperature source (ULTS) (below 250°C). For the LTS, the heating filament is around the aluminium oxide crucible to provide uniform heating, and the thermocouple is under the crucible to record the temperature. For the ULTS, the crucible is covered by a thick metal holder to have a uniform heat distribution and for the thermocouple connection. The tungsten light bulb is mounted under the metal holder for heating instead of a tungsten filament. Two additional metal shields are under the crucible to minimise direct heating from the light bulb to the crucible. Therefore, the material inside the crucible can be heated slowly for thermally sensitive organic materials to reduce the possibility of degradation. Four quartz crystal microbalances (QCMs) are mounted on the top of the evaporation sources (three LTS and one ULTS) to monitor the deposition rate simultaneously. This system allows us to run multisource evaporation simultaneously to control and fine-tune the perovskite composition. Also, independent source shutters and shields are on the top and the side of evaporated sources to minimise cross-contamination. All these components are installed a chamber with inner cooling walls, connected to circulated chilled water. Therefore, the shield, QCMs, and the chamber inner wall are kept at -20°C during the evaporation. The design can help reduce the re-evaporation from the chamber and potentially stick unwanted by-products to the walls, an element we consider crucial for controlled evaporation of many perovskite precursors. There is one QCM for the high-temperature source (HTS) to evaporate metal (Cu or Ag). The distance between QCMs and the ULTS, LTS, and HTS are around 32, 35 and 45 cm, respectively. A specially designed LN₂ tank is used to speed up the pumping speed and also to trap any chemicals (parent molecules or by-products). This “cold trap” can reduce batch-to-batch variation, and I have found this crucial for reproducible results. A dry roughing pump (Edwards, nXDS dry scroll pumps, 10i) and a turbo pump are used to provide a high vacuum environment. I have noticed that the pump speed of a rough pump is critical to perovskite film quality and device performance.

The substrate stage can fit with a 10 cm by 10 cm holder and it is connected to the in-house cooling water (roughly 18-20 °C). The substrate temperature can affect the sticking coefficient (especially organic material), re-evaporation and the nucleation of perovskite components. Therefore, it is important to keep it at room temperature. In addition, the substrate stage rotates at 11 r.p.m. during evaporation for a better spatial uniformity.

For a given evaporation, the sources are heated to reach their temperature Idle (T_{Idle}) and the source shutters are opened to track the evaporation rate. Next, the source temperature is increased, depending on the material, to achieve the desired rate for each material. Finally, when the rate reaches its capture region, the substrate shutter is opened to start the deposition.

To calibrate the tooling factor, the material is deposited on a microscope slide and the thickness is measured by Dektak profilometer in comparison to the monitor thickness on the QCM. We are aware of that the tooling factor could not be the same for each substrate and is different during the multisource evaporation. But the calibration on the microscope slide provides a starting point for empirical optimisation for different perovskite compositions to get the optimum results. We have calibrated the tooling factor for FAI, PbI_2 , CsI, CsBr, and $PbBr_2$ to have a better control of composition during the evaporation, however, cross-contamination could not be avoided entirely between each QCMs. All the deposition is conducted when the chamber working pressure at 1 to 3×10^{-6} mbar and the substrate temperature is controlled by an in-house cooling system (around $17-20$ °C). We note that the device performance is better when the chamber pressure is below 3×10^{-6} mbar.

The calibration of PbI_2 sample is provided in the following. The tooling factor is set as 100% and the PbI_2 deposition is set as 200 nm. When the deposition is done, the samples are scratched with a sharp tweezer and measured by a profilometer. The results are shown in Figure 3.2 where the average film thickness was 73.3 nm, therefore the tooling factor of PbI_2 is $73.3/200\%$, 36.65%. Here the standard deviation of PbI_2 film uniformity is 2.98 nm across the substrate area of 10×10 cm².

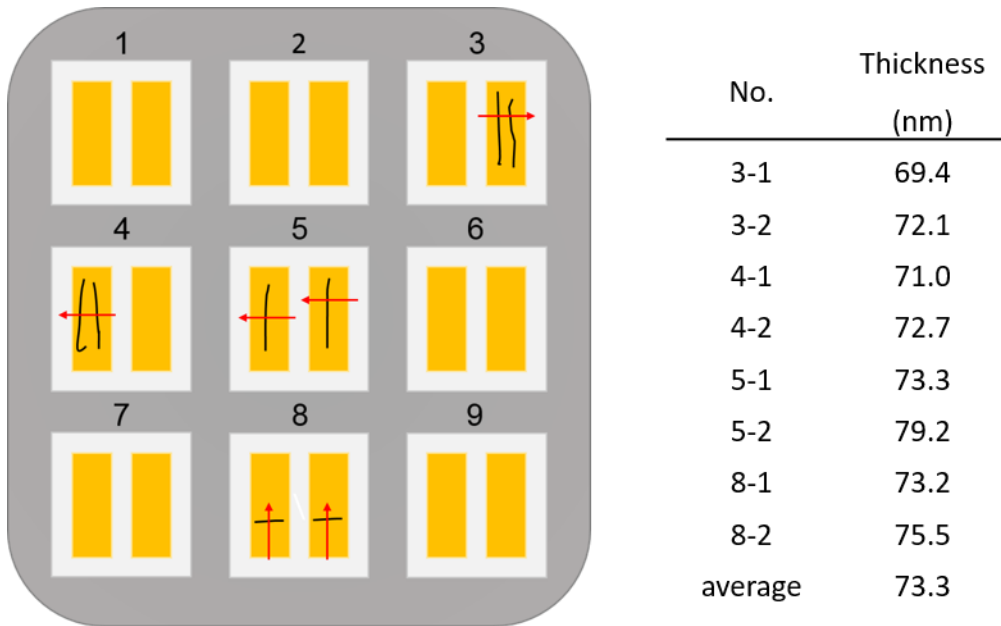


Figure 3.2. Example of tooling factor calibration of PbI_2 film with 9 substrates across the $10 \times 10 \text{ cm}^2$ size substrate holder. The film thickness is tested with substrates at a different location and the corresponding thickness is shown on the right.

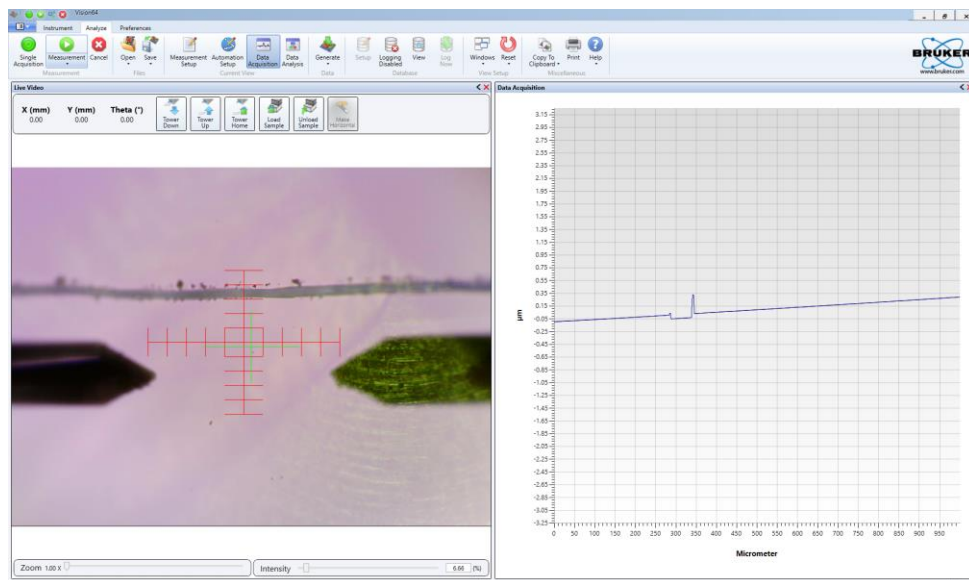


Figure 3.3. A screenshot of the profilometer scan for PbI_2 film measurement. A sharp tweezer scratches the samples to provide the thickness variation. During the scan, the equipment tip scans from the direction of PbI_2 , glass to PbI_2 .

3.2 Material, film, and device preparation

3.2.1 Film or solar cell fabrication

This section shows the general approach to fabricating films and solar cells used throughout this thesis. The following chapters will provide more detailed information regarding the optimisation of each protocol. In this thesis, the p-i-n (inverted) device architecture, ITO glass/HTL/perovskite/ETL/electrode is used for several reasons. (1) the fabrication process of inverted perovskite solar cell employs low temperature annealing (below 150°C), showing the advantage of flexible (plastic) substrate and tandem solar cells. (2) the Pb/Sn perovskite solar cell shows relatively low device performance in normal device architecture. (3) for a perovskite/Silicon tandem solar cell, an inverted perovskite structure can match with high-performance silicon cell.

Substrate cleaning

Patterned ITO glass (1-inch x 1-inch, 15 ohm/cm², Kintec) was cleaned in the sonication bath with the following steps for 15 minutes each, deionised water, acetone, and isopropanol. The cleaned substrate is transferred to UV-ozone chamber (UVC1014, NanoBioAnalytics) for another 15 minutes post-treatment. I have found that with UV-Ozone treatment, the device performance is better with higher J_{SC} and FF, compared to those with O₂ plasma treatment. The reason might be O₂ plasma is more aggressive treatment than UV-Ozone and the former might damage or oxidise the ITO substrate (different ITO composition or vary the work function).^{97,98} Therefore, in this thesis, all the substrates are treated with UV-Ozone.

Poly(triaryl amine) (PTAA) spin-coating

PTAA (Sigma) solution is prepared by mixing it into toluene with a concentration of 2 mg/ml in anhydrous toluene (Sigma) and stirring the solution overnight. To spin the PTAA, the solution is dropped on the substrate and spin coated at 5000 rpm (1000 rpm/s ramp) for 30 seconds with the spin-coater lid closed, followed by post-annealing at 100 °C for 10 minutes. PTAA powder is stored in an N₂-filled glovebox.

[2-(9*H*-Carbazol-9-yl)ethyl]phosphonic Acid (2-PACz) spin-coating

2-PACz (Tokyo Chemical Industry, TCI) solution is prepared by adding the powder in a vial with a 10 mM concentration in anhydrous ethanol. The solution is sonicated for 15 mins to ensure the powder is completely dissolved. The solution is dropped onto the substrate and spin coated at 2000 r.p.m. for 30 seconds (with the lid open), with a post-annealing at 100 °C for 10 mins. The substrates are washed twice with ethanol at 5000 r.p.m. for 30 seconds (dynamic dropping of 120 µl ethanol during this process) and the substrate is heated at 100 °C for 5 mins in the glovebox. This treatment is to produce a thin 2-PACz coating as the phosphoric acid functional group can chemically adsorb on the ITO and the multilayers is washed away by ethanol. The thin 2-PACz is for Pb/Sn perovskite deposition. The 2-PACz powder is stored in a N₂-filled glovebox.

[2-(3,6-Dimethoxy-9*H*-carbazol-9-yl)ethyl]phosphonic Acid (MeO-2PACz) spin-coating

MeO-2PACz (TCI) solution is prepared by adding the powder in a vial with a 4 mM solution in ethanol. The solution is sonicated for 15 mins before use. The solution is dropped on the cleaned ITO and spun at 3000 r.p.m. for 30 seconds (with the lid open) followed by post-annealing at 100 °C for 10 minutes in the glovebox. No further wash step was employed. MeO-2PACz substrate is for perovskite evaporation. MeO-2PACz powder is stored in a dry box.

PEDOT:PSS deposition

Commercial PEDOT:PSS (Clevios P VP AI 4083) is diluted by methanol with a 1:3 v:v ratio. The solution is sonicated for 20 mins before use. Before spin-coating, a Nylon (0.45 µm size) filter is used to remove aggregated polymer. 200 µl diluted PEDOT:PSS is spin coated on the substrates with 4000 r.p.m. for 30 seconds with a ramp time of 1000 r.p.m./s and the deposited films were annealed at 120 °C for 20 mins in air. After annealing, the samples are transferred to the glovebox immediately for Pb/Sn perovskite deposition. The PEDOT:PSS solution is stored in 2 to 6 °C environment.

Perovskite evaporation

The cleaned ITO substrates are transferred to the perovskite evaporator in the glovebox. During the evaporation, the substrates stage was kept at around 18°C temperature, while the chamber wall is at -15 to -20 °C temperature. To achieve the bandgap of 1.62 eV, the precursor deposition rates were 1 Å/s for FAI, 0.6 Å/s for PbI₂, and 0.1 Å/s for CsBr in Chapter 4. For the wide bandgap perovskite, the fourth source PbBr₂ is employed for multisource evaporation. For the 1.77 eV bandgap perovskite, the deposition rates were 1 Å/s for FAI, 0.6 Å/s for PbI₂, 0.2 Å/s for PbBr₂ and 0.1 Å/s for CsBr. In Chapter 5, we set the tooling factor of PbI₂ and PbBr₂ to 93.6 % and 115.2 % to fine-tune the deposition rate and get the rate of 0.434 Å/s for PbI₂, 0.156 Å/s. for PbBr₂. The FAI, PbI₂, and PbBr₂ powder was refilled every time before evaporation. The crucible size is 2 c.c. and we load the chemical powder to reach 40%, 60% and 30% of height. The distance between sources to the substrate holder is around 35 cm. During deposition, the working pressure is between 1 to 3x10⁻⁶ mbar. After evaporation, the perovskite films are annealed on the hotplate inside the glovebox at 135°C. The annealing time was 90 mins for 1.62 eV sample and 30 mins for others. Note that it is important to use a high-pumping speed roughing pump to remove any by-products during evaporation to achieve high efficient solar cells. We obtain the FAI from Greatcell solar, PbI₂, PbBr₂ from TCI, and CsBr from Sigma.

Surface passivation

Ethylenediammonium diiodide (EDAI, Sigma) (0.5 mg/ml) is dissolved in mixed IPA and toluene (volume ratio 1:1) at 70 °C heating and stirring for 2 hours. The solution is filtered with 0.22 µm Polytetrafluoroethylene (PTFE) membrane before use as the EDAI is not dissolved in the mixed solvent completely. 120 µl of EDAI solution is quickly dropped onto the perovskite film and spin coated at 4000 r.p.m. for 20 seconds. The film is annealed at 100 °C for 5 minutes.

Electron transporting and buffer layer deposition

Solution process: PCBM (Merck) (20 mg/ml in anhydrous Chlorobenzene, sigma) is prepared by stirring the solution at 70°C for 3 hours. The PCBM solution is spin-coated dynamically on the perovskite film at 1200 rpm for 30 seconds with the lid open when the perovskite film is

cooled down. The film is dried at room temperature in the glovebox for 20 minutes. The buffer layer, Bathocuproine (BCP, Alfa Aesar), is spin-coated dynamically on PCBM at 2000 rpm for 30 seconds. BCP is dissolved in anhydrous IPA (Sigma) and is sonicated for 30 mins.

Organic evaporation process: Perovskite films are back-transferred to the perovskite evaporator for C60 (Sigma or Creaphys) deposition. The deposition rate is kept at 0.1 Å/s for the first 10 nm and increased to 0.2 Å/s to achieve 20 nm thick layer. BCP is evaporated at a rate of 0.1 Å/s to achieve 8 nm. The chamber pressure was below 10^{-5} mbar during the evaporation.

Back electrode deposition

Ag or Cu is thermal-evaporated in the evaporator with a deposition rate of 0.1 Å/s for the first 2 nm, 0.4 Å/s to 10 nm, and 1 Å/s to 120 nm.

Pb/Sn narrow bandgap perovskite solution

All the precursors are mixed in one vial in the following sequence, SnF₂ (0.1 M, Sigma), SnI₂ (1 M, Sigma), CsI (0.5 M, Sigma), PbI₂ (1 M, Alfa), and FAI (1.5 M, Greatcell) are weighed to achieve the concentration of 2 M in a mixed DMF: DMSO of 3:1 volume ratio for the composition of FA_{0.75}Cs_{0.25}Pb_{0.5}Sn_{0.5}I₃. The NBG perovskite solution is prepared in an N₂-filled glovebox (H₂O and O₂ below 1 ppm) for 3 hours stirring at room temperature. Before use, the solution is filtered by 0.22 μm PTFE filter. A 120-μl perovskite solution is spread on ITO and spin coated at 4000 r.p.m. for 40 s. After 10s of spinning, the gas quenching method is used for 15-20 s until perovskite film turns to brown. The samples are moved to a hotplate for post-annealing at 120 °C for 8 mins. The EDAI surface passivation method is the same as above.

Solution-processed Pb-based perovskite film preparation (Benchmarking stoichiometry)

To understand the composition of evaporated perovskite films, we solution-process a series of films with the composition of $\text{FA}_{1-x}\text{Cs}_x\text{Pb}(\text{I}_{1-y}\text{Br}_y)_3$, where x and y are varied from 0.1 to 0.46. The precursor stoichiometry determines the composition here. A 1 M precursor solution is prepared by dissolving FAI, PbI_2 , CsI, and PbBr_2 in DMF/DMSO (4:1). Before the spin-coating process, we purge the N_2 -filled glovebox for 15 minutes to achieve a clean atmosphere. To fabricate the films, 50 μl of perovskite precursor solution is deposited on a clean glass substrate (see cleaning procedure above) and spin-coated at 1000 rpm for 10 s and 6000 rpm for 20 s. At 5 seconds before the end of the second spinning step, we drop 100 μl of chlorobenzene on the middle of the substrate (antisolvent method). After the spinning process, the perovskite films are immediately moved to a hotplate and were annealed at 100°C for 30 minutes. The spin-coating process is optimised for an integrated spin-coater in an MBraun glovebox with the lid open.

SnO_x deposition by atomic layer deposition (ALD)

The ALD system is Picosun R-200 advance, which enable to deposit a film on 8-inch wafer with 6 different precursors. Our ALD system is integrated into an N_2 -filled glovebox. ALD-SnO_x deposition is employed with (TDMA)Sn and deionised water H_2O as precursors. The base chamber pressure is around 10 mbar and the deposition recipe of $t_1/t_2/t_3/t_4$ of TDMASn pulse/ N_2 purge/ H_2O pulse/ N_2 purge time are 0.6 s, 10 s, 0.1 s, and 10 s for 300 cycles (target thickness: 30 nm SnO_x). The temperature of the source bottle, line, and substrate are kept at 75, 90, and 100°C . The boost system is on with N_2 as a carrier gas to increase the vapour of TDMASn. The choice of ALD-SnO_x is for the interconnection layer of tandem solar cell between WBG perovskite and NBG perovskite. The dense and uniform ALD-SnO_x works as an effective electron transportation layer and a protection layer for further solution-process (PEDOT:PSS or perovskite solution).

All-perovskite tandem solar cells fabrication

The cleaned ITO substrates are transferred to the glovebox for MeO-2PACz coating. After the coating, we transferred the substrates to the perovskite evaporator for a bandgap of 1.77 eV perovskite deposition. After perovskite deposition, we annealed the perovskite at 135°C for 30 mins in an N_2 -filled glovebox to improve perovskite quality. The EDAI passivation is

employed on the cooled perovskite film before deposition of 20 nm of C60. After that ALD-SnOx deposition was employed with (TDMA)Sn and deionised water H₂O as precursors to achieve 30 nm SnOx. After the deposition, the samples were transferred to the evaporator for 1 nm Au deposition. The diluted PEDOT:PSS (1:3 v:v in methanol) was spin coated on the substrates with 4000 r.p.m. for 30 seconds with a ramp time of 1000 r.p.m./s and the deposited films were annealed at 120 °C for 20 mins in air. After annealing, the samples are transferred to the glovebox immediately for Pb/Sn perovskite deposition. After narrow bandgap perovskite deposition, EDAI passivation treatment is used. To finish the device, C60, BCP and Cu were thermal-evaporated on the perovskite with 20 nm, 8 nm, and 120 nm, respectively. A UV-curable epoxy (Blufixx) is used to encapsulate the perovskite active area to prevent degradation from air, especially O₂.

3.3 Film and device characterisation

3.3.1 X-ray diffraction pattern measurement

A Bruker D8 ADVANCE system with a copper focus X-ray tube (K α : 1.54 Å) is used to obtain the XRD patterns with an operating voltage of 40 kV. The scan range for 2 θ was from 5° to 55° with a step size of 0.01° and a dwell time of 0.15 s per step. The measurement is conducted in air for WBG perovskite and in an air-tight sample holder (sealed the samples inside the N₂-filled glovebox) for Pb/Sn perovskite films. We calculate the stoichiometry of the evaporated perovskite film based on our previous work. In general, we prepared solution-processed films with different amounts of A and X components. With Vegard's law for composition ranges in the same phase, the evolution of perovskite peak shift is based on the composition variation, therefore we can acquire a composition map versus XRD peak position %. The structural analysis in Chapter 4 is carried out by the TOPAS 5 software where we run an indexing fitting procedure to determine the possible space groups. A Pawley refinement is used to check these space groups and obtain the space group based on the best fits.

3.3.2 Scanning electron microscopy (SEM)

The surface morphology and cross-sectional image of the perovskite thin films/devices are observed using a field-emission scanning electron microscope (ZEISS LEOGEMINI 1530VP FEG-SEM) with a beam energy of 2 kV, an in-lens detector and secondary electron detection mode. The samples are mounted by carbon tape on the holder.

3.3.3 Photoluminescence quantum efficiency (PLQE)

PLQE measurements are conducted by using 520 nm-continuous wave laser excitation under a 60 mW/cm² (1 sun equivalent photon number unless stated otherwise). At a given measurement, the laser power is measured by a compact power meter (PM16-130, thorslab) and the laser spot size is measured to calculate the power density. In this thesis, the procedures for measuring and calculating PLQE follow the protocol designed by previous work.⁹⁹ In short, three measurements need to be done to calculate the PLQE, (1) blank measurement, to record laser power, (2) laser illuminate directly on sample to record the laser attenuation and PL emission from samples, (3) laser illuminate into the integrated sphere to understand the laser absorption and sample emission based on the light reflected from an integrated sphere. The optical fibre is mounted on an integrating sphere to collect the PL emission and coupled to an Andor iDus Si (for Pb-based perovskite)/InGaAs (for Pb/Sn perovskite with emission above 950 nm) detector. All the samples are encapsulated with UV-curable epoxy inside the glovebox before the measurement.

The Quasi Fermi Level Splitting (QFLS) calculation is based on the following.

$$QFLS = k_B T \ln \left(PLQE \frac{J_{sc}}{J_{0,rad}} \right)$$

$$J_{sc} = q \int EQE_{PV}(E) \Phi_{AM1.5G}(E) dE$$

$$J_{0,rad} = q \int \alpha(E) \Phi_{BB}(E) dE$$

where $\alpha(E)$ is the absorption coefficient.

3.3.4 Hyperspectral optical microscopy measurements

Hyperspectral PL measurements are acquired using a widefield microscope (IMA VISTM, Photon Etc.) equipped with a 1040×1392 resolution silicon CCD camera. We excite the films with a 405 nm, continuous wave laser, and obtain the PL maps in reflectance mode with a 100x (0.9 NA) objective. We employ a tunable Bragg filter to obtain the spectrally resolved maps from 700 nm to 850 nm with a step size of 2 nm. The excitation power density is calibrated with a power meter to be 60 mW/cm^2 (one sun equivalent photon number).

3.3.5 Time-resolved photoluminescence (TRPL) measurements

TRPL spectra are obtained using time-correlated single photon counting (TCSPC) on an FLS1000-dd-stm fluorescence spectrometer (Edinburgh Instruments). The samples are excited using a 448.4 nm pulsed laser (Edinburgh Instruments, HPL-450) with a repetition rate of 20 kHz and pulse width of 102.1 ps. The laser intensity is at a fluence of $8.5 \text{ nJ/cm}^2/\text{pulse}$. An emission monochromator bandwidth of 2 nm with 450 nm laser was used and a 680 nm long pass filter is employed to prevent scattered light from entering the UV-VIS PMT-980 detector.

3.3.6 UV–Vis measurements

UV-Vis transmittance spectra are collected on an Agilent 8453 UV–vis spectrophotometer by using a tungsten (310–1100 nm) lamp for illumination. It is equipped with a photodiode array for detection.

3.3.7 Solar cell performance

To determine solar cell performance, a calibrated light source (Xe lamp or LED lamps) with one sun AM 1.5G spectra is used for terrestrial measurement. Typically, a solar cell is connected to a source measurement unit to record its current as a function of voltage either

under light illumination (light J-V scan) or dark. Under dark measurement, the solar cell shows a diode behaviour where at forward bias, the current can pass through the device, and at reverse bias, a limited current can go through the device. For an ideal diode under dark measurement, the current density curve is following:

$$J_{dark}(V) = J_0(e^{\frac{qV}{K_B T}} - 1)$$

where J_0 is a constant, K_B is Boltzmann's constant.

This dark current is generated by the potential difference between the p-n junction in the cell and the current direction opposites to the photocurrent. Therefore, the net current density in the cell is :

$$J(V) = J_{sc} - J_{dark}(V)$$

Under V_{OC} condition (device net current is zero), the above equation can be adapted to

$$V_{OC} = \frac{KT}{q} \ln\left(\frac{J_{sc}}{J_0} + 1\right)$$

This equation shows that the V_{OC} is logarithmically increased with incident light intensity.

From the J-V curve plot in **Figure 3.4**, it shows that the V_{OC} is positive and the solar cell generates power when the applied voltage is between 0 and V_{OC} . If the V is negative, the solar cells can be used as a photodetector under illumination and if the V is higher than V_{OC} , the device is working as a light emitting diode.

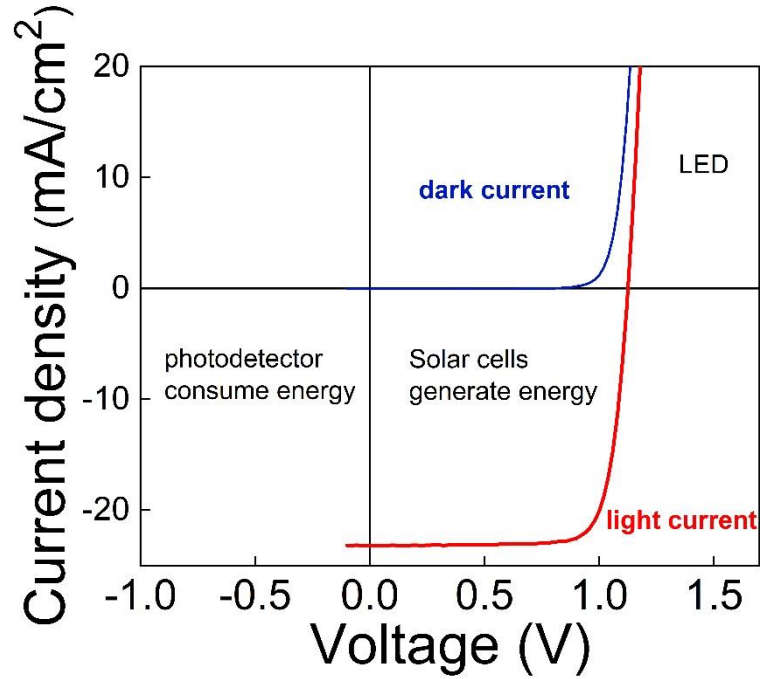


Figure 3.4. A JV curve showing different optoelectronic device applications.

In an operating solar cell, the power density is defined by

$$P = JV$$

When P reaches the maximum power point, the corresponding current point and voltage point are called J_m and V_m . The ratio between $V_m J_m$ and $V_{oc} J_{sc}$ is called FF which is the square area of the JV curve.

$$FF = \frac{V_m J_m}{V_{oc} J_{sc}}$$

The solar cell efficiency η is the power density output at the operating condition as a fraction of incident power density P_{in} . Therefore,

$$\eta = \frac{V_{oc} J_{sc} FF}{P_{in}}$$

Current-voltage (J-V) curves are measured under the illumination of a xenon lamp (Abet Sun 2000 Solar Simulators, AAB class) with one sun intensity (100 mW/cm^2 , AM 1.5G), calibrated with a reference Silicon diode. The device performance is recorded with a source meter, Keithley 2636A, controlled by a LabVIEW program. The J-V curve is obtained by providing external bias from Keithley between 2.1 V to -0.1 V, 1.3 V to -0.1 V, and 0.9 V to -0.1 (reverse

scan) for tandem, WBG, and NBG solar cells (also forward scan). During the measurement, a step size of 20 mV and a scan rate of 100 ms/V are used. The solar cell active area is 15.5 or 13.8 mm², defined by the overlapping area between Ag and ITO. An aperture mask of 8.1 mm² size is employed during the measurement. The WBG perovskite solar cells were measured under one sun AM 1.5G condition with a calibrated KG5 filter reference cell by a xenon lamp from Abet Sun 2000 Solar Simulators (AAB class). For NBG perovskite solar cell, a KG2 filter reference cell was used to calibrate the light intensity. We use Sunbrick G2V LEDs solar simulator with AAA class for all-perovskite tandem solar cells measurement. The spectral mismatch of solar simulator is <5% according to manufacturer. The solar cells measurements are conducted in the air with no temperature control system. Most devices are encapsulated (UV-curable epoxy) in an N₂-filled glovebox before the test. We noticed that the device V_{OC} of WBG perovskite is slightly higher with encapsulation.

3.3.8 Suns-V_{OC} measurement

Intensity-dependent Sun-V_{OC} measurement is measured by a variety of neutral density filters to attenuate the light intensity for JV-scans.^{100,101}

The Pseudo-JV curve is obtained by

$$PJ(I) = J_{SC,1sun} - J_{SC}(I)$$

Since the measurement is conducted under open-circuit conditions, the net charge is zero in the cell, which can calculate the pseudo-FF when there is no charge transport loss.

3.3.9 Radiative V_{OC} and Urbach energy calculation^{45,102}

To understand the maximum power conversion efficiency of a semiconductor with a given bandgap, the Shockley ideal diode is used to define radiative recombination by the detailed-balance principle.

$$V_{OC} = \frac{k_B T}{q} \ln \left(\frac{J_{SC}}{J_0} \right)$$

where q is element charge, k_B is Boltzmann constant, T is temperature, J_{SC} is the short-circuit current, J_0 is dark saturation current. The expressions of J_{SC} and J_0 are given by:

$$J_{SC} = q \int_0^{\infty} EQE_{PV}(E) \phi_{AM1.5}(E) dE$$

$$J_0 = \frac{q}{EQE_{EL}} \int_0^{\infty} EQE_{PV}(E) \phi_{BB}(E) dE$$

Where $\phi_{BB}(E) = \frac{2\pi E^2}{h^3 c^2} \frac{1}{\exp\left(\frac{E}{k_B T}\right) - 1}$, ϕ_{BB} is the blackbody spectrum at room temperature

In the radiative limit, we set EQE_{EL} to 1,

$$V_{OC,rad} = \frac{k_B T}{q} \ln\left(\frac{\int EQE_{PV}(E) \phi_{AM1.5}(E) dE}{\int EQE_{PV}(E) \phi_{BB}(E) dE}\right)$$

3.3.10 External quantum efficiency (EQE)

EQE from a solar cell can provide information on spectral response to understand the incident photon-to-electron conversion efficiency at a different wavelength. In general, a broadband light source is used with a monochromator to shine on the solar cell and the generated photocurrent is recorded with a function of wavelength. The current signal is low due to the low light intensity, therefore, a chopper and lock-in-amplifier are employed to enhance the signal-to-noise ratio. As the incident light energy varies at a different wavelength, a calibrated cell with a known spectral response needs to be measured first to determine the samples spectral response. The measured EQE spectra can be calculated to the J_{SC} based on the following equation.

$$J_{SC} = q \int AM\ 1.5G\ EQE d\lambda$$

An incident photon flux based on the AM1.5 G spectrum as a function of wavelength is shown in **Figure 3.5**.

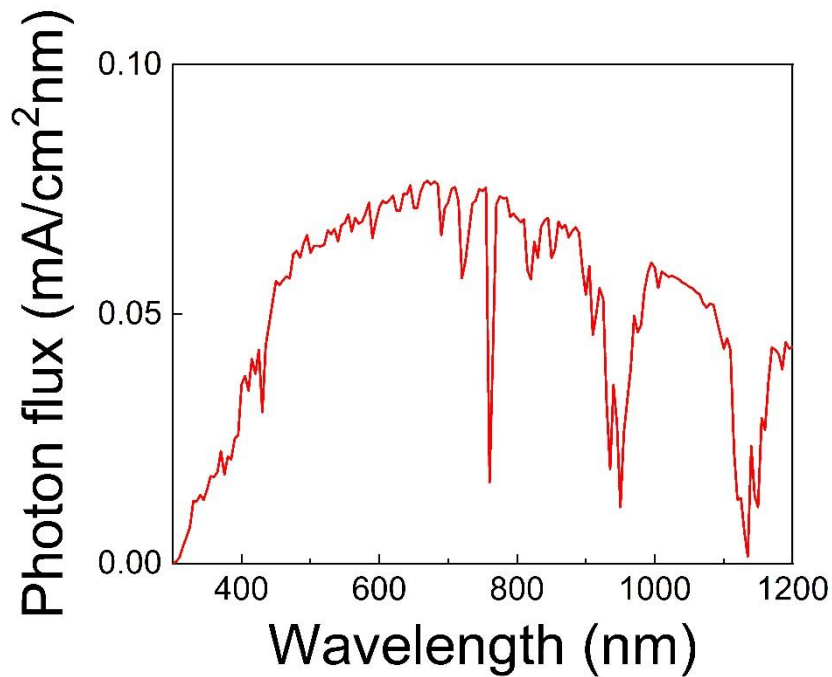


Figure 3.5. A calculated photon flux with the unit of mA/cm²nm based on AM 1.5 G spectra as a function of wavelength.

A Bentham PVE300 system equipped with dual lamps of xenon-quartz and tungsten halogen lamps are used. A silicon reference cell is used to measure the signal response for calibration. For WBG perovskite (NBG) solar cells, the response scan was obtained from a spectral range of 300 to 850 (1100) nm with a step size of 5 nm. For tandem solar cells, a green LED bias with 530 nm emission was used for low bandgap subcell measurement and an infrared LED bias with 940 nm emission was used for WBG subcell measurement. During all measurements, a transformer (Bentham S400 474) with a frequency of 300 Hz is employed for Si reference cell and perovskite solar cells measurement.

Chapter 4. High-efficiency perovskite solar cells based on multisource evaporation

Abstract

Halide perovskites of the form ABX_3 have shown outstanding properties for solar cells. The highest reported compositions consist of mixtures of A-site cations methylammonium (MA), formamidinium (FA) and cesium, and X-site iodide and bromide ions, and are produced by solution processing. However, it is unclear whether solution processing will yield sufficient spatial performance uniformity for large-scale photovoltaic modules or compatibility with deposition of multilayered tandem solar cell stacks. In addition, the volatile MA cation presents long-term stability issues. In this chapter, we report the multisource vacuum deposition of $FA_{0.7}Cs_{0.3}Pb(I_{0.9}Br_{0.1})_3$ perovskite thin films with high-quality morphological, structural, and optoelectronic properties. We find that the controlled addition of excess PbI_2 during the deposition is critical for achieving high performance and stability of the absorber material, and we fabricate p-i-n solar cells with stabilised power output of 18.2%. We also reveal the sensitivity of the deposition process to a range of parameters, including substrate, annealing temperature, evaporation rates, and source purity, providing a guide for further evaporation efforts. Our results demonstrate the enormous promise for MA-free perovskite solar cells employing industry-scalable multisource evaporation processes.

*This chapter is adapted from **Yu-Hsien Chiang**, Miguel Anaya, Samuel D Stranks. Multisource Vacuum Deposition of Methylammonium-Free Perovskite Solar Cells. *ACS Energy Letter*. 2020.*

4.1 Introduction

Vacuum deposition is a mature technique in the semiconductor industry to fabricate highly uniform and pinhole-free films at a large scale on different types of substrates including planar or textured surfaces.^{19,73,83,103,104} Furthermore, vacuum deposition allows strict control over film composition and thickness, which will be critical for achieving sufficient film uniformity at scale.¹⁰⁵ To date, the PCE of perovskite solar cells fabricated by simultaneous multisource deposition is still lagging behind their solution-processed counterparts, in part because of the more limited literature around the vacuum deposition of perovskite films relative to the solution-processed literature, which has a lower equipment entry barrier. There is also a number of nontrivial challenges unique to vapour deposition, including optimising source evaporation rates, growth processes, and engineering solutions to prevent source cross-talk of volatile substances, to name a few. The highest PCE of a vacuum-deposited perovskite solar cell is 20.8% based on a MAPbI₃ composition, with an encouraging 18.2% for a 20 cm² device.^{106,107} However, the volatile character of the MA cation hampers the stability of the device, especially at temperatures above 80 °C, presenting hurdles for such cells to pass all critical photovoltaic stress tests to validate long-term stability.^{82,108,109} Therefore, evaporation of MA-free perovskite compositions represents a promising new direction albeit a significant challenge for the field. Borchert et al. reported evaporated FAPbI₃-based n-i-p solar cells with PCE of 15.8% and stabilised power output (SPO) of 14.2%.⁸⁴ However, pure FAPbI₃ perovskite will compromise operational stability as the black-phase readily converts to a yellow δ -phase at room temperature because of the large FA cation distorting the cubic structure.¹¹⁰ In order to stabilise the black perovskite phase, Gil-Escrig et al. proposed a mixed cation and mixed halide FA_{0.5}Cs_{0.5}Pb(I_{0.83}Br_{0.17})₃ composition to achieve a PCE of 9.6%, though there was still δ -phase FAPbI₃ observed in the film.⁸³ As a result, the addition of MA was required to suppress the formation of the unwanted yellow δ -phase, leading to better perovskite films and a higher PCE of 16%. There remains a challenge to vacuum deposit MA-free mixed cation, mixed halide perovskite films to achieve the required combination of both film stability and solar cell performance that could ultimately rival the parameters of their solution-processed counterparts.

In this chapter, we present a three-source thermal evaporation vacuum deposition protocol simultaneously using FAI, PbI₂, and CsBr sources to attain high-quality and highly

reproducible $\text{FA}_{0.7}\text{Cs}_{0.3}\text{Pb}(\text{I}_{0.9}\text{Br}_{0.1})$ thin films. We identify that the resulting film quality is highly sensitive to a number of experimental parameters, including substrate surface, source purities, relative evaporation rates between the sources, and annealing temperature, highlighting critical parameters that need global consideration for further device developments. We found that the optimal film structure and morphology was attained by inclusion of a small excess of PbI_2 , which also led to higher photoluminescence quantum efficiencies (PLQEs) and longer charge carrier lifetimes. We fabricate p-i-n solar cells with a planar architecture, achieving an SPO of 18.2%, which is to date the highest performance for a vacuum-deposited MA-free based perovskite. Such cells, deposited on p-i-n architectures and fabricated at low temperature, are compatible with more complicated multilayer tandem stacks and flexible, lightweight substrates.

4.2 Multisource evaporation of perovskite films

We simultaneously evaporated FAI, CsBr and PbI_2 to form mixed-cation lead mixed-halide perovskite films. For any given deposition, the source rates were fixed by allowing the respective source temperatures to vary (see **Figure 4.1**). We used a profilometer to calibrate the tooling factors of the individual precursors and final perovskite film to confirm film uniformity across $10 \times 10 \text{ cm}^2$ (See **Table 4.1** for deposition parameters such as tooling factor, Z-factor and substrate rotation speed, and Chapter 3 for further details). The final perovskite film thickness was set to typical perovskite solar cell device absorber layer values ($\sim 500 \text{ nm}$) to ensure that absorption of light is maximised. Based on the absorption coefficient of metal-halides perovskite family, 500 nm perovskite should be enough to absorb all possible incident light with the bandgap of our choice here.

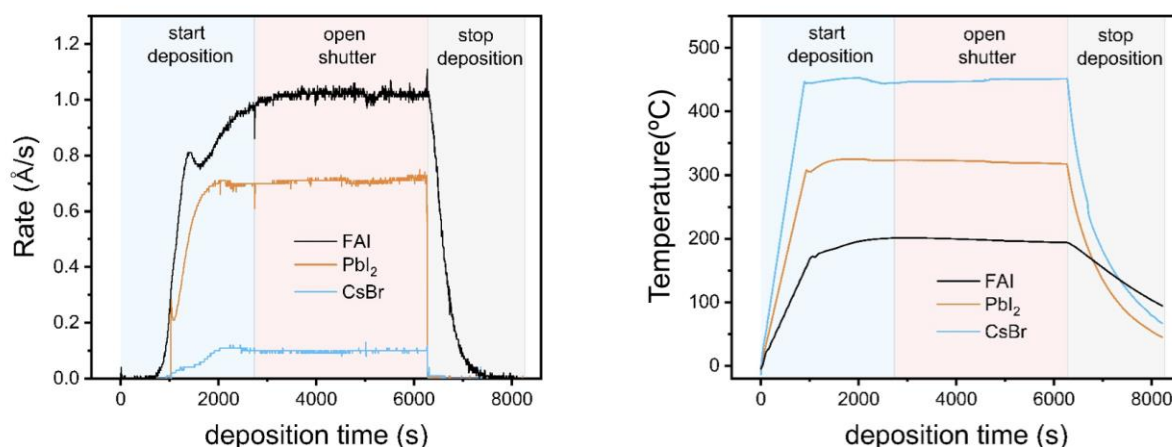


Figure 4.1. Parameters of a multi-sourced evaporation process for a typical batch of a control film $\text{FA}_{0.7}\text{Cs}_{0.3}\text{Pb}(\text{I}_{0.9}\text{Br}_{0.1})_3$, showing the deposition rate (left panel) and sublimed temperature (right panel) of FAI, PbI_2 and CsBr.

Table 4.1. Parameters for the substrate rotation speed and the evaporation conditions for the different precursors employed for the optimised (5% excess PbI_2) perovskite films

	FAI	PbI_2	CsBr	substrate
Z-factor	1	1	1.41	

Tooling factor (%)	40	36.1	25	
Density (g/cm ³)	2.22	6.16	4.52	
Rate (Å/s)	1	0.7	0.1	
Speed (rpm)				11
Temperature (°C)				18-20

We modified the nominal film composition by changing the relative ratios of the rates for each source for a given deposition run, converging on a combination of rates that give a nominal stoichiometric composition corresponding approximately to $\text{FA}_{0.7}\text{Cs}_{0.3}\text{Pb}(\text{I}_{0.9}\text{Br}_{0.1})_3$,

4.2.1 Determination of chemical formula

As the sticking coefficient of each material is different, the deposited perovskite composition cannot be determined by deposition rate.^{78,111} Furthermore, the deposition tooling factor is calibrated when one material is deposited, not for multisource evaporation. Therefore, the composition is decided by the stoichiometry of solution-processed film with the procedure described below.

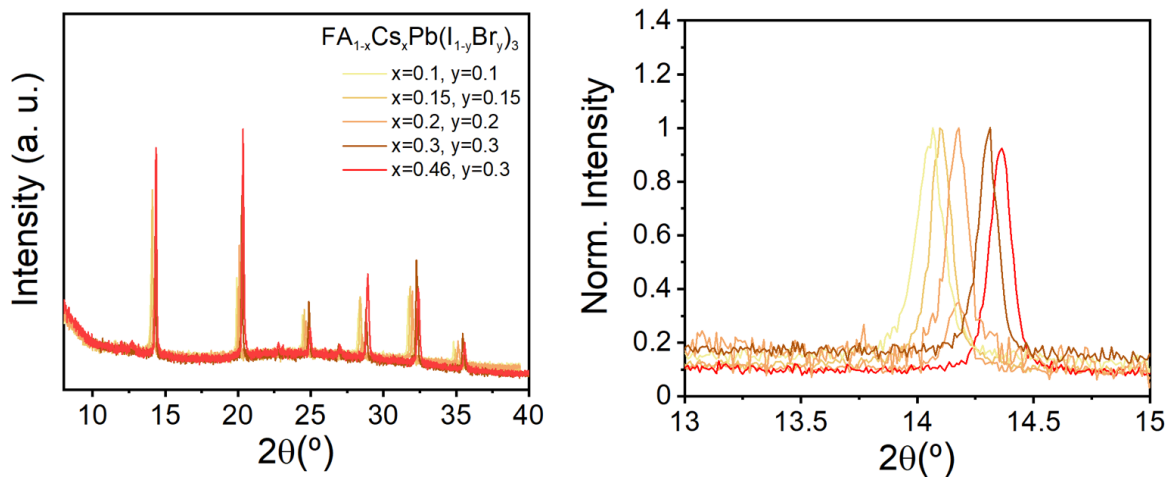


Figure 4.2. XRD patterns of a series of solution-processed films with $\text{FA}_{1-x}\text{Cs}_x\text{Pb}(\text{I}_{1-y}\text{Br}_y)_3$ composition, where x and y take a range of values between 0.1 – 0.46. The right panel shows a zoom around the key perovskite peaks used in the analysis in Figure 4.3.

A series of perovskite films are prepared by solution processing with different Cs and Br fractions and characterised their bulk properties by extracting peak positions of the perovskite XRD peaks (**Figure 4.2**). We estimate the stoichiometry of the solution-processed films by considering the concentration of A and X components in the precursor solutions.^{82,112} By assuming Vegard’s law for composition ranges which maintain the same phase¹¹³, in **Figure 4.3**, we estimate the evolution of the perovskite peak in the: i) $\text{FA}_{1-x}\text{Cs}_x\text{PbI}_3$ (green curve), ii) $\text{FAPb}(\text{I}_{1-y}\text{Br}_y)_3$ (blue curve) and iii) $\text{FA}_{1-x}\text{Cs}_x\text{Pb}(\text{I}_{1-x}\text{Br}_x)_3$ (black curve) perovskite families. Specifically, we use the XRD peaks from the $\text{FA}_{0.7}\text{Cs}_{0.3}\text{Pb}(\text{I}_{0.7}\text{Br}_{0.3})_3$ and $\text{FA}_{0.54}\text{Cs}_{0.46}\text{Pb}(\text{I}_{0.7}\text{Br}_{0.3})_3$ films to determine the specific influence of Cs on the lattice parameter, hence determining the slope of the green curve. We note that the green line is only plotted up to $x = 0.67$ in order to maintain the cubic perovskite phase, avoiding phase transitions.¹¹⁴ We determine the slope of the blue curve by considering experimental XRD peaks of the films in which we change the Br fraction, i.e. $\text{FA}_{0.9}\text{Cs}_{0.1}\text{Pb}(\text{I}_{0.9}\text{Br}_{0.1})_3$ and $\text{FA}_{0.3}\text{Cs}_{0.7}\text{Pb}(\text{I}_{0.3}\text{Br}_{0.7})_3$. Also, we decouple the influence of Cs using the blue line dependence; this isolates the effect of Br on the lattice parameter, i.e. the $\text{FAPb}(\text{I}_{1-y}\text{Br}_y)_3$ family. By knowing the specific influence of Cs and Br on the lattice parameter, we can thus generate the line corresponding to $\text{FA}_{1-x}\text{Cs}_x\text{Pb}(\text{I}_{1-x}\text{Br}_x)_3$ (black curve). These plots match our experimental data (gray circles) and those values reported for $\text{FA}_{0.7}\text{Cs}_{0.3}\text{PbI}_3$, FAPbBr_3 and FAPbI_3 in the literature (colored circles),^{115–117} validating the approach. We apply this methodology to estimate the composition of our evaporated perovskite by assuming that Cs:Br ratio is kept to 1:1, in line with the source of Cs and Br being CsBr. Therefore, we predict the lattice constant calibration curve of the $\text{FA}_{1-x}\text{Cs}_x\text{Pb}(\text{I}_{1-y}\text{Br}_y)_3$ family, where $x = 3y$, and represent it on the red curve. The experimental perovskite peak for our evaporated material (star point) lies on the curve, indicating the final perovskite composition is $\text{FA}_{0.7}\text{Cs}_{0.3}\text{Pb}(\text{I}_{0.9}\text{Br}_{0.1})_3$. We note that the precision in the XRD peak position is $\pm 0.01^\circ$, determined by the step size of the measurement, which translates to a propagated error contribution from the XRD measurements to the halide/cesium fraction of only $\sim 0.5\%$. We also note that we employed XRD measurements to ascertain bulk properties, which would not be possible with surface-sensitive XPS

measurements, and to avoid the complications of quantitative compositional analyses and potential beam damage that need to be considered in EDX measurements.

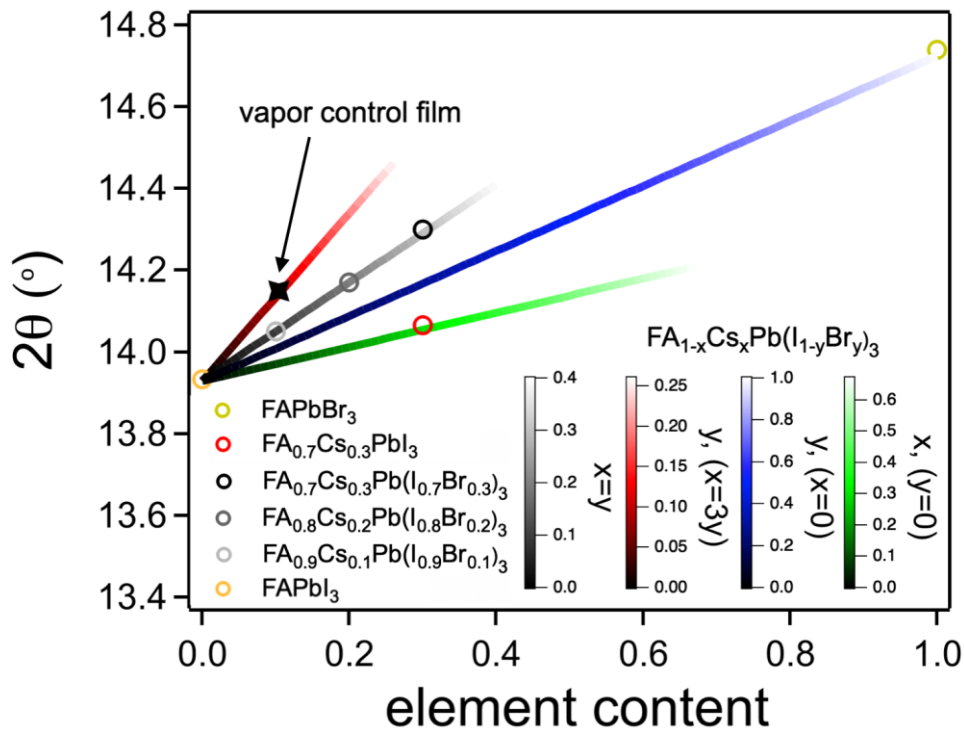


Figure 4.3. Plot used to estimate the final composition of the evaporated films (see the composition in the figure).

4.2.2 Optimisation of film annealing temperature

Scanning electron microscopy (SEM) images reveal that morphological grains in as-deposited films on UV-Ozone etched glass are ~ 50 nm in size (**Figure 4.4a**), but after annealing the deposited films at 150°C for 30 minutes larger entities of up to $1\text{-}2\ \mu\text{m}$ form (**Figure 4.4b**), consistent with the sharpening of the XRD peaks upon annealing (Figure 4.1.4 (c)). We show in **Figure 4.4c** the progression of the room-temperature XRD profiles as the post-deposition annealing temperature is changed, revealing an increase in the peak at $2\theta = 14.15^\circ$ corresponding to the black absorbing perovskite phase identified as the (011) peak (**Figure**

4.4.d) Although the perovskite film annealed at 150°C exhibits the largest grain sizes and highest perovskite-peak crystallinity, there is a new CsPbI₃ peak at ~10°, indicating the presence of an unwanted additional phase. Therefore, we identified 135°C as the optimum annealing temperature.

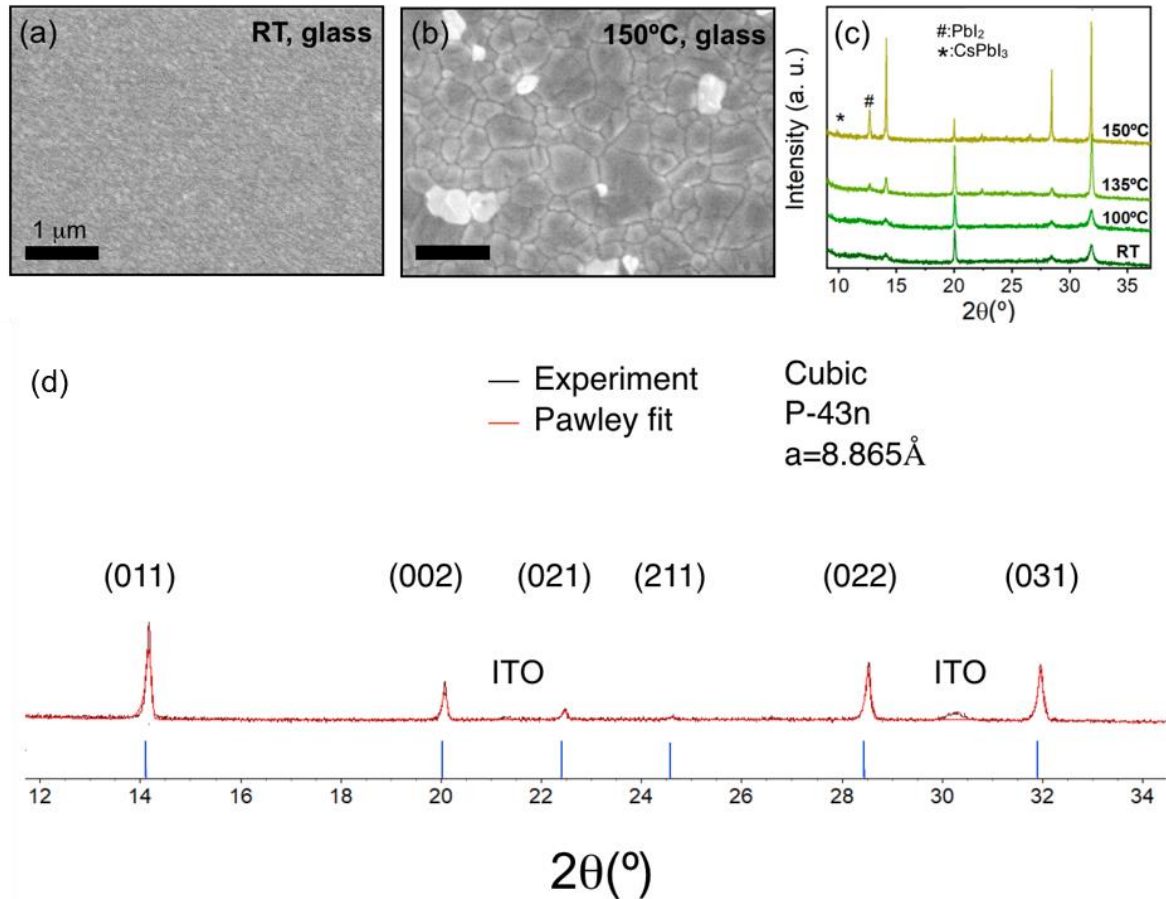


Figure 4.4. SEM top view images showing the morphology of evaporated FA_{0.7}Cs_{0.3}Pb(I_{0.9}Br_{0.1})₃ perovskite films as-deposited (a) and after 30 minutes of annealing at 150°C (b). (c) Room-temperature XRD patterns corresponding to evaporated perovskite films on glass following annealing at different temperatures for 30 minutes. Peaks corresponding to additional PbI₂ and CsPbI₃ phases are labelled; the other peaks correspond to the alloyed perovskite. The perovskite XRD peaks are assigned based on Pawley refinements. (d) the experimental data of the XRD pattern of the stoichiometric control sample on ITO/PTAA (annealed at 135°C), and the Pawley refinement to determine the structure and phase. The blue lines corresponding to the reflection pattern for P-43n.

4.2.3 Substrate dependence

The perovskite film composition/stoichiometry and properties are particularly sensitive to the underlying substrate, likely because of different surface chemistry in each case. The exposed surface with different functional group can affect the evaporated materials' sticking coefficient and the following growth. We find that the perovskite grain size when deposited on the bottom p-type solar cell contact poly(triarylamine) (PTAA, **Figure 4.5b**) is significantly larger than that of the film deposited on glass (**Figure 4.5a**). Likewise, the perovskite crystallinity and structure orientation also vary with the substrate, with the perovskite deposited on PTAA showing stronger black perovskite phase-related reflections than when the material is evaporated on glass (**Figure 4.4**). Thus, to ensure we optimise the material growth on the specific substrate relevant to our devices, we herein performed depositions on PTAA substrates with an underlying indium tin oxide (ITO) layer and an annealing temperature of 135 °C, unless stated otherwise.

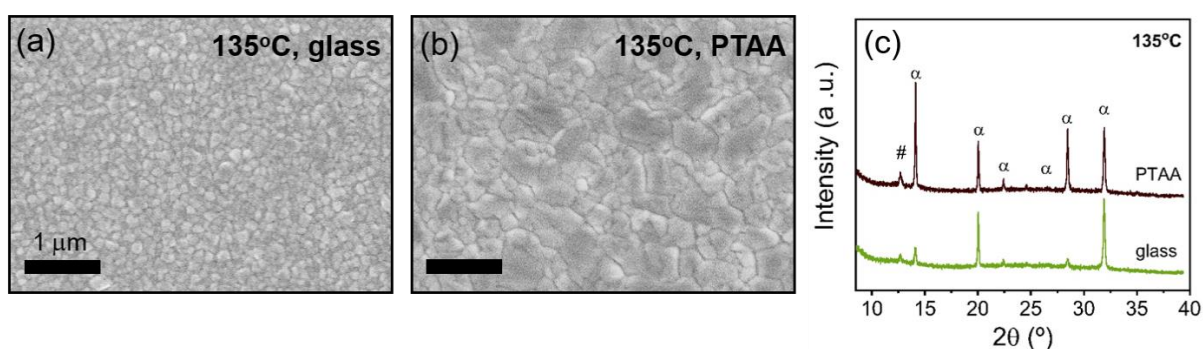


Figure 4.5. SEM top view images displaying the morphology differences when the perovskite films $\text{FA}_{0.7}\text{Cs}_{0.3}\text{Pb}(\text{I}_{0.9}\text{Br}_{0.1})_3$ are evaporated on glass (a) and PTAA (b) and annealed at an optimum temperature of 135°C, and their corresponding XRD patterns (c). The perovskite XRD peaks are assigned based on Pawley refinements.

4.3 Evaporated film stability

Perovskite films in general can be sensitive to light, moisture, and/or heat. In this section, the film stability is analysed to evaluate the possible degradation path in evaporated perovskite film. To test the atmospheric stability of the stoichiometric films, we stored them in ambient air with a relative humidity of $50 \pm 5\%$ for a period of 5 days and assessed changes in the XRD patterns (Figure 4.6a). We find that the samples stored in air showed substantial phase segregation over time under exposure, with the appearance of two new peaks at $2\theta = 10^\circ$ and 13.1° that we assign to the orthorhombic CsPbI_3 yellow-phase.^{118–120}

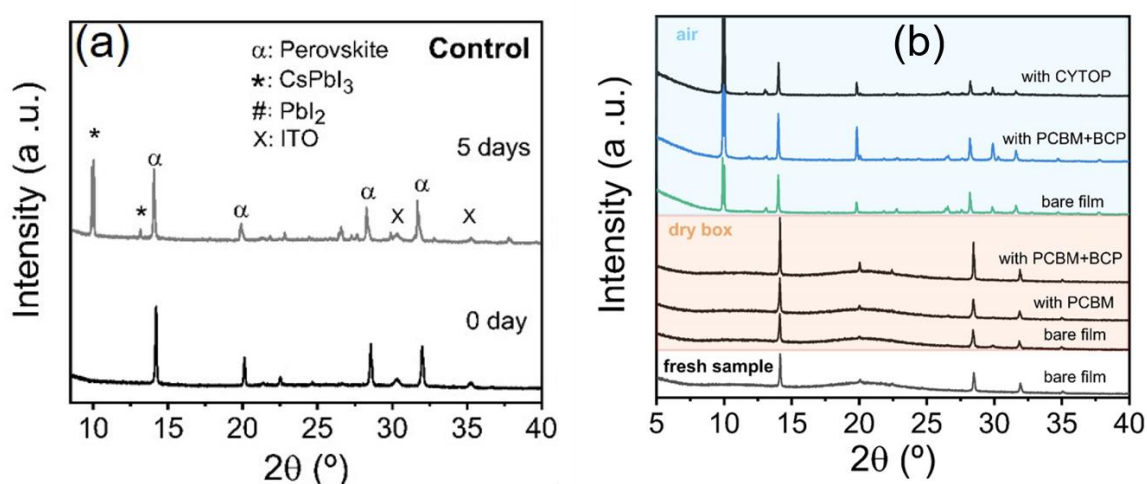


Figure 4.6. Structural characterisation of evaporated $\text{d FA}_{0.7}\text{Cs}_{0.3}\text{Pb}(\text{I}_{0.9}\text{Br}_{0.1})_3$ perovskite thin films on ITO/PTAA substrates. (a) XRD diffraction patterns as prepared (and annealed), and after storage in air at 50% relative humidity for 5 days. We assign the peak at $\sim 10^\circ$ to CsPbI_3 , though we note that this phase could also contain fractions of bromide. (b) The structure stability test by XRD with evaporated perovskite films coated with different contact layers on top. CYTOP is an amorphous fluoropolymer with low moisture and air permeability ($<10^{-12} \text{ cm}^3 \text{ cm}/(\text{cm}^2 \text{ s Pa})$). The “air” and “dry box” labels in the figure indicate when the samples were stored in an atmosphere with a relative humidity of $50 \pm 5\%$ and $<10\%$, respectively. To avoid moisture degradation, the fresh and “dry box” samples were kept in an air-tight sample holder during the XRD measurement.

To understand the degradation here, the contact layers for device fabrication, PCBM and BCP, are used to protect the samples; however, this does not mitigate the degradation process in the presence of moisture (**Figure 4.6**). The experiment is performed by keeping the samples in air with a relative humidity of $50\% \pm 5\%$. Furthermore, an amorphous fluoropolymer, CYTOP, with low moisture and air permeability is deposited on the top of perovskite but it still fails to protect the perovskite from degradation. We identify moisture as the primary cause of this degradation because the perovskite quality is preserved when we store the samples in dry air (relative humidity $<10\%$, a closed box with continued N_2 gas purging) and the stability does not show obvious variation with different contact layer.

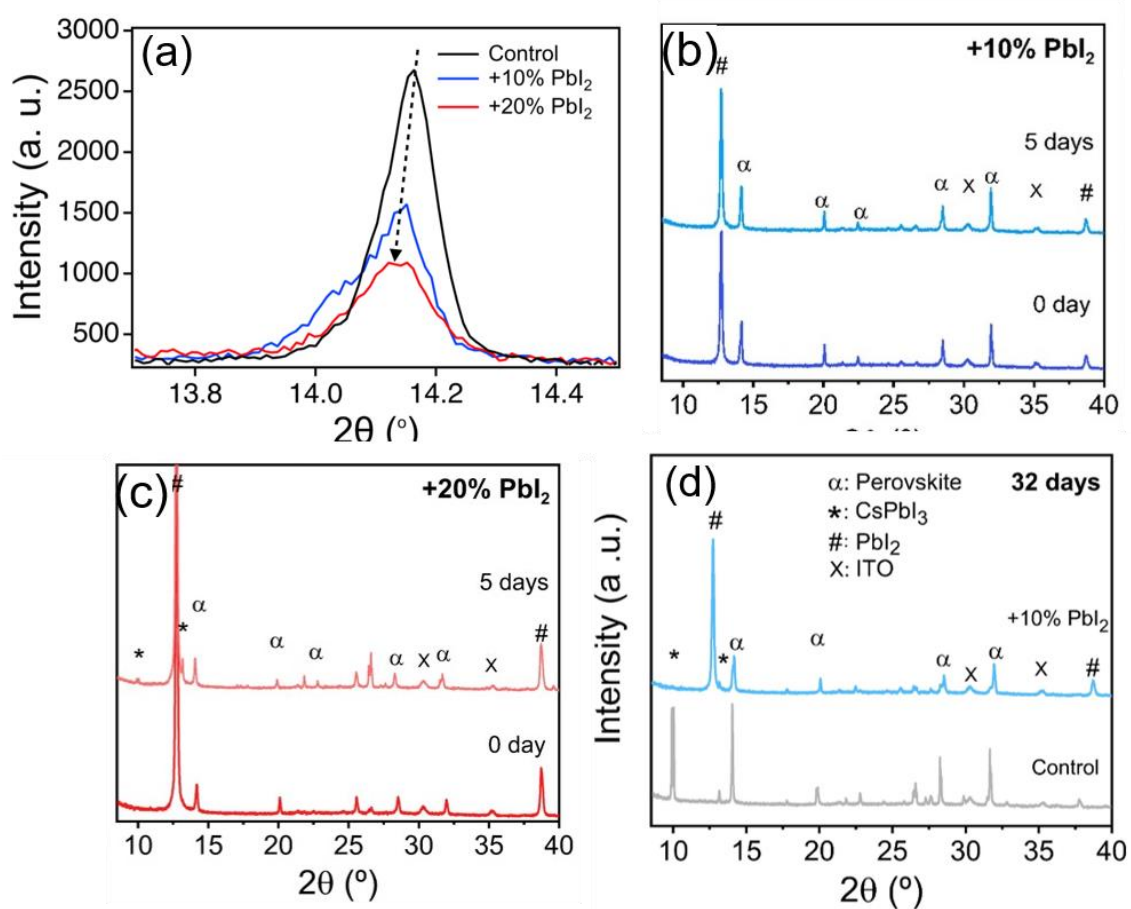


Figure 4.7. Structural characterisation of evaporated $FA_{0.7}Cs_{0.3}Pb(I_{0.9}Br_{0.1})_3$ perovskite thin films on ITO/PTAA substrates (a) Zoom-in XRD of the (011) perovskite peak with different excess PbI_2 during the evaporation, (b) with +10%, (c) with +20% perovskite before and after storage in air at 50% relative humidity for 5 days, (d) The air stability test comparison between control and +10% PbI_2 perovskite film deposited on PTAA/ITO substrate, storage in the air for 32 days.

To study the effect of composition on film stability, we vary the PbI_2 precursor evaporation rate to fine-tune its content in the final film to achieve +10% and +20% excess with respect to the stoichiometric control sample. Excess PbI_2 in solution-processed perovskite has proved to improve the perovskite film quality.^{121,122} To confirm this effect can be applied on the evaporated perovskite, the air stability test has been performed. The addition of PbI_2 results in strong XRD peaks at $2\theta = 12.7^\circ$ (corresponding to crystalline PbI_2), concomitant with a slight decrease in the perovskite (011) peak ($2\theta = 14.14^\circ$ and 14.12°) for both the +10% and +20% (**Figure 4.7a**) samples. Nevertheless, we find that the stability under ambient conditions is remarkably increased for the films with excess PbI_2 , with no detectable phase segregation observed after 5 days for the +10% PbI_2 sample and only a small amount of orthorhombic CsPbI_3 signal noticeable after 32 days in humid air (**Figure 4.7b-d**). We also find that the films with excess PbI_2 do not show degradation even after 8 h of heating at 135°C inside a nitrogen-filled glovebox (**Figures 4.8a-b**), which we attribute to the MA-free nature of the system.⁸²

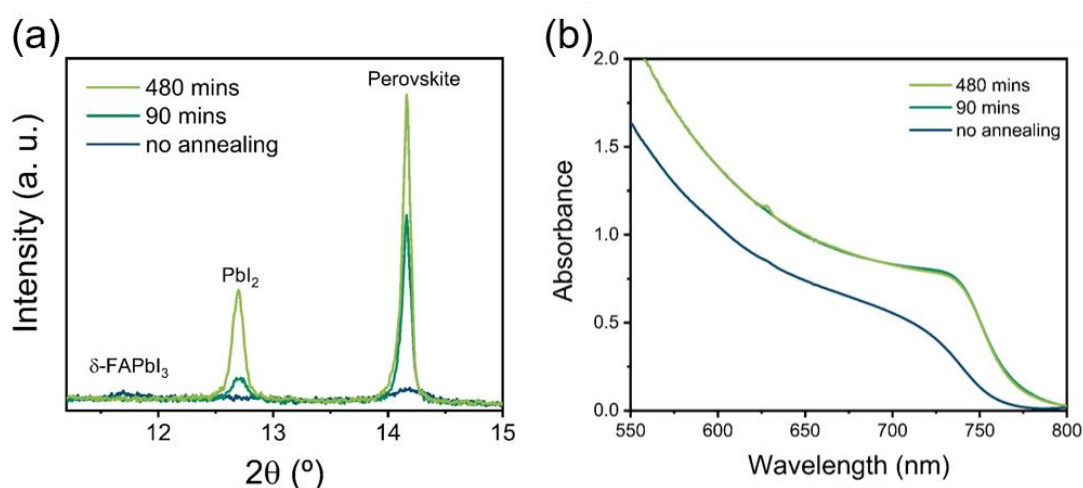


Figure 4.8. (a-b) XRD patterns and UV-vis spectra of evaporated perovskite films ($\text{FA}_{0.7}\text{Cs}_{0.3}\text{Pb}(\text{I}_{0.9}\text{Br}_{0.1})_3$) without or with annealing at 135°C for 90 or 480 mins.

SEM images show that the addition of PbI_2 causes a decrease and homogenisation in the size of the perovskite grains from an average size of ~ 335 nm for the control (**Figure 4.9a**) to ~ 209 nm for +10% (**Figure 4.9b**) and even smaller grain sizes for +20% samples (**Figure 4.9c**). Moreover, we find that the excess PbI_2 forms as clusters as revealed by bright areas in the micrographs, which are particularly evident in the +20% sample.⁴⁶ We propose that the excess PbI_2 particularly situated at the grain boundaries could form a protection layer against moisture infiltration.¹²³ The grain size is further calculated by Image-J (see **Figure 4.9d-e** and the grain

distribution is plotted. The data shows the clear trend of perovskite size is smaller with more excess PbI_2 . These results are in line with the slight broadening in the perovskite peaks in the XRD patterns (**Figure 4.7a**). The underlying grain size in the +20 % sample is difficult to calculate as many PbI_2 -rich domains are covering on the surface. We assume the bright area is PbI_2 due to our previous correlative experiment and the presence of PbI_2 peak in XRD.¹²⁴

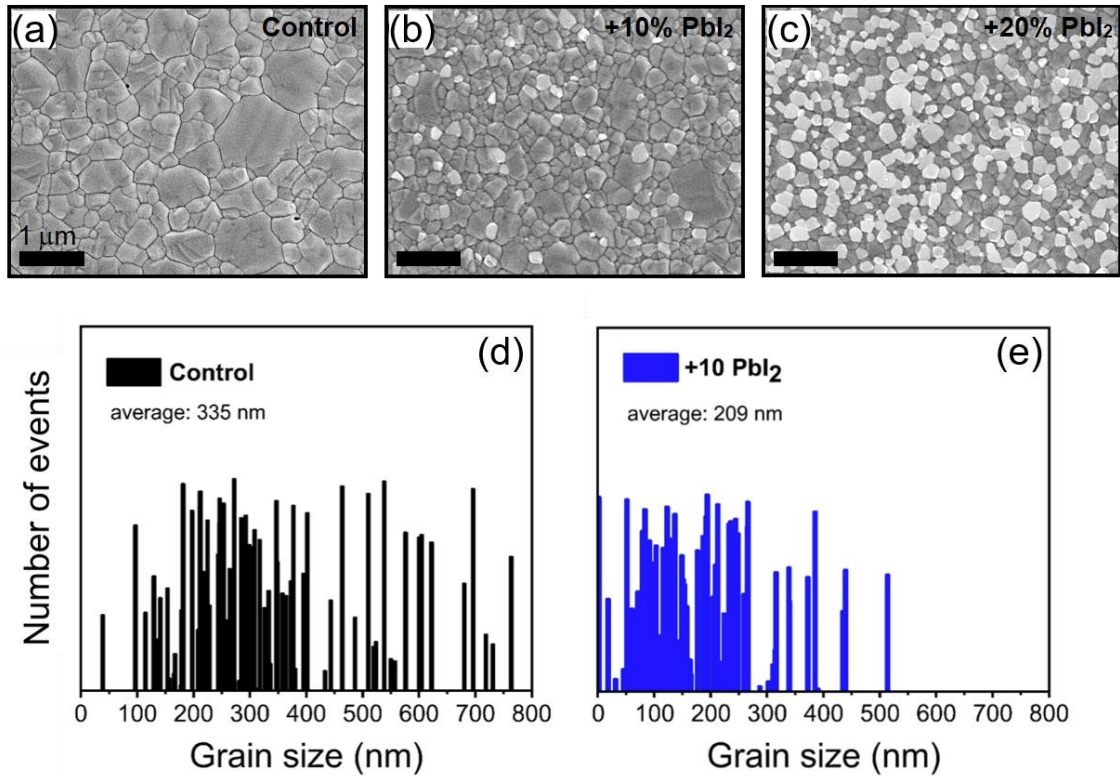


Figure 4.9. (a–c) SEM micrographs of the films with control, +10% and +20% excess PbI_2 in perovskite film ($\text{FA}_{0.7}\text{Cs}_{0.3}\text{Pb}(\text{I}_{0.9}\text{Br}_{0.1})_3$). The grain size distribution of perovskite films with (d) control and (e) +10 PbI_2 perovskite film on PTAA/ITO substrate. The grain size was obtained by calculating the square-root of the grain area estimated using the software ImageJ.

We also note that our optimal parameters change when using a different PbI_2 supplier, further emphasising the sensitivity of the process. In **Figure 4.10**, we prepare a perovskite by the exact same protocol, however, different perovskite crystallographic structure is shown. This information is vital for lab-to-lab reproducibility and industrial manufacturing, showing the importance of precursor choice. We have also noticed that even if the PbI_2 is from same supplier, there is still a batch-to-batch variation, especially in device V_{OC} . Besides, even the “control device” shows the reasonable performance, once the post passivation treatment is employed, the device performance drops significant with certain batches of PbI_2 .

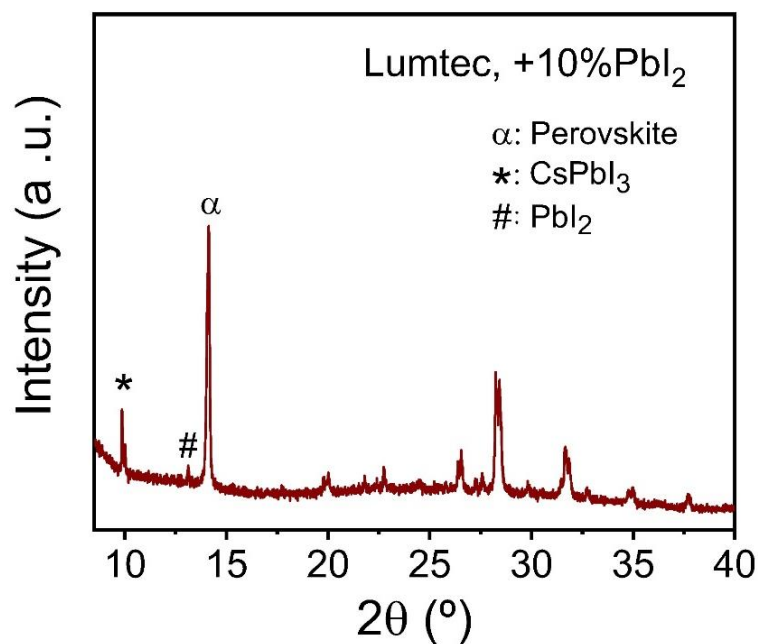


Figure 4.10. XRD pattern of a +10% PbI_2 evaporated perovskite film ($\text{FA}_{0.7}\text{Cs}_{0.3}\text{Pb}(\text{I}_{0.9}\text{Br}_{0.1})_3$) by using Lumtec PbI_2 as a precursor, indicating the sensitivity to the PbI_2 source and the deposition process in the final characteristics of the perovskite. The XRD data was measured in air, and we saw degradation of the film after 15 mins, with the appearance of a CsPbI_3 peak.

4.4 Characterise optoelectronic properties of evaporated perovskite films

4.4.1 Absorption and PL characteristics

To assess the resulting optoelectronic properties of the films, we show absorbance spectra in **Figure 4.11a**, revealing an absorption onset at ~ 765 nm for the control film which red-shifts to ~ 767 nm and ~ 775 nm with 10% and 20% PbI_2 excess, respectively. We find a similar trend in the PL peaks, which also red-shift by ~ 2 nm and ~ 10 nm with addition of 10% and 20% excess PbI_2 , respectively (**Figure 4.11b**). We associate these reduced absorption onset and emission energies to a higher fraction of $\text{I}/(\text{I}+\text{Br})$ in the lattice structure (i.e. dilution of Br), which is consistent with the shift of the perovskite peak toward lower angle in XRD (**Figure 4.7a**).

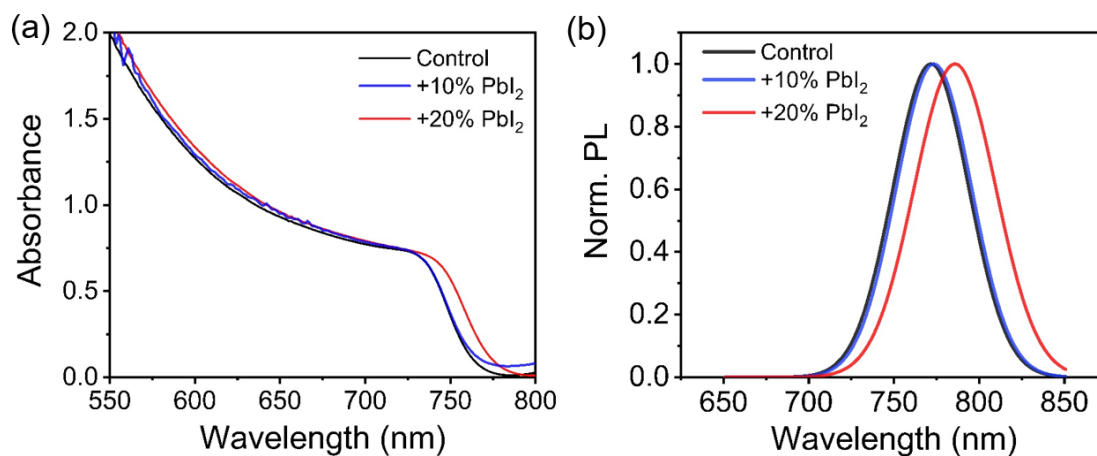


Figure 4.11. UV-Vis absorption (a) and normalised photoluminescence (PL) (b) spectra (excitation at 520 nm) of evaporated $\text{FA}_{0.7}\text{Cs}_{0.3}\text{Pb}(\text{I}_{0.9}\text{Br}_{0.1})_3$ perovskite films with different quantities of excess PbI_2 with respect to the stoichiometric control.

We also find that the PLQE of the films on glass under approximately 1-sun equivalent excitation density (520-nm CW laser at 60 mW/cm²) is enhanced in the samples with 10% and 20% excess PbI₂, with PLQE values of 0.5 % and 0.3 %, respectively, compared to 0.2 % measured for the control sample (see **Figure 4.12a** for PL Peaks). We attribute this observation to the passivating nature of PbI₂ in the perovskite films.^{121,122} This passivation of defects may also be related to the improved air stability of perovskite films with 10% PbI₂ incorporation, in line with proposed links between non-radiative centres and sites of instability (such as ion migration and environmental susceptibility).^{125,126}

The quasi-fermi level splitting (QFLS) in **Figure 4.12b** is calculated based on PLQE data. The QFLS can provide a measure of the quality of the samples as it shows the potential V_{OC} in the devices. Three set of samples are measured, perovskite on glass, perovskite on PTAA/glass, and PCBM deposited perovskite on PTAA/glass, thus revealing the non-radiative loss in perovskites with different contact. First, the perovskite on glass shows the QFLS number of 1.19 eV, indicating the bulk/surface loss of 140 mV from the radiative value 1.33 V for bandgap of 1.62 eV). Once the bottom contact layer, PTAA, is used, the QFLS number drops to 1.16 eV. Further loss by introducing the top contact, PCBM, on perovskite, shows the QFLS of 1.13 eV which is close to the V_{OC} from JV scan measurement. From this experiment, the loss in perovskite device can be understood and targeted passivation studies can mitigate these losses.

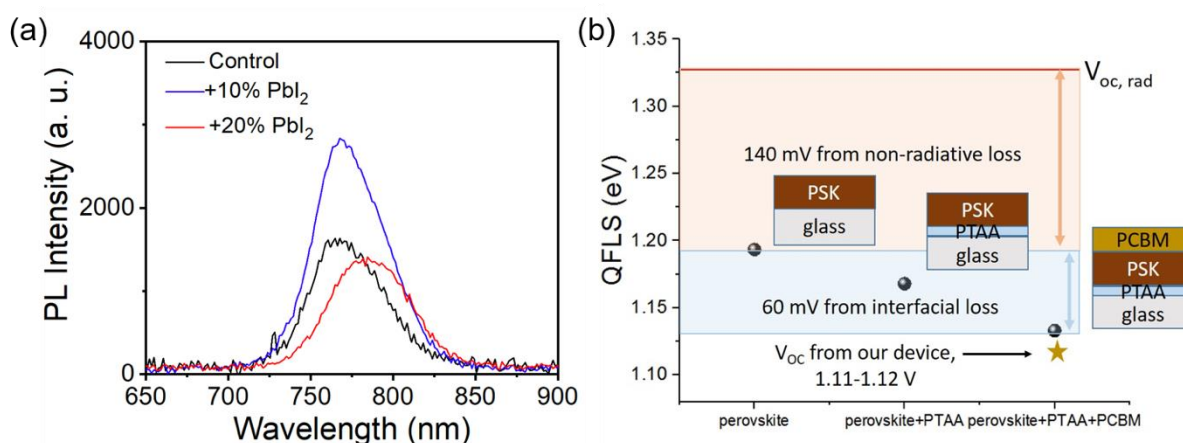


Figure 4.12. (a) PL spectra (excitation at 520 nm) of evaporated perovskite (FA_{0.7}CS_{0.3}Pb(I_{0.9}Br_{0.1})₃) with different excess of PbI₂. (b) The quasi-fermi level splitting analysis for the perovskite (10% sample) with n-type and p-type transporting layer, calculated from the PLQE results. The black and star symbols are based on film PLQE and device V_{OC} measurements (10% PbI₂ device), respectively.

Further, time-resolved PL measurements under fluences similar to 1 sun illumination reveal an initial fast component but long lifetime components for the control, 10% and 20% perovskite films of 401 ns, 204 ns and 130 ns, respectively, where lifetime is defined as the time taken to fall to $1/e$ of the initial intensity of the long decay component (**Figure 4.13**). These values are an order of magnitude longer than the values of a few nanoseconds reported for most of evaporated perovskite films in the literature to date.^{84,127} We note there is an initial fast decay component in all of our samples that is likely due to non-radiative recombination and is consistent with the PLQE values being significantly less than unity; it is likely that further surface passivation work will reduce these losses further.

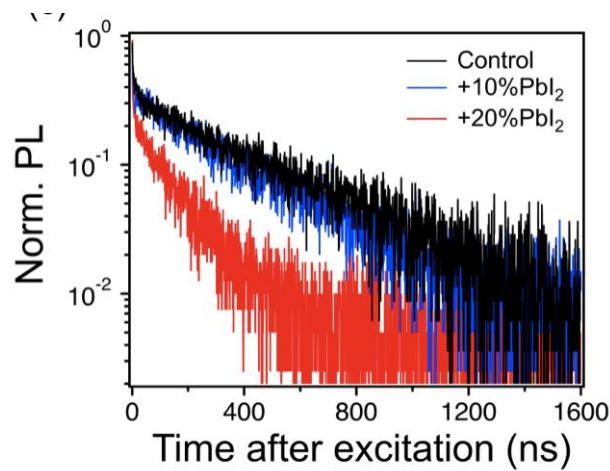


Figure 4.13. (c) TRPL measurements for the different perovskite films ($\text{FA}_{0.7}\text{Cs}_{0.3}\text{Pb}(\text{I}_{0.9}\text{Br}_{0.1})_3$) with excitation at 407 nm (repetition rate of 0.5 MHz, fluence of 5 $\text{nJ}/\text{cm}^2/\text{pulse}$).

4.5 Evaporated perovskite solar cells with inverted structure.

4.5.1 composition engineering for high-efficient perovskite solar cells

After analysing the evaporated perovskite quality with different amounts of PbI_2 during the evaporation, solar cells are fabricated to further verify the effects of PbI_2 on optoelectronic performance. We fabricated solar cell devices with an inverted architecture: ITO/PTAA/evaporated perovskite/phenyl-C61-butyric acid methyl ester (PCBM)/bathocuproine (BCP)/silver (Ag) and encapsulated them with a glass cover slide in a nitrogen-filled glovebox. We display in **Figure 4.14** schematic of the device architecture along with a cross-sectional SEM image, which shows a perovskite film with a thickness of ~ 490 nm with large, homogeneous morphological grains. We compare the performance of devices under AM 1.5 G illumination with different amounts of PbI_2 in Table 4.2.1 and show the corresponding current–voltage (J–V) curves in **Figure 4.14**. For the stoichiometric perovskite composition (no excess PbI_2), the device presents a PCE of 15.5%, an open-circuit voltage (V_{OC}) of 1.08 V, a short-circuit current density (J_{SC}) of 20.4 mA/cm^2 , and a fill factor (FF) of 70.4%. With the addition of 10% excess PbI_2 , both V_{OC} and J_{SC} are increased to 1.12 V and 22.8 mA/cm^2 , respectively, yielding a PCE of 17.8%. We note that the measured voltage of 1.12 V matches the value expected from PLQE measurements (See Chapter 2.2.3) of the full device stack under solar illumination conditions (0.05%, **Figure 4.12b**). For 20% excess PbI_2 , the device performance drops to 16.1% with lower J_{SC} and FF, likely because of the excess PbI_2 as an insulator starting to hinder charge transport or collection. In general, with more PbI_2 the device open-circuit voltage increases, which is in line with the increased luminescence efficiency and passivation effects.

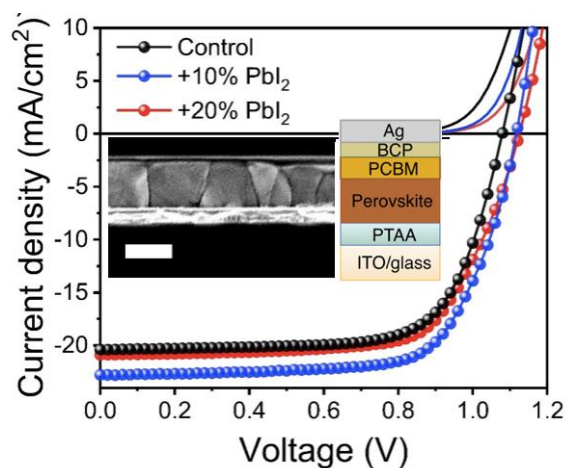


Figure 4.14. J-V curves of evaporated perovskite ($\text{FA}_{0.7}\text{Cs}_{0.3}\text{Pb}(\text{I}_{0.9}\text{Br}_{0.1})_3$) for solar cells with different quantities of excess PbI_2 measured under AM 1.5G ($100 \text{ mW}/\text{cm}^2$ irradiance), along with corresponding dark curves. The curves are from the reverse scan (sweeping from 1.2 V to -0.1 V. During the measurement, a scan rate of 100 ms/V was used). A cross-section SEM image (scale bar is 500 nm) and a schematic of the employed solar cell architecture are shown in the inset.

Table 4.2. Device performance parameter from the reverse scans of the $\text{FA}_{0.7}\text{Cs}_{0.3}\text{Pb}(\text{I}_{0.9}\text{Br}_{0.1})_3$ solar cells with different amounts of excess PbI_2 with respect to the control.

	V_{oc} (V)	J_{sc} (mA/cm^2)	FF (%)	PCE (%)
Control	1.08	-20.4	70.4	15.5
5%	1.06	-23.0	74.6	18.1
10%	1.12	-22.8	70.1	17.8
20%	1.12	-20.9	68.7	16.1

4.5.2 Optimised perovskite solar cells

Finally, we further optimise the PbI_2 excess and find that our best-performing solar cells are based on a perovskite composition with 5% excess PbI_2 (**Table 4.2**). This composition results in a small fraction of crystalline PbI_2 in the final films that provides a compromised balance of passivation and stabilisation of the films without hindering current collection (related to current density) or increasing series resistance (related to fill factor); the PbI_2 entities in these films are too small to be resolved in SEM images (see **Figure 4.15** for film characterisation). We show the device performance statistics in **Figure 4.16** with forward (from short circuit to open circuit) and reverse scan (from open circuit to short circuit) results from 35 independent devices across five different batches. We note that the batch-to-batch variation is low (see **Figure 4.17**). The device metrics are highly reproducible with an average PCE for reverse and forward scans of $16.8 \pm 0.8\%$ and $16.2 \pm 0.9\%$, respectively. We observed no degradation in performance of an encapsulated device over a period of 18 days stored in air (**Figure 4.18**), reflecting the film stability observed in samples with excess PbI_2 . We display the external quantum efficiency (EQE) of our champion device in **Figure 4.16b**, with values greater than 80% for the working spectral range 400–775 nm, demonstrating an excellent photon-to-electron conversion efficiency. Interestingly, the spectrum shows oscillating features that are fingerprints of light interference phenomena arising from the high optical quality of the device stack. The SPO of the champion device reaches 18.2% with negligible hysteresis effect between the forward and backward curves (**Figure 4.16c**). This result represents the best performing MA-free perovskite solar cell by vacuum deposition to date. Li et al. have reported that the evaporated MAPbI_3 perovskite solar cell without surface passivation treatment shows poor operational stability, reducing the PCE to 80% of initial performance in 10 hours.¹⁰⁷ In our MA-free system, a proof of principle stability test shows that the champion device composition retains ~90% of its initial efficiency after 35 h under continuous operation at maximum power point (**Figure 4.18**), which is an encouraging result for vacuum-deposited MA-free perovskite solar cells given the device stack has not been optimised (no surface passivation and using Ag as electrode) for stability.

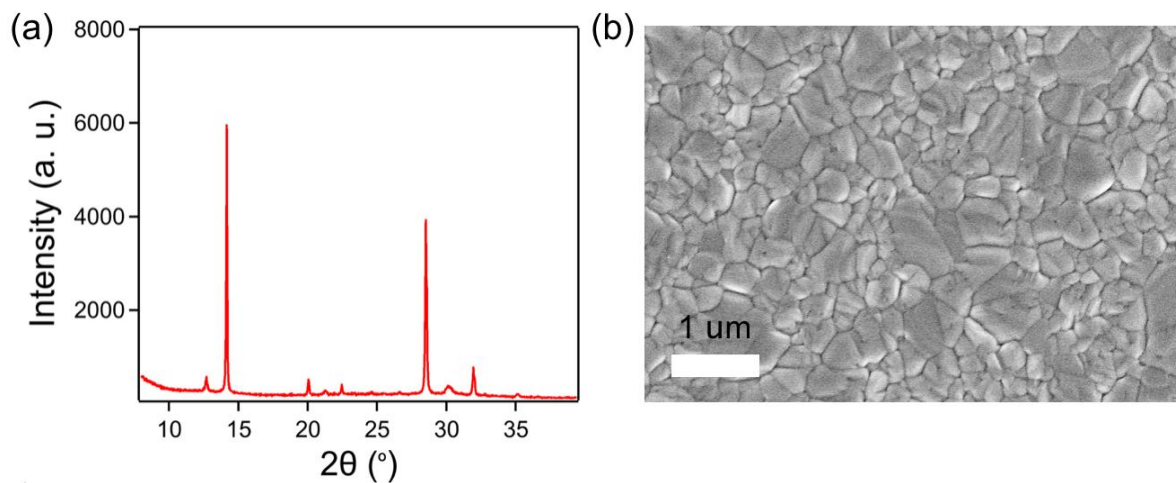


Figure 4.15. The structural and morphological characterisation of the evaporated perovskite film ($\text{FA}_{0.7}\text{Cs}_{0.3}\text{Pb}(\text{I}_{0.9}\text{Br}_{0.1})_3$) with 5% excess PbI_2 deposited on a PTAA/ITO substrate. (a) XRD pattern and (b) top-view SEM image of the film.

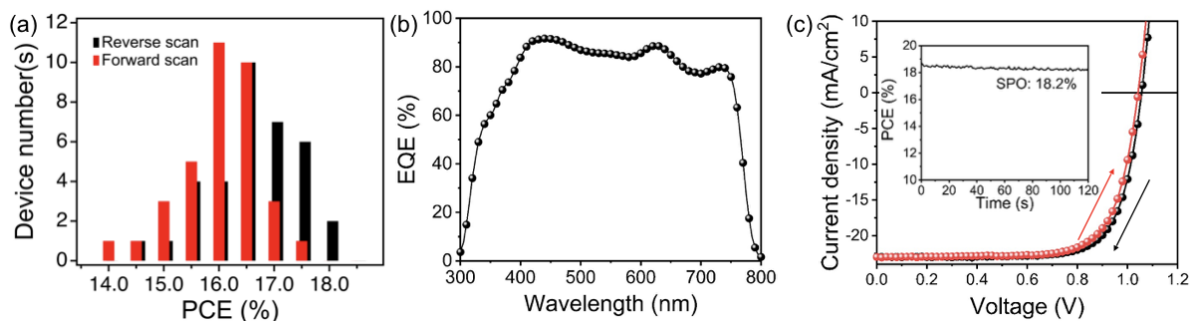


Figure 4.16. (a) Histogram of device performance from 35 independent devices with the $\text{FA}_{0.7}\text{Cs}_{0.3}\text{Pb}(\text{I}_{0.9}\text{Br}_{0.1})_3$ perovskite including 5% excess PbI_2 . The results from reverse (1.2 V to -0.1 V, black curve) and forward (-0.1 V to 1.2 V, red curve) scans are distinguished. During the measurement, a scan rate of 100 ms/V was used. (b) EQE measurement for the champion device. (c) Forward (red) and reverse (black) J-V curves of a champion device. The inset figure is the stabilised power output (SPO) measurement, maintaining the bias at maximum power point of the reverse scan at 0.88 V and measuring the photocurrent.

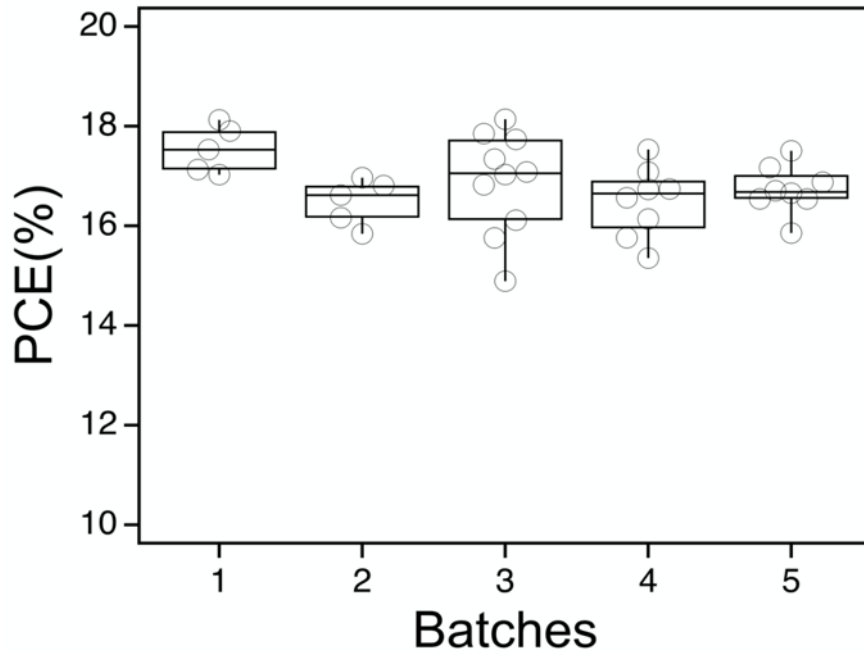


Figure 4.17. Device performance for 5% PbI_2 excess evaporated perovskite ($\text{FA}_{0.7}\text{Cs}_{0.3}\text{Pb}(\text{I}_{0.9}\text{Br}_{0.1})_3$) solar cells from reverse scan measurement of J-V scan under 1 sun AM 1.5G illumination across five different batches.

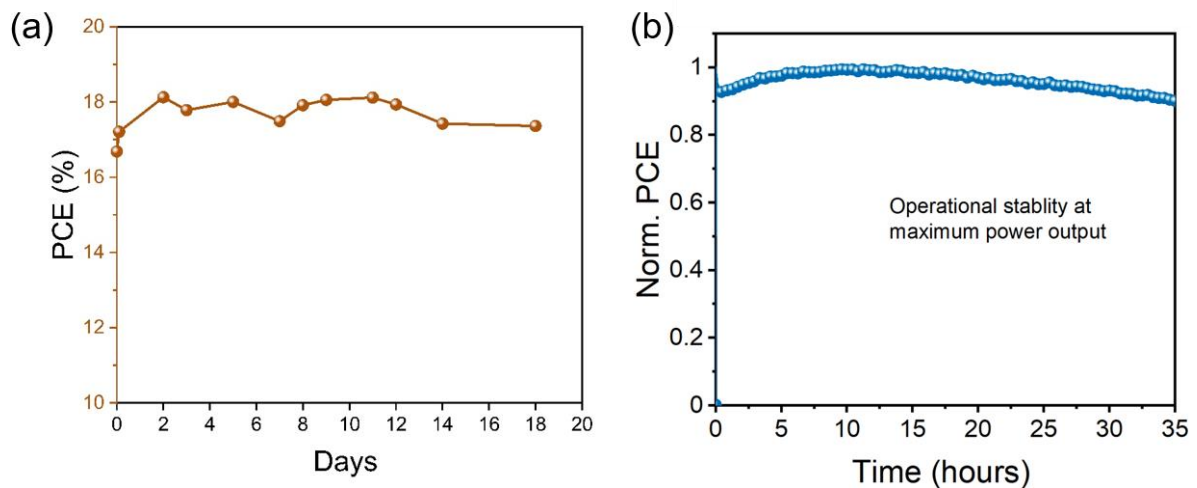


Figure 4.18. (a) The shelf-stability test of an encapsulated device measured over a period of 18 days, with the devices stored and measured in air. The J-V measurements are under 1 sun AM 1.5G illumination. The PCE here is the value from the reverse scan of the J-V curve. (b) Operational stability test of encapsulated solar cells in air under AM 1.5 G 1-sun intensity light

at maximum power point based on the initial reverse scan (0.8 V). We note there is no UV filter.

4.5.3 The effect of deposition rate on perovskite film and device quality.

We also observe that hysteresis between the forward and reverse scans is low in each of the devices (**Figure 4.19a**), though the hysteresis significantly increases if the PbI_2 deposition rate is unstable in a given batch (**Figure 4.19b**). This observation is also reflected in a far less homogeneous films when the PbI_2 evaporation rate is unstable, with clear phase segregation in the case of unstable rates (**Figure 4.19c-d**). These results emphasise the importance of the composition, achieved through precisely controlled deposition rates, to yield high-quality perovskite films and devices by vapor deposition.

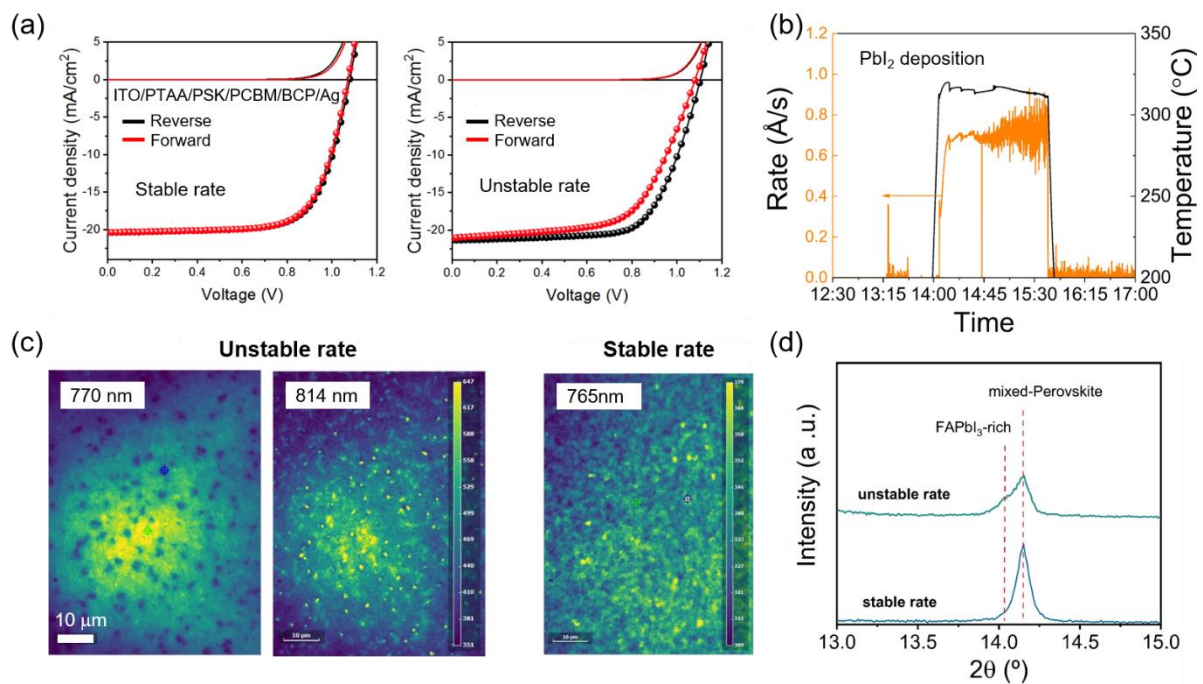


Figure 4.19. JV-curves for evaporated perovskite ($\text{FA}_{0.7}\text{Cs}_{0.3}\text{Pb}(\text{I}_{0.9}\text{Br}_{0.1})_3$) solar cells (+10% PbI_2) deposited with a stable (left panel) and unstable (right panel) rate. During the measurement, a scan rate of 100 ms/V was used. A more pronounced hysteresis effect can be seen in the device with an unstable rate during the film deposition. (b) Variation in PbI_2 rate

and temperature during an unstable perovskite evaporation batch. (c) Hyperspectral photoluminescence (PL) maps of evaporated perovskite films (+10% excess PbI_2) on glass. The left and middle maps correspond to a sample obtained with an unstable deposition rate. The PL peak distributions are spatially and spectrally inhomogeneous, showing maxima at 770 and 814 nm, which is indicative of phase segregation. The right map is the PL signal from a film obtained with a stable deposition rate, showing a single peak emission spectrum with its maximum at 765 nm. (d) XRD patterns to understand the crystalline structure of the perovskite film (10% excess PbI_2) deposited with stable and unstable rates. When the evaporation rate is unstable, we observe an asymmetric perovskite peak with a shoulder at lower 2θ , corresponding to FAPbI_3 -rich domains.⁸ For the perovskite film deposited with a stable rate, there is negligible asymmetry in the XRD peak (blue curve). Note: the hyperspectral measurement was conducted with the help of Dr. Miguel Anaya.

4.6 Conclusion

We simultaneously used three thermal sources to evaporate MA-free perovskite films with $\text{FA}_{0.7}\text{Cs}_{0.3}\text{Pb}(\text{I}_{0.9}\text{Br}_{0.1})_3$ compositions. We found that an excess of PbI_2 from the nominal stoichiometric composition enhances the film stability and optoelectronic properties, yielding a higher PLQE and long charge carrier lifetimes. We demonstrate solar cells with a *p-i-n* architecture showing stabilised power output of 18.2%, which is the highest performance for a fully vapor-deposited MA-free system at the time of the work. We highlight the extreme sensitivity of the resulting film and device properties to a range of processing conditions including precursor rates and stability, precursor supplier, post-annealing temperature and underlying substrates, providing clear guidelines for further optimisation and deposition of different compositions. These results provide a major step towards MA- and solvent-free, scalable and reproducible methodologies suitable for the adoption of the perovskite technology in production chains and applications such as multijunction devices where solution methods are less preferred.

Chapter 5. Efficient all-perovskite tandem solar cells by dual-interface optimisation of vacuum-deposited wide-bandgap perovskite

Tandem perovskite solar cells beckon as lower cost alternatives to conventional single junction solar cells, with all-perovskite tandem photovoltaic architectures showing power conversion efficiencies up to 26.4%. Solution-processing approaches for the perovskite have enabled rapid optimisation of perovskite solar technologies, but new deposition routes are necessary to enable modularity and scalability, facilitating further efficiency improvements and technology adoption. Here, we utilise 4-source vacuum deposition method to deposit $FA_{0.7}Cs_{0.3}Pb(I_xBr_{1-x})_3$ perovskite, where the bandgap is widened through fine control over the halide content. We show how the combined use of a MeO-2PACz self-assembled monolayer as hole transporting material and passivation of the perovskite absorber with ethylenediammonium diiodide reduces non-radiative losses, with this dual-interface treatment resulting in efficiencies as high as 17.8% in solar cells based on vacuum deposited perovskites with a bandgap of 1.76 eV. By similarly passivating a narrow bandgap $FA_{0.75}Cs_{0.25}Pb_{0.5}Sn_{0.5}I_3$ perovskite and combining it with sub-cells of evaporated $FA_{0.7}Cs_{0.3}Pb(I_{0.64}Br_{0.36})_3$, we report a 2-terminal all-perovskite tandem solar cell with champion open circuit voltage and power conversion efficiency of 2.06 V and 24.1%, respectively. The implementation of our dry deposition method enables high reproducibility in complex device architectures, opening avenues for modular, scalable multi-junction devices where the substrate choice is unrestricted.

This chapter has submitted for review and the pre-print version can be found in arXiv:2208.03556.¹²⁸

5.1 Introduction

Multi-junction solar cells constitute the most practical way to achieve power conversion efficiencies (PCEs) beyond the radiative efficiency limits of single-junction solar cells. Multi-junction technologies employ photo-absorbers with complementary bandgaps to collectively harvest a broader portion of the solar spectrum whilst minimising thermalisation losses upon hot-carrier relaxation. The highest performance solar cell report to date is from a triple-junction based on III-V semiconductors with a strain-balanced quantum well stack, achieving a PCE of 39.5%.¹²⁹ However, their high cost due to complex fabrication processes that involve high temperatures limits their accessibility and versatility. These costs are historically limiting the use of III-V solar cells in terrestrial power applications and restrict their use to high-value applications such as powering satellites or space vehicles.

Halide perovskites are generating enormous excitement as thin film absorbers for high-performance solar cells, showing a unique combination of features that include low-temperature processing and resilience to electronic defects.¹³⁰ With a compositionally tunable ABX_3 crystal structure, where A = methylammonium (MA), formamidinium (FA) and/or Cs, B = Pb and/or Sn, and X = Cl, Br, I, the bandgap of 3D perovskites can be varied from 1.2 eV to 3.0 eV. This absorption tunability, combined with high absorption coefficients and charge carrier mobilities, make these materials promising for both single and multi-junction thin film solar cells.^{12,27,89,131} Indeed, the record PCE single-junction perovskite and all-perovskite tandem solar cells have reached PCEs of 25.7% and 26.4%,^{71,72} respectively, representing the most efficient emerging PV systems to date. These outstanding outcomes result from years of work from myriads of research groups mostly working with solution processed approaches that allow rapid screening and optimisation. However, solution approaches ultimately present limitations for manufacturing due to the use of toxic solvents and potential issues with dissolving underlying layers, the latter limiting the underlying materials and substrates.

Vacuum deposition processes show great promise to overcome barriers related to large-area coating, integration into flexible, lightweight substrates and novel device patterns while ensuring high thickness control and conformal film uniformity, all with a solvent-free technique. To date, fully evaporated perovskite solar cells have achieved PCEs of 20.7% and 21.4% on small active area ($< 0.2 \text{ cm}^2$) by co-evaporation and sequential evaporation, respectively,^{106,107} and PCE of 18.1% over larger area (21 cm^2).¹⁰⁷ While the community has

concentrated most efforts on evaporating MAPbI₃ perovskite solar cells,^{73,106,107,111} we and others have demonstrated that MA-free, mixed halide systems are viable candidates to achieve thermally stable perovskite devices.^{132–135} Importantly, the dry nature of the technique represents an ideal approach to stack different perovskite films for tandem device architectures on a range of underlying contacts and substrates, an approach that opens avenues for a highly efficient yet low-cost thin film, light-weight perovskite technology.

Nevertheless, only a handful of works have reported fully-evaporated perovskites for their application in multi-junction cells, with most of the examples focusing on deposition processes to combine perovskite and silicon subcells in a tandem fashion.^{19,136,137} As for all-perovskite tandem systems, Ávila *et al.* reported a vacuum deposited MAPbI₃-MAPbI₃ perovskite solar cell with an outstanding V_{OC} of 2.3 eV and a PCE of 18%, demonstrating the potential of the technique to attain building blocks for tandem devices.¹³⁸ However, perovskite bandgaps in this work were not optimised to minimise energy losses while maximising current matching for AM1.5 illumination. Optical modelling suggests that a PCE >35% cell efficiency is potentially achievable in all-perovskite tandems under realistic conditions.^{10,20,139} This value is conditioned by the absorption spectrum of the rear subcell as the narrowest perovskite bandgaps demonstrated so far are in the range between 1.20 eV to 1.30 eV based on alloyed Pb/Sn compositions. The bandgap of the optimum front (wide bandgap) subcell for that constraint is between 1.70 to 1.80 eV, though little further loss is seen when the bandgap is lowered further to 1.65 eV when light coupling between layers is taken into account.⁹² One challenge in realising these WBG perovskite materials is they inevitably require mixed halide compositions, and they hence suffer from light-induced phase segregation, forming Br and I rich sub domains that reduce the open-circuit voltage (V_{OC}).^{52,70,140–142} Lidón *et al.* reported a wide bandgap (1.77 eV) perovskite with a composition of FA_{0.61}Cs_{0.39}Pb(I_{0.70}Br_{0.30})₃ displaying a V_{OC} of up to 1.21 V, the best-to-date for a vacuum deposited system.¹³² Yet, this V_{OC} is still 240 mV below the radiative efficiency limit of 1.45 V for a 1.77 eV bandgap, indicating significant losses in the best WBG perovskite solar cells. Interestingly, it has been recently shown that low radiative efficiency in bulk mixed halide perovskites and energy misalignment between the perovskite and contact layers are the main losses in wide bandgap perovskite solar cells, and a device V_{OC} of over 1.33 V (for a 1.77 eV bandgap) is achievable even in the presence of halide segregation.^{70,143} These results overall show the complex compromise between perovskite phase stabilisation and device stack optimisation required to attain vacuum deposited WBG perovskite solar cells relevant for tandem architectures.

In this work, we employ a 4-source co-evaporation technique to systematically vary the bandgap of $\text{FA}_{0.7}\text{Cs}_{0.3}\text{Pb}(\text{Br}_x\text{I}_{1-x})_3$ films from 1.62 eV to 1.80 eV for their subsequent integration in an all-perovskite tandem device. We show how contact layer optimisation by using (2-(3,6-Dimethoxy-9H-carbazol-9-yl)ethyl)phosphonic acid (MeO-2PACz) as hole transporting material (HTM) minimises interfacial recombination and leads to PCEs of 20.7% for a 1.62 eV perovskite, which is among the highest PCE reported for a vacuum deposited perovskite system. The addition of higher Br fractions to blueshift the absorption onset for wide bandgap subcells introduces defects, as demonstrated by a reduction in the photoluminescence quantum efficiency (PLQE) and a higher Urbach energy, which is particularly exacerbated at 1.80 eV where substantial phase segregation readily occurs. We demonstrate that ethylenediammonium diiodide (EDAI) is an effective passivation agent for these evaporated perovskites, resulting in PLQEs enhanced by an order of magnitude. Applying the HTM and EDAI dual-interface treatment yields devices with a V_{OC} of 1.26 V for a 1.76 eV bandgap, which is 190 mV below the radiative limit and represents the lowest V_{OC} loss reported in evaporated WBG perovskite systems so far. Furthermore, we demonstrate the versatility of the EDAI passivation approach by applying it to solution-processed, narrow bandgap perovskite solar cells displaying a V_{OC} of 0.86 V based on MA-free, Pb/Sn absorbers with a bandgap of 1.28 eV. An EDAI-passivated 2-terminal tandem architecture combining the evaporated $\text{FA}_{0.7}\text{Cs}_{0.3}\text{Pb}(\text{I}_{0.64}\text{Br}_{0.36})_3$ perovskite with the solution-processed $\text{FA}_{0.75}\text{Cs}_{0.25}\text{Pb}_{0.5}\text{Sn}_{0.5}\text{I}_3$ perovskite results in a PCE of 24.1%, the highest for evaporation-based all-perovskite tandem solar cells. This result shows the potential of the scalable and industry-relevant evaporation technique for realising efficient and modular all-perovskite tandem solar cells.

5.2 Hole transporting/perovskite interface optimisation

5.2.1 Evaporated perovskite film quality

Defects at the perovskite-hole transporting layer interface are known to cause significant non-radiative losses in p-i-n devices,⁴² limiting their applicability for tandem architectures where high voltages are required. Al-Ashouri *et al.* reported that the non-radiative losses arising from the interface between perovskite and the typically employed poly[bis(4-phenyl)(2,4,6-trimethylphenyl)amine (PTAA) can be substantially reduced when replacing the latter by a self-assembled monolayer (SAM), MeO-2PAC or 2-PACz, leading to higher device V_{OC} .^{11,63} In order to explore this effect and optimize MA-free evaporated systems, we fabricate devices with an architecture consisting of ITO / HTM / perovskite (500 nm) / C60 (25 nm) / BCP (8 nm) / Cu. We initially employ our recently reported 3-source evaporation protocol¹⁸ (**Figure 5.1**) to deposit $FA_{0.7}Cs_{0.3}Pb(I_{0.9}Br_{0.1})_3$ absorbers (using FAI, PbI_2 and CsBr as evaporation sources) on different HTMs, namely 2-PACz, PTAA and MeO-2PAC, with the absorber exhibiting a bandgap of 1.62 eV extracted via the inflection point of an external quantum efficiency (EQE) measurement. Scanning electron microscopy (SEM, **Figure 5.2**) images do not show significant differences in surface morphology, suggesting that the perovskite growth is similar on these different organic layers. The perovskite grain sizes are about 100-300 nm with bright PbI_2 domains. To further understand the perovskite quality, we perform PLQE measurements which can reveal the radiative recombination processes. The PLQE of these samples shows that less non-radiative recombination occurs in the perovskite/MeO-2PACz structure, with it being a factor of 3.3 and 5 times higher than perovskite deposited on 2-PACz and PTAA, respectively (**Figure 5.3**). In XRD, we didn't see any obvious difference in perovskite crystallinity or phases on different HTMs (**Figure 5.3**).

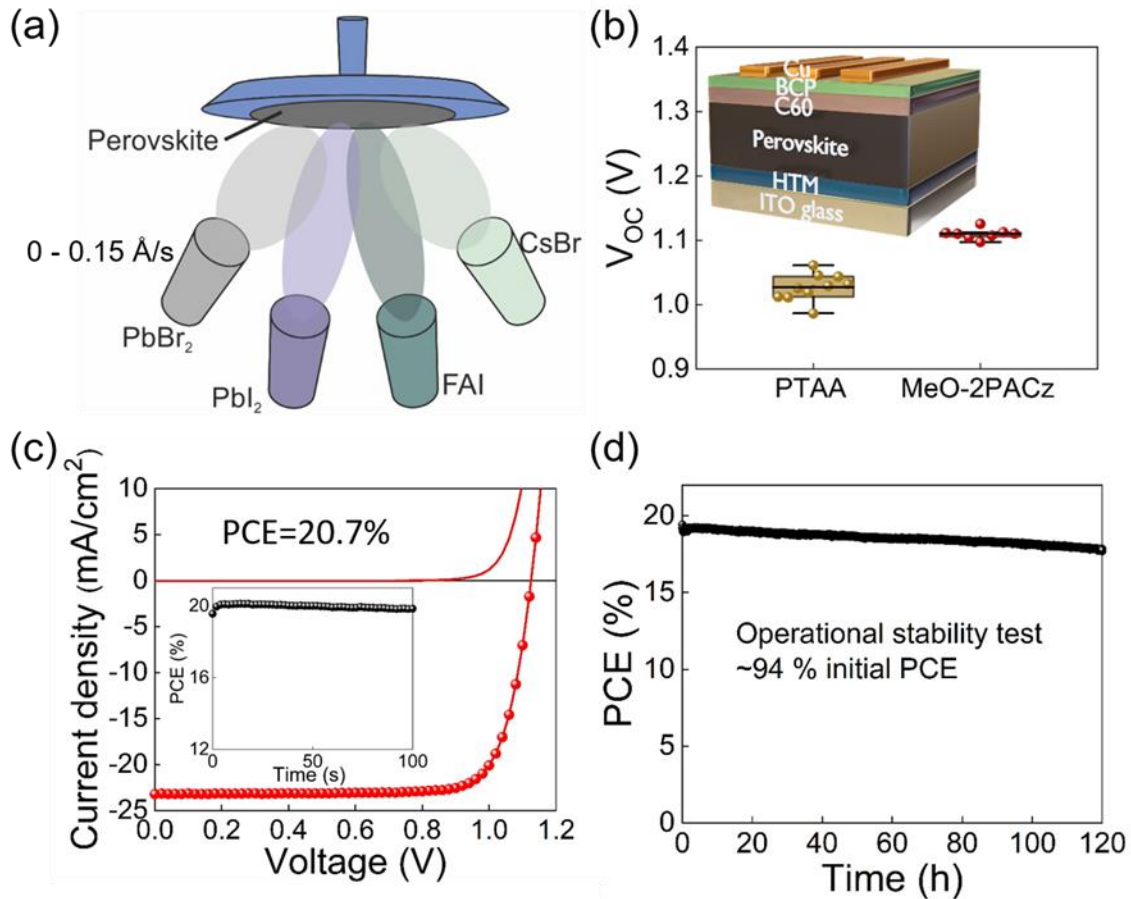


Figure 5.1. (a) Diagram of the thermal evaporation system where four sources (i.e. FAI, PbBr₂, PbI₂ and CsBr) are employed to deposit high quality FA_{0.7}Cs_{0.3}Pb(I_xBr_{1-x})₃ thin films. FAI, PbI₂ and CsBr evaporation rates are kept at 1, 0.6 and 0.1 Å/s, respectively, and the PbBr₂:PbI₂ deposition rate ratio varies to tune the bandgap. (b) Effect of different HTMs (i.e. PTAA, and MeO-2PACz) on the V_{OC} statistics of evaporated FA_{0.7}Cs_{0.3}Pb(I_{0.9}Br_{0.1})₃ perovskite solar cells (PbBr₂ rate is 0). Inset device architecture employed. The box/whisker plot contains the 1.5 interquartile range, the median value and data distribution from 8 devices. (c) J-V curve of the champion FA_{0.7}Cs_{0.3}Pb(I_{0.9}Br_{0.1})₃ perovskite solar cells (scan rate of 100 ms/V) with the inset showing a stabilised power output measurement. (d) Operational stability test of an encapsulated device at 0.94 V fixed bias under continuous 1 sun illumination.

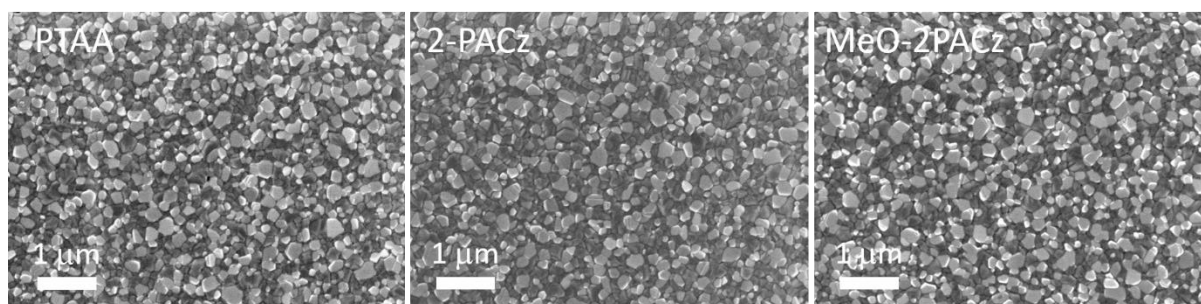


Figure 5.2. SEM comparison between evaporated perovskite ($\text{FA}_{0.7}\text{Cs}_{0.3}\text{Pb}(\text{I}_{0.9}\text{Br}_{0.1})_3$, 1.62 eV) film deposited on PTAA, 2-PACz or MeO-2PACz layers.

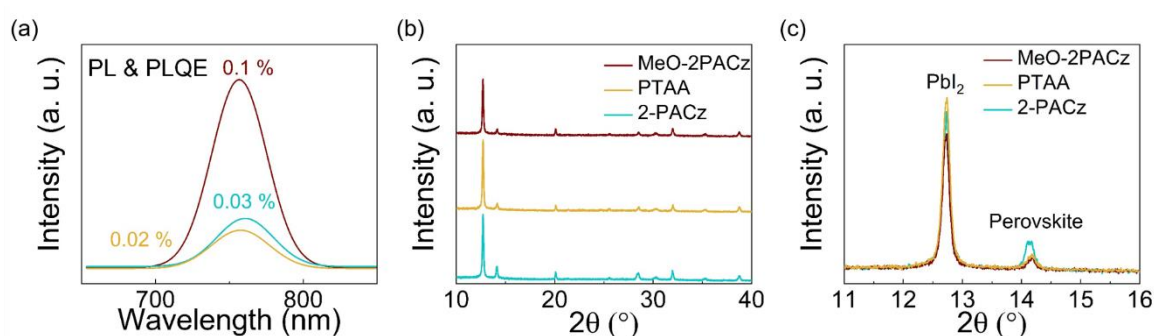


Figure 5.3. PL(QE) and XRD comparison of evaporated perovskite ($\text{FA}_{0.7}\text{Cs}_{0.3}\text{Pb}(\text{I}_{0.9}\text{Br}_{0.1})_3$, 1.62 eV) film on top of 2-PACz, MeO-2PACz or PTAA layers.

5.2.2 The effect of HTMs on solar cell performance

Figure 5.1b shows that the MeO-2PACz based devices display a substantially higher V_{OC} with less variation between devices (1.11 V on average) than the other HTMs (**Figure 5.4a**), with the trend consistent with higher PLQE and in different batches (Indeed, the devices based on 2-PACz show s-kinks in the current-voltage (J-V) curves, resulting in very low performance (**Figure 5.4b**). Though the batch 2 is better than batch 1 (experimental variation), the trend of different HTMs in terms of device V_{OC} is consistent.

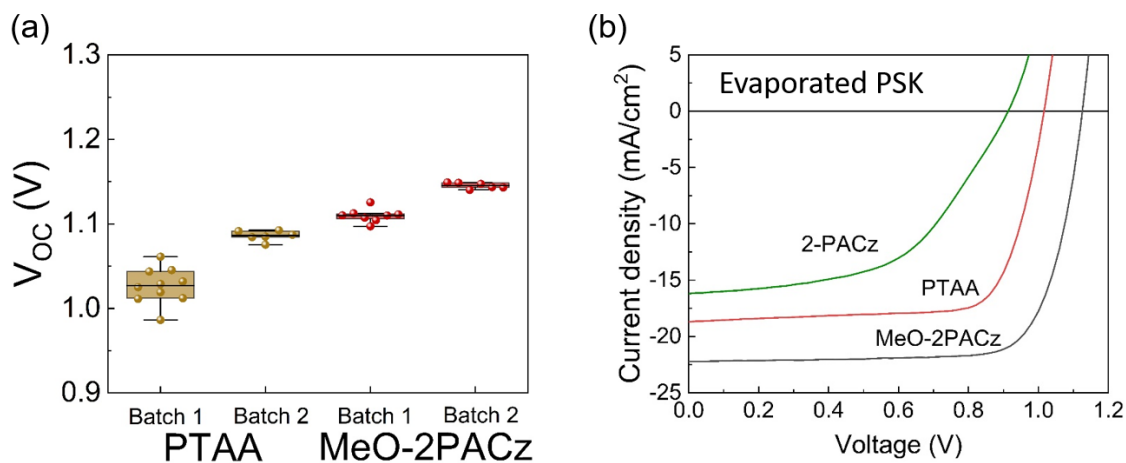


Figure 5.4. (a) The V_{OC} statistics of evaporated $\text{FA}_{0.7}\text{Cs}_{0.3}\text{Pb}(\text{I}_{0.9}\text{Br}_{0.1})_3$ perovskite solar cells (PbBr₂ rate is 0) on PTAA or MeO-2PACz from 2 batches fabrication. The box/whisker plot contains the 1.5 interquartile range, the median value. (b) JV curves of evaporated perovskite (1.62 eV, $\text{FA}_{0.7}\text{Cs}_{0.3}\text{Pb}(\text{I}_{0.9}\text{Br}_{0.1})_3$ perovskite) on PTAA, MeO-2PACz and 2-PACz HTMs (scan rate, 100 ms/V).

This result is in quite stark contrast to the high performance achieved in solution-processed systems on 2-PACz, even though we employ the same deposition parameters for all HTMs.^{11,63} We have also fabricated solution-process perovskite films with a composition of $\text{FA}_{0.7}\text{Cs}_{0.3}\text{Pb}(\text{I}_{0.8}\text{Br}_{0.2})_3$, on 2-PACz or MeO-2PACz and measured their device performance. This result shows that 2-PACz device demonstrates slightly better device PCE, compared to the MeO-2PACz counterpart, consistent with literature. We note that re-optimisation of different evaporated perovskite compositions and deposition parameters might yield improved performance on 2PACz. Our champion device reaches a PCE of 20.7% when the evaporated perovskite is deposited on MeO-2PACz (**Figure 5.1c**), which is the highest MA-free perovskite solar cells reported for multisource evaporation. Further, the device retains 90% of its initial performance after 120 hours under one sun illumination and a fixed bias at maximum power point with no substrate temperature control during the measurement (**Figure 5.4d**). We find that this front interface optimisation is critical to ensure maximised voltages for subsequent integration of the cells as building blocks in tandem devices

5.3 Composition engineering of evaporated WBG perovskite films

5.3.1 Structure, morphology and bandgap

To widen the bandgap of the perovskite for its use as front subcell in a tandem device, we add PbBr_2 as a fourth evaporation source to tune the bandgap by employing $\text{PbBr}_2:\text{PbI}_2$ rate ratios from 0.11 to 0.318. XRD patterns shown in **Figure 5.5a** confirm Br incorporation into the perovskite structure as the PbBr_2 evaporation rate is increased, with the (011) perovskite peak shifting to higher 2θ as a consequence of a smaller d-spacing. The full XRD patterns are shown in **Figure 5.1 (b)**. We estimate the stoichiometry of the evaporated perovskite films using XRD across a range of control films to generate a calibration curve in **Figure 5.5c** and display the resulting chemical formulae in **Table 5.1**. The lines are extracted from our previous publication (also see **Chapter 4**),¹³⁵ where we prepared a series of perovskite compositions based on solution-process. We measured the samples of $\text{FA}_{0.9}\text{Cs}_{0.1}\text{Pb}(\text{I}_{0.9}\text{Br}_{0.1})_3$, $\text{FA}_{0.8}\text{Cs}_{0.2}\text{Pb}(\text{I}_{0.8}\text{Br}_{0.2})_3$, $\text{FA}_{0.7}\text{Cs}_{0.3}\text{Pb}(\text{I}_{0.7}\text{Br}_{0.3})_3$ and $\text{FA}_{0.54}\text{Cs}_{0.46}(\text{I}_{0.7}\text{Br}_{0.3})_3$ with XRD and deconvolute the effect of A or X site on lattice constant shift.² The black line, red line and green line represent the 2θ shift based on the effect of Cs, Br and Cs/Br incorporated in perovskite structure. The blue dots are the lattice constant of evaporated perovskite films in this work with different PbBr_2 to PbI_2 ratio. With this trend, we assign the evaporated perovskite composition. We determine the corresponding bandgaps as the inflection point of the first derivative in the EQE spectrum (**Figure 5.5d**), observing that the bandgap vary between 1.62 to 1.80 eV (**Table 5.1**) confirming the increase in bandgap upon additional Br incorporation.

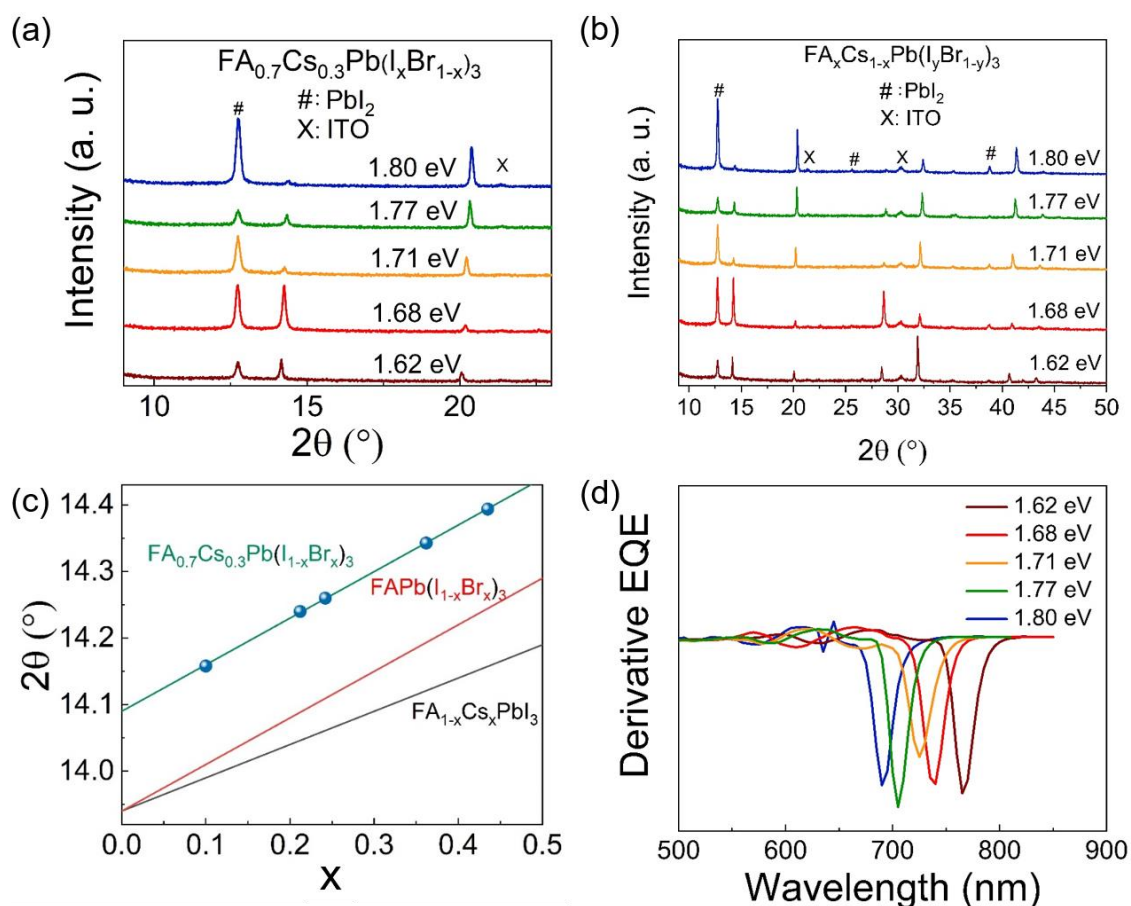


Figure 5.5. (a) Zoom in and (b) full region of XRD pattern of evaporated $\text{FA}_{0.7}\text{Cs}_{0.3}\text{Pb}(\text{I}_x\text{Br}_{1-x})_3$ thin films deposited on MeO-2PACz/ITO showing different bandgaps: 1.62 eV (dark red curve), 1.68 eV (red), 1.71 eV (orange), 1.77 eV (green) and 1.80 eV (blue). (c) The evolution of lattice constant versus perovskite composition of $\text{FA}_{1-x}\text{Cs}_x\text{PbI}_3$ (black), $\text{FAPb}(\text{I}_{1-x}\text{Br}_x)_3$ (red) and $\text{FA}_{0.7}\text{Cs}_{0.3}\text{Pb}(\text{I}_{1-x}\text{Br}_x)_3$ (green). (d) The first derivative of EQE to extract the bandgap of the perovskites in solar cells.

Top view SEM images (**Figure 5.6**) show perovskite grain sizes in the range of 100 to 300 nm for all compositions as well as the presence of PbI_2 evidenced by bright clusters, consistent with the PbI_2 signal observed in the XRD patterns.¹²⁴ In a previous report, we showed that the presence of excess PbI_2 enhances the optoelectronic properties of these vacuum deposited perovskites and their stability when exposed to ambient conditions.^{121,122,135} To understand this observation and give further insight into the chemical composition, we (Miguel Anaya and Kyle Frohna, conducted this measurement) perform synchrotron-based nano-X-ray fluorescence (nXRF) measurements on our samples. The nanoprobe nature of the technique

allows us to extract Br:Pb maps with a spatial resolution of ~ 50 nm (**Figure 5.7**). Evaporated perovskites with bandgaps between 1.62 eV and 1.77 eV show excellent film homogeneity, which is particularly striking when comparing to a standard solution-processed ‘triple-cation’ $\text{FA}_{0.79}\text{MA}_{0.16}\text{Cs}_{0.05}\text{Pb}(\text{I}_{0.83}\text{Br}_{0.17})_3$ perovskite film (bandgap of 1.62 eV), where we have found that the compositional heterogeneity is related to defects and carrier funnelling.^{130,144} Nevertheless, the 1.80 eV-bandgap evaporated film exhibits several areas with Br-rich clusters, suggesting a suboptimal intermixing of compounds in samples with the highest explored Br content, which is known to drastically hamper stability.¹⁴⁵

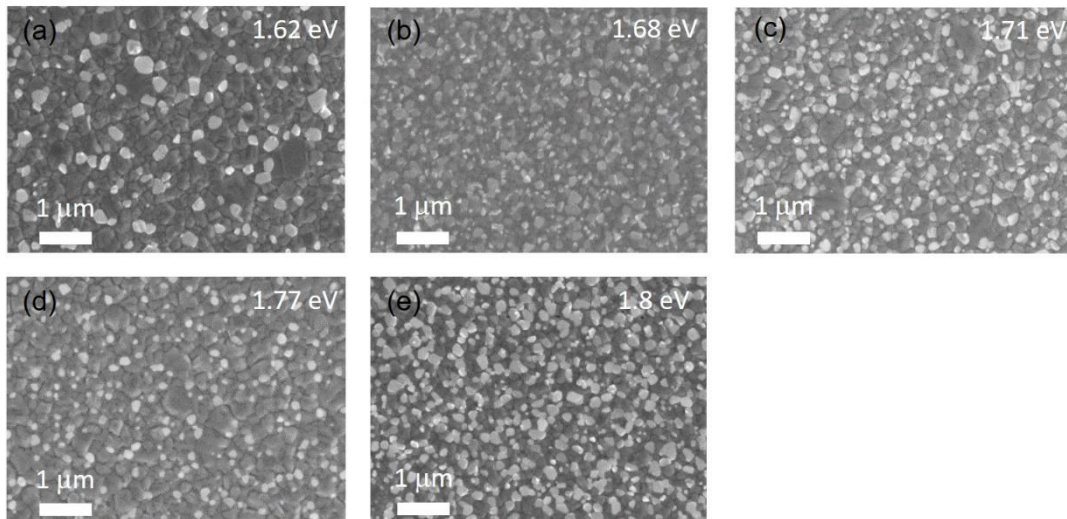


Figure 5.6. The SEM morphology of different bandgap evaporated perovskite ($\text{FA}_{0.7}\text{Cs}_{0.3}\text{Pb}(\text{I}_{1-x}\text{Br}_x)_3$) on MeO-2PACz/ITO.

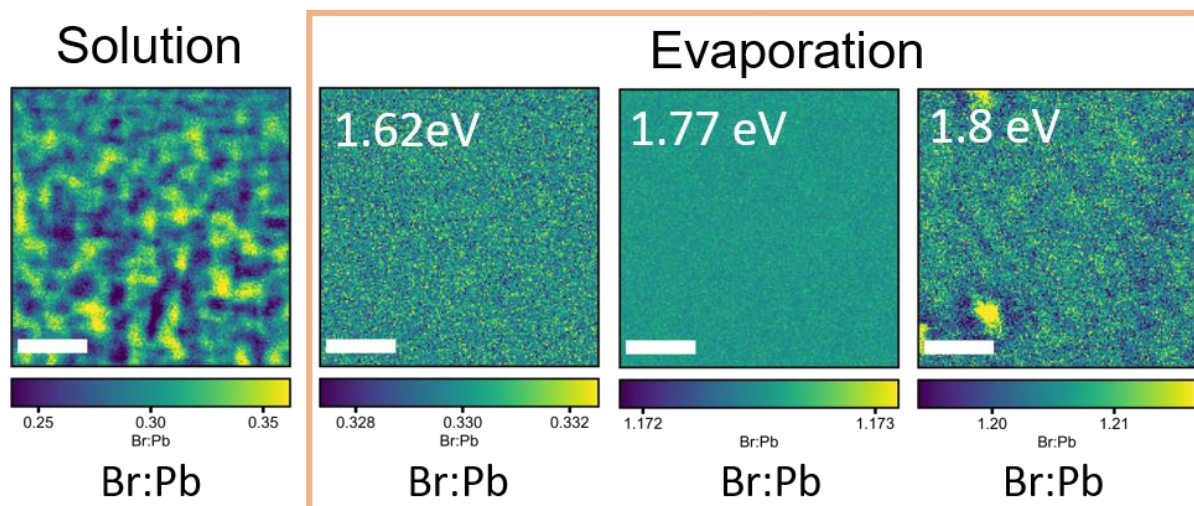


Figure 5.7. Synchrotron-based nXRF mapping for solution-processed triple-cation perovskite ($\text{Cs}_{0.05}(\text{FA}_{0.83}\text{MA}_{0.17})_{0.95}\text{Pb}(\text{I}_{0.83}\text{Br}_{0.17})_3$) and evaporated perovskites ($\text{FA}_{0.7}\text{Cs}_{0.3}\text{Pb}(\text{I}_{1-x}\text{Br}_x)_3$) with bandgaps of 1.62 eV, 1.77 eV and 1.80 eV. The Br:Pb mapping is shown in here. Scale bars are of 2 μm . Collaborators, Dr. Miguel Anaya and Kyle Frohna, conducted this measurement.

5.3.2 Photoluminescence study on perovskites with different bandgaps

Steady-state photoluminescence (PL) measurements also reflect the bandgap variation (**Figure 5.8**), with a clear tunability in the PL peak position from 1.62 to 1.80 eV. A major issue hindering the applicability of WBG perovskite is their phase instability under illumination. To evaluate this, we use a 520-nm continuous-wave laser at 5 suns intensity ($300 \text{ mW}/\text{cm}^2$) to excite encapsulated samples and monitor their PL over time. Samples with bandgaps in the range between 1.62 and 1.77 eV show excellent emission stability, with no significant changes in their PL spectra over time at these photon doses. In contrast, severe phase segregation occurs in the 1.80 eV perovskite during the first minutes under illumination, (**Figure 5.8b-d**), potentially linked to the substantial halide heterogeneity observed by nXRF. The low emission PL peak in here is corresponding to the phase segregation, the photocarriers tunnel to the iodide-rich domain for recombination, which reduce the V_{OC} output. Evaluation of the charge carrier lifetime by time-resolved photoluminescence (TRPL) with 450 nm pulsed laser indicates lower optoelectronic quality in the wide bandgap perovskites when compared with the standard 1.62 eV counterparts (**Figure 5e**). Both samples show a common quick decay in

the first 40 ns attributed to quenching by the contacts. The subsequent PL decay of the 1.77 eV evaporated perovskite deposited on top of the MeO-2PACz/ITO contact shows faster (84 ns) mono-exponential decay with respect to that of the control 1.62 eV sample (394 ns),^{41,146} where mono-exponential decays are expected in experiments with such low carrier densities.¹⁸ We attribute the faster decay associated with Shockley–Read–Hall (SRH) recombination to an increase in the trap density when we replace fractions of I by Br in the perovskite composition, though we note the carrier densities may differ due to different quenching efficiencies at the contacts between the samples and this may in turn influence the subsequent lifetimes. The summarised peak position change of these perovskite samples is shown in **Figure 5.8f** where the peak positions of 1.62 eV and 1.77 eV perovskite do not show obvious shift and the peak position of 1.8 eV perovskite counterpart reveals the PL shift from 690 nm to 770 nm.

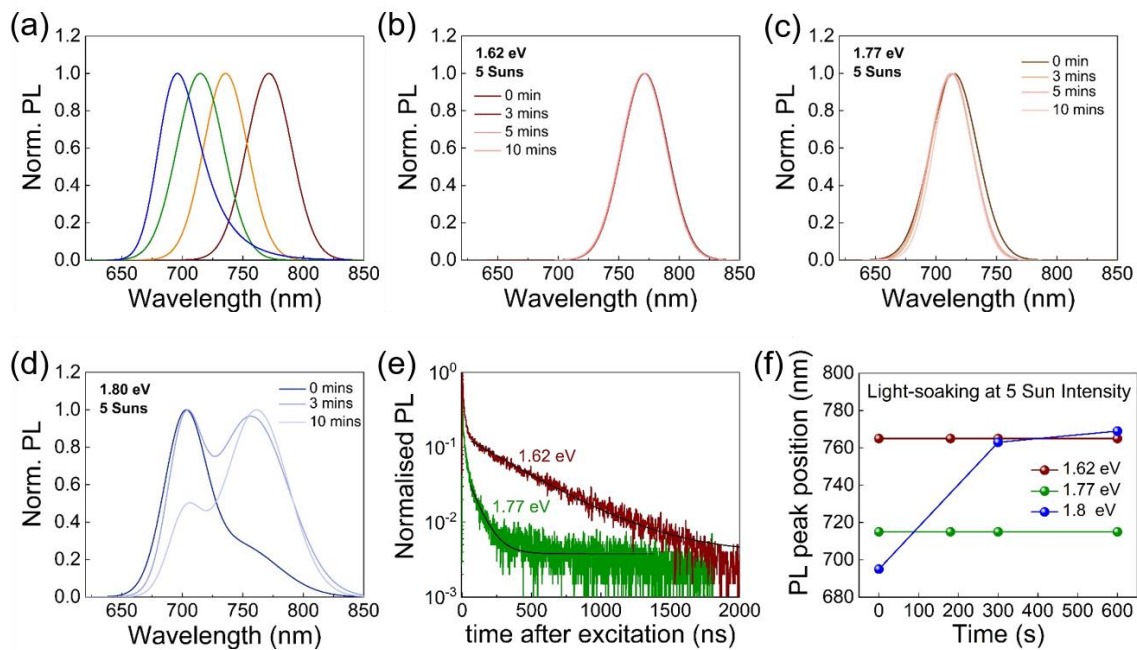


Figure 5.8. (a) normalised PL spectra of a series of evaporated $\text{FA}_{0.7}\text{Cs}_{0.3}\text{Pb}(\text{I}_x\text{Br}_{1-x})_3$ thin films deposited on MeO-2PACz/ITO showing different bandgaps: 1.62 eV (dark red curve), 1.71 eV (orange), 1.77 eV (green) and 1.80 eV (blue). PL peak evolution over time of (b) 1.62 eV, (c) 1.77 eV and (d) 1.8 eV evaporated perovskite films under continuous illumination at 5 Suns (300 mW/cm^2) with a 520 nm laser. (e) Time-resolved photoluminescence decays for 1.62 eV and 1.77 eV evaporated perovskite films on MeO-2PACz excited with a 450 nm laser at a fluence of $8.5 \text{ nJ/cm}^2/\text{pulse}$. Samples were excited and light collected from the top side. We attribute the fast decay during the first 40 ns results from the ITO/ MeO-2PACz quenching. (f) summarised PL peak position evolution of evaporated perovskite films with different bandgaps during light soaking with 5 sun intensity.

5.3.3 Single junction solar cell performance

We fabricate single-junction solar cells based on the different perovskite compositions to evaluate their performance when integrated into working devices. We use the device architecture, ITO/MeO-2PACz/evaporated-perovskite/C60/BCP/Cu and show the J-V curves in **Figure 5.9a** and EQE spectra in **Figure 5.9b**. We used MeO-2PACz instead of PTAA as the former shows less non-radiative recombination loss with perovskite film. These measurements demonstrate efficient photocarrier-to-electron conversion for all devices, and a blue-shifted absorption onset upon Br addition to the perovskite composition. The device V_{OC} monotonically increases for higher perovskite bandgaps (**Figure 5.9c**), with the highest V_{OC} of 1.24 V observed for the 1.77 eV evaporated perovskite (**Table 5.1**). There is no further voltage gain for a device based on a 1.80 eV bandgap absorber. We associate this V_{OC} saturation to the serious phase segregation (**Figure 5.8**), which produces low gap clusters onto which charge carriers funnel, confirming 1.77 eV as our optimal wide bandgap composition.

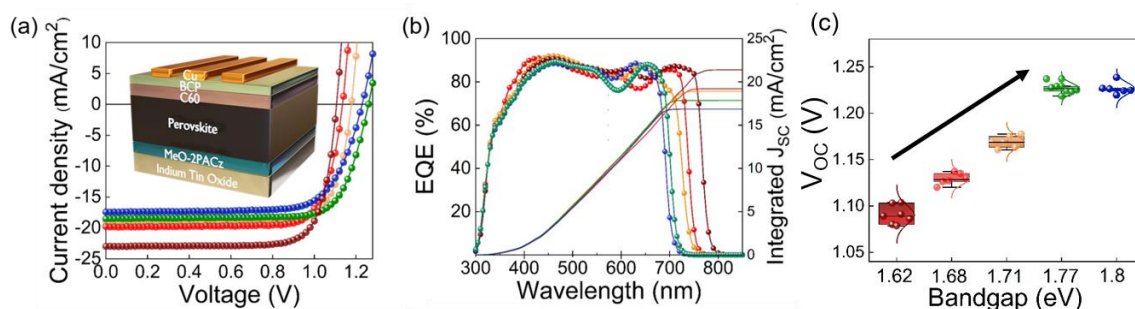


Figure 5.9. (a) J-V curves at AM1.5G illumination of evaporated solar cells based on perovskites with different bandgaps ($\text{FA}_{0.7}\text{Cs}_{0.3}\text{Pb}(\text{I}_x\text{Br}_{1-x})_3$): 1.62 eV (dark red curve), 1.68 eV (red), 1.71 eV (orange), 1.77 eV (green) and 1.80 eV (blue). See Table 1 for compositions. EQE spectra and the corresponding integrated J_{sc} (b) and the V_{OC} statistics (c) for the series of devices are shown in panel (a). The box/whisker plots contain the 1.5 interquartile range, the median value, and the data distribution of the V_{OC} .

Table 5.1. Champion PV performance metrics for evaporated perovskite solar cells of the different bandgap.

Bandgap (eV)	V _{OC} (V)	J _{SC} (mA/cm ²)	FF (%)	PCE (%)	Composition	PbBr ₂ rate (Å/s)
1.62	1.11	-23.0	78.70	20.0	FA _{0.7} Cs _{0.3} Pb(I _{0.9} Br _{0.1}) ₃	0
1.68	1.14	-19.8	78.50	17.6	FA _{0.7} Cs _{0.3} Pb(I _{0.78} Br _{0.21}) ₃	0.06
1.71	1.18	-19.1	78.39	17.7	FA _{0.7} Cs _{0.3} Pb(I _{0.75} Br _{0.24}) ₃	0.1
1.77	1.24	-18.5	69.22	15.9	FA _{0.7} Cs _{0.3} Pb(I _{0.64} Br _{0.36}) ₃	0.127
1.80	1.23	-17.4	72.92	15.6	FA _{0.7} Cs _{0.3} Pb(I _{0.56} Br _{0.44}) ₃	0.15

To gain further understanding on our device losses, we calculate the estimated $V_{OC,rad}$ based on the Urbach fit of EQE spectra to obtain the extended EQE tail for dark current calculation (**Figure 5.10** see Experimental Methods **section 3.3.9**) and represent the V_{OC} loss associated with the different evaporated composition in **Figure 5.9**.^{44,102} We observe that the V_{OC} loss increases from 196 mV to 251 mV when we tune the perovskite bandgap from 1.62 eV to 1.80 eV. The Urbach energy also rises with the bandgap energy from 13.5 meV to 19.0 meV. These observations indicate higher electronic disorder upon Br addition and are consistent with the increased trap densities revealed from the PL measurements.¹³⁰ These results suggest that the evaporated FA_{0.7}Cs_{0.3}Pb(I_{0.64}Br_{0.36})₃ perovskite with a 1.77 eV bandgap is our best candidate for use as front absorber in a tandem architecture with sufficient photo-stability and remarkable, though still suboptimal, V_{OC} .

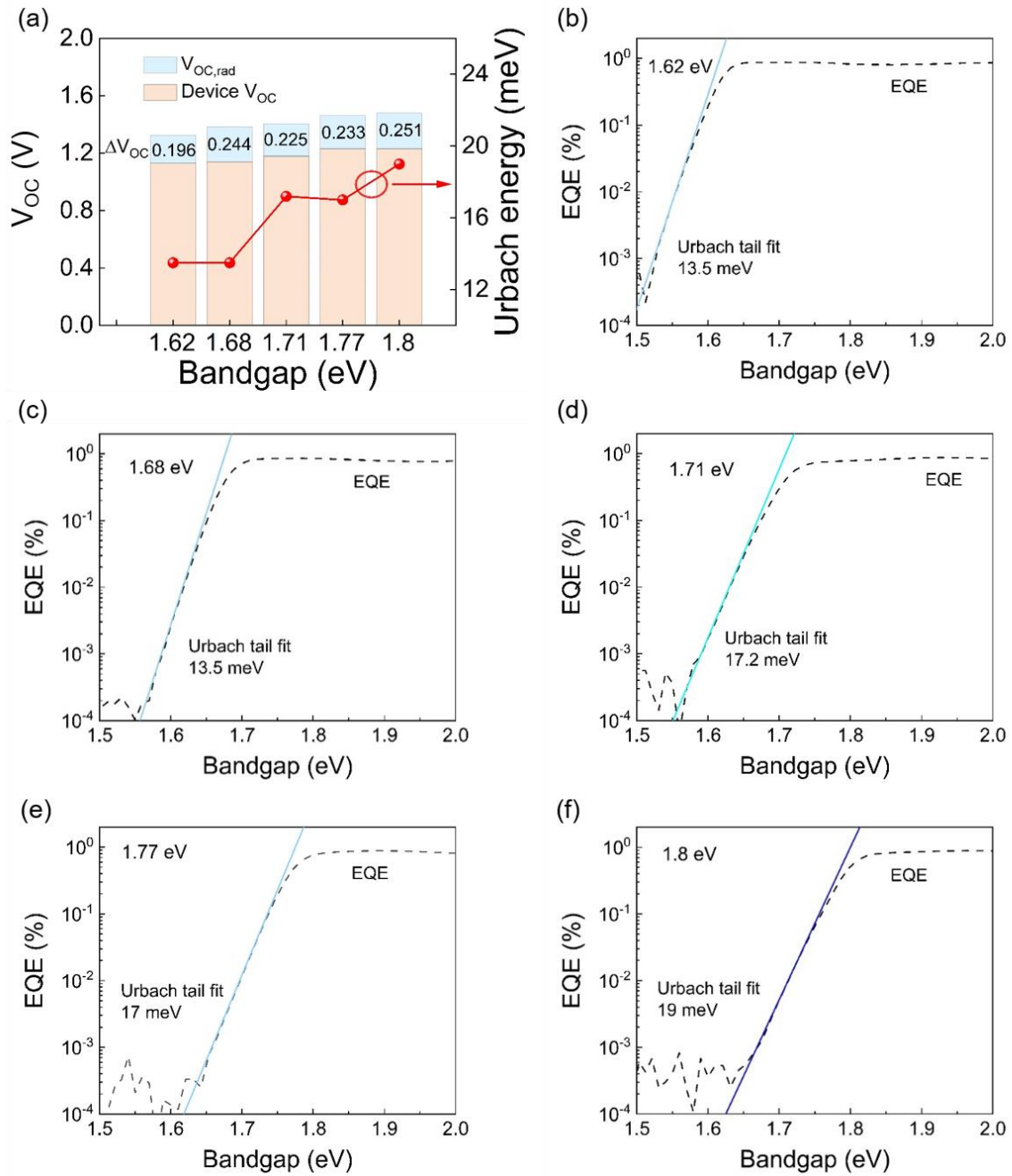


Figure 5.10. (a) Measured V_{OC} , calculated V_{OC} loss and Urbach energy extracted from EQE for champion devices based on different bandgap, evaporated perovskite samples ($FA_{0.7}Cs_{0.3}Pb(I_xBr_{1-x})_3$). (b)-(f) the Urbach tail fit for EQE spectra of different perovskite solar cells.

5.4 Perovskite/electron transport layer interface optimisation

5.4.1 Surface passivation of EDAI treatment on WBG perovskite film

With the losses associated with the front perovskite interface minimised by employing an HTM based on MeO-2PACz, we now focus on overcoming the losses arising from the rear perovskite interface. To this end, we passivate the 1.77 eV evaporated $\text{FA}_{0.7}\text{Cs}_{0.3}\text{Pb}(\text{I}_{0.64}\text{Br}_{0.36})_3$ perovskite using a post-treatment based on spin-coating a layer of EDAI (table 5.2) in mixed isopropanol (IPA) and toluene.¹⁴⁷ The EDAI is prepared by adding 1 mg of the material in a mixed IPA and toluene solvents with a 1:1 volume ratio and the solution is stirred for 2 hours. The EDAI is not fully dissolved in the mixed solvent; therefore, we use a 0.22 μm filter to remove the residual EDAI powder before use. We observe an order-of-magnitude improvement in PLQE from 0.01 % to 0.1 % after surface passivation of the thin film with EDAI, which corresponds to a large reduction of non-radiative losses (**Figure 5.11**). We note that PLQE measurements are taken on samples deposited on MeO-2PACz/glass to ensure the perovskite formation is relevant to devices, and that SEM images do not show obvious surface roughening which could otherwise promote better light outcoupling (**Figure 5.12a-b**). We then thermally evaporate C_{60} on top of the perovskite to have a complete device stack and observe the PLQE drops to 0.02 %. On the contrary, the PLQE of the device stack without EDAI treatment is below our detection limit ($\ll 0.005\%$), proving the passivation effect of EDAI (**Figure 5.13c**). This result is consistent with previous reports where interfacial losses between perovskite and C_{60} are severe.¹⁴⁸ XRD measurements show incorporation of iodide into the perovskite upon EDAI passivation with the peak shift (**Figure 5.13d-e**), while no low angle peak is observed which discards significant formation of 2D perovskite as reported by others.¹⁴⁹ Finally, TRPL measurements show prolonged charge carrier lifetimes in the EDAI-passivated sample (**Figure 5.13f**), strengthening the viability of the approach to increase charge carrier diffusion lengths in eventual devices under operation.¹⁵⁰

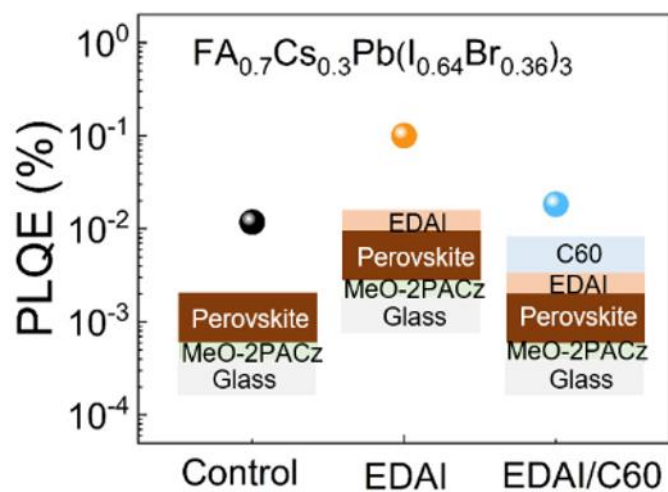


Figure 5.11. PLQE values for FA_{0.7}Cs_{0.3}Pb(I_{0.64}Br_{0.36})₃ (1.77 eV) evaporated perovskite film, with EDAI treatment and with EDAI treatment plus C60 contact layer.

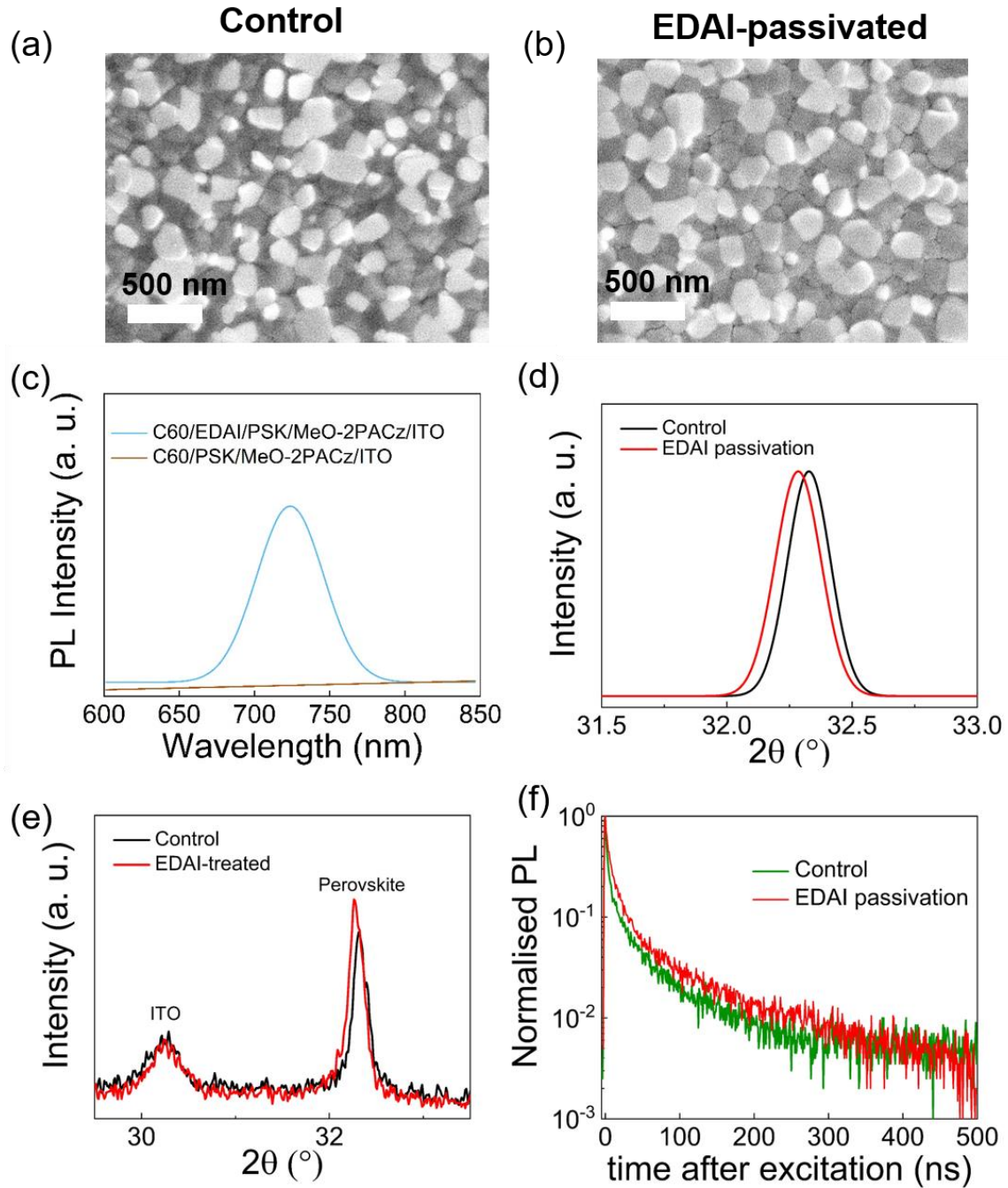


Figure 5.12. (a-b) SEM image of 1.77 eV bandgap evaporated perovskite with $\text{FA}_{0.7}\text{Cs}_{0.3}\text{Pb}(\text{I}_{0.64}\text{Br}_{0.36})_3$ composition before and after EDAI passivation. (c) PL spectra of full stack evaporated perovskite $\text{FA}_{0.7}\text{Cs}_{0.3}\text{Pb}(\text{I}_{0.64}\text{Br}_{0.36})_3$ with and without EDAI passivation, showing the outstanding passivation effect. (d-e) XRD of 1.77 eV evaporated perovskite film before and after EDAI passivation. The ITO substrate peak is shown as a reference peak. (f) TRPL of evaporated perovskite films ($\text{FA}_{0.7}\text{Cs}_{0.3}\text{Pb}(\text{I}_{0.64}\text{Br}_{0.36})_3$) with and without EDAI passivation on MeO-2PACz/ITO glass. The measurement was conducted with a 448.4 nm pulsed laser and an excited density of 8.5 nJ/cm²/pulse.

5.4.2 Solar cell performance of EDAI treatment on WBG perovskite film

We fabricate solar cells (based on the device architecture in **Figure 5.9**) where the 1.77 eV evaporated perovskite is passivated with EDAI and show the JV curves in **Figure 5.13a**. We observe a substantial improvement in V_{OC} and Fill Factor (FF) with respect to the unpassivated sample. In particular, the V_{OC} reaches 1.26 V, which is the highest value reported so far to the best of our knowledge in a p-i-n, MA-free perovskite solar cell processed by vapour deposition.^{13,93,143,151–162} The champion device is shown in **Table 5.3** with a PCE of 17.8%. In **Figure 5.13b**, we survey the literature, including solution-process and vacuum deposited WBG perovskite (>1.7 eV) film for inverted solar cells with MA-free composition. The 90% and 100% SQ limit lines are included in the figure. We note that the perovskite bandgap slightly reduces from 1.77 eV to 1.76 eV as a result of iodine incorporation upon EDAI passivation (**Figure 5.14a-b**), consistent with our XRD results. Further analysis of the EQE curves shows a concomitant reduction in Urbach energy from 17.0 to 15.5 meV (**Figure 5.14c**). The V_{OC} loss after EDAI-treated devices reduces by around 40 mV based on the $V_{OC, rad}$ calculation (see Chapter 3 for method). Interestingly, this number is close to the average V_{OC} gain from J-V scans.

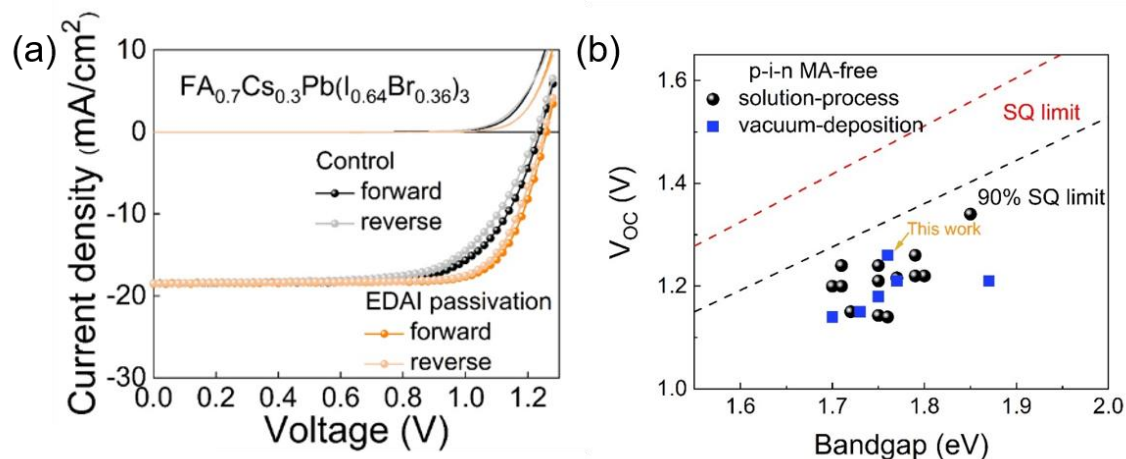


Figure 5.13. (a) J-V curves for control and EDAI-passivated $FA_{0.7}Cs_{0.3}Pb(I_{0.64}Br_{0.36})_3$ based solar cell in the dark (no symbols) and under 1 sun AM 1.5 G illumination (line and symbols). See device parameters in **Table 5.2**. (b) Literature survey of V_{OC} of solution-process or vacuum deposited wide bandgap (>1.7 eV) film perovskite solar cells with MA-free composition.

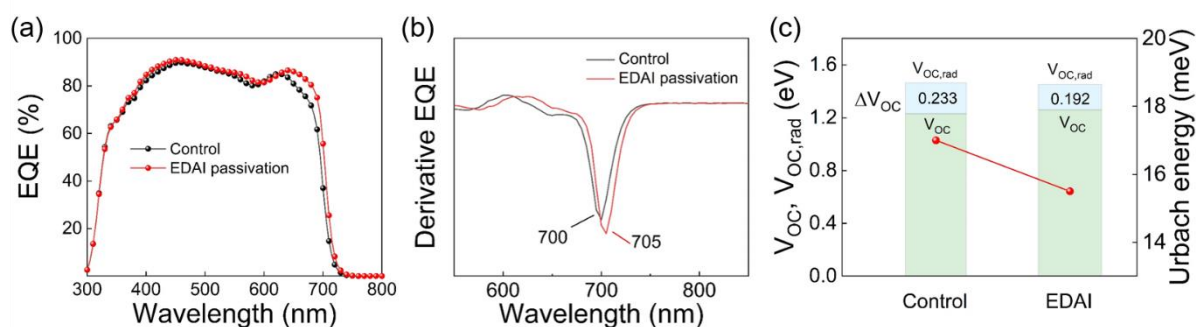


Figure 5.14. (a) EQE of 1.77/1.76 eV perovskite ($\text{FA}_{0.7}\text{Cs}_{0.3}\text{Pb}(\text{I}_{0.64}\text{Br}_{0.36})_3$) solar cells with and without EDAI passivation. (b) the first derivative of EQE spectra 1.77/1.76 eV perovskite solar cells with and without EDAI passivation to show the bandgap shift after passivation. (c) The measured V_{OC} , estimated $V_{\text{OC,rad}}$ and Urbach energy of wide gap perovskite solar cells ($\text{FA}_{0.7}\text{Cs}_{0.3}\text{Pb}(\text{I}_{0.64}\text{Br}_{0.36})_3$) with and without EDAI passivation. The left axis is showing the V_{OC} and $V_{\text{OC,rad}}$ and the right axis is showing the Urbach energy.

Table 5.2 Chemical structure of EDAI.

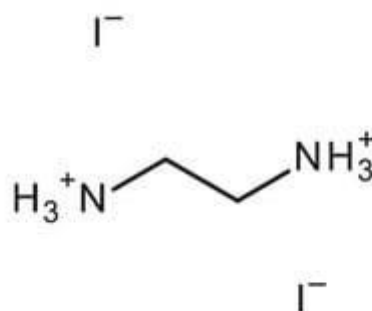


Table 5.3. Champion PV performance metrics for evaporated WBG (1.77 eV) perovskite solar cells with and without EDAI treatment.

WBG (1.77 eV/1.76 eV) perovskite solar cells					
	V_{OC}	J_{SC} (mA/cm^2)	FF	PCE	V_{OC} loss
	(V)		(%)	(%)	(mV)
Control	1.24	-18.5	69.7	16.0	230

EDAI-treated	1.26	-18.5	76.5	17.8	190
--------------	------	-------	------	------	-----

We also show the batch-to-batch variation of control and EDAI-passivated solar cells in **Figure 5.15** and observe a 1.4% absolute increase in average PCE, demonstrating the reproducibility of EDAI passivation.

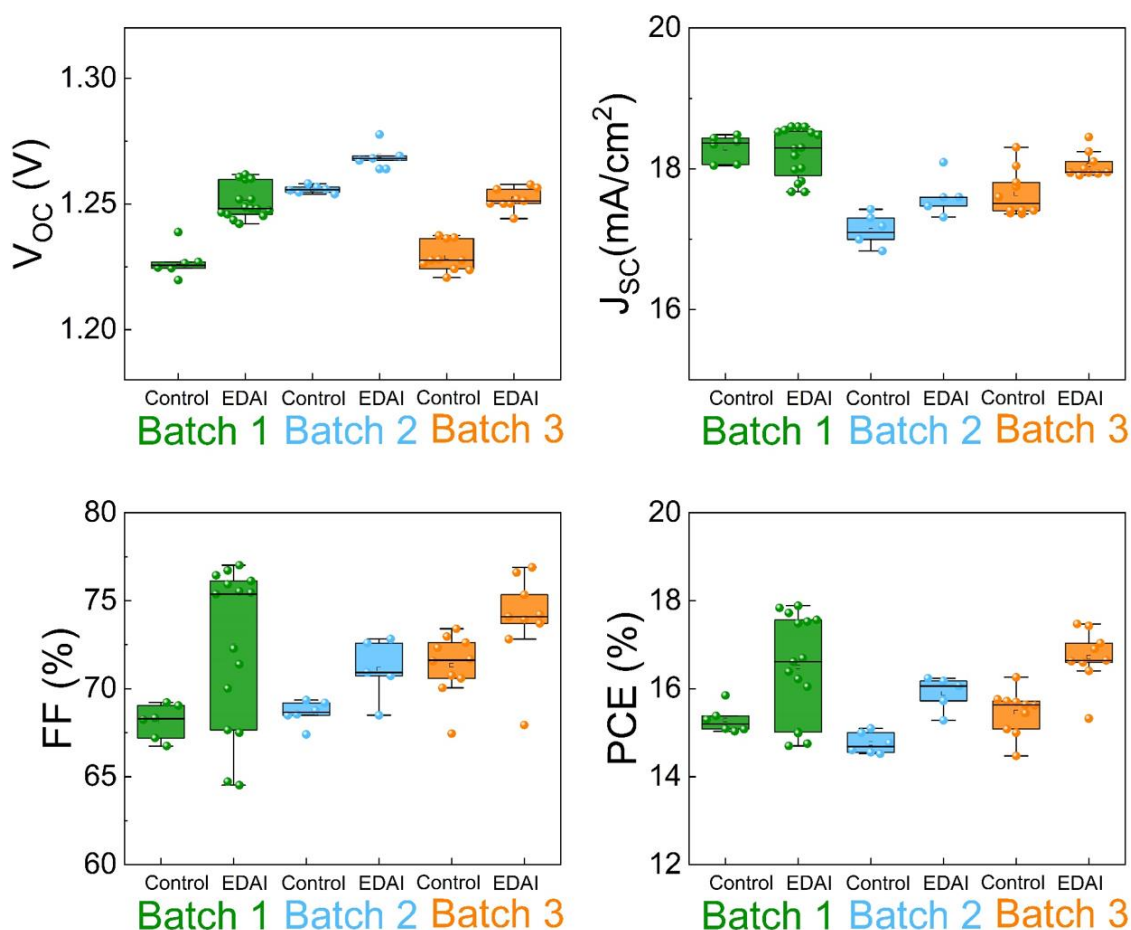


Figure 5.15. The batch-to-batch variation of V_{OC} , J_{sc} , FF and PCE with and without EDAI passivation of evaporated perovskite solar cell with 1.77 eV ($FA_{0.7}Cs_{0.3}Pb(I_{0.64}Br_{0.36})_3$).

5.4.3 Performance loss analysis in WBG solar cells

Figure 5.16. shows a comparison between the quasi-Fermi level splitting value extracted from PLQE data (see **section 3.3.2** for details on the calculations) and the actual device V_{OC} for both

the control and the passivated sample. A difference between those values relates to the relative importance of intrinsic perovskite non-radiative recombination processes and the effect of the additional interface introduced by the C_{60} layer with energetic offsets.¹⁶³ To have a better understanding of the passivation effect on the FF, we conduct a light intensity-dependent measurement of the V_{OC} and extract the ideality factor. Using these data to extract pseudo-JV curves,¹⁶⁴ we deconvolute the effect of charge transport and non-radiative losses within the devices, showing 79.0 % and 85.5% FF when there is no charge transport loss. Figure 4e summarises the results, highlighting the reduction in the non-radiative losses for the EDAI-passivated samples. In contrast, we have identified an absolute 10% FF reduction from charge transport losses in both control and EDAI passivated samples, indicating that further optimisation to find ideal contact layers is still required. The EDAI passivation strategy also better stabilises the device V_{OC} under light soaking compared to the unpassivated control

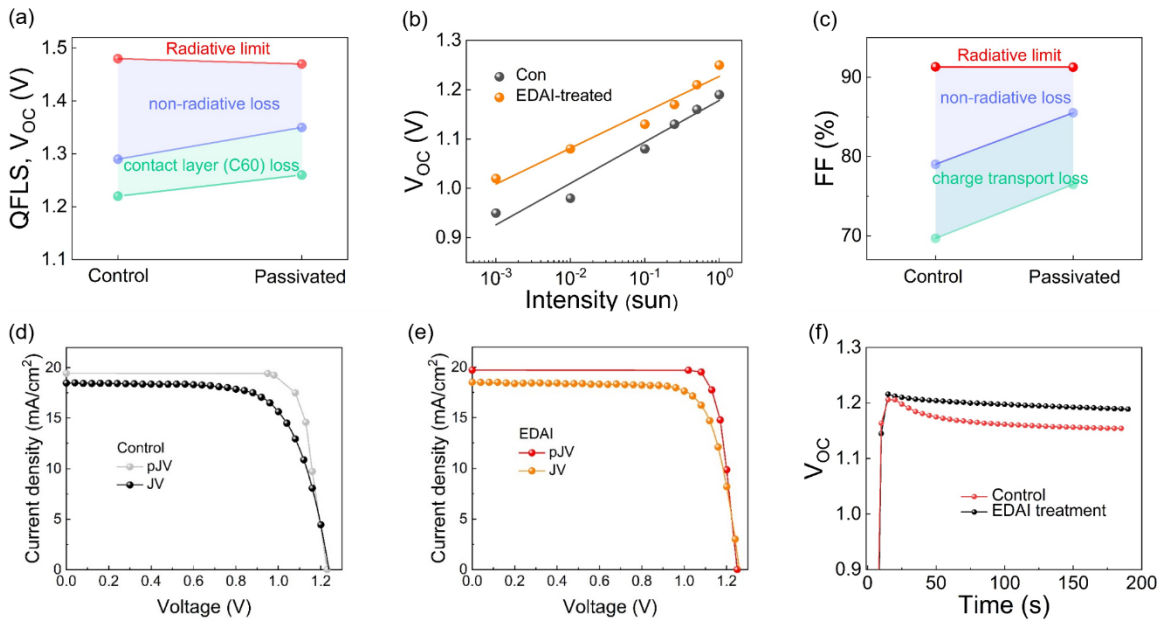


Figure 5.16. (a) Radiative limit, pseudo (non-radiative loss) from PLQE measurement and experimental values of the V_{OC} (QFLS) (b) V_{OC} as a function of incident light intensity, showing an ideal factor of 1.46 and 1.27, (c) FF calculation for control and EDAI-treated devices (d) and (e) The pseudo-JV curve measurement of control and EDAI-treated ($\text{FA}_{0.7}\text{Cs}_{0.3}\text{Pb}(\text{I}_{0.64}\text{Br}_{0.36})_3$) perovskite solar cells. In here, we set the current density value to 95% of the radiative limit at 1 sun illumination. (f) V_{OC} tracking under a function of time under AM 1.5 G illumination for control and EDAI-treated devices. The samples are evaporated perovskite solar cell with a composition of $\text{FA}_{0.7}\text{Cs}_{0.3}\text{Pb}(\text{I}_{0.64}\text{Br}_{0.36})_3$.

5.5 Narrow bandgap perovskite for all-perovskite tandem solar cells

For all-perovskite tandem solar cells, numerous studies have been working on NBG Pb-Sn cells and the interlayers.^{17,93,155,158,159,165,166} Several reports have indicated that the Sn²⁺ oxidation, either with extrinsic oxygen or during the film formation processing (solvent effect and/or non-uniform nucleation) is detrimental to optoelectronic properties,^{167,168} therefore, additives or dopants have been incorporated to improve the Pb-Sn perovskite quality^{56,57}. Surface passivation treatments are another popular strategy for defect reduction to enhance device performance. To date, state-of-the-art all perovskite tandem solar cells reported by Xiao et al. use zwitterionic molecules to inhibit Sn²⁺ oxidation in FA_{0.7}MA_{0.3}Pb_{0.5}Sn_{0.5}I₃ perovskite films and achieve device performance of 25.6%, though their WG perovskite only shows a V_{OC} of 1.21 eV with 1.77 eV bandgap.⁷²

5.5.1 Film characterisation of solution-processed Pb/Sn perovskite solar cells

We spin-coated Pb/Sn perovskite on 2-PACz HTM in an N₂-filled glovebox where the H₂O and O₂ level are below 0.1 ppm and characterise the film quality. From XRD (**Figure 5.17a**), we observe highly structure orientation (note: the rise curve between 2θ of 15° to 25° is from an air-tight sample holder). In terms of perovskite surface morphology, the grain size is around 300 nm to 800 nm (**Figure 5.17b**). The UV-vis spectrum and PL show the absorption onset and emission is approximately 970 nm (**Figure 5.17c**). The bandgap of perovskite is 1.27 eV, based on the first derivative of EQE (**Figure 5.17d**). These data show that our Pb/Sn film fabrication is successful with narrow bandgap features and pin-hole free layer for further fabrication of solar cells.

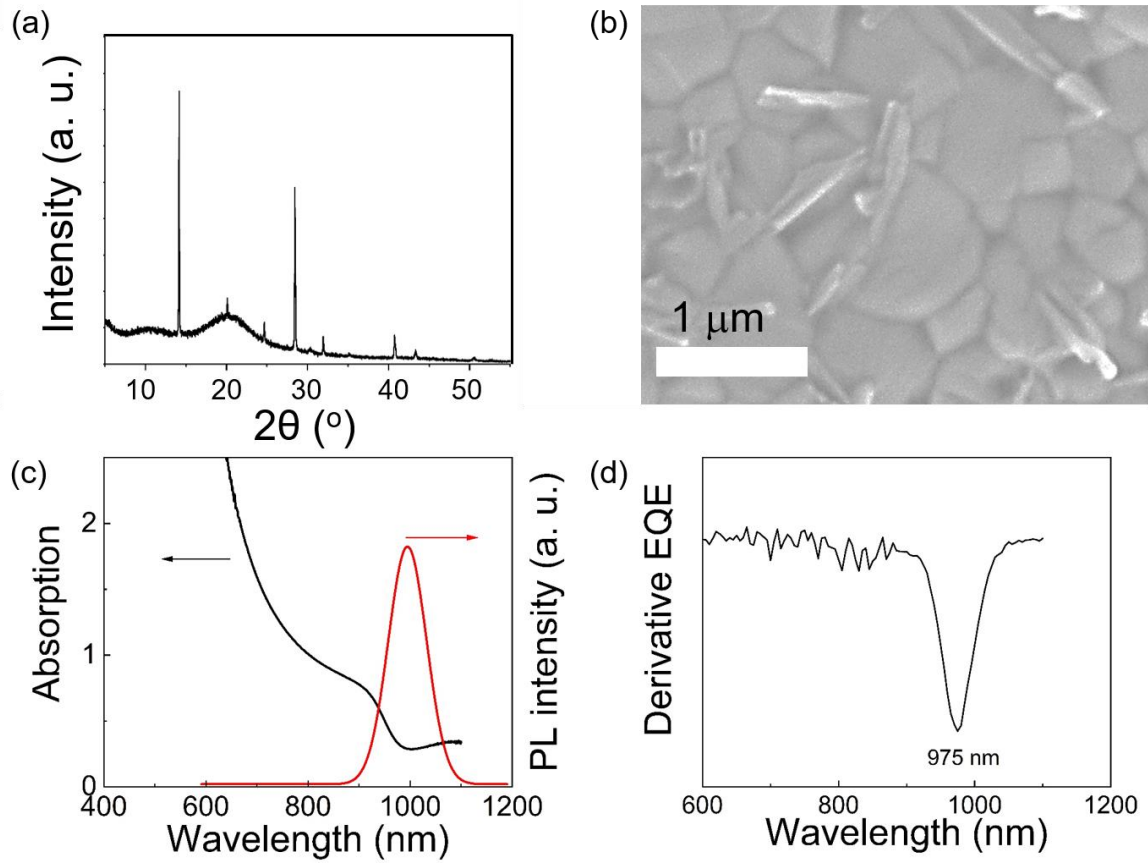


Figure 5.17. Solution-processed Pb/Sn perovskite with a composition of $\text{FA}_{0.75}\text{Cs}_{0.25}\text{Pb}_{0.5}\text{Sn}_{0.5}\text{I}_3$ on 2-PACz film. (a) XRD (Note: the rise curve between 2θ of 15° to 25° is from an air-tight sample holder), (b) SEM, (c) UV- Vis, PL spectra and (e) derivative EQE of NBG perovskite solar cells.

5.5.2 EDAI passivation effect on NBG perovskite solar cells

In order to demonstrate a narrow bandgap subcell suitable for a tandem configuration, we first develop devices based on an ITO/2-PACz/FA_{0.75}Cs_{0.25}Pb_{0.5}Sn_{0.5}I₃/C60/BCP/Cu architecture where the perovskite, in this case, is deposited by solution processing and the contact layers above perovskite are deposited by thermal evaporation. The EDAI passivation substantially improves the V_{oc} in these narrow bandgap perovskite solar cells, increasing PCE from 12.4 % (average: 11.2%) to 19.4% (average: 18.4%) by improving FF and V_{oc} (**Figure 5.18a**).¹⁴⁷ Two important pieces of information here for EDAI passivation treatment are (1) the mixed IPA and toluene solvents system is vital as IPA can wash away and damage the perovskite quality, therefore, the use of diluted IPA is the key (2) the Pb/Sn perovskite film needs to be cooled down after perovskite annealing. We do not see an onset shift in EQE after EDAI passivation (**Figure 5.18b**) or any morphology variation (**Figure 5.19**). The hypothesis is that the iodine from EDAI might penetrate the perovskite structure and heal the defect. When EDAI is used on a mixed halide perovskite system, it increases the I: Br ratio and reduces the bandgap. On the other hand, EDAI-passivated the Pb/Sn sample, the perovskite composition here is pure I sample, therefore, no bandgap change is observed. The summarised V_{oc} enhancement of our 1.77 eV and 1.27 eV bandgap perovskite is shown in **Figure 5.18d**, demonstrating a manifest passivation effect. For Pb/Sn solar cells, we see a reduction in V_{oc} loss from 382 mV to 140 mV when comparing devices without and with EDAI passivation, respectively. Furthermore, we calculate the Urbach energy from devices' EQE and show that the Urbach energy reduces from 21.5 meV to 20 meV (**Figure 5.20**) of the perovskite absorber after EDAI passivation, consistent with reduced non-radiative loss in perovskite film and less electronic disorder by EDAI treatment.

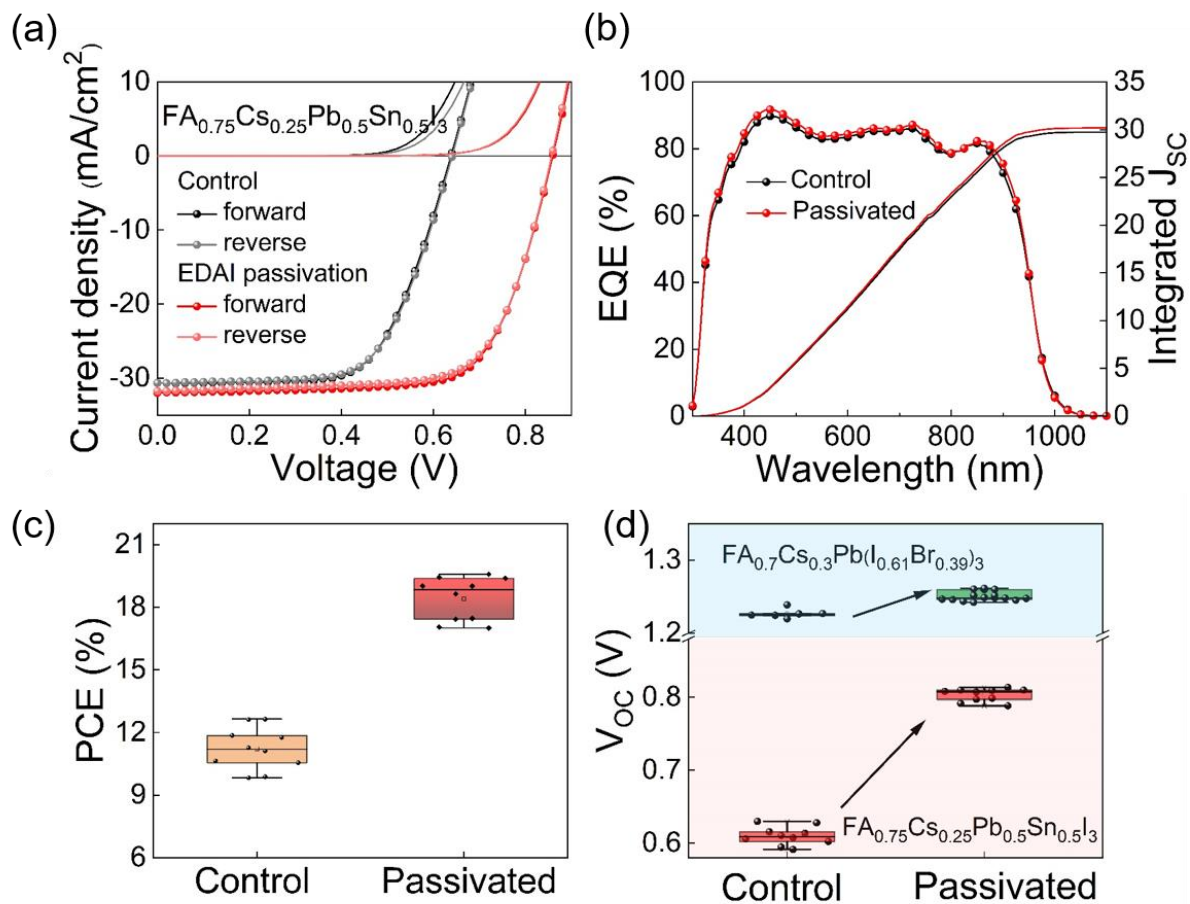


Figure 5.18. (a) J-V curves for control and EDAI-passivated, $\text{FA}_{0.75}\text{Cs}_{0.25}\text{Pb}_{0.5}\text{Sn}_{0.5}\text{I}_3$ solar cell in the dark (no symbols) and under AM 1.5 G illumination (line and symbols). During the measurement, a scan rate of 100 ms/V was used. See device parameters in **Table 5.3**. (b) EQE of solution-processed Pb/Sn perovskite solar cells without (black) and with (red) EDAI passivation. (c) PCE distribution of solution-processed Pb/Sn perovskite before and after EDAI passivation. (d) V_{OC} statistics for devices based on $\text{FA}_{0.7}\text{CS}_{0.3}\text{Pb}(\text{I}_{0.64}\text{Br}_{0.36})_3$ and $\text{FA}_{0.75}\text{CS}_{0.25}\text{Pb}_{0.5}\text{Sn}_{0.5}\text{I}_3$ with and without EDAI passivation.

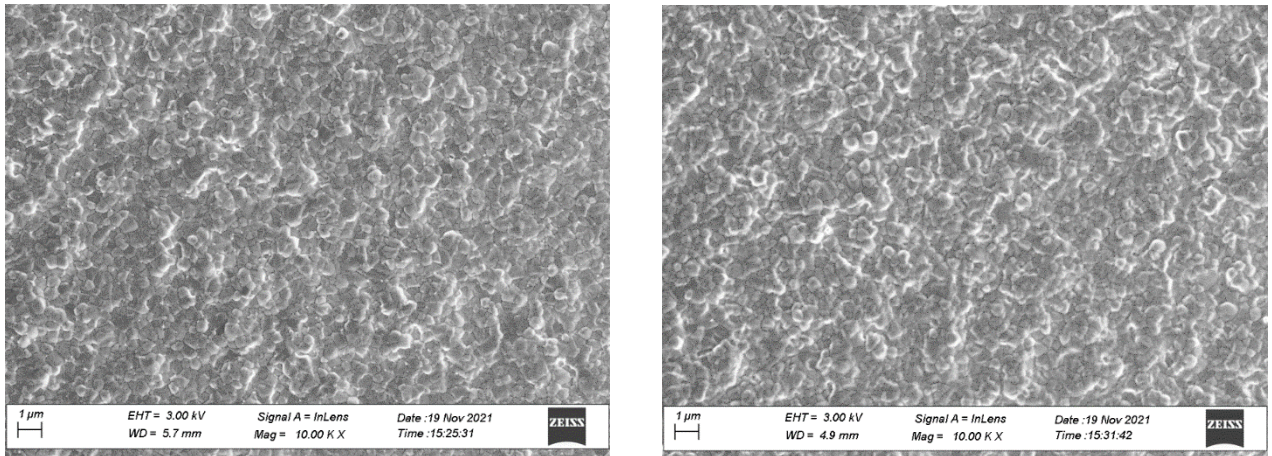


Figure 5.19. SEM morphology of solution-processed Pb/Sn perovskite film ($\text{FA}_{0.75}\text{Cs}_{0.25}\text{Pb}_{0.5}\text{Sn}_{0.5}\text{I}_3$) without (left) and with (right) EDAI passivation.

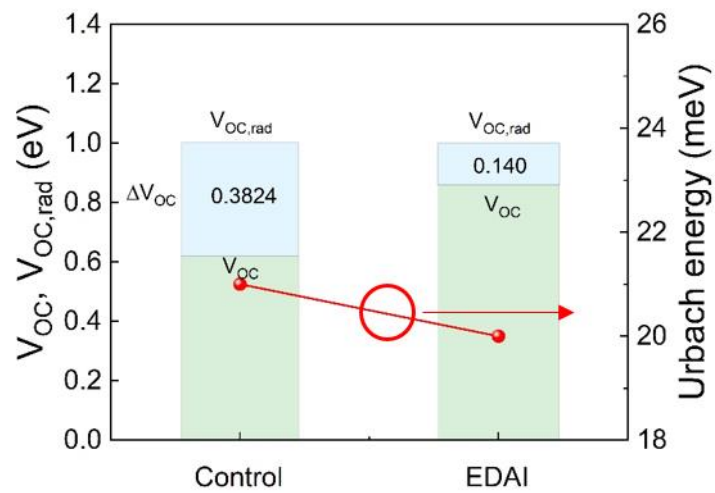


Figure 5.20. The measured V_{OC} , estimated V_{OC} and Urbach energy of solution-processed low gap perovskite solar cells ($\text{FA}_{0.75}\text{Cs}_{0.25}\text{Pb}_{0.5}\text{Sn}_{0.5}\text{I}_3$) with and without EDAI passivation. The left axis shows the V_{OC} and $V_{OC,rad}$ and the right axis shows the Urbach energy.

Table 5.3. Champion PV performance metrics solution processed narrow bandgap (1.28 eV) perovskite solar cells with and without EDAI treatment.

Narrow bandgap (1.28 eV) perovskite solar cells					
	V _{oc} (V)	J _{sc} (mA/cm ²)	FF (%)	PCE (%)	V _{oc} loss (mV)
Control	0.64	-30.6	64.3	12.6	380
EDAI-treated	0.86	-32.0	70.6	19.4	140

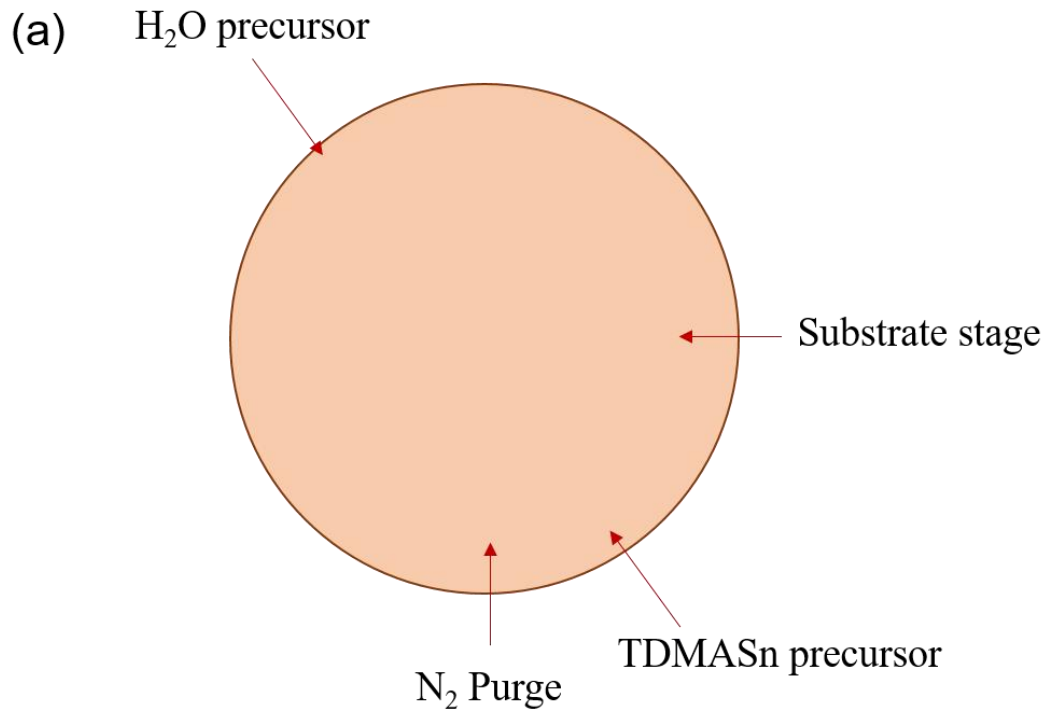
5.6 All-perovskite tandem solar cells

5.6.1 ALD SnO_x deposition

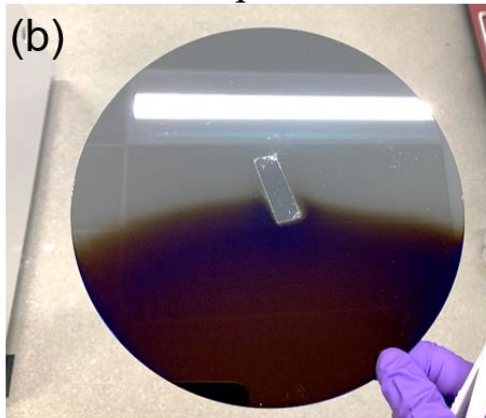
For 2T all-perovskite tandem solar cell, it is necessary to deposit a recombination junction to connect two subcells and for carrier recombination. The ALD-SnO_x deposition is performed on a Picosun R-200 advanced system, which can deposit a film on up to 8-inch wafers. The ALD system is integrated into an N₂-filled glovebox to prevent any potential degradation by air. We use Tetrakis(dimethylamido)tin(IV) (TDMASn) for the Sn source and use H₂O as an oxidant in our deposition. During the process, the substrate stage is kept at 100°C as higher temperatures might cause thermal damage to perovskite. The deposition recipe of ALD-SnO_x is shown in **Table 5.4**. The deposited SnO_x films are shown in **Figure 5.21**, and it is seen that a higher source temperature (from 55°C to 75°C) is needed to increase the TDMASn precursor pressure to cover the whole wafer.

Table 5.4. The ALD-SnO_x deposition recipe on Silicon wafer and perovskite film.

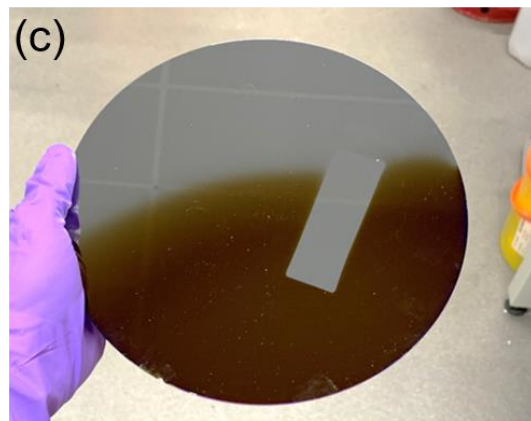
TDMASn Source temperature (°C)	TDMASn Pulse time (s)	N ₂ Purge time (s)	H ₂ O pulse time (s)	N ₂ Purge time (s)	Shown in Figure
55	0.6	10	0.2	10	5.21b
65	0.6	10	0.2	10	5.21c
75	0.6	10	0.2	10	5.21d
75	0.6	10	0.1	10	5.21e



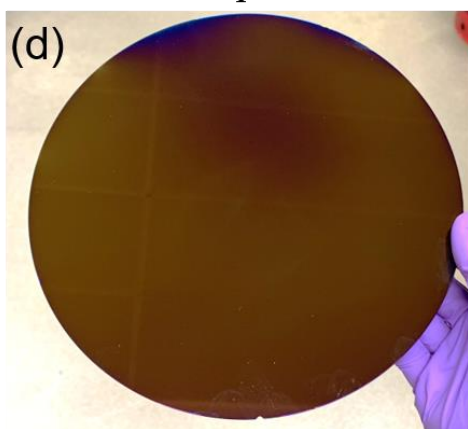
Substrate temperature: 55°C



Substrate temperature: 65°C



Substrate temperature: 75°C



Substrate temperature: 75°C

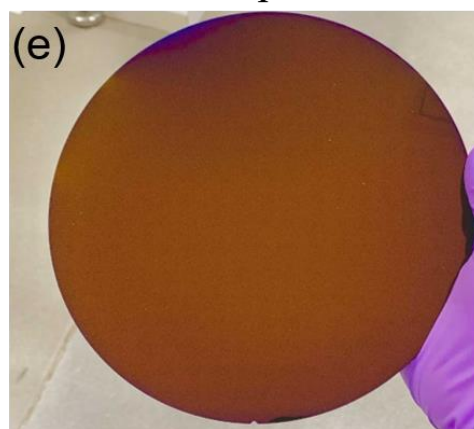


Figure 5.21. (a) Diagram of the position of the sources of TDMASn and H₂O injection position, and the N₂ purge direction in the ALD system. (b)-(e) photos of SnO_x film, growth on 8-inch silicon wafer, based on the deposition recipe in **Table 5.4**.

5.6.2 Development of all-perovskite tandem solar cells

To test ALD-SnO_x film is compatible with our WBG solar cells, we fabricate the solar cells with ITO/MeO-2PACz/PSK/C60/SnO_x/Cu. In this architecture, the BCP is replaced by SnO_x. The J-V curve is shown in **Figure 5.22**, where the device performance is similar to that without the SnO_x film but with BCP as a buffer layer. This shows that the ALD process for SnO_x deposition is not affecting the subcell performance.

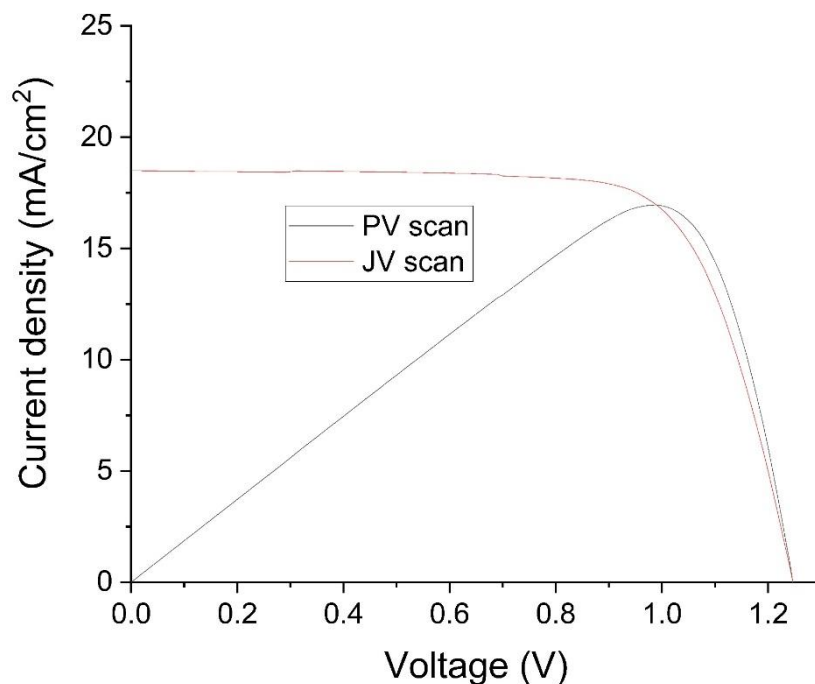


Figure 5.22. The J-V curve of passivated WBG perovskite (FA_{0.7}CS_{0.3}Pb(I_{0.64}Br_{0.36})₃) solar cell with 1.76 eV with ALD-SnO_x on top of C₆₀ instead of BCP. In the PV is power-voltage scan. During the measurement, a scan rate of 100 ms/V was used.

We prepare our all-perovskite tandem solar cell using the architecture from sections 5.4.2 and 5.5.2, and introduce SnO_x to form a recombination junction (**Figure 5.23a**). The device performance shows an s-kink shape with low FF, suggesting poor charge transportation. We further introduce a thin metal layer with 1 nm of Cu or Au,⁹³ to improve the conductivity in the recombination junction. After using thin-metal on SnO_x , the device performance are much lower. We, therefore, employ another HTM, PEDOT:PSS deposited on SnO_x for NBG solar cell deposition (**Figure 5.23b**), however, the s-kink shape JV curve is shown again. Another thin polyethylenimine (PEIE) is deposited on C60 before the ALD process as a report has shown that it can improve the nucleation process during ALD.¹³ However, PEIE does not improve device performance but affects the batch-to-batch variation. Once 1 nm Au is deposited between SnO_x and PEDOT:PSS, a reasonable JV curve is present. To sum up, we note that the choice of Au (as opposed to Cu, for instance) for the recombination junction is essential to ensure good charge transport. Also, 2-PACz for NBG subcell in our tandem architecture has a negative impact on charge transport, which we attribute to phosphoric acid groups not anchoring well to the Au clusters.⁹⁵ Therefore, we utilise PEDOT:PSS instead of 2-PACz for the tandems.

The optimised architecture of the tandem device is shown in **Figure 5.24a** and is comprised of ITO/MeO-2PACz/ $\text{FA}_{0.7}\text{Cs}_{0.3}\text{Pb}(\text{I}_{0.64}\text{Br}_{0.36})_3$ /EDAI/C60/ALD- SnO_x /Au/PEDOT:PSS/ $\text{FA}_{0.75}\text{Cs}_{0.25}\text{Pb}_{0.5}\text{Sn}_{0.5}\text{I}_3$ /C60/BCP/Cu. A ~ 1 nm Au cluster layer is used between the SnO_x and the PEDOT:PSS layers to improve charge recombination and enhance device V_{OC} and FF.

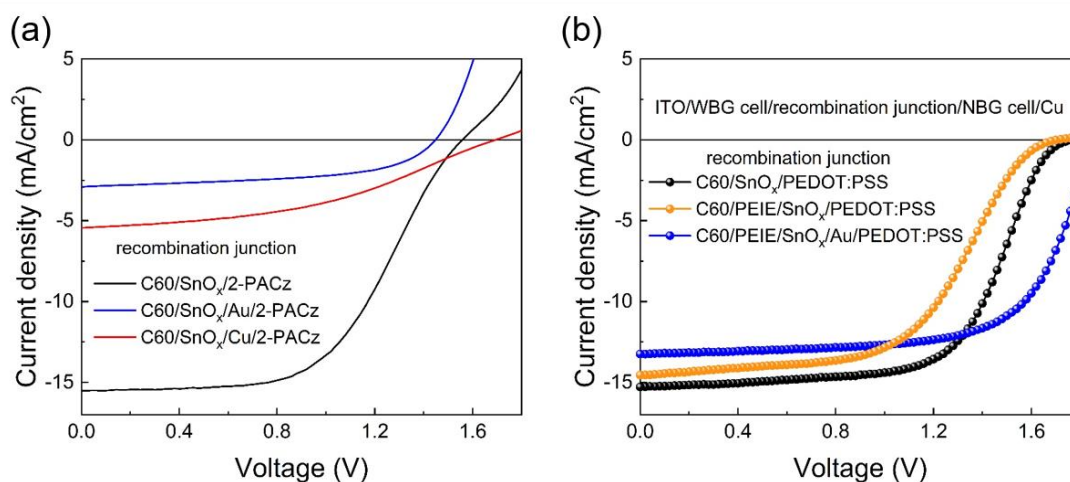


Figure 5.23. All perovskite tandem solar cells with different interlayers (a) 2-PACz, 2-PACz/Au or 2-PACz/Cu and (B) SnO_x/PEDOT:PSS, PEIE/SnO_x/Au/PEDOT:PSS PEIE/SnO_x/PEDOT:PSS between wide bandgap and narrow bandgap perovskite films. During the measurement, a scan rate of 100 ms/V was used.

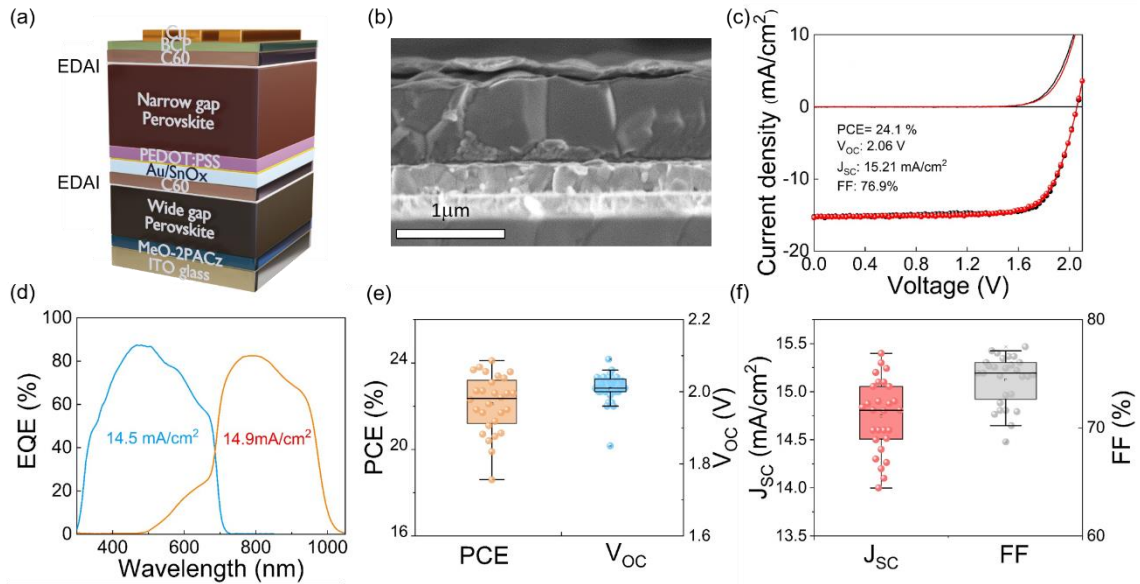


Figure 5.24 (a) Schematics and (b) cross-sectional SEM image displaying the architecture of the all-perovskite tandem solar cell. (c) J-V curve of the champion tandem device, reaching a 24.1% PCE for forward scan. (d) EQE spectra of the evaporated-based WBG (blue curve) and solution-based NBG (orange) perovskite subcells comprising the all-perovskite tandem device. The distribution of device performance across four batches (28 devices) is shown in figure (e) and (f) with an average PCE of 22.1%. During the measurement, a scan rate of 100 ms/V was used.

Table 5.5 Champion PV performance metrics for 2-terminal all-perovskite tandem solar cells.

V _{OC} (V)	J _{SC} (mA/cm ²)	FF (%)	PCE (%)
2.06	-15.2	76.9	24.1

Figure 5.24b displays a SEM cross-section image of the tandem device under study, where the thickness of WBG and NBG perovskites are 300 nm and 800 nm, respectively, to match the current of each subcell. **Figure 5.24c** shows the J-V curves of the champion all-perovskite tandem solar cell, showing a PCE of 24.1%, with a V_{oc} of 2.06 V, a J_{sc} of 15.2 mA/cm² and a FF of 76.9 % from forward scan direction and negligible hysteresis between the forward and backward scans. This PCE is the highest reported value so far for an all-perovskite tandem solar cell where at least one subcell is prepared by vacuum deposition. Compared to the sum V_{oc} of the champion subcells, the tandem device shows a small voltage loss of 60 mV, which we attribute to the interconnecting layer that requires further optimisation. The stabilised performance output is in **Figure 5.25** with a PCE of 23.2% at a fixed bias of 1.74V. **Figure 5.24d** shows the EQE spectra where the integrated J_{sc} extracted for the WBG and NBG subcells are 14.5 and 14.9 mA/cm², respectively.

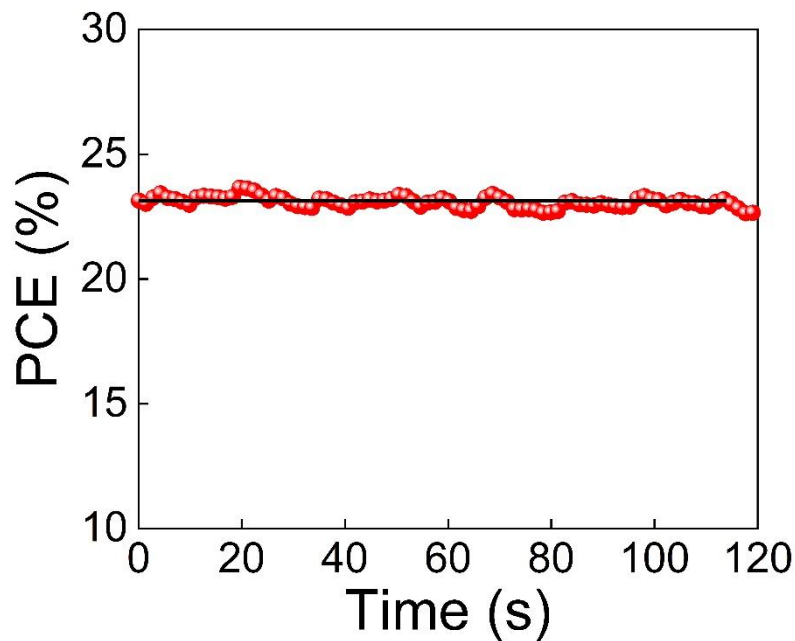


Figure 5.25. The stabilised power output measurement of our device with a fixed bias at 1.74 V, reaching PCE of 23.2%.

This result constitutes the first integration of an evaporated building block in an all-perovskite tandem architecture where the bandgaps of the absorbers employed complementary harvest regions of the spectrum. The high optical quality, pin-hole free character, and fine controlled thickness of the evaporated subcell enables the subsequent deposition of recombination layers and narrow bandgap subcells to attain efficient all-perovskite tandem solar cells. The device statistic data for the PCE and the V_{OC} , and J_{SC} and FF are displayed in **Figure 5.24e and f**, showing a standard deviation of 1.5 % in PCE and confirming reasonable reproducibility across four batches. The storage lifetime test was measured with four encapsulated devices kept in air and shown excellent stability with above 92% initial PCE after 26 days (**Figure 5.26**).

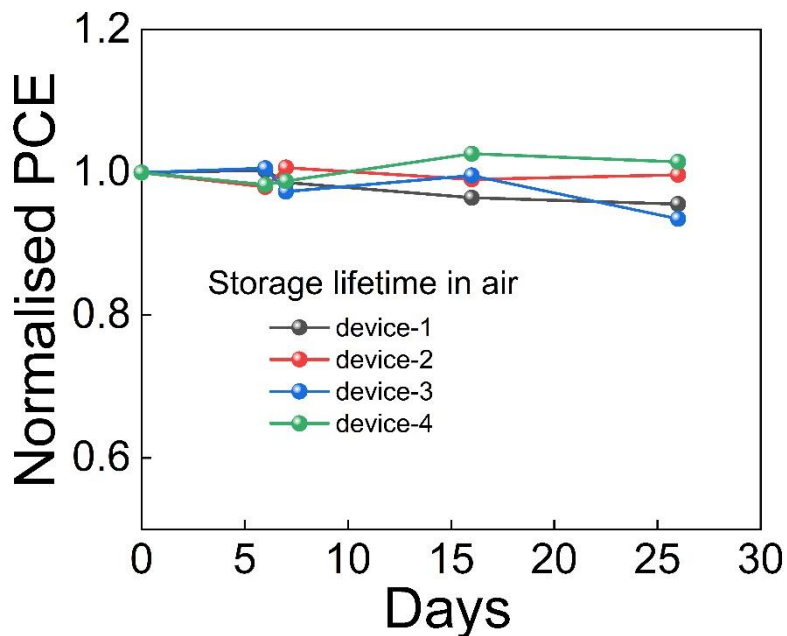


Figure 5.26. The storage solar cells stability test in air of encapsulated (in N_2 -filled glovebox) tandem device.

5.7 Toward 30% of all-perovskite tandem solar cells (ongoing work)

Followed by the work above, there are three major losses in our all-perovskite tandem solar cell, (1) the V_{OC} loss in WBG perovskite due to low PLQE of $\sim 0.01\%$ for a pin contact structure, indicating a significant non-radiative recombination process in our device. (2) the absorption loss from NBG Pb/Sn perovskite, as the perovskite thickness (~ 750 nm in our device) is not enough to harvest all the photons in NIR. (3) the RJ layer with Au and PEDOT:PSS combination reduces the incident light to NBG perovskite.

The PLQE of perovskite on MeO-2PACz is around 0.01% , suggesting a potential space to improve the radiative recombination process. Though the EDAI successfully improves the film quality and boosts the PLQE by an order of magnitude to 0.1% , this number is still far below the radiative limit. To passivate the perovskite further, we have employed a bithiophene ethylammonium iodide (2T, provided by the group of Prof. Letian Douin in Purdue University) in p-i-n evaporated WBG perovskite solar cell described in Chapter 5 and studied surface recombination. The 2T is mixed with EDAI solution and spin-coated on top of perovskite for a post-treatment. Interestingly, the mixed solution can further improve the device V_{OC} by 30 mV in average (**Figure 5.27a**), compared to the one with a pure EDAI solution counterpart. Also the device FF is improved, showing that an additional layer on perovskite does not impede the charge transportation (**Figure 5.27b**). The EQE measurement of control, EDAI-treated, and EDAI+2T treated devices are shown in (**Figure 5.27c**), demonstrating no spectral response loss with additional layer passivation, leading to a similar J_{SC} in these samples. We speculate that the EDAI and 2T can passivate different perovskite defects and have a complementary effect to minimise the non-radiative loss and improve the device performance. The hyperspectral PL, confocal PL, and photoemission electron microscopy measurements (collaborate with the group of Prof. Dani in OIST) are conducted to study this passivation effect in detail.

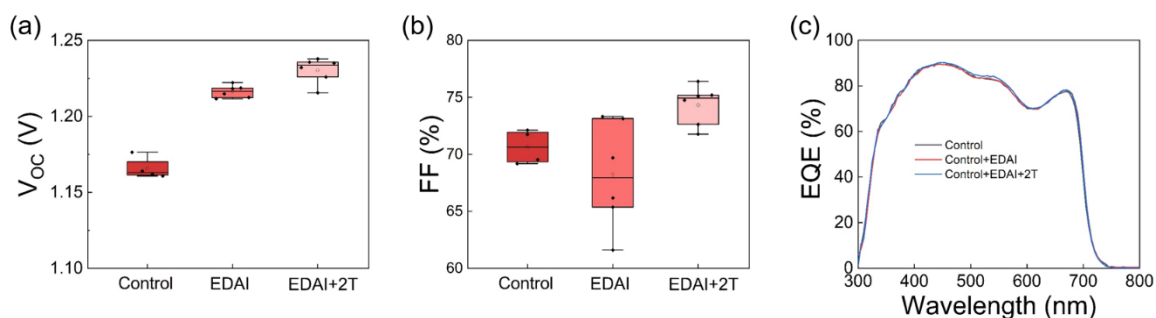


Figure 5.27. The evaporated WBG perovskite ($\text{FA}_{0.7}\text{Cs}_{0.3}\text{Pb}(\text{I}_{0.64}\text{Br}_{0.36})_3$) solar cell with different surface passivation treatments, (a) V_{OC} and (b) FF distribution of control, EDAI-treated and EDAI+2T treated solar cell, (c) the EQE measurement of these solar cells, showing nearly identical spectrum.

After improving the quality of WBG perovskite, we now focus on the light-harvesting in NBG perovskite. To improve the J_{SC} in NBG and all-perovskite tandem solar cells, a thicker NBG perovskite film is required. One of the challenges in Pb/Sn perovskite is device V_{OC} suffers with increased thickness as the bulk perovskite defects induce non-radiative loss.^{72,169} In here, the thickness variation is prepared by increasing Pb/Sn solution from 2.0 M, 2.2 M to 2.4 M with the same composition of $\text{FA}_{0.75}\text{Cs}_{0.25}\text{Pb}_{0.5}\text{Sn}_{0.5}\text{I}_3$, shown in Chapter 5. The solar cells are prepared with ITO/PEDOT:PSS/PbSn-perovskite/EDAI/C60/BCP/Cu. The V_{OC} distribution of different concentrations of perovskite solar cells are shown in **Figure 5.28a** where a clear trend of V_{OC} dropping with higher perovskite concentration is present. The device EQE is measured (**Figure 5.28b**), and the enhancement of EQE between 800 nm to 950 nm is shown from 2 M (black) to 2.2 M (red) device. However, the EQE drops in the entire spectrum of 2.4 M solar cells, suggesting that thick perovskite hinders charge transportation, possibly due to traps.

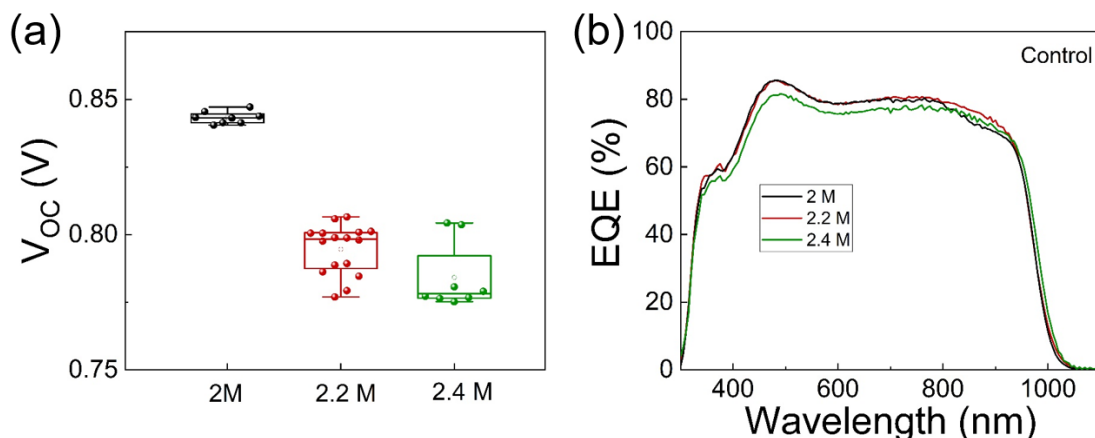


Figure 5.28. The NBG perovskite solar cells, prepared by different perovskite solution concentrations. (a) V_{OC} variation and (b) the EQE spectrum.

To solve this issue, a survey of perovskite dopants to passivate bulk perovskite has been studied. The Gallic acid (GA, **Figure 5.29a**) has been chosen as the hydroxyl and acetic acid functional groups can bond with Sn^{2+} to prevent its oxidation and passivate the defects. GA has been used for pure Sn-based perovskite to show the property of anti-oxidant to suppress the formation of Sn^{4+} defect.¹⁷⁰ Therefore, GA-doped Pb/Sn perovskite solution improves the device performance and stability in their work. In here, GA is used in Pb/Sn perovskite to study the passivation effect on thickness-dependent experiments. In **Figure 5.29 b-c**, the V_{OC} evolution of different amounts of GA dopant in different perovskite concentrations for solar cells is shown. The GA-doped Pb/Sn perovskite shows noticeable V_{OC} improvement for both 2.2 M and 2.4 M devices. The optimum result demonstrates a 50 mV improvement from a 2.2 M Pb/Sn perovskite solar cell with a 0.4% GA doping. In **Figure 5.29 d-e**, we show the FF variation with GA-doped Pb/Sn perovskite solar cells, where a 3% absolute improvement can be seen in 2.2 M samples but the FF goes down with 2.4 M counterparts. In **Figure 5.29 f**, a 2.4 M perovskite solar cell reveals a better EQE response with a 0.5% GA incorporation. This result shows that with GA incorporation, a higher J_{SC} is achievable. We note that the spin-coating protocol for different perovskite concentrations might need further optimisation.

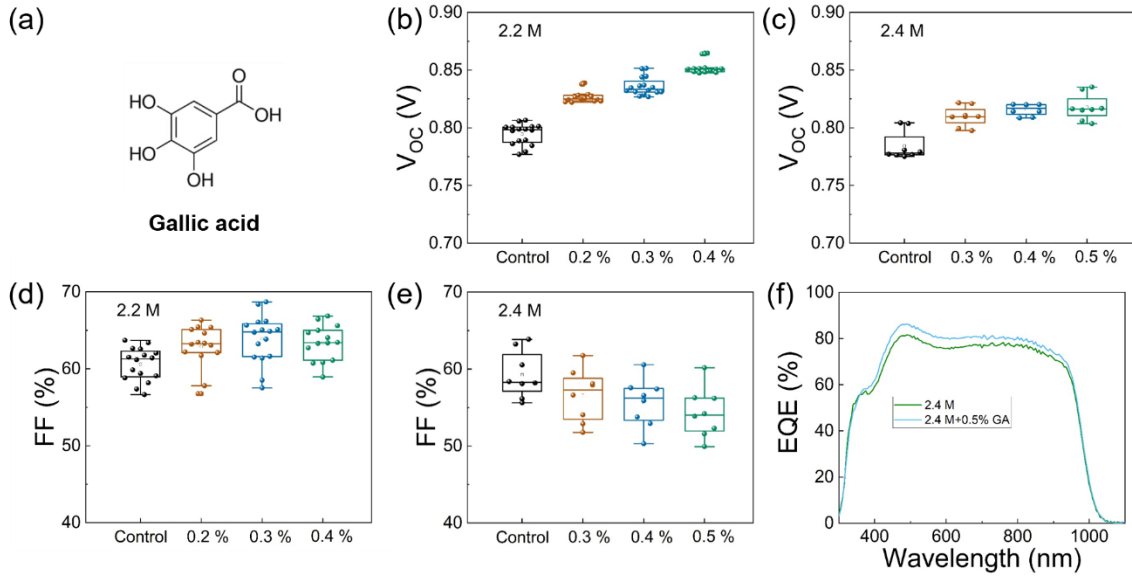


Figure 5.29. (a) Molecule structure of Gallic acid (GA). (b-c) V_{OC} and (d-f) FF evolution of 2.2 and 2.4 M Pb/Sn perovskite solar cells with different amounts of GA incorporation. (f) the EQE spectrum of 2.4 M device without and with GA.

To sum up, the passivation for WBG and NBG show promising results by dual surface passivation and bulk chemical dopant, respectively. The better V_{OC} and J_{SC} are demonstrated, leading to a potential improvement for all-perovskite tandem solar cells in future.

5.8 Conclusion

Our work employs a dual-interface treatment to maximise the performance of evaporated perovskite devices, which show great promise when implemented into tandem architectures. We employ a 4-source vacuum deposition method to demonstrate $\text{FA}_{0.7}\text{Cs}_{0.3}\text{Pb}(\text{I}_x\text{Br}_{1-x})_3$ perovskites of tunable bandgap. Engineering the device architecture via the use of a MeO-2PACz layer as HTM demonstrates a 20.7% PCE in a 1.62 eV bandgap perovskite solar cell, which is the highest MA-free device performance in a multi-source evaporated system. Several evaporation sources enable fine-tuning of the halide content and we use it to report a phase stable $\text{FA}_{0.7}\text{Cs}_{0.3}\text{Pb}(\text{I}_{0.64}\text{Br}_{0.36})_3$ with a 1.77 eV bandgap and minimised non-radiative losses when treated with EDAI. This passivation method is versatile and reproducible, and we extend it to Pb/Sn based narrow bandgap perovskite solar cells to build a 2-terminal tandem solar cell that shows a PCE of 24.1% with an excellent V_{OC} of up to 2.06 V. Our result is a key step towards all-vapour deposited tandems and encourages future work to develop narrow bandgap perovskites benefiting from the scalable, conformal and reproducible character of vacuum deposition methods. These systems open a myriad of possibilities for enhanced modularity, including exploring new recombination layers not compatible with solution-processed perovskite and integrating advanced photonic strategies to push perovskite photovoltaics to their limits. Further device loss study and improvement is ongoing, and we have revealed new passivation strategies to improve the performance of all-perovskite tandem solar cell potentially.

Chapter 6. Evaporated perovskite for a broad range of applications

The works in this chapter demonstrate the versatility of applications of evaporated perovskite layers including at larger scale.

6.1. Evaporated perovskite for perovskite-silicon tandem solar cells

Si solar cells have achieved a PCE of 26% and dominates the current PV market. These Si cells show a textured monocrystalline structure with the pyramidal surface on both sides, based on the nature of the anisotropic etching process. The randomly textured surface provides the benefit of light-trapping to reduce front-surface reflectance and scatter light into the silicon bottom to increase current density. To improve the solar cell performance beyond the SQ limit, an add-on layer of metal-halide perovskite on top of silicon for tandem design is a possible route as a WBG perovskite can have an excellent current match with Si. The record perovskite-silicon tandem solar cell has achieved a certified PCE of 31%, showing a promising result of combining the technology of perovskite and Si. Nowadays, most metal-halide perovskite is prepared by solution-processing, which is difficult to deposit on a few μm height pyramids. In literature, a polished Si wafer is used to solve the film deposition issue for perovskite-Si tandem study. However, the polish process requires surface etching with a chemical-mechanical process, which increases the fabrication cost. Therefore, a deposition method for uniform coating is necessary.

Vacuum deposition shows the advantage of solvent-free and uniform deposition on various surfaces, revealing the great potential to fabricate perovskite-silicon tandem solar cells. The silicon cells are provided by collaborators, the group of Stefaan De Wolf in KAUST. The architecture of silicon solar cell is ITO/nc-Si (n)/a-SiH (i)/c-Si/a-Si:H (i)/a-Si:H (p)/ITO/Ag, and the detailed fabrication process can be found in their previous publication. We prepare multisource evaporated perovskite and spin-coat MeO-2PACz on the the textured surface, as described in Chapters 3 and 5. After perovskite deposition, the top-view and cross-sectional SEM are measured to understand the uniformity of the perovskite coating. In **Figure 6.1**, the

perovskite layer shows a continuous film on the textured surface without pin-holes, reflecting a key advantage of vacuum deposition over solution processing.

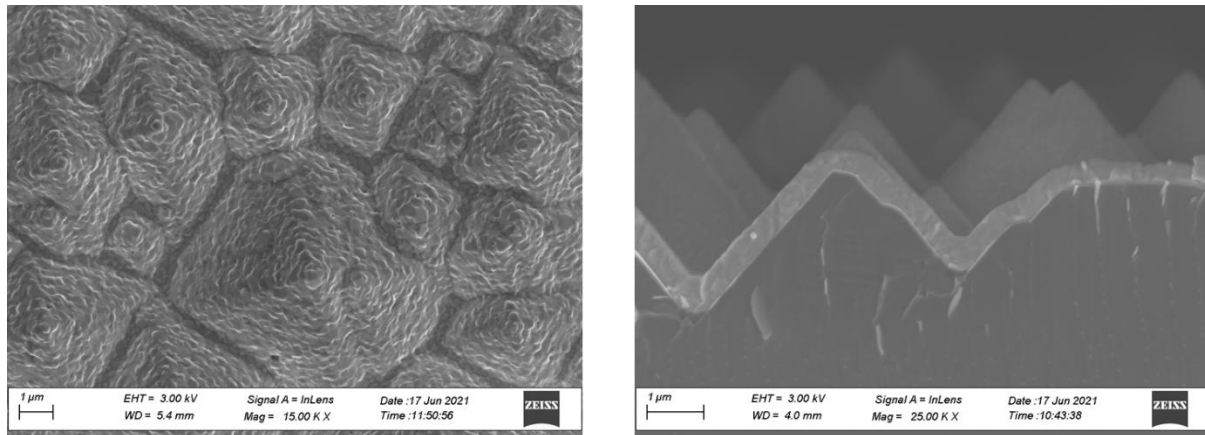


Figure 6.1. (a) top-view and (a) cross-sectional SEM images of evaporated perovskite ($\text{FA}_{0.7}\text{Cs}_{0.3}\text{Pb}(\text{I}_{0.9}\text{Br}_{0.1})_3$) on textured Si solar cells.

The architecture of perovskite/Si solar cells used here is shown in **Figure 6.2a**. Hyperspectral PL mapping (**Figure 6.2b-d**) is employed to understand the PL intensity, peak position and corresponding surface geometry. In the reflection of the white lamp measurement, the bright spots are the pyramids, and the dark regions are the valleys. Combining the PL intensity and position with the geometry map, we could know that perovskite PL and emissive PL position on different surface morphology and a red-shifted PL position of around 10 nm, compared to the valley area. One possible scenario is that the sticking coefficient differs in the pyramid and valley areas. The average PL peak position in the whole map is shown in **Figure 6.2e**, and we also compare this data to the PL position on the MeO-2PACz/ITO substrate (flat substrate). The PL position is observed to be red-shifted by 12 nm in the textured sample. Furthermore, the perovskite crystal structure on the flat or textured surface is different in XRD measurement (**Figure 6.2f**), showing no excess PbI_2 and a shift of perovskite peak to lower 2θ degree. A re-adsorption effect of vapour deposition has been reported on the textured surface, especially on low sticking coefficient materials.¹⁷¹ These results suggest that our FAI could have the same effect on re-absorption and red-shift of the perovskite PL. We conclude that the perovskite film quality is highly sensitive to the substrate morphology; further optimisation is required, in particular to achieve the excess PbI_2 we have found to be essential for a highly efficient vapour-deposited perovskite solar cell.

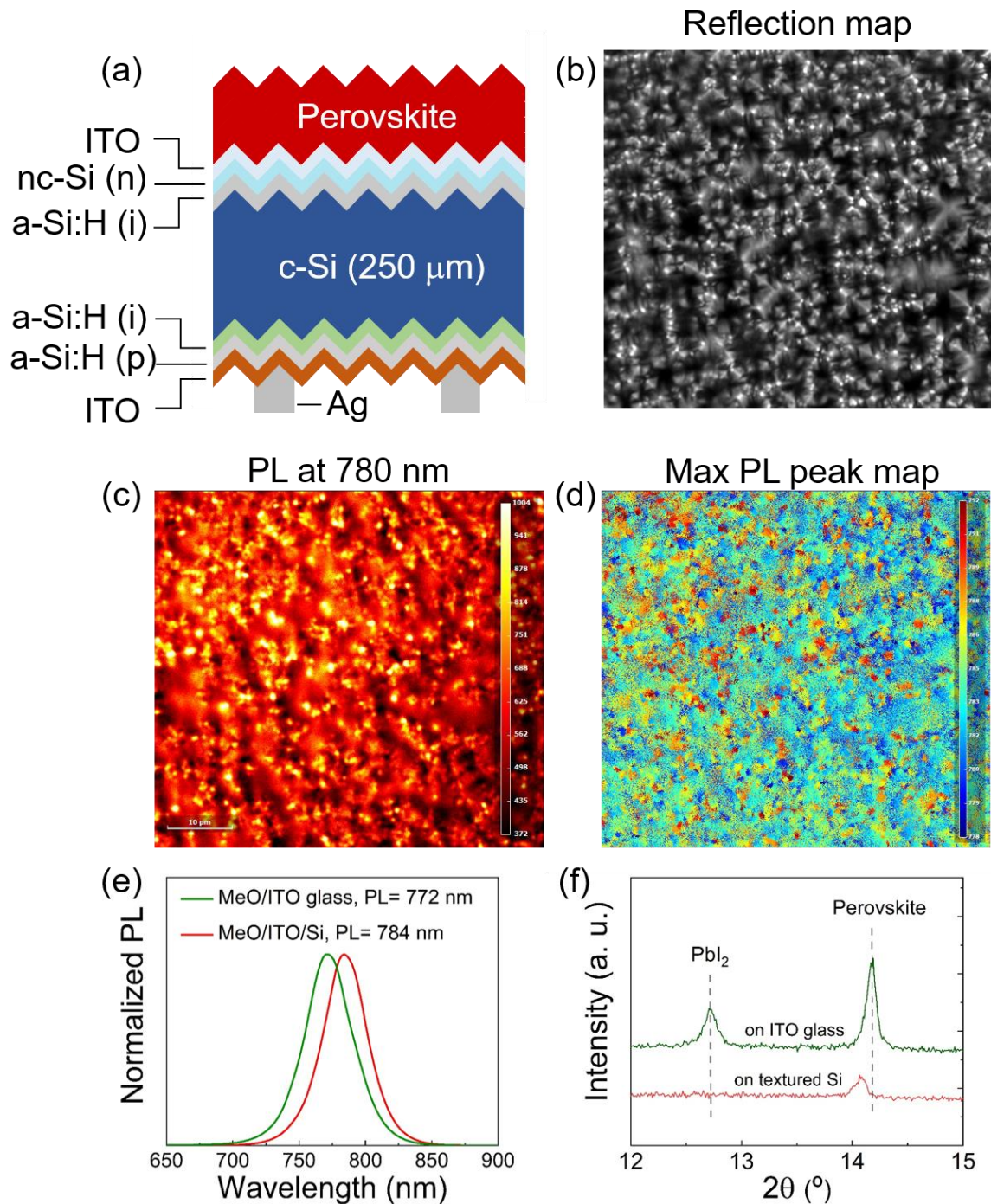


Figure 6.2. (a) half-device architecture of evaporated perovskite ($\text{FA}_{0.7}\text{Cs}_{0.3}\text{Pb}(\text{I}_{0.9}\text{Br}_{0.1})_3$) on Si solar cells. Si cell is fabricated by Dr. Erkan Aydin and Dr. Michele De Bastiani. Hyperspectral images (measured with Dr. Miguel Anaya) of evaporated perovskite film on textured Si (b) reflection map, (c) PL intensity map, (d) and max PL peak map. Comparison between evaporated perovskite on MeO/ITO glass and MeO/ITO Si textured cell with (e) normalised PL and (f) XRD pattern.

As the perovskite film quality is affected by the underlying morphology, an optimisation of the evaporation process, especially FAI deposition rate, is required. Here, we fix the deposition rate of PbI_2 and CsBr but vary the FAI. For these depositions, the perovskite thickness is set at 765 nm. The detailed deposition recipe is shown in **Figure 6.3a**. The XRD patterns of perovskite with different recipes are demonstrated in **Figure 6.3b**, where we can see the control sample (D, on ITO substrate) is showing a typical evaporated perovskite diffraction pattern with excess PbI_2 signal. As the amount of FAI rate during the evaporation is reducing from 1 $\text{\AA}/\text{s}$ to 0.7 $\text{\AA}/\text{s}$ (maintain the rate of PbI_2 and CsBr at 0.6 $\text{\AA}/\text{s}$ and 0.1 $\text{\AA}/\text{s}$, respectively), we have seen that the perovskite peak in XRD gradually shifted to a higher degree with the excess PbI_2 signal (**Figure 6.2f** and **Figure 6.3b**). This result shows that the textured morphology might increase the sticking coefficient of FAI as non-adsorbed FAI vapour can re-bounce and re-adsorb on other surfaces. Therefore, 30% less FAI is required for a textured surface, compared to a flat surface. Cross-sectional SEM images of a full perovskite-silicon tandem solar cell is measured by our collaborators in KAUST. In **Figure 6.3c-e**, the perovskite film thickness of recipes A, B and C are 380 nm, 430 nm and 430 nm, respectively, which are far from our set thickness of 765 nm. Therefore, a geometry factor needs to be included to achieve the desired perovskite thickness on the textured substrate for enough light absorption. Furthermore, from the cross-sectional SEM images, we can see more bright areas in the low FAI sample (A), corresponding to PbI_2 rich domains, which is consistent with our XRD measurement.

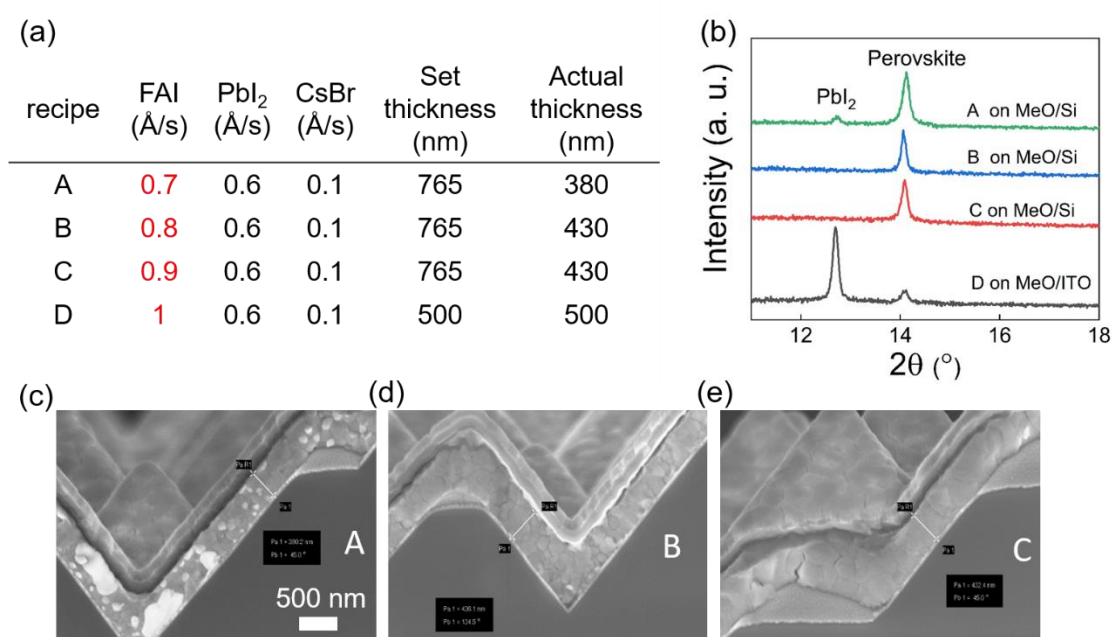


Figure 6.3. (a) The deposition recipe and film thickness of evaporated perovskite ($\text{FA}_{0.7}\text{Cs}_{0.3}\text{Pb}(\text{I}_{0.9}\text{Br}_{0.1})_3$) on textured Si cell or ITO substrate. (b) the XRD pattern of recipe A to D, (c-e) the cross-sectional SEM images (measured by Dr. Erkan Aydin) of complete perovskite-Si tandem solar cell with the deposition recipes of A-C.

The device performance of A, B and C perovskite deposition for tandem solar cells are shown in **Figure 6.4a**. The reduced FAI rate during evaporation (from C to A) provides higher device V_{OC} , showing the importance of excess PbI_2 for higher device performance. Further deposition optimisation is necessary to achieve decent device performance. We note that there is shunting in the perovskite subcell in sample C. The EQE spectra of the tandem solar cells are shown in **Figure 6.4b**, where there is no response in sample C, corresponding with shunting behaviour in the JV scan. Sample A shows less spectral response between 600 nm to 780 nm due to the thinner perovskite layer (see also **Figure 6.3a**). The total reflectance loss is also present here and demonstrates a minimised loss with both textured side design. To understand the perovskite deposition on the textured surface, a nano-Fourier transform infrared spectroscopy would be very helpful to conduct an FAI map and correlate this to surface morphology.

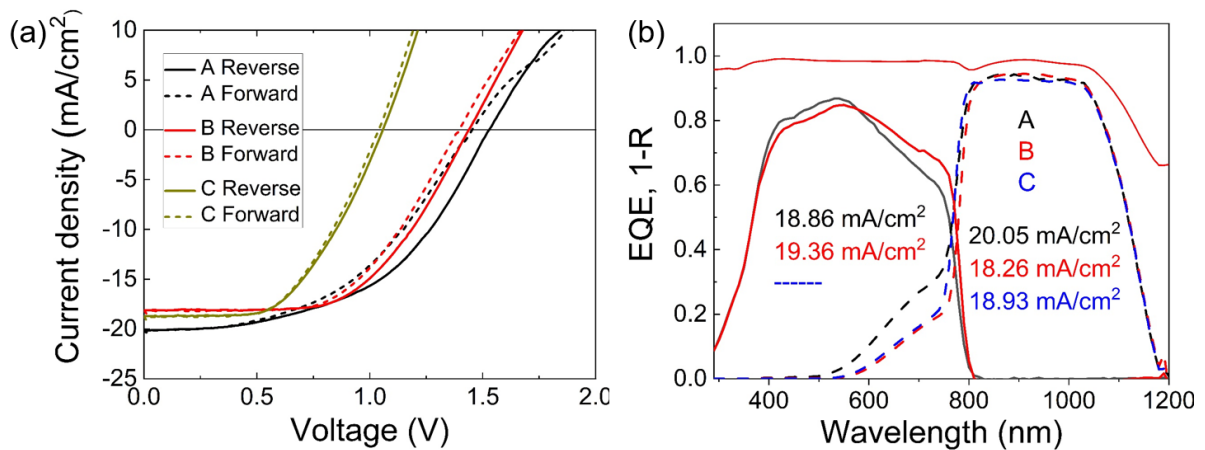


Figure 6.4. Perovskite-Si tandem solar cell based on different deposition protocols of A-C. (a) the JV-scans. (b) EQE measurement.

6.2 Fully-evaporated perovskite solar cells for solar fuel production.

One advantage of evaporation is that it can be used for large-scale deposition to produce pin-holes free and uniform layers. In this project, the fully evaporated (including all the CTLs) perovskite solar cell has been explored and adapted to a large-scale substrate (5x3 cm², **Figure 6.5a**). The device architecture is the following: FTO glass/Spiro-TTB/perovskite/C60/BCP/Cu. As the Spiro-TTB can re-evaporate from the TCO surface at high temperature (>135 °C) and reduce the device performance significantly, we change our perovskite recipe of post-annealing from 135°C to 120 °C for 20 mins. The device performance of a large-scale device is around 5% PCE with a 10 cm² size active area (**Figure 6.5c**). The low FF is due to the FTO substrate's high resistance; therefore, the module or metal finger design (see **Figure 6.5b**) can be introduced to reduce the sheet resistance.¹⁷² We have tested the design of metal fingers, with 100 nm Au layers on FTO substrate before the spiro-TTB evaporation. However, the device performance shows less PCE than no metal coating counterparts. The reason could be that our spiro-TTB is too thin (25 -50 nm) to cover the surface of metal fingers and cause direct contact between Au and Perovskite. To further demonstrate the vacuum deposition capacity, we deposit perovskite on a 10 x 10 cm² size flexible substrate, showing a uniform coating for large-scale deposition **Figure 6.5d**.

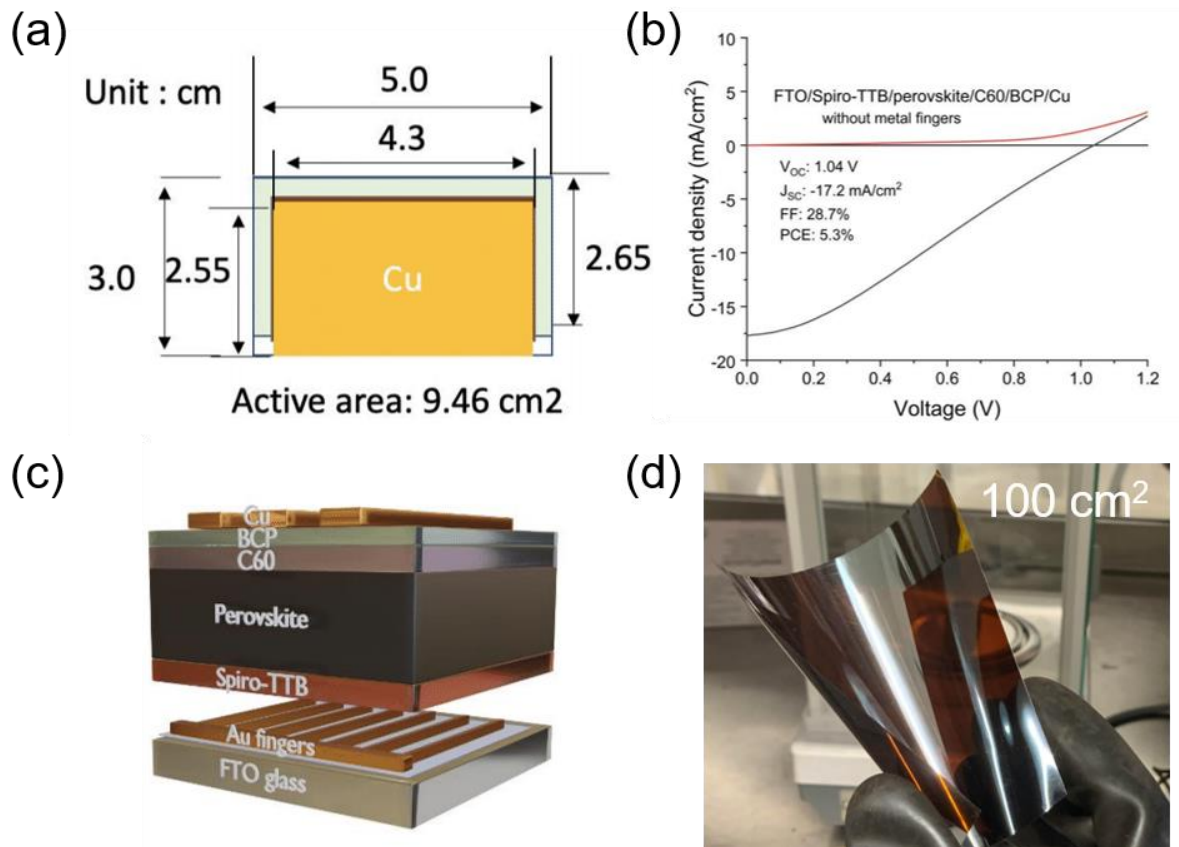


Figure 6.5. (a) A large-scale device pattern with a 5x3 cm² size and an active area of 9.46 cm². (b) J-V curve of a large-scale device with a 9.46 cm² active area. (c) the design of metal fingers to reduce resistance from FTO substrate. (d) A flexible substrate of 100 cm² size with perovskite deposition by multisource evaporation. Perovskite composition: (FA_{0.7}Cs_{0.3}Pb(I_{0.9}Br_{0.1})₃).

Beyond solar cells application, we collaborated with the group of Prof. Erwin Reisner, including Dr Motiar Rahaman and Dr Virgil Andrei, to develop scalable “artificial leaf” tandem photoelectrochemical (PEC) devices. The concept of artificial leaf is mimicking the photosynthesis process in the natural plants, which convert the sun light to photoelectrochemical energy. Perovskite is an excellent light harvesting material and can transfer carriers efficiently. Therefore, we integrate our perovskite photoabsorbers and catalysts, connecting in series to complete the reaction process. These devices consist of a BiVO₄ photoanode, a halide perovskite solar cell combining with a CuIn alloy catalyst as photocathode (**Figure 6.4 a-c**). In this system, the BiVO₄ photoanode can harvest the light below 500 nm wavelength for O₂ evolution.¹⁷³ The perovskite photocathode can provide a high over-potential (> 1.0 V) for CuIn alloy catalyst to conduct reduction of CO₂ and protons to CO

and H₂, showing a fully autonomous syngas production.¹⁷⁴ Furthermore, the photoelectrodes are connected directly in a back-to-back architecture, forming a standalone, “artificial leaf” device.

To scale up this system, we prepared a 10×10 array of perovskite-BiVO₄ artificial leaves (5×3 cm² total substrate area, ~9.5 cm² photoactive area) (**Figure 6.4e**). The overall PEC system is constructed in a 0.6×0.4 m² gas-tight large-scale reactor (made by 3D printer), and an airtight container collects the syngas product. To prepare 10 x 10 array devices, we use the equipment across the Department of Chemistry, Physics and Chemical Engineering and Biotechnology. In addition, for solar cell fabrication of a 10 x 10 array, Dr Miguel Anaya and Dr Edoardo Ruggeri are involved in cleaning substrates and contact layer deposition.

A vital innovation of this modular design in the photoreactor is that the standalone 10 cm² PEC tandem cell works independently. This provides a significant advantage over the current PV panel, as the failure of one 10 cm² device does not affect other leaves. Therefore, our system performs low maintenance and autonomous fuel production without external energy inputs (i.e. pumps, flow systems or motors) to support the system.

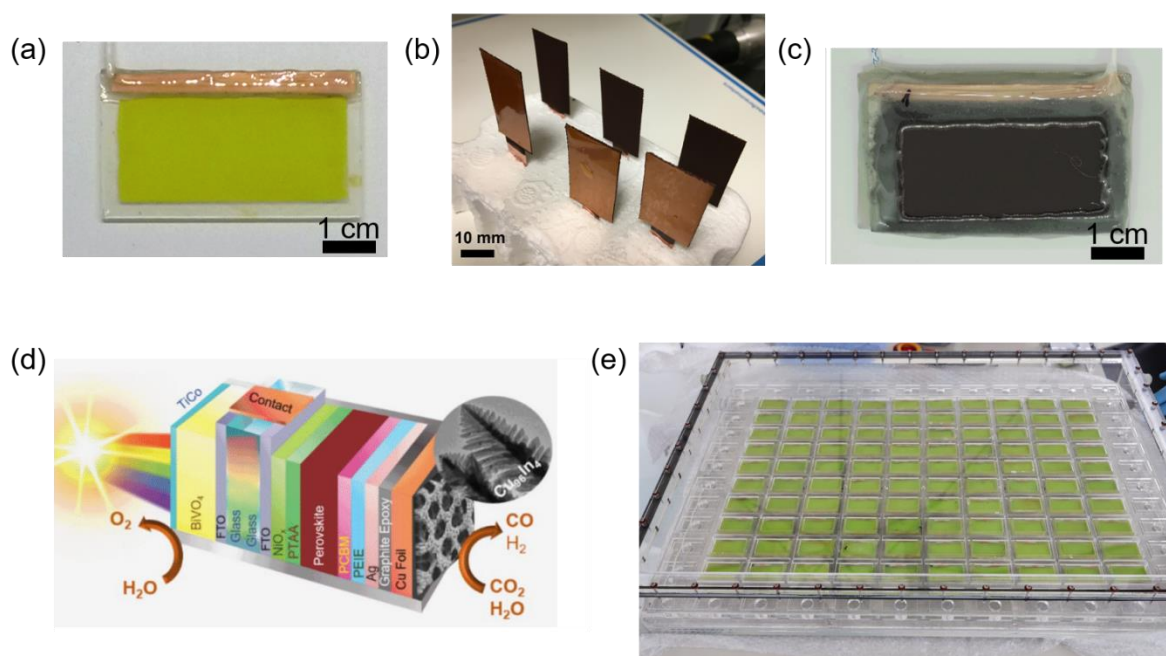


Figure 6.5. (a) Photographs of the ~10 cm² BiVO₄ photoanode for O₂ evolution (b) CuIn alloy for CO₂ reduction. (c) Perovskite-BiVO₄ tandem device shown from the CuIn catalyst. (d) an artificial leaf tandem photoelectrochemical device architecture. (e) a 10 x10 array (total device

area: 1,000 cm²) of perovskite-BiVO₄ artificial leaves in a reactor. Figure (d) is adapted from ¹⁷⁴. Perovskite composition: (FA_{0.7}Cs_{0.3}Pb(I_{0.9}Br_{0.1})₃).

Chapter 7. Conclusion and outlook

7.1 Perovskite evaporation summary

In this thesis, we have carefully developed deposition protocols for multisource evaporation of a range of halide perovskite absorber materials. The tooling factor calibration, source and rate control parameters, precursor quality, device optimisation and evaporator maintenance have been explored and we identify how sensitive the resulting film quality is to these properties. This system is able to evaporate metal-halide perovskite with different compositions and thickness on a variety of substrates, opening promising avenues for various optoelectronic devices application (solar cells, LED or X-ray detectors).

7.2 Summary of this thesis

Chapter 4 highlights the importance of substrate choices (or underlying layer before perovskite). It can significantly affect the perovskite morphology and preferred structural orientation. Excess PbI_2 for perovskite leads to improvement in perovskite air stability, PLQE and device performance. The QFLS calculation was conducted to analyse the power loss from bulk perovskite film, ETL and HTL contact, indicating the further optimisation path to improve the device V_{OC} . One crucial thing is revealing that the evaporation rate is critical to dictate the halide distribution in perovskite film and also affects the JV curve behaviour. In Chapter 5, we start to address the QFLS loss based on the results from chapter 4 and optimise the interface between HTM/perovskite to improve the device performance. Furthermore, evaporated C60 and BCP are used instead of spin-coating PCBM and BCP to fulfil the fully evaporated perovskite solar cells in future. By optimising the bottom contact loss, the device V_{OC} is improved by around 50 mV with MeO-2PACz, compared to the one with PTAA, and the device PCE can achieve >20%. All-perovskite tandem solar cells are employed to further improve the device performance. The PbBr_2 precursor as a fourth source is utilised to increase the perovskite bandgap. The XRD, PL, TRPL, nano-XRF measurement are done to analyse the film quality with the device data to select the promising composition for all-perovskite tandem solar cell. A bandgap of 1.77 eV perovskite shows a reasonable V_{OC} whilst minimising phase

segregation and is used for tandem solar cells. The surface passivation treatment by EDAI for WBG perovskite is used to minimise the device loss and the device loss analysis is performed. Further development of all-perovskite tandem solar cell with ALD-SnO_x and Pb/Sn perovskite devices are also optimised. In the end, a 24.1% all-perovskite tandem solar cell is presented, showing a tandem device based on multisource evaporation. Finally, we demonstrate that perovskite can be used in a broad range of applications. The perovskite deposited on textured Si solar cell shows uniform coating, enable to keep the pyramid morphology for improving light trapping. The sticking coefficient is affected by surface morphology, revealing that perovskite formation is different. Beyond solar cells, we develop artificial leaf tandem photoelectrochemical (PEC) devices with a 5 x 3 cm² size, showing the potential to fabricate autonomous fuel production. This thesis expands the knowledge of multisource evaporation of perovskite film and applies this to solar cell applications.

7.3 Key findings from cumulative experience

We have identified several factors that can affect the quality of perovskite films and the performance of resulting solar cells. First, a very “clean” substrate is vital to have a uniform perovskite coating, as the substrate's surface energy can affect the sticking coefficient of perovskite precursors. Pin-holes or composition variation can be observed if the substrate is not sufficiently clean. The criteria of a clean substrate for evaporation is much higher than solution-processed film analogues. Secondly, for the perovskite evaporation, the precursor's quality can cause considerable device variation, even though from bulk measurements such as XRD the perovskite structure variation appears negligible. For PbI₂, we use fresh PbI₂ powder in every batch. I have noticed that the resulting perovskite solar cells show huge variation “after” EDAI surface passivation due to the quality of PbI₂. We suspect that the perovskite structure in the nanoscale could be different, and the surface treatment, accompanied with solvent, IPA, might reconstruct the surface and affect the device performance if the PbI₂ is of suboptimal quality. A comprehensive study by scanning electronic diffraction measurements might be helpful to address this.

Another precursor, FAI, shows batch-to-batch device performance variation; even though the manufacturer believes their material quality is consistent. The FAI powder is fresh every time before the deposition, and evaporation temperature of FAI must be controlled very carefully. We have also noticed the chamber pressure variation when the FAI is overheated, and the remaining powder turns dark from white.¹⁷⁵ We have a particular batch of FAI from Greatcell Solar providing excellent device performance. Unfortunately, this batch has sold out. It becomes critical to establish methodologies to ensure the quality of precursors batches is high but also reliable and reproducible over time. We encourage companies to pay attention to this very important task, which is key for the successful implementation of perovskite technologies in industrial mass production processes.

To have a better deposition rate, the QCM for PbI_2 is changed each time before the deposition (to ensure sure the QCM lifetime is >92% at the start of each run). Also, the PID parameter of the temperature source need to be optimised for different chemicals as their heat-to-deposition rate response is different. Moreover, the pumping speed of the evaporator is essential to the perovskite quality. The faster pumping speed has the ability to remove impurities/by-products during evaporation, leading to a better device performance. Our evaporator chamber has experienced a severe contamination due to the by-products of phenethylammonium iodide (PEAI) for 2D perovskite deposition. The PEAi evaporating temperature is as low as 100°C, and it might form a gas phase after evaporation, existing in the chamber without sticking in the cold wall or chamber for a period of time. Our 3D perovskite sample, therefore, could not be reproduced for around 6 months until a thorough chamber cleaning, including the chamber wall, inner cold wall, substrate stage, chamber stage, cold trap, the chamber area close to the pump and turbo. Hence, I suggest a careful evaluation is essential before using a new organic chemical.

7.4 Outlook and future work

We have demonstrated the possibility of using multisource evaporation for perovskite deposition and solar cell fabrication. There are several paths to make perovskite technology have a real impact and transfer the knowledge from lab research to industrial manufacturing to provide sustainable energy.

- (1) *Reproducibility investigation*: If we simplify the multisource evaporation process for perovskite deposition, we would initially assume that for any evaporation, we “only” need to control the temperature of each precursor to have the desired rate for a specific perovskite composition. However, there are several issues here. First, the perovskite precursor quality plays an important role here. Even if the material is from the same supplier; there is still batch-to-batch variation. Hence, the material quality analysis is critical, and how it relates to the defects, crystal structure, PL in perovskite film is essential. Furthermore, the by-products, especially from organic material, are critical to device performance. The cold walls and LN₂ trap system can mitigate the by-products and improve reproducibility, but these designs might be a challenge for a manufacturing line due to the cost.
- (2) *High-efficient perovskite film quality*: To date, most evaporated perovskite films show low PLQE (<1%), compared to their solution-processed counterpart. For solution-based perovskites, the optimisation can be screened rapidly by composition engineering, additives or dopants strategy, anti-solvent process and/or solvents ratio tuning, leading to highly efficient samples. However, for multisource evaporation, we are limited by the number of evaporation sources, chamber design and the potential of material degradation during the evaporation. Also, we have shown that commonly used contact layer (2-PACz, for example) is not suitable for vacuum-deposited perovskite. A thorough investigation is required to improve radiative recombination in evaporated perovskite and understand the fundamental reasons for these differences. The choices of perovskite precursors and/or contact layers might need to expand from the current multisource evaporation system.
- (3) *All-perovskite tandem solar cells*: To achieve a 30% all-perovskite tandem solar cell, a reasonable WBG and NBG perovskite with a minimise optical loss as a RJ layer is

required. Here, if 1 % PLQE of p-i-n-stack layers from WBG and NBG with a bandgap of 1.77 eV and 1.25 eV is achievable, the sub-cell device V_{OC} can reach 1.36 V and 0.88 V, respectively, resulting in a sum V_{OC} of 2.24 V for 2T all-perovskite tandem solar cells. However, the state-of-the-art tandem device demonstrates a V_{OC} of 2.13 V,¹⁷⁶ showing that further improvement is still possible. A 90% EQE (considering all the optical loss from TCO substrate and parasitic loss in CTL) in 1.25 eV NBG perovskite solar cell can achieve 33.8 mA/cm² which is reasonable as many reports have shown J_{SC} close to this number.^{72,147} In a tandem system, two subcells are connected in series; therefore, the J_{SC} is limited by current from the lowest current output. Assuming the current matching in two subcells is ideal, we should be able to get 16.9 mA/cm² in tandem device. To combine the V_{OC} and J_{SC} , we should be able to get a PCE of 30.3 %, where we assume the FF is 80%. In fact, a FF of 80% in tandem solar cell and 1% PLQE in NBG p-i-n have been reported.^{72,147} However, WBG perovskite still shows relative low PLQE, leading to a significant loss in device V_{OC} . Therefore, to achieve a 30% all-perovskite solar cell, the development of WBG perovskite solar cells is important.

(4) *Scalability*: Vacuum deposition is a well-established system in industrial manufacture. This technology is potentially valuable for large-scale perovskite. We deposited a perovskite film on a 10x10 cm² plastic substrate, demonstrating a scale-up and flexible concept. Further studies to solve the sheet resistance of TCO is essential by metal fingers or modular design.

Reference

1. Ritchie, H. Global primary energy consumption by source. *Our World in Data* (2021).
2. Birol, F. World Energy Outlook 2019. (2019).
3. *World Energy Resources 2013 Survey*. (2013).
4. *World Energy Outlook 2021*. (2021).
5. Becquerel. Recherches sur les effets de la radiation chimique de la lumiere solaire au moyen des courants electriques. *Comptes Rendus de L'Academie des Sciences* **9**, 145–149 (1839).
6. *Best Research-Cell Efficiency Chart*. (2022).
7. Sopian, K., Cheow, S. L. & Zaidi, S. H. An overview of crystalline silicon solar cell technology: Past, present, and future. *AIP Conference Proceedings* **1877**, 020004 (2017).
8. Feldman, D. *et al.* U.S. Solar Photovoltaic System and Energy Storage Cost Benchmark: Q1 2020. (2020).
9. Chung, J. *et al.* Record-efficiency flexible perovskite solar cell and module enabled by a porous-planar structure as an electron transport layer. *Energy Environ. Sci.* **13**, 4854–4861 (2020).
10. Anaya, M., Lozano, G., Calvo, M. E. & Míguez, H. ABX₃ Perovskites for Tandem Solar Cells. *Joule* **1**, 769–793 (2017).
11. Al-Ashouri Amran *et al.* Monolithic perovskite/silicon tandem solar cell with >29% efficiency by enhanced hole extraction. *Science* **370**, 1300–1309 (2020).
12. Noh, J. H., Im, S. H., Heo, J. H., Mandal, T. N. & Seok, S. I. Chemical Management for Colorful, Efficient, and Stable Inorganic–Organic Hybrid Nanostructured Solar Cells. *Nano Lett.* **13**, 1764–1769 (2013).
13. Palmstrom, A. F. *et al.* Enabling Flexible All-Perovskite Tandem Solar Cells. *Joule* **3**, 2193–2204 (2019).

14. Chang, H.-Y., Tsai, C.-Y., Lin, Y.-Q., Shih, T.-S. & Lin, W.-C. Total body burden arising from a week's repeated dermal exposure to N,N-dimethylformamide. *Occup Environ Med* **62**, 151 (2005).
15. Roß, M., Stutz, M. B. & Albrecht, S. Revealing the Role of Methylammonium Iodide Purity on the Vapor-Phase Deposition Process of Perovskites. *Solar RRL*, 2200500 (2022).
16. Stranks, S. D. & Snaith, H. J. Metal-halide perovskites for photovoltaic and light-emitting devices. *Nature Nanotechnology* **10**, 391–402 (2015).
17. Tong Jinhui *et al.* Carrier lifetimes of >1 μ s in Sn-Pb perovskites enable efficient all-perovskite tandem solar cells. *Science* **364**, 475–479 (2019).
18. deQuilettes, D. W. *et al.* Charge-Carrier Recombination in Halide Perovskites. *Chem. Rev.* **119**, 11007–11019 (2019).
19. Sahli, F. *et al.* Fully textured monolithic perovskite/silicon tandem solar cells with 25.2% power conversion efficiency. *Nature Materials* **17**, 820–826 (2018).
20. Leijtens, T., Bush, K. A., Prasanna, R. & McGehee, M. D. Opportunities and challenges for tandem solar cells using metal halide perovskite semiconductors. *Nature Energy* **3**, 828–838 (2018).
21. MØLLER, CHR. KN. Crystal Structure and Photoconductivity of Cæsium Plumbohalides. *Nature* **182**, 1436–1436 (1958).
22. Weber, D. CH₃NH₃PbX₃, ein Pb(II)-System mit kubischer Perowskitstruktur / CH₃NH₃PbX₃, a Pb(II)-System with Cubic Perovskite Structure. **33**, 1443–1445 (1978).
23. Gholipour, S. & Saliba, M. Chapter 1 - Bandgap tuning and compositional exchange for lead halide perovskite materials. in *Characterization Techniques for Perovskite Solar Cell Materials* (eds. Pazoki, M., Hagfeldt, A. & Edvinsson, T.) 1–22 (Elsevier, 2020). doi:10.1016/B978-0-12-814727-6.00001-3.
24. Kojima, A., Teshima, K., Shirai, Y. & Miyasaka, T. Organometal Halide Perovskites as Visible-Light Sensitizers for Photovoltaic Cells. *J. Am. Chem. Soc.* **131**, 6050–6051 (2009).
25. Kim, H.-S. *et al.* Lead Iodide Perovskite Sensitized All-Solid-State Submicron Thin Film Mesoscopic Solar Cell with Efficiency Exceeding 9%. *Scientific Reports* **2**, 591 (2012).

26. Lee, M. M., Teuscher, J., Miyasaka, T., Murakami, T. N. & Snaith, H. J. Efficient Hybrid Solar Cells Based on Meso-Superstructured Organometal Halide Perovskites. *Science* **338**, 643–647 (2012).
27. Stranks, S. D. *et al.* Electron-Hole Diffusion Lengths Exceeding 1 Micrometer in an Organometal Trihalide Perovskite Absorber. *Science* **342**, 341 (2013).
28. Stranks, S. D., Hoye, R. L. Z., Di, D., Friend, R. H. & Deschler, F. The Physics of Light Emission in Halide Perovskite Devices. *Advanced Materials* **31**, 1803336 (2019).
29. Richter, J. M. *et al.* Ultrafast carrier thermalization in lead iodide perovskite probed with two-dimensional electronic spectroscopy. *Nature Communications* **8**, 376 (2017).
30. Fu, J. *et al.* Hot carrier cooling mechanisms in halide perovskites. *Nature Communications* **8**, 1300 (2017).
31. Guo, Z. *et al.* Long-range hot-carrier transport in hybrid perovskites visualized by ultrafast microscopy. *Science* **356**, 59–62 (2017).
32. Luo, D., Su, R., Zhang, W., Gong, Q. & Zhu, R. Minimizing non-radiative recombination losses in perovskite solar cells. *Nature Reviews Materials* **5**, 44–60 (2020).
33. Price, M. B. *et al.* Hot-carrier cooling and photoinduced refractive index changes in organic–inorganic lead halide perovskites. *Nature Communications* **6**, 8420 (2015).
34. Bretschneider, S. A. *et al.* Quantifying Polaron Formation and Charge Carrier Cooling in Lead-Iodide Perovskites. *Advanced Materials* **30**, 1707312 (2018).
35. Miyata, K., Atallah, T. L. & Zhu, X.-Y. Lead halide perovskites: Crystal-liquid duality, phonon glass electron crystals, and large polaron formation. *Science Advances* **3**, e1701469.
36. Stranks, S. D. *et al.* Recombination Kinetics in Organic-Inorganic Perovskites: Excitons, Free Charge, and Subgap States. *Phys. Rev. Applied* **2**, 034007 (2014).
37. Staub, F., Rau, U. & Kirchartz, T. Statistics of the Auger Recombination of Electrons and Holes via Defect Levels in the Band Gap—Application to Lead-Halide Perovskites. *ACS Omega* **3**, 8009–8016 (2018).
38. Chen, B., Rudd, P. N., Yang, S., Yuan, Y. & Huang, J. Imperfections and their passivation in halide perovskite solar cells. *Chem. Soc. Rev.* **48**, 3842–3867 (2019).

39. Shockley, W. & Queisser, H. J. Detailed Balance Limit of Efficiency of p-n Junction Solar Cells. *Journal of Applied Physics* **32**, 510–519 (1961).
40. Wurfel, P. The chemical potential of radiation. *Journal of Physics C: Solid State Physics* **15**, 3967–3985 (1982).
41. Stolterfoht, M. *et al.* Visualization and suppression of interfacial recombination for high-efficiency large-area pin perovskite solar cells. *Nature Energy* **3**, 847–854 (2018).
42. Stolterfoht, M. *et al.* The impact of energy alignment and interfacial recombination on the internal and external open-circuit voltage of perovskite solar cells. *Energy Environ. Sci.* **12**, 2778–2788 (2019).
43. Kirchartz, T., Márquez, J. A., Stolterfoht, M. & Unold, T. Photoluminescence-Based Characterization of Halide Perovskites for Photovoltaics. *Advanced Energy Materials* **10**, 1904134 (2020).
44. Tress, W. *et al.* Predicting the Open-Circuit Voltage of CH₃NH₃PbI₃ Perovskite Solar Cells Using Electroluminescence and Photovoltaic Quantum Efficiency Spectra: the Role of Radiative and Non-Radiative Recombination. *Advanced Energy Materials* **5**, 1400812 (2015).
45. Tress, W. Perovskite Solar Cells on the Way to Their Radiative Efficiency Limit – Insights Into a Success Story of High Open-Circuit Voltage and Low Recombination. *Advanced Energy Materials* **7**, 1602358 (2017).
46. Luo, D. *et al.* Enhanced photovoltage for inverted planar heterojunction perovskite solar cells. *Science* **360**, 1442 (2018).
47. Jiang, Q. *et al.* Surface passivation of perovskite film for efficient solar cells. *Nature Photonics* **13**, 460–466 (2019).
48. Yang, S. *et al.* Tailoring Passivation Molecular Structures for Extremely Small Open-Circuit Voltage Loss in Perovskite Solar Cells. *J. Am. Chem. Soc.* **141**, 5781–5787 (2019).
49. Tauc, J. Optical properties and electronic structure of amorphous Ge and Si. *Materials Research Bulletin* **3**, 37–46 (1968).
50. Krückemeier, L., Rau, U., Stolterfoht, M. & Kirchartz, T. How to Report Record Open-Circuit Voltages in Lead-Halide Perovskite Solar Cells. *Advanced Energy Materials* **10**, 1902573 (2020).

51. Rau, U., Blank, B., Müller, T. C. M. & Kirchartz, T. Efficiency Potential of Photovoltaic Materials and Devices Unveiled by Detailed-Balance Analysis. *Phys. Rev. Applied* **7**, 044016 (2017).
52. Hoke, E. T. *et al.* Reversible photo-induced trap formation in mixed-halide hybrid perovskites for photovoltaics. *Chem. Sci.* **6**, 613–617 (2015).
53. Knight, A. J. & Herz, L. M. Preventing phase segregation in mixed-halide perovskites: a perspective. *Energy Environ. Sci.* **13**, 2024–2046 (2020).
54. Barker, A. J. *et al.* Defect-Assisted Photoinduced Halide Segregation in Mixed-Halide Perovskite Thin Films. *ACS Energy Lett.* **2**, 1416–1424 (2017).
55. Brennan, M. C., Draguta, S., Kamat, P. V. & Kuno, M. Light-Induced Anion Phase Segregation in Mixed Halide Perovskites. *ACS Energy Lett.* **3**, 204–213 (2018).
56. Braly, I. L. *et al.* Current-Induced Phase Segregation in Mixed Halide Hybrid Perovskites and its Impact on Two-Terminal Tandem Solar Cell Design. *ACS Energy Lett.* **2**, 1841–1847 (2017).
57. Haruyama, J., Sodeyama, K., Han, L. & Tateyama, Y. First-Principles Study of Ion Diffusion in Perovskite Solar Cell Sensitizers. *J. Am. Chem. Soc.* **137**, 10048–10051 (2015).
58. Meloni, S. *et al.* Ionic polarization-induced current–voltage hysteresis in $\text{CH}_3\text{NH}_3\text{PbX}_3$ perovskite solar cells. *Nature Communications* **7**, 10334 (2016).
59. Azpiroz, J. M., Mosconi, E., Bisquert, J. & De Angelis, F. Defect migration in methylammonium lead iodide and its role in perovskite solar cell operation. *Energy Environ. Sci.* **8**, 2118–2127 (2015).
60. Zhou, Y., Poli, I., Meggiolaro, D., De Angelis, F. & Petrozza, A. Defect activity in metal halide perovskites with wide and narrow bandgap. *Nature Reviews Materials* **6**, 986–1002 (2021).
61. Oranskaia, A., Yin, J., Bakr, O. M., Brédas, J.-L. & Mohammed, O. F. Halogen Migration in Hybrid Perovskites: The Organic Cation Matters. *J. Phys. Chem. Lett.* **9**, 5474–5480 (2018).

62. Barboni, D. & De Souza, R. A. The thermodynamics and kinetics of iodine vacancies in the hybrid perovskite methylammonium lead iodide. *Energy Environ. Sci.* **11**, 3266–3274 (2018).
63. Al-Ashouri, A. *et al.* Conformal monolayer contacts with lossless interfaces for perovskite single junction and monolithic tandem solar cells. *Energy Environ. Sci.* **12**, 3356–3369 (2019).
64. McMeekin, D. P. *et al.* A mixed-cation lead mixed-halide perovskite absorber for tandem solar cells. *Science* **351**, 151–155 (2016).
65. Bush, K. A. *et al.* Compositional Engineering for Efficient Wide Band Gap Perovskites with Improved Stability to Photoinduced Phase Segregation. *ACS Energy Lett.* **3**, 428–435 (2018).
66. Mosconi, E. & De Angelis, F. Mobile Ions in Organohalide Perovskites: Interplay of Electronic Structure and Dynamics. *ACS Energy Lett.* **1**, 182–188 (2016).
67. Gratia, P. *et al.* Intrinsic Halide Segregation at Nanometer Scale Determines the High Efficiency of Mixed Cation/Mixed Halide Perovskite Solar Cells. *J. Am. Chem. Soc.* **138**, 15821–15824 (2016).
68. Unger, E. L. *et al.* Roadmap and roadblocks for the band gap tunability of metal halide perovskites. *J. Mater. Chem. A* **5**, 11401–11409 (2017).
69. Yu, Y. *et al.* Synergistic Effects of Lead Thiocyanate Additive and Solvent Annealing on the Performance of Wide-Bandgap Perovskite Solar Cells. *ACS Energy Lett.* **2**, 1177–1182 (2017).
70. Mahesh, S. *et al.* Revealing the origin of voltage loss in mixed-halide perovskite solar cells. *Energy Environ. Sci.* **13**, 258–267 (2020).
71. Jeong, J. *et al.* Pseudo-halide anion engineering for α -FAPbI₃ perovskite solar cells. *Nature* **592**, 381–385 (2021).
72. Lin, R. *et al.* All-perovskite tandem solar cells with improved grain surface passivation. *Nature* **603**, 73–78 (2022).
73. Liu, M., Johnston, M. B. & Snaith, H. J. Efficient planar heterojunction perovskite solar cells by vapour deposition. *Nature* **501**, 395–398 (2013).

74. Malinkiewicz, O. *et al.* Perovskite solar cells employing organic charge-transport layers. *Nature Photonics* **8**, 128–132 (2014).
75. Ono, L. K., Leyden, M. R., Wang, S. & Qi, Y. Organometal halide perovskite thin films and solar cells by vapor deposition. *Journal of Materials Chemistry A* **4**, 6693–6713 (2016).
76. Momblona, C. *et al.* Efficient vacuum deposited p-i-n and n-i-p perovskite solar cells employing doped charge transport layers. *Energy Environ. Sci.* **9**, 3456–3463 (2016).
77. Olthof, S. & Meerholz, K. Substrate-dependent electronic structure and film formation of MAPbI₃ perovskites. *Scientific Reports* **7**, 40267 (2017).
78. Lohmann, K. B. *et al.* Control over Crystal Size in Vapor Deposited Metal-Halide Perovskite Films. *ACS Energy Lett.* **5**, 710–717 (2020).
79. Roß, M. *et al.* Co-Evaporated Formamidinium Lead Iodide Based Perovskites with 1000 h Constant Stability for Fully Textured Monolithic Perovskite/Silicon Tandem Solar Cells. *Advanced Energy Materials* **11**, 2101460 (2021).
80. Heinze, K. L. *et al.* Importance of methylammonium iodide partial pressure and evaporation onset for the growth of co-evaporated methylammonium lead iodide absorbers. *Scientific Reports* **11**, 15299 (2021).
81. Borchert, J. *et al.* Impurity Tracking Enables Enhanced Control and Reproducibility of Hybrid Perovskite Vapor Deposition. *ACS Appl. Mater. Interfaces* **11**, 28851–28857 (2019).
82. Turren-Cruz, S.-H., Hagfeldt, A. & Saliba, M. Methylammonium-free, high-performance, and stable perovskite solar cells on a planar architecture. *Science* **362**, 449 (2018).
83. Gil-Escrig, L. *et al.* Vacuum Deposited Triple-Cation Mixed-Halide Perovskite Solar Cells. *Advanced Energy Materials* **8**, 1703506 (2018).
84. Borchert, J. *et al.* Large-Area, Highly Uniform Evaporated Formamidinium Lead Triiodide Thin Films for Solar Cells. *ACS Energy Lett.* **2**, 2799–2804 (2017).
85. Lin, Q., Armin, A., Nagiri, R. C. R., Burn, P. L. & Meredith, P. Electro-optics of perovskite solar cells. *Nature Photonics* **9**, 106–112 (2015).
86. Pérez-del-Rey, D., Boix, P. P., Sessolo, M., Hadipour, A. & Bolink, H. J. Interfacial Modification for High-Efficiency Vapor-Phase-Deposited Perovskite Solar Cells Based on a Metal Oxide Buffer Layer. *J. Phys. Chem. Lett.* **9**, 1041–1046 (2018).

87. Chen, C.-Y. *et al.* All-Vacuum-Deposited Stoichiometrically Balanced Inorganic Cesium Lead Halide Perovskite Solar Cells with Stabilized Efficiency Exceeding 11%. *Advanced Materials* **29**, 1605290 (2017).
88. Anaya, M., Lozano, G., Calvo, M. E. & Míguez, H. ABX₃ Perovskites for Tandem Solar Cells. *Joule* **1**, 769–793 (2017).
89. Eperon Giles E. *et al.* Perovskite-perovskite tandem photovoltaics with optimized band gaps. *Science* **354**, 861–865 (2016).
90. Eperon, G. E. *et al.* Perovskite-perovskite tandem photovoltaics with optimized band gaps. *Science* **354**, 861–865 (2016).
91. Hörantner, M. T. *et al.* The Potential of Multijunction Perovskite Solar Cells. *ACS Energy Lett.* **2**, 2506–2513 (2017).
92. Bowman, A. R. *et al.* Relaxed Current Matching Requirements in Highly Luminescent Perovskite Tandem Solar Cells and Their Fundamental Efficiency Limits. *ACS Energy Lett.* **6**, 612–620 (2021).
93. Lin, R. *et al.* Monolithic all-perovskite tandem solar cells with 24.8% efficiency exploiting comproportionation to suppress Sn(ii) oxidation in precursor ink. *Nature Energy* **4**, 864–873 (2019).
94. Yu, Z. *et al.* Simplified interconnection structure based on C60/SnO_{2-x} for all-perovskite tandem solar cells. *Nature Energy* **5**, 657–665 (2020).
95. Datta, K. *et al.* Monolithic All-Perovskite Tandem Solar Cells with Minimized Optical and Energetic Losses. *Advanced Materials* **34**, 2110053 (2022).
96. Abdollahi Nejand, B. *et al.* Scalable two-terminal all-perovskite tandem solar modules with a 19.1% efficiency. *Nature Energy* **7**, 620–630 (2022).
97. Destruel, P. *et al.* Influence of indium tin oxide treatment using UV–ozone and argon plasma on the photovoltaic parameters of devices based on organic discotic materials. *Polymer International* **55**, 601–607 (2006).
98. Sugiyama, K., Ishii, H., Ouchi, Y. & Seki, K. Dependence of indium–tin–oxide work function on surface cleaning method as studied by ultraviolet and x-ray photoemission spectroscopies. *Journal of Applied Physics* **87**, 295–298 (2000).

99. de Mello, J. C., Wittmann, H. F. & Friend, R. H. An improved experimental determination of external photoluminescence quantum efficiency. *Advanced Materials* **9**, 230–232 (1997).
100. Caprioglio, P. *et al.* On the Relation between the Open-Circuit Voltage and Quasi-Fermi Level Splitting in Efficient Perovskite Solar Cells. *Advanced Energy Materials* **9**, 1901631 (2019).
101. Stolterfoht, M. *et al.* Approaching the fill factor Shockley–Queisser limit in stable, dopant-free triple cation perovskite solar cells. *Energy Environ. Sci.* **10**, 1530–1539 (2017).
102. Krückemeier, L., Rau, U., Stolterfoht, M. & Kirchartz, T. How to Report Record Open-Circuit Voltages in Lead-Halide Perovskite Solar Cells. *Advanced Energy Materials* **10**, 1902573 (2020).
103. Holloway, H., Richards, J. L., Bobb, L. C., Perry, J. & Zimmerman, E. Oriented Growth of Semiconductors. IV. Vacuum Deposition of Epitaxial Indium Antimonide. *Journal of Applied Physics* **37**, 4694–4699 (1966).
104. Kazmerski, L. L., White, F. R., Ayyagari, M. S., Juang, Y. J. & Patterson, R. P. Growth and characterization of thin-film compound semiconductor photovoltaic heterojunctions. *Journal of Vacuum Science and Technology* **14**, 65–68 (1977).
105. Swartwout, R., Hoerantner, M. T. & Bulović, V. Scalable Deposition Methods for Large-area Production of Perovskite Thin Films. *ENERGY & ENVIRONMENTAL MATERIALS* **2**, 119–145 (2019).
106. Pérez-del-Rey, D., Boix, P. P., Sessolo, M., Hadipour, A. & Bolink, H. J. Interfacial Modification for High-Efficiency Vapor-Phase-Deposited Perovskite Solar Cells Based on a Metal Oxide Buffer Layer. *J. Phys. Chem. Lett.* **9**, 1041–1046 (2018).
107. Li, J. *et al.* Highly Efficient Thermally Co-evaporated Perovskite Solar Cells and Mini-modules. *Joule* **4**, 1035–1053 (2020).
108. Juarez-Perez, E. J., Hawash, Z., Raga, S. R., Ono, L. K. & Qi, Y. Thermal degradation of CH₃NH₃PbI₃ perovskite into NH₃ and CH₃I gases observed by coupled thermogravimetry–mass spectrometry analysis. *Energy Environ. Sci.* **9**, 3406–3410 (2016).
109. Khenkin, M. V. *et al.* Consensus statement for stability assessment and reporting for perovskite photovoltaics based on ISOS procedures. *Nature Energy* **5**, 35–49 (2020).

110. Zheng, X. *et al.* Improved Phase Stability of Formamidinium Lead Triiodide Perovskite by Strain Relaxation. *ACS Energy Lett.* **1**, 1014–1020 (2016).
111. Kim, B.-S., Gil-Escrig, L., Sessolo, M. & Bolink, H. J. Deposition Kinetics and Compositional Control of Vacuum-Processed CH₃NH₃PbI₃ Perovskite. *J. Phys. Chem. Lett.* **11**, 6852–6859 (2020).
112. Gao, X.-X. *et al.* Stable and High-Efficiency Methylammonium-Free Perovskite Solar Cells. *Advanced Materials* **32**, 1905502 (2020).
113. Nahory, R. E., Pollack, M. A., Johnston, W. D. & Barns, R. L. Band gap versus composition and demonstration of Vegard's law for In_{1-x}GaxAsyP_{1-y} lattice matched to InP. *Appl. Phys. Lett.* **33**, 659–661 (1978).
114. Schelhas, L. T. *et al.* Insights into operational stability and processing of halide perovskite active layers. *Energy Environ. Sci.* **12**, 1341–1348 (2019).
115. Yu, Y. *et al.* Improving the Performance of Formamidinium and Cesium Lead Triiodide Perovskite Solar Cells using Lead Thiocyanate Additives. *ChemSusChem* **9**, 3288–3297 (2016).
116. Subbiah, A. S. *et al.* Stable p-i-n FAPbBr₃ Devices with Improved Efficiency Using Sputtered ZnO as Electron Transport Layer. *Advanced Materials Interfaces* **4**, 1601143 (2017).
117. Yuan, D.-X., Gorka, A., Xu, M.-F., Wang, Z.-K. & Liao, L.-S. Inverted planar NH₂CHNH₂PbI₃ perovskite solar cells with 13.56% efficiency via low temperature processing. *Phys. Chem. Chem. Phys.* **17**, 19745–19750 (2015).
118. Marronnier, A. *et al.* Anharmonicity and Disorder in the Black Phases of Cesium Lead Iodide Used for Stable Inorganic Perovskite Solar Cells. *ACS Nano* **12**, 3477–3486 (2018).
119. Sutton, R. J. *et al.* Cubic or Orthorhombic? Revealing the Crystal Structure of Metastable Black-Phase CsPbI₃ by Theory and Experiment. *ACS Energy Lett.* **3**, 1787–1794 (2018).
120. Becker, P. *et al.* Low Temperature Synthesis of Stable γ -CsPbI₃ Perovskite Layers for Solar Cells Obtained by High Throughput Experimentation. *Advanced Energy Materials* **9**, 1900555 (2019).

121. Jacobsson, T. J. *et al.* Unreacted PbI₂ as a Double-Edged Sword for Enhancing the Performance of Perovskite Solar Cells. *J. Am. Chem. Soc.* **138**, 10331–10343 (2016).
122. Park, B. *et al.* Understanding how excess lead iodide precursor improves halide perovskite solar cell performance. *Nature Communications* **9**, 3301 (2018).
123. Petrus, M. L. *et al.* The Influence of Water Vapor on the Stability and Processing of Hybrid Perovskite Solar Cells Made from Non-Stoichiometric Precursor Mixtures. *ChemSusChem* **9**, 2699–2707 (2016).
124. Yang, X. *et al.* Buried Interfaces in Halide Perovskite Photovoltaics. *Advanced Materials* **33**, 2006435 (2021).
125. Stranks, S. D. Nonradiative Losses in Metal Halide Perovskites. *ACS Energy Lett.* **2**, 1515–1525 (2017).
126. Wang, R. *et al.* A Review of Perovskites Solar Cell Stability. *Advanced Functional Materials* **29**, 1808843 (2019).
127. Chirvony, V. S. *et al.* Short Photoluminescence Lifetimes in Vacuum-Deposited CH₃NH₃PbI₃ Perovskite Thin Films as a Result of Fast Diffusion of Photogenerated Charge Carriers. *J. Phys. Chem. Lett.* **10**, 5167–5172 (2019).
128. Chiang, Y.-H. *et al.* Efficient all-perovskite tandem solar cells by dual-interface optimisation of vacuum-deposited wide-bandgap perovskite. (2022) doi:10.48550/ARXIV.2208.03556.
129. France, R. M. *et al.* Triple-junction solar cells with 39.5% terrestrial and 34.2% space efficiency enabled by thick quantum well superlattices. *Joule* **6**, 1121–1135 (2022).
130. Frohna, K. *et al.* Nanoscale chemical heterogeneity dominates the optoelectronic response of alloyed perovskite solar cells. *Nature Nanotechnology* (2021) doi:10.1038/s41565-021-01019-7.
131. Eperon, G. E. *et al.* Formamidinium lead trihalide: a broadly tunable perovskite for efficient planar heterojunction solar cells. *Energy Environ. Sci.* **7**, 982–988 (2014).
132. Gil-Escrig, L. *et al.* Efficient Wide-Bandgap Mixed-Cation and Mixed-Halide Perovskite Solar Cells by Vacuum Deposition. *ACS Energy Lett.* **6**, 827–836 (2021).

133. Igual-Muñoz, A. M., Ávila, J., Boix, P. P. & Bolink, H. J. FAPb_{0.5}Sn_{0.5}I₃: A Narrow Bandgap Perovskite Synthesized through Evaporation Methods for Solar Cell Applications. *Solar RRL* **4**, 1900283 (2020).
134. Igual-Muñoz, A. M. *et al.* Room-Temperature Vacuum Deposition of CsPbI₂Br Perovskite Films from Multiple Sources and Mixed Halide Precursors. *Chem. Mater.* **32**, 8641–8652 (2020).
135. Chiang, Y.-H., Anaya, M. & Stranks, S. D. Multisource Vacuum Deposition of Methylammonium-Free Perovskite Solar Cells. *ACS Energy Lett.* **5**, 2498–2504 (2020).
136. Roß, M. *et al.* Co-Evaporated Formamidinium Lead Iodide Based Perovskites with 1000 h Constant Stability for Fully Textured Monolithic Perovskite/Silicon Tandem Solar Cells. *Advanced Energy Materials* **11**, 2101460 (2021).
137. Aydin, E. *et al.* Interplay between temperature and bandgap energies on the outdoor performance of perovskite/silicon tandem solar cells. *Nature Energy* **5**, 851–859 (2020).
138. Ávila, J. *et al.* High voltage vacuum-deposited CH₃NH₃PbI₃–CH₃NH₃PbI₃ tandem solar cells. *Energy Environ. Sci.* **11**, 3292–3297 (2018).
139. Eperon, G. E., Hörantner, M. T. & Snaith, H. J. Metal halide perovskite tandem and multiple-junction photovoltaics. *Nature Reviews Chemistry* **1**, 0095 (2017).
140. Brivio, F., Caetano, C. & Walsh, A. Thermodynamic Origin of Photoinstability in the CH₃NH₃Pb(I_{1-x}Br_x)₃ Hybrid Halide Perovskite Alloy. *J. Phys. Chem. Lett.* **7**, 1083–1087 (2016).
141. Bischak, C. G. *et al.* Origin of Reversible Photoinduced Phase Separation in Hybrid Perovskites. *Nano Lett.* **17**, 1028–1033 (2017).
142. Draguta, S. *et al.* Rationalizing the light-induced phase separation of mixed halide organic–inorganic perovskites. *Nature Communications* **8**, 200 (2017).
143. Oliver, R. D. J. *et al.* Understanding and suppressing non-radiative losses in methylammonium-free wide-bandgap perovskite solar cells. *Energy Environ. Sci.* **15**, 714–726 (2022).
144. Doherty, T. A. S. *et al.* Performance-limiting nanoscale trap clusters at grain junctions in halide perovskites. *Nature* **580**, 360–366 (2020).

145. Brennan, M. C., Draguta, S., Kamat, P. V. & Kuno, M. Light-Induced Anion Phase Segregation in Mixed Halide Perovskites. *ACS Energy Lett.* **3**, 204–213 (2018).
146. Stranks, S. D. *et al.* Recombination Kinetics in Organic-Inorganic Perovskites: Excitons, Free Charge, and Subgap States. *Phys. Rev. Applied* **2**, 034007 (2014).
147. Hu, S. *et al.* Optimized carrier extraction at interfaces for 23.6% efficient tin–lead perovskite solar cells. *Energy Environ. Sci.* **15**, 2096–2107 (2022).
148. Warby, J. *et al.* Understanding Performance Limiting Interfacial Recombination in pin Perovskite Solar Cells. *Advanced Energy Materials* **12**, 2103567 (2022).
149. Zhang Taiyang *et al.* Bication lead iodide 2D perovskite component to stabilize inorganic α -CsPbI₃ perovskite phase for high-efficiency solar cells. *Science Advances* **3**, e1700841.
150. Lu, J. *et al.* Diammonium and Monoammonium Mixed-Organic-Cation Perovskites for High Performance Solar Cells with Improved Stability. *Advanced Energy Materials* **7**, 1700444 (2017).
151. Longo, G. *et al.* Fully Vacuum-Processed Wide Band Gap Mixed-Halide Perovskite Solar Cells. *ACS Energy Lett.* **3**, 214–219 (2018).
152. Lin, Y. *et al.* Matching Charge Extraction Contact for Wide-Bandgap Perovskite Solar Cells. *Advanced Materials* **29**, 1700607 (2017).
153. Khadka, D. B., Shirai, Y., Yanagida, M., Noda, T. & Miyano, K. Tailoring the Open-Circuit Voltage Deficit of Wide-Band-Gap Perovskite Solar Cells Using Alkyl Chain-Substituted Fullerene Derivatives. *ACS Appl. Mater. Interfaces* **10**, 22074–22082 (2018).
154. Zheng, X. *et al.* Defect passivation in hybrid perovskite solar cells using quaternary ammonium halide anions and cations. *Nature Energy* **2**, 17102 (2017).
155. Zhao, D. *et al.* Efficient two-terminal all-perovskite tandem solar cells enabled by high-quality low-bandgap absorber layers. *Nature Energy* **3**, 1093–1100 (2018).
156. Hu, M., Bi, C., Yuan, Y., Bai, Y. & Huang, J. Stabilized Wide Bandgap MAPbBr_xI_{3-x} Perovskite by Enhanced Grain Size and Improved Crystallinity. *Advanced Science* **3**, 1500301 (2016).

157. Chen, C. *et al.* Achieving a high open-circuit voltage in inverted wide-bandgap perovskite solar cells with a graded perovskite homojunction. *Nano Energy* **61**, 141–147 (2019).
158. Leijtens, T. *et al.* Tin–lead halide perovskites with improved thermal and air stability for efficient all-perovskite tandem solar cells. *Sustainable Energy Fuels* **2**, 2450–2459 (2018).
159. Yang, Z. *et al.* Enhancing electron diffusion length in narrow-bandgap perovskites for efficient monolithic perovskite tandem solar cells. *Nature Communications* **10**, 4498 (2019).
160. Brinkmann, K. O. *et al.* Perovskite–organic tandem solar cells with indium oxide interconnect. *Nature* **604**, 280–286 (2022).
161. Gil-Escrig, L. *et al.* Efficient Wide-Bandgap Mixed-Cation and Mixed-Halide Perovskite Solar Cells by Vacuum Deposition. *ACS Energy Lett.* **6**, 827–836 (2021).
162. Chen, W. *et al.* Monolithic perovskite/organic tandem solar cells with 23.6% efficiency enabled by reduced voltage losses and optimized interconnecting layer. *Nature Energy* **7**, 229–237 (2022).
163. Caprioglio, P. *et al.* On the Relation between the Open-Circuit Voltage and Quasi-Fermi Level Splitting in Efficient Perovskite Solar Cells. *Advanced Energy Materials* **9**, 1901631 (2019).
164. Stolterfoht, M. *et al.* How To Quantify the Efficiency Potential of Neat Perovskite Films: Perovskite Semiconductors with an Implied Efficiency Exceeding 28%. *Advanced Materials* **32**, 2000080 (2020).
165. Kapil, G. *et al.* Tin-Lead Perovskite Fabricated via Ethylenediamine Interlayer Guides to the Solar Cell Efficiency of 21.74%. *Advanced Energy Materials* **11**, 2101069 (2021).
166. Li, C. *et al.* Low-bandgap mixed tin–lead iodide perovskites with reduced methylammonium for simultaneous enhancement of solar cell efficiency and stability. *Nature Energy* **5**, 768–776 (2020).
167. Saidaminov, M. I. *et al.* Conventional Solvent Oxidizes Sn(II) in Perovskite Inks. *ACS Energy Lett.* **5**, 1153–1155 (2020).
168. Gupta, S., Cahen, D. & Hodes, G. How SnF₂ Impacts the Material Properties of Lead-Free Tin Perovskites. *J. Phys. Chem. C* **122**, 13926–13936 (2018).

169. Yu, Z. *et al.* Gradient Doping in Sn–Pb Perovskites by Barium Ions for Efficient Single-Junction and Tandem Solar Cells. *Advanced Materials* **34**, 2110351 (2022).
170. Wang, T. *et al.* Highly Air-Stable Tin-Based Perovskite Solar Cells through Grain-Surface Protection by Gallic Acid. *ACS Energy Lett.* **5**, 1741–1749 (2020).
171. Karabacak, T. Thin-film growth dynamics with shadowing and re-emission effects. *Journal of Nanophotonics* **5**, 052501–052501 (2011).
172. da Silva Filho, J. M. C., Gonçalves, A. D., Marques, F. C. & de Freitas, J. N. A Review on the Development of Metal Grids for the Upscaling of Perovskite Solar Cells and Modules. *Solar RRL* **6**, 2100865 (2022).
173. Andrei, V. *et al.* Scalable Triple Cation Mixed Halide Perovskite–BiVO₄ Tandems for Bias-Free Water Splitting. *Advanced Energy Materials* **8**, 1801403 (2018).
174. Rahaman, M. *et al.* Selective CO production from aqueous CO₂ using a Cu₉In₄ catalyst and its integration into a bias-free solar perovskite–BiVO₄ tandem device. *Energy Environ. Sci.* **13**, 3536–3543 (2020).
175. Kroll, M. *et al.* Insights into the evaporation behaviour of FAI: material degradation and consequences for perovskite solar cells. *Sustainable Energy Fuels* **6**, 3230–3239 (2022).
176. Green, M. A. *et al.* Solar cell efficiency tables (Version 60). *Progress in Photovoltaics: Research and Applications* **30**, 687–701 (2022).